A Survey of the Molecular Interstellar Medium of Nearby Galaxies using the Herschel Space Observatory

by

Julia Rebecca Kamenetzky

B.A., Cornell College, 2008

M.S., University of Colorado, 2010

A thesis submitted to the

Faculty of the Graduate School of the

University of Colorado in partial fulfillment

of the requirements for the degree of

Doctor of Philosophy

Department of Astrophysical and Planetary Sciences

2014

This thesis entitled:
A Survey of the Molecular Interstellar Medium of Nearby Galaxies using the Herschel Space Observatory
written by Julia Rebecca Kamenetzky
has been approved for the Department of Astrophysical and Planetary Sciences

Prof. Jason Glenn

Prof. John Bally

Prof. Julie Comerford

Prof. Jeremy Darling

Prof. Veronica Vaida

Date

The final copy of this thesis has been examined by the signatories, and we find that both the content and the form meet acceptable presentation standards of scholarly work in the above mentioned discipline.

Kamenetzky, Julia Rebecca (Ph.D., Astrophysics)

A Survey of the Molecular Interstellar Medium of Nearby Galaxies using the Herschel Space Observatory

Thesis directed by Prof. Jason Glenn

Molecular gas is the raw material of star formation. The ^{12}CO $J = 1 \rightarrow 0$ line is well known to trace the bulk of the cool molecular gas in the interstellar medium of nearby galaxies. New data from the *Herschel* Space Observatory, however, indicates that higher-energy CO rotational lines (e.g. CO $J = 6 \rightarrow 5$) are emitted from significantly warmer molecular gas. Studying this warmer, more luminous gas can provide useful clues for understanding the excitation of molecular gas by star formation.

This work establishes a pipeline to simultaneously model the physical conditions of cool and warm CO gas using the CO spectral line energy distributions from $J = 1 \rightarrow 0$ to $J = 13 \rightarrow 12$. We confirm that, in a variety of galaxies, CO is emitted from a low-pressure/high-mass component traced by the low-J lines and a high-pressure/low-mass component that dominates the luminosity. An initial survey of 17 infrared-luminous galaxy systems observed by the *Herschel*-SPIRE Fourier Transform Spectrometer (FTS) investigates how the physical properties and excitation mechanisms of the warm/cool CO vary with total infrared luminosity, dust mass, atomic fine-structure emission, and more. This work includes an in-depth discussion of the systematic effects of two-component CO modeling as well as comparisons of the derived physical conditions to those of Galactic star-forming regions and high-redshift submillimeter galaxies.

Dedication

Dedicated to my grandmother, Sofia Kamenetzky, for blazing the trail.

Acknowledgements

If I could actually thank all the people that deserve acknowledgement for six years of work, it would take much more than one page. The first thanks must go to my advisor, Jason Glenn, for overseeing this research as well as my professional development, and whose confidence in me opened up so many new opportunities. Thank you for not letting me run away scared before I even got started. Dick McCray became a secondary advisor as well, introducing me to the amazing Supernova 1987A and many new collaborators. Dick, I hope I can emulate your unbridled enthusiasm for adventure in science and life (but you've set the bar pretty high). Naseem Rangwala, Phil Maloney, and Alex Conley have been my go-to experts for so many questions, this thesis would have been next to impossible to complete without their assistance. John Bally stepped up in the interpretation phase of the survey, and the work is undoubtedly better for it. I have collaborated with many more excellent researchers than I can continue to list, but I will just leave a special shout-out to the Z-Spec team for welcoming me in my very first year of research.

I owe much of my ability to get through graduate school to being raised by a tribe of modern-day Amazon warriors (that was me thanking my family). Erin and Susanna, the months leading up to Comps I were only bearable because of you. Thanks to everyone who has contributed to my understanding of science education; I can't emphasize how important this has been to me. This thesis could not have been completed if not for ample refreshing distractions: my friends both new and old, Rocky Mountain Steel Bands, the CU Rec Center, and plenty of Disney soundtracks. Bryce, of all the things in my life for which I could thank you, the most important is: balance.

Contents

Chapter

Tables

Table

Figures

Figure

Chapter 1

Introduction

"There remains a major gap in our knowledge, namely, observations of the cool gas: the fuel for star formation in galaxies. Put simply, current studies probe the products of the process of galaxy formation, but miss the source." - Carilli & Walter [26]

"Thus the interstellar medium is not merely a passive substrate within which stars evolve; it constitutes their direct partner in the Galactic ecosystem, continually exchanging matter and energy with them and controlling many of their properties." - Ferrière [56]

The interplay between the interstellar medium (ISM) and star formation, evolution, and destruction is an important force in the determination of galactic evolution over time. The ISM is enriched with heavy metals only produced in the thermonuclear reactions of stars, and infused with energy from stellar winds and supernova explosions. These modified conditions then affect future star formation, and therefore the interaction is not a one-way street, but a cycle of matter/energy from the ISM, to stars, and back.

1.1 Star Formation History of Galaxies

The star formation (SF) history of the universe began with a steady rise in SF during reionization, followed by a peak at $z \sim 1$ to 3 (the epoch of galaxy assembly). Finally, there was an order-of-magnitude decrease in cosmic SF from $z \sim 1$ to the present [26]. At the current time, star formation is dominated by galaxies of far-infrared luminosity $L_{\rm FIR}$ (8-1000 μm) $\leq 10^{11}$ $L_{\odot}$, which corresponds to a star-formation rate (SFR) ≤ 10 $M_{\odot}$ yr^{-1}, as opposed to $z \sim 2$, when the

Table 1.1. Gas Phases of the Interstellar Medium

Phase	Density [cm^{-3}]	Temperature [K]	Typical Tracers
Hot Ionized Medium (HIM)	< 0.01	$> 10^5$	highly-ionized UV absorption lines, soft-x-ray bg
Warm Ionized Medium (WIM), HII regions	0.1	8000	Hα, optical, IR, radio emission lines
Warm Neutral Medium (WNM), intercloud gas	0.5	8000	HI 21 cm line, Lyα, optical/UV absorption lines
Cold Neutral Medium (CNM), diffuse HI clouds	50.0	80	HI 21 cm line, Lyα, optical/UV absorption lines
Molecular	> 50	10	CO J$=1\rightarrow0$
- Clouds, $\sim 10-100$ pc, 10^{3-4} $M_\odot$	50-500	10	
- Clumps, ~ 1 pc, $50-500$ $M_\odot$	10^{3-4}	10-20	
- Cores, ~ 0.1 pc, $0.5-5$ $M_\odot$	10^{4-5}	8-12	

Note. — Adapted from Table 1.1 of Tielens [168], with molecular properties from Kennicutt & Evans [83] and Bergin & Tafalla [12], and observational tracers from Ferrière [56]. The molecular properties refer to the Galactic disk, not the central molecular zone.

majority of SF was in galaxies with SFRs of ~ 100 $M_\odot$ yr^{-1}. There appear to be two modes of SF in galaxies. One mode, termed the "main sequence" of galaxies, is defined by a tight correlation between SFR and stellar mass (a constant specific star formation rate, sSFR, which is SFR divided by stellar mass). Another set of galaxies define a "starburst" mode which demonstrate higher SFRs for their stellar masses, likely driven by merging [145].

As the quote that opened this chapter stated, much of what we know about the SF history of galaxies was determined by studying the products of SF. This work establishes a set of tools to study the molecular gas conditions — the materials for star formation — via carbon monoxide (CO). Before specifically examining CO, we will first discuss the different phases of the interstellar medium.

1.2 The Interstellar Medium

The rich environment of the interstellar medium is divided into a few different phases of study, summarized in Table 1.1. Star formation, on the scale of galaxies, is a hierarchical process. The hot material on larger scales, e.g. accretion onto galaxies, subsequently cools and smaller scales are established.

In the molecular medium, Table 1.1 summarizes the changing properties from clouds, to clumps (the site of clusters) and cores (the site of individual or binary star formation). Molecular

clouds are generally defined by a notable change from the surrounding medium, for example in pressure, density or chemical composition; observationally, their boundaries are denoted by low-J CO, typically $J = 1 \rightarrow 0$. Their structures are known as Photo-Dissociation Regions or Photon-Dominated Regions [PDRs, 174, 72], and can be thought of as layered like an onion. In the center, both CO and H_2 exist in molecular form; hence, CO is commonly used as a tracer for H_2 emission (see Section 1.3). In the layer surrounding the center, carbon is primarily photodissociated into atomic or ionized form (C and C^+), but a significant portion of hydrogen is still in molecular form due to either self-shielding or dust-shielding. Because CO does not co-exist with the H_2 in this layer, it is known as CO-"dark gas," and may account for 30% of the molecular mass in PDRs [189]. The outermost layer, exposed to the ultraviolet (UV) radiation of massive stars, is composed of mainly ionized H and C.

The physical conditions of the molecular gas are the result of the balance of heating and cooling processes. Some heating sources are: cosmic rays, UV heating from O and B stars (PDRs), X-ray emission from AGN (X-ray dominated regions, XDRs), and mechanical heating due to turbulence or shocks. Cooling can come from atomic fine structure lines, FIR emission from dust, and molecular line emission.

1.3 Carbon Monoxide as Tracer of Molecular Gas

Though H_2 is the most abundant molecule in the ISM, it is not often used to trace molecular mass. H_2 lacks a permanent dipole moment and has weak lines due to long spontaneous decay lifetimes. Perhaps more importantly, the two lowest rotational transitions are 510 and 1,015 K above the ground state and thus require a higher temperature to excite than that of the bulk of the molecular gas. Fortunately, carbon and oxygen are also abundant in the molecular ISM, and carbon monoxide (CO) is formed in molecular clouds; its low excitation energy, low critical density, and abundance make it much more useful for tracing the distribution of H_2 gas.

CO was first observed via $J = 1 \rightarrow 0$ emission from the Orion nebula by Wilson et al. [188]. Extragalactic detections occurred shortly thereafter [142, 159]. Though Galactic and extragalactic

millimeter observations largely occured in parallel, Kennicutt & Evans [83] note a key difference between Galactic and extragalactic observations of molecular clouds: in the Galaxy, we can study the physical process of molecular clouds contracting and fragmenting up close. Because we do not have such resolution in other galaxies, we instead have "focused on the collective effects of star formation, integrated over entire star-forming regions, or often over entire galaxies." As such, extragalactic researchers often rely on "scaling laws, and other parameteric descriptions" for what we know about star formation on such large scales. One such law is the CO-to-H_2 conversion factor, X_{CO}, a relationship between CO $J = 1 \rightarrow 0$ luminosity and molecular mass, reviewed in Bolatto et al. [16]. An underlying principle of many such laws is that "the luminosity of CO is a measure of the number of emitting structures times the mean luminosity per structure" [83]. Another law is the correlation between $L_{\rm FIR}$ and SFR [82].

Absorption by water molecules limits our ability to observe CO from Earth; atmospheric windows allow observation of CO $J = 1 \rightarrow 0$, $J = 2 \rightarrow 1$, and $J = 3 \rightarrow 2$ from some sites, but higher-excitation lines are harder, if not impossible, to measure. The first observations of CO $J = 6 \rightarrow 5$ (690 GHz) from starburst galaxies (NGC 253, M82, IC 342) were reported in Harris et al. [69] using the James Clerk Maxwell Telescope (JCMT) on the summit of Mauna Kea, Hawaii. The authors called the detections "nearly indisputable proof of the existence of gas that is both warm and dense." They speculated that the emission was either coming from moderately excited widespread gas or small regions of highly excited gas (as a well-mixed but separate component from the low-excitation gas) and that it was likely heated by a mechanism other than star formation (cosmic-rays/turbulence, perhaps related to high-mass star formation and supernova remnants).

Bright $J = 6 \rightarrow 5$ lines can be observed in ideal conditions, but little about the CO beyond that line was available until the launch of the *Herschel* Space Observatory in 2009. The Spectral and Photometric Imaging REceiver (SPIRE) Fourier Transform Spectrometer [66] onboard *Herschel* simultaneously observed spectra from 447-1550 GHz, which for nearby galaxies encompasses the ^{12}CO $J = 4 \rightarrow 3$ to $J = 13 \rightarrow 12$ transitions, among other molecular and atomic fine structure lines. For many prominent nearby galaxies, such as M82, Arp 220, and NGC 1068, the emission from

the higher-J lines of CO has proven to be far more luminous than would have been predicted from ground-based observations restricted to low-J lines [e.g. 125, 80, 139, 161, 143, 133]. The predictions of Harris et al. [69] about the existence of warm gas were true, and not just in extremely bright starburst galaxies. The presence of ubiquitious, highly-excited CO emission from galaxies was the catalyst for the work in this thesis. Because the warmer CO is so much more luminous, it represents a greater role in the total energy budget of the gas, and must be considered to study the feedback interactions with cosmic rays, UV light from stars, X-rays from AGN, or mechanical heating.

1.4 Outline of Remainder of Thesis

Chapters 2 and 3 of this thesis are reproduced versions of published papers. I have not included work published as part of completion of my M.S. degree, a study of the dense gas tracers in NGC 1068 [79]. Chapter 2 is a Letter which describes the first observations of rotationally-excited CO from a supernova remnant, SN1987A. Though it does not concern extragalactic ISM properties, it is an excellent introduction to the use of the CO molecule for determining physical conditions of gas under the assumption of local thermodynamic equilibrium (LTE). Non-LTE modeling is introduced in Chapter 3, a case study of the nearby starburst galaxy M82. This chapter establishes the Bayesian likelihood analysis using the non-LTE code RADEX, applied to a fully sampled map from the *Herschel* SPIRE Fourier Transform Spectrometer.

Chapters 4 and 5 detail the bulk of my thesis work, the creation and usage of a pipeline for molecular gas analysis in nearby galaxies observed with the *Herschel* SPIRE Fourier Transform Spectrometer. The two chapters together compose one paper to be submitted for publication. Chapter 4 outlines the observations and methodology used for the planned initial publication of 17 infrared-luminious galaxy systems, including the results. Chapter 5 includes the discussion and interpretation of the results. Chapter 6 describes proposed future work based on this thesis, including high-resolution follow-up with the Atacama Large Millimeter Array (ALMA) and preview of the full survey of all galaxies observed with the Herschel FTS.

The Appendices both supplement the main chapters and detail additional work I have un-

dertaken during my graduate career. Appendix A contains the spectral line maps associated with Chapter 3. Appendices B and C are associated with the survey work, detailing some notes on individual galaxies and photometry fluxes from the literature, respectively. The next two appendices contain some extra, unpublished work done to characterize the derivation of physical conditions from fewer lines than are available with *Herschel* (e.g. from ALMA, AppendixD), and the SPIRE-FTS line profiles and spectral cube creation (Appendix E). The final three appendices include more detail, equations, and quantities used for LTE temperatures and masses (F), radiative transfer of CO (G), and units in radio astronomy (H).

Chapter 2

Carbon Monoxide in the Cold Debris of Supernova 1987A

2.1 Preface

This short paper appeared in the Astrophysical Journal Letters, Volume 773, L34 [81]. While not about the extragalactic ISM, this work is a good introduction to the use of ^{12}CO for measuring physical conditions of molecular gas. In this case, the analysis assumed the molecules were in local thermodynamic equilibrium, saving non-LTE methods and analysis for subsequent chapters of this thesis.

2.2 Abstract

We report spectroscopic and imaging observations of rotational transitions of cold CO and SiO in the ejecta of SN1987A, the first such emission detected in a supernova remnant. In addition to line luminosities for the CO J=1-0, 2-1, 6-5, and 7-6 transitions, we present upper limits for all other transitions up to J=13-12, collectively measured from the Atacama Large Millimeter Array (ALMA), the Atacama Pathfinder EXperiment (APEX), and the *Herschel* Spectral and Photometric Imaging REceiver (SPIRE). Simple models show the lines are emitted from at least 0.01 $M_\odot$ of CO at a temperature > 14 K, confined within at most 35% of a spherical volume expanding at ~ 2000 km s^{-1}. Moreover, we locate the emission within $1''$ of the central debris. These observations, along with a partial observation of SiO, confirm the presence of cold molecular gas within supernova remnants and provide insight into the physical conditions and chemical processes in the ejecta. Furthermore, we demonstrate the powerful new window into supernova ejecta offered

by submillimeter observations.

2.3 Introduction

The ejecta of supernovae (SN) encode important information about the SN explosion dynamics, the nucleosynthetic yield, and the formation of interstellar dust and molecules. At optical and X-ray wavelengths, the dominant feature of SN 1987A is a rapidly brightening $1.66 \pm 0.03''$ [124] ring of "hot spots" where the blast wave is colliding with the innermost of three circumstellar rings [109]. In the radio, this ring can be seen as two bright lobes of emission [118, 197]. Inside this ring, optical and near-infrared spectra showed that the debris from the progenitor's stellar interior is clumped into chemically distinct fragments, originating from the nucleosynthesis that took place before and during the supernova explosion. As the remnant cooled, dust formed and began to obscure the inner ejecta from view at optical wavelengths within the first few years. It was recently estimated that the ejecta of SN1987A contains 0.4-0.7 $M_\odot$ of dust at a temperature of 20 K [105]. Fortunately, observations at far-infrared (FIR) to millimeter wavelengths pierce through the dust, providing a window into the cool interior [15, 87].

A small mass (10^{-3} $M_\odot$) of hot, vibrationally excited CO was seen 192 days after the explosion [96], but the emission faded below detection limits after ∼600 days, when the gas became too cool to excite vibrational transitions [95, 700 K at 800 days]. Theoretical models predict that CO formation would continue after that time, yielding ~ 0.1 $M_\odot$ of CO [32, 33] by 1000 days. Such a mass of CO would have important implications for the evolution of the ejecta, as discussed in Cherchneff & Sarangi [33]: first, dust synthesis can be limited by the depletion of elements by molecules, and second, CO is a powerful coolant, and a cooler environment will favor more efficient dust and molecule formation.

The ejecta of at least 8 other supernove have been observed in the vibrational CO fundamental (4.65 μm) or first overtone (2.3 μm) bands, all within the first few years after their explosion [33, see references listed within their Table 1]. A notable addition is the 300 year old Cassiopeia A remnant, where Rho et al. [141] detected vibrationally excited ^{12}CO with a mass of $\sim 10^{-6}$ $M_\odot$

and temperature as high as 900-1400 K. Until now no direct evidence (via *rotational* molecular emission) had been found for cold (< 900 K) molecular gas within supernova remnants, and no measurement made between ~ 2 and 300 years post-explosion. With the Atacama Large Millimeter Array (ALMA), we have now imaged the ejecta of SN1987A and, for the first time, detected rotational transitions of CO inside a supernova remnant.

2.4 Observations

2.4.1 ALMA

SN 1987A was observed with ALMA at wavelengths of 2.6 mm (Band 3) and 1.3 mm (Band 6) between April and August 2012. During the 2012 Early Science period, ALMA had only a fraction of its final spatial resolution and sensitivity, but could already obtain synthesized beam spatial resolutions of $\sim 1.6 \times 1.5''$ and $0.6 \times 0.5''$, respectively. Observation dates and parameters are listed in Table 2.1. Both bands were observed using Frequency Division Mode (FDM), i.e. 488 kHz channels, to enable detection of any narrow emission lines (none were detected), and later averaged to 50 km s^{-1} spectral resolution (corresponding to one hundred sixty 19 MHz channels in Band 3). The bandwidth per spectral window was 1.875 GHz. All observations used quasars J0538-440 and J0637-752 as bandpass and phase calibrators,respectively. Callisto was observed as an absolute flux calibrator; the absolute flux scale was then applied to the X352 and X1c blocks by equating the flux densities of the two quasars to the flux densities calibrated against a solar system object. System temperature and precipitable water vapor (PWV) calibrations were applied before standard bandpass and complex gain (phase) calibration. In the synthesis imaging, the robust parameter was set to 0, midway between natural and uniform weighting [21].

We have detected emission from the rotational lines of ^{12}CO J=1-0 (115.3 GHz, 2.6mm) and J=2-1 (230.6 GHz, 1.3mm), as well as the red wing of SiO J=5-4 at 217.1 GHz Figure 2.1 is a color composite image showing the ^{12}CO 2-1 emission detected by ALMA (red) and other emission (Hα and [Si I]+[Fe II]) for comparison. The origin of the ^{12}CO J=2-1 emission, marginally larger

Table 2.1. ALMA Observational Parameters

UID (uid://)	Band	Date (2012)	# Ant[a]	PWV [mm]	Int[b] [min]	RMS[c] [mJy bm^{-1}]	BL_{RMS}[d] [m]	BL_{max}[d] [m]
A002/X3c5ee0/X24b	3[e]	05 Apr	16/18	3.1	25	0.13	220	403
A002/X3c7a84/X1c	3	06 Apr	14/17	3.7	25	0.12	225	402
A002/X3c8f66/X352	6[f]	07 Apr	14/17	3.7	25	0.20	225	402
A002/X45f1dd/Xd13	6	15 Jul	16/19	1.3	12	0.14	213	402
A002/X494155/X8be	6	10 Aug	22/23	1.4	25	0.09	194	402

[a]Effective number of antennae after flagging / the total number in the array at the time.

[b]Time on the science target, not including calibration overhead.

[c]RMS (root mean square) noise is measured over a width of 100 km s^{-1}

[d]Baseline.

[e]100.1–103.9 and 112.2-118.8 GHz.

[f]212.5–216.3 and 228.7–232.4 GHz.

Table 2.2. Fitted Line Parameters.

Line	FWHM [km s^{-1}]	Central Velocity [km s^{-1}]	Peak Intensity [mJy/beam]	Integrated Flux [Jy km s^{-1}]	Luminosity[a] [10^{31} erg s^{-1}]
^{12}CO 1-0	2270 ± 190	300 ± 100	4.8 ± 0.3	11.6 ± 1.2	1.33 ± 0.14
^{12}CO 2-1	2150 ± 50	390 ± 20	20.0 ± 0.7	46.0 ± 1.9	10.5 ± 0.4

Note. — Uncertainties are one standard deviation. In subsequent analysis we added in quadrature a 10% continuum subtraction error and a 15% (10%) absolute flux calibration error for ^{12}CO 1-0 (2-1), leading to total line luminosity uncertainties 0.28×10^{31} and 1.5×10^{31} erg s^{-1}, respectively.

[a] Luminosities are calculated using a distance of 50 kpc throughout this work [123].

in extent than the beam (unresolved), is shown here to be less than 1″ in extent and located at the center of the debris. The spectrum shown in Figure 2.2 of the center of the remnant includes some continuum emission. However, consistent with observations by Lakićević et al. [88], this can be identified with the synchrotron emission from the ring. The line profiles are broad (FWHM $\sim$ 2200 km s^{-1}, Table 2.2), consistent with the near-infrared [Si I]+[Fe I] lines [84] and ^{12}CO rotational-vibrational models [96], confirming an origin from the expanding ejecta (and a constant expansion velocity over time). The lines are narrower than those (4,500 to 11,000 km s^{-1}) of ejecta metal lines observed in the visible [59], indicating that the ^{12}CO emission originates from a more centrally-condensed source.

Although our intention with Band 6 was to observe the ^{12}CO J=2-1 line, the red wing of the ^{28}SiO J=5-4 line at 217.11 GHz appeared in the upper sideband. If it has the same profile as ^{12}CO J=2-1, then the amplitude would be 20 ± 5 mJy. Because we do not measure the full flux in the line, we do not conduct further analysis at this time. We see a faint hint of the isotopic ^{29}SiO line at 214.39 GHz (at about 1/10 the estimated amplitude of ^{28} SiO, though narrower), but with marginal statistical significance.

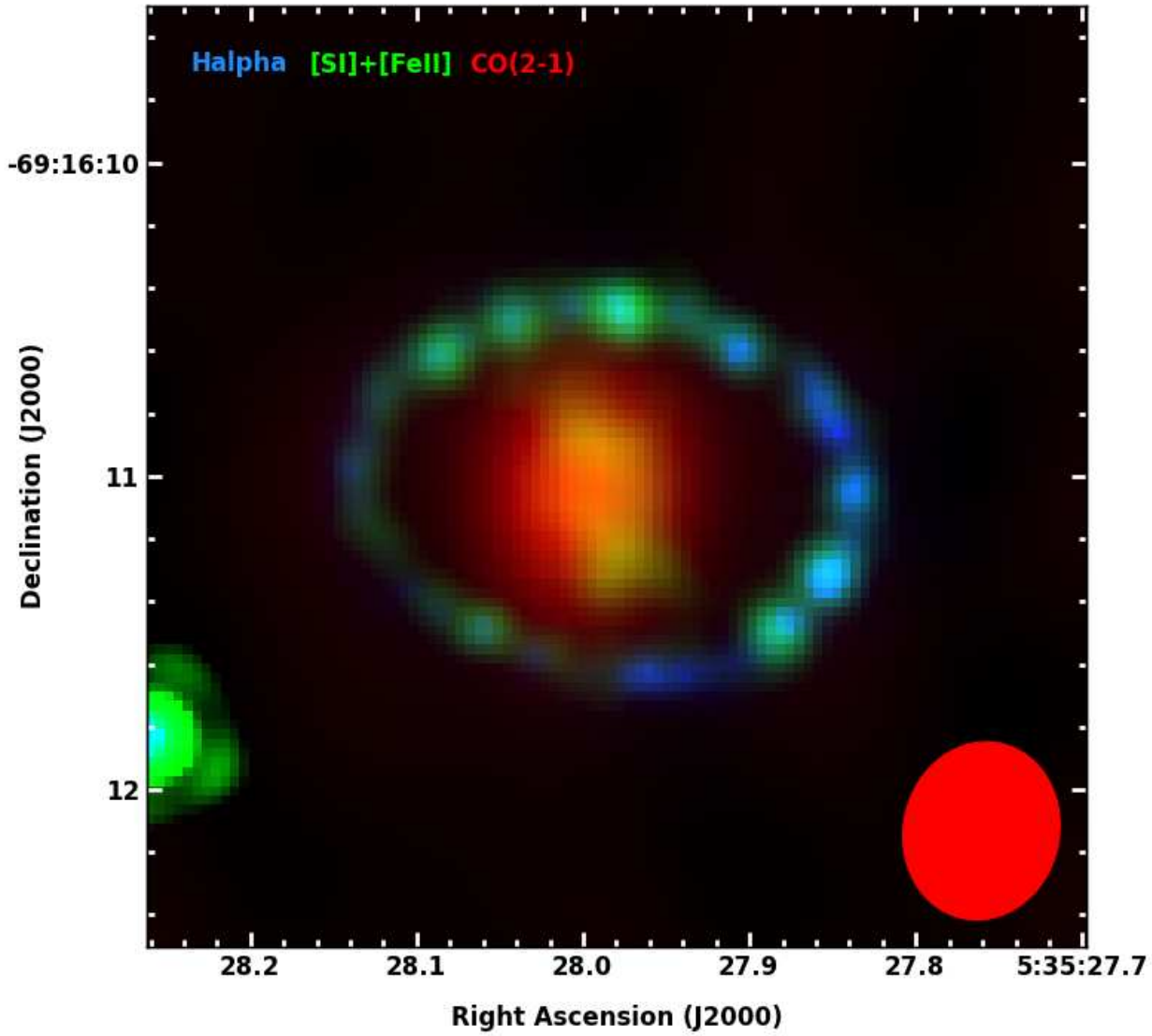

Figure 2.1 A color composite image of SN 1987A. The unresolved ^{12}CO 2-1 line emission detected by ALMA is shown in red, and the red ellipse in the corner is the synthesized beam. Also shown are the Hα emission (blue) and [Si I]+[Fe II] 1.644 μm emission (green in the ring; yellow in the ejecta) observed with the Hubble Space Telescope [91].

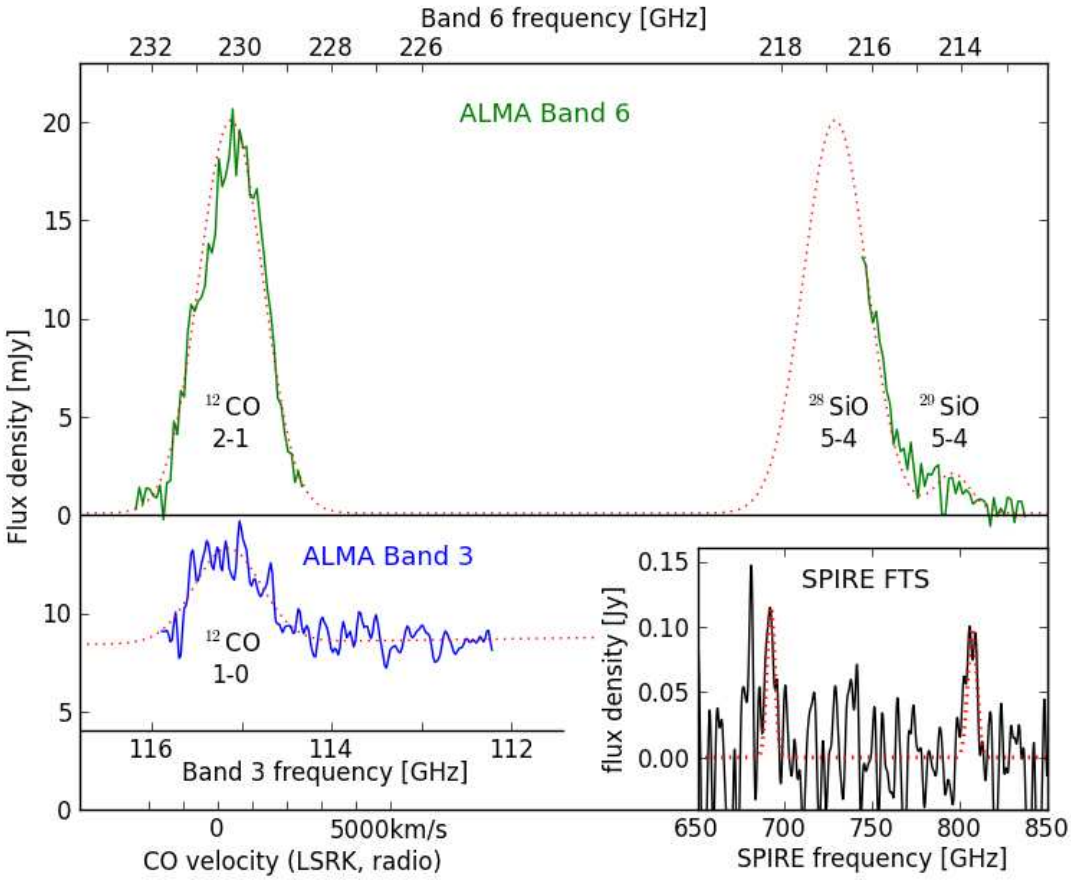

Figure 2.2 ALMA spectra at the center of SN1987A. The 2.6mm Band 3 (bottom left) and the 1.3mm Band 6 (top) are plotted with a common velocity axis calculated for the ^{12}CO 1-0 and 2-1 lines, respectively. The dotted lines are the best-fit Gaussians to the ^{12}CO lines, ^{28}SiO and ^{29}SiO and a continuum with synchrotron spectral index of -0.8. A zoomed-in portion of the continuum-subtracted SPIRE spectrum is shown in the bottom right, with the best-fit Gaussians of the J=6-5 and J=7-6 lines as dotted lines.

2.4.2 APEX

We also observed the ^{12}CO J=3-2 line of SN 1987A using the Atacama Pathfinder Experiment (APEX) in Chile (European Southern Observatory proposal ID: 090.D-0515(A)). We used the SHeFI receiver [120] at the central frequency of 345.796 GHz, and upper side band and wobbler beam switching mode with two different chopping distances of 40 and 45″. The back end system has 8192 × 2 channels of 61 kHz width. The two bands are 4 GHz wide each (1 GHz overlapping). The system temperature was typically 200 K. We chose 1.5 hours (of the most stable sky conditions) of the total 4.5 hours of data acquired over four days (2012 October 6, 8, 10 and 16, PWV from 0.2–0.7 mm). The focus was checked with Jupiter, *o* Cet and R Dor; the pointing was regularly checked and updated on the nearby pointing source R Dor. The antenna temperature was converted to main beam temperature and then to flux in Jy using 41 Jy K^{-1} (for the 17″ beam). We subtracted the baseline after combining all the spectra using the CLASS software and obtained an upper limit on the ^{12}CO J=3-2 line of 94 mJy (5.2 $\times 10^{32}$ erg s^{-1}).

2.4.3 SPIRE

The ^{12}CO J=4-3 to J=13-12 transitions are encompassed by the SPIRE [66] Fourier Transform Spectrometer (FTS, 447 to 1550 GHz) onboard the *Herschel* Space Observatory [134]. SN1987A was observed by SPIRE on 2012 June 12 for $\sim$ 4 hours (Observation ID 1342246989, proposal GT2_mbarlow_1) as part of the MESS program [67] and reduced in HIPE v11. We detected two lines, J=7-6 and J=6-5, at (7.0 ± 2.5) and $(8.0 \pm 2.0) \times 10^{-18}$ W m^{-2}. In luminosity, they are (2.01 $\pm$0.8) and $(2.4 \pm 0.6) \times 10^{33}$ erg s^{-1}, respectively. These lines were fit with a FWHM of 2300 km s^{-1} (Figure 2.2), consistent in origin with the emission measured by ALMA. Those two CO lines fall in the lowest noise region of the entire band (the sensitivity is wavelength dependent), though we were also able to derive upper limits of 1.3-5.2 $\times 10^{-17}$ W m^{-2} for the remaining lines. In increasing order of J_{up} from 4 to 13, excluding 6 and 7, the upper limits are 1.5, 1.3, 1.4, 2.6, 3.0, 4.0, 3.0, and 5.2 $\times 10^{-17}$ W m^{-2}.

To determine the upper limits, we took an artificial ^{12}CO input spectrum with zero continuum and all eight lines given fluxes of 8.7 $\times 10^{-18}$ W m^{-2} and very narrow widths. We then broadened the lines with a Gaussian function having a FWHM of 2300 km s^{-1}. We added the broadened ^{12}CO line spectrum, multiplied by flux scaling factors ranging from 1 to 10, to the observed SLW and SSW subspectra in order to judge the flux scaling factor needed for each ^{12}CO line to yield a definite detection (as judged by a line flux measurement that yielded a line flux within 30% of the input value).

2.5 Interpretation

Most of the emitting ^{12}CO is expected to reside in chemically distinct clumps, composed mostly of oxygen and carbon, in the inner supernova debris [108, 78]. We interpret the observed ^{12}CO emission lines with a simplified model, in which a total mass M_{CO} of ^{12}CO molecules is found in clumps of uniform density and temperature (T_{CO}) that occupy a volume V_{CO} of the inner debris. We assume that the inner debris is confined within a freely expanding sphere of volume V_{max} defined by radius $R = vt = 2000$ km s$^{-1}\times$ 25 years. (Note that the diameter, twice this expansion radius, fully encompasses the FWHM of the line emission). The clumps occupy a fraction, f_{CO}, of that total volume, such that $V_{max} \times f_{CO} = V_{CO}$. In reality, the carbon/oxygen zone is likely composed of clumps that do vary in chemical composition, density, and temperature [77]. Because we do not resolve individual clumps, we are modeling the bulk properties that describe the sum of the ^{12}CO emission. We calculate the luminosities using the Sobolev escape probability approximation [28], where the expressions for the line luminosity, escape probability (P_{esc}), and the Sobolev optical depth (τ_S) take simple forms in the case of freely expanding supernova debris [108, equations 5-9]. Optically thin emission depends only on M_{CO} and T_{CO}, whereas at high optical depths, the line luminosity is described by the optically thick limit and depends only on V_{CO} and T_{CO}.

In the above model, we assume that the lines are in Local Thermodynamic Equilibrium (LTE) with their surroundings and the populations of the rotational levels are described by an excitation temperature equal to the kinetic temperature, T_{CO}. The higher-J transitions are less

likely to be in LTE; radiative decays tend to depopulate higher-J rotational levels. In general, the population levels and line luminosities will depend on the product of the collision partner density (likely oxygen, carbon, O_2 and other ^{12}CO molecules) and collision rate coefficients, which are unknown for these species. To make a rough estimate, we examined the collisional rate coefficients for H_2 + CO [192], H + CO [8], and H_2O + CO [64]. The critical densities for the J=2-1 line are one to two orders of magnitude below the modeled density of the O/C clumps [78, 1.8×10^5 cm^{-3} at 25 years], indicating that these lines are well approximated by LTE. The rate cofficients for the proxy species vary significantly for the higher-J lines, introducing considerable uncertainties in modeling the level populations. Therefore, the LTE predictions for the spectral line energy distributions (SLEDs, as shown in Figure 2.3) should be considered upper limits for lines above J=3-2; the actual line luminosities for the same physical conditions will be lower. This means that the current SPIRE upper limits cannot constrain the physical parameters of our model, but the J=6-5 and 7-6 detections can exclude parameters that predict low LTE luminosities.

We first consider the fluxes of the ^{12}CO J=1-0 and 2-1 lines measured by the ALMA, which are in LTE. We can determine a robust lower limit to the mass by assuming that the J= 1-0 line is optically thin, which yields $M_{CO} > 0.01$ M$_\odot$ at < 10 K. However, the line luminosity ratio $L_{2-1}/L_{1-0} = 7.9 \pm 2.0$ is not consistent with the ratio > 20 expected in the optically thin case. Instead, it is consistent with the ratio of 8 expected in the optically thick case ($L_{\mathrm{J,J-1}}/L_{1,0} \approx \mathrm{J}^3$) in the Rayleigh-Jeans approximation, valid for temperatures above 10 K. This case, L_{thick}, defines an upper limit to the line emission because the specific intensity of radiation emitted by a surface cannot exceed the Planck function, $B_\nu(T_{CO})$. The ^{12}CO J=3-2 line is probably also optically thick; assuming so, we predict a luminosity of $3.4 \times L_{2-1} = 3.6 \times 10^{32}$ ergs^{-1} and a peak flux of 65 mJy, lower than the upper limit from APEX.

As mentioned, for a freely expanding volume, the resulting value of L_{thick} depends only on the net *volume*, V_{CO}, of the emitting material and the excitation temperature, independent of M_{CO}. The product of T_{CO} and V_{CO} is 5.3×10^{52} cm^3 K.

Figure 2.3 shows the ALMA and SPIRE line luminosities from this work along with example

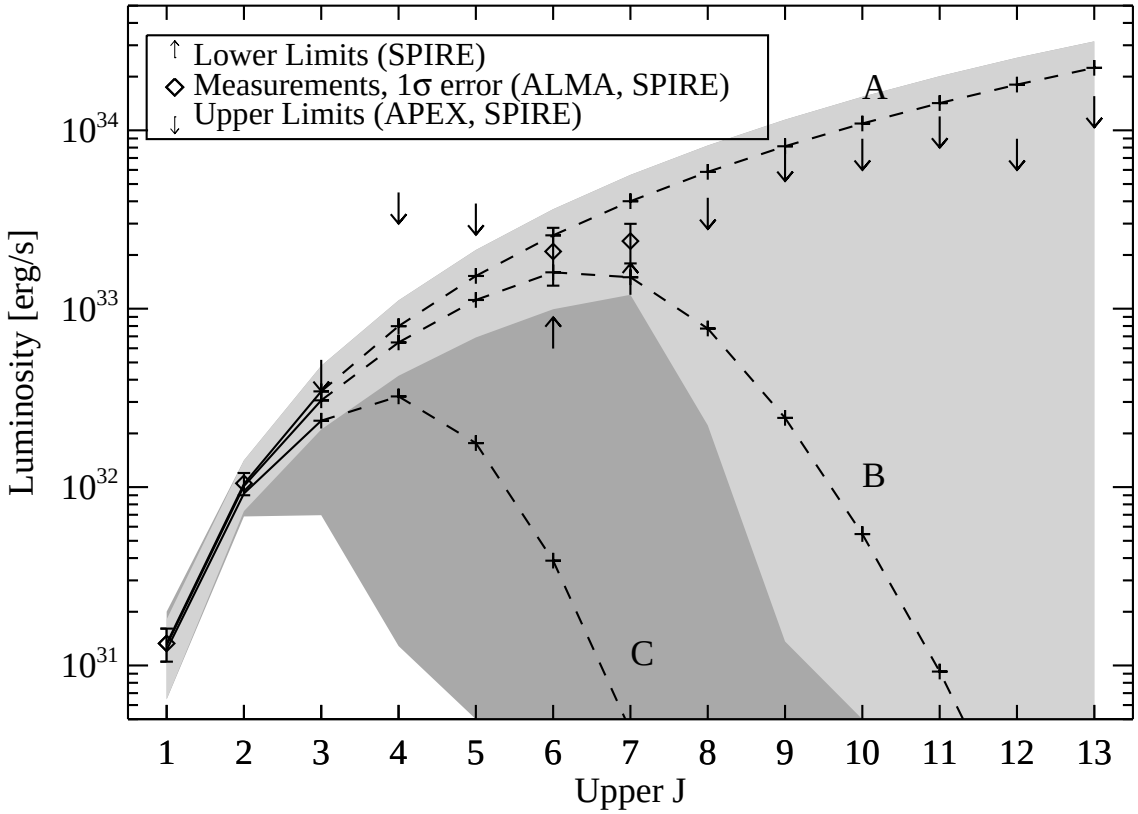

Figure 2.3 ^{12}CO measurements and upper limits with example spectral line energy distributions (SLEDs). Diamonds, downward arrows, and upward arrows (at the base of the arrow) indicate measurements, lower limits, and upper limits, respectively. The light gray shaded region illustrates possible LTE SLEDs consistent with ALMA measurements and SPIRE lower limits (solutions of at least 5% of the maximum likelihood solution); the dark gray region indicates additional (low-T_{CO}, high-f_{CO}) solutions that are excluded by SPIRE lower limits. Lines A, B, and C are example LTE SLEDs; lines are dashed above J=3-2 to indicate that LTE is an upper limit and the true luminosity is likely lower than this curve. Line A [B, C] corresponds to T_{CO} = 132 [27, 13] K, M_{CO} = 0.55 [0.063,0.028] $M_\odot$, f_{CO} = 0.025 [0.141,0.348]. Lines A and B may both be consistent with available data despite arising from very different physical conditions; Line C is an example of a set of conditions that can be excluded given the SPIRE J=6-5 and J=7-5 measurements.

SLEDs (labeled A, B, and C), all of which are consistent with the ALMA measurements, despite arising from very different physical conditions. We cannot constrain the mass from optically thick emission, but we can find a minimum mass at which the emission is optically thick and reproduces the ALMA observations. For all combinations of temperature and $f_{CO} < 1$, the minimum mass is 0.01 $M_\odot$ (3σ lower limit).

Though the SPIRE lines cannot be modeled accurately, we can rule out any parameter space whose LTE luminosity does not reach the lower limits of the two measured lines. In Figure 2.3, the lower limits are given by the SPIRE measurements minus 2σ (upward arrows). The parameter space excluded by the SPIRE lines is highlighted by the dark gray region, clearly excluding low-T_{CO} and high-f_{CO} solutions. The light gray region shows possible SLEDs allowed by the ALMA, APEX, and SPIRE measurements and contains only temperatures greater than 14 K and filling factors less than 0.35; the minimum mass to satisfy these conditions is still 0.01 $M_\odot$.

2.6 Discussion and Conclusions

From the above analysis, the C/O clumps in SN1987A contain at least 0.01 $M_\odot$ of ^{12}CO, an order of magnitude greater than measured in the first few years after the explosion [96]. The implication is that ^{12}CO has continued to form over the past 25 years. According to a model of the evolution of the optical and near-IR emission line spectrum [78] at $t = 8$ years, the carbon/oxygen clumps have a mass of carbon plus oxygen of 0.58 $M_\odot$ and a filling factor $f_{C/O} = 0.02$. Such a small filling factor would imply a higher ^{12}CO temperature (> 100 K) and at least 0.2 $M_\odot$ of ^{12}CO (1σ lower limit).

Other studies have specifically examined molecule formation within the distinct chemical zones of the ejecta. For example, a 15 $M_\odot$ progenitor at solar metallicity may form > 0.2 $M_\odot$ of ^{12}CO, a significant amount of which is formed as early as 600 days after the explosion [33]. As the progenitor of SN1987A is most likely a 19 ± 3 $M_\odot$ blue giant with metallicity similar to the Large Magellanic Cloud [190, 1/3-1/4 solar], we can also compare to results from Population III stars (with zero metallicity). Cherchneff & Dwek [32] found similar results for a Pop III 20 $M_\odot$

progenitor, estimating 0.27 $M_\odot$ of ^{12}CO produced on the same timescale. The velocity adopted for the CO model presented here matches that used in the Cherchneff & Dwek [32] study (2242 km s^{-1}). Though our observations alone can provide only a minimum mass, the combination of the ALMA spectra results with the model computed by Jerkstrand et al. [78] is consistent with theoretical models of molecule formation that have been untested until now.

In addition to the lower limits for temperature and mass, *Herschel*-SPIRE provides an upper limit to the total ^{12}CO luminosity. Recently, using the photometric capability of *Herschel* (100-500 μm), the far-IR luminosity of the debris of SN1987A was measured to be 8.45 $\times 10^{35}$ erg s^{-1}, and was attributed to thermal emission radiated by a massive reservoir of cold dust grains in the ejecta by Matsuura et al. [105]. The lack of detection with SPIRE FTS in the same wavebands provides an upper limit to the contribution from rotationally excited ^{12}CO molecules to the Far-IR luminosity, with ^{12}CO contributing at most 8.4%. This demonstrates that emission from dust grains is still the most viable explanation for the excess FIR emission detected with *Herschel*.

We have presented measurements for four ^{12}CO rotational transitions in the ejecta of SN1987A, as well as upper limits for eight additional lines. The unprecedented angular resolution of ALMA firmly locates this emission as originating from the inner ejecta. The J=2-1 and J=1-0 lines are optically thick and require at least 0.01 $M_\odot$ of ^{12}CO. These results, combined with previous dust results from *Herschel*, illustrate a SN environment filled with cool molecules and gas merely 25 years after the explosion. These results are not only the first of their kind, they are also exciting as a demonstration for future work. Unlike optical observations, where the redshifted emission is largely obscured by dust, (sub)millimeter observations can see the entire velocity range of the debris. Surfaces of constant Doppler shift are planar sections of the freely expanding SN debris, and the ^{12}CO lines are sufficiently bright that we will be able to image the debris in 3 dimensions with resolution better than 0.02″ through Doppler tomography with the full ALMA array [75, 40, 91]. ALMA will be able to do the same with different molecules (e.g. SiO) to probe chemically distinct regions, which likely have different morphologies.

Chapter 3

Herschel-SPIRE Imaging Spectroscopy of Molecular Gas in M82

3.1 Preface

This paper appeared in the Astrophysical Journal, Volume 753, Page 70 [80]. It can be considered a case-study of one galaxy which establishes a primary component of the methodology for the survey presented in the next few chapters, namely that of non-LTE Bayesian likelihood modeling of CO with RADEX. Unlike the survey, which relies only on single-beam observations of galaxies, this work presents and discusses a fully sampled map of M82.

3.2 Abstract

We present new *Herschel*-SPIRE imaging spectroscopy (194-671 μm) of the bright starburst galaxy M82. Covering the CO ladder from J = 4 $\rightarrow$ 3 to J = 13 $\rightarrow$ 12, spectra were obtained at multiple positions for a fully sampled $\sim$ 3 x 3 arcminute map, including a longer exposure at the central position. We present measurements of ^{12}CO, ^{13}CO, [C I], [N II], HCN, and HCO$^+$ in emission, along with OH$^+$, H_2O^+ and HF in absorption and H_2O in both emission and absorption, with discussion. We use a radiative transfer code and Bayesian likelihood analysis to model the temperature, density, column density, and filling factor of multiple components of molecular gas traced by ^{12}CO and ^{13}CO, adding further evidence to the high-J lines tracing a much warmer ($\sim$ 500 K), less massive component than the low-J lines. The addition of ^{13}CO (and [C I]) is new and indicates that [C I] may be tracing different gas than ^{12}CO. No temperature/density gradients can be inferred from the map, indicating that the single-pointing spectrum is descriptive of the

bulk properties of the galaxy. At such a high temperature, cooling is dominated by molecular hydrogen. Photon-dominated region (PDR) models require higher densities than those indicated by our Bayesian likelihood analysis in order to explain the high-J CO line ratios, though cosmic-ray enhanced PDR models can do a better job reproducing the emission at lower densities. Shocks and turbulent heating are likely required to explain the bright high-J emission.

3.3 Introduction

M82 is a nearly edge-on galaxy, notable for its spectacular bipolar outflow and high IR luminosity [5.6×10^{10} $L_\odot$, 149]. Though its high inclination angle of 77° makes it difficult to determine, M82 is likely a SBc barred spiral galaxy with two trailing arms [107]. Its redshift-independent distance is about 3.4 ± 0.2 Mpc [36], and after correcting the commonly cited redshift (0.000677, de Vaucouleurs et al. [39]) with WMAP-7 parameters to the 3K CMB reference frame, we find a redshift of 0.000939. Given this distance we assume a conversion of 17 pc/″.

Due to its proximity, M82 is an exceptionally well-studied starburst galaxy. High star formation rates [9.8 $M_\odot$ yr^{-1}, likely enhanced by interactions with M81, 196] and a large gas reservoir produce bright molecular and atomic emission lines. Such lines can yield important information on the interaction between the interstellar medium (ISM) and star formation (SF) processes, such as the influence of SF on the ISM through photon-dominated region (PDR) or other excitation, as traced by intermediate to high-J CO rotational lines.

Ground-based studies of CO in M82 are numerous [184, 103, 180, 179, 182], examining both morphology and physical conditions of the gas. High-resolution CO maps of the 1 kpc disk indicate that the emission is largely concentrated in three areas: a northeast lobe, southwest lobe, and to a lesser extent, a central region [see Figure 1 of 180]. The two lobes are separated dynamically, as can be seen in position-velocity diagrams [Figure 3 of 180]. Outside of the disk, molecular gas emission is also detected in the halo/outflow [166, 178].

In addition to examining the morphology of molecular gas, CO emission lines can be used to determine the physical conditions of the molecular gas in galaxies. Previously, due to terrestrial

atmospheric opacity, only the first few lines in the CO emission ladder could be studied. The first studies of higher-J lines (described below) have indicated that they can trace components of gas separate from those measurable with low-J lines. Many of the most interesting questions about galaxy formation, evolution, and star formation concern the balance of different energy sources, i.e. what role might cosmic rays, ultraviolet light from stars, X-rays from powerful AGN, or turbulent motion play in the star formation history of various galaxies? In what way does star formation influence the molecular gas, and vice versa? Estimating the influence of these various energy sources, however, often depends on knowing the physical conditions of the gas. We therefore model physical conditions of these high-J lines first in order to inform our later discussion on energy sources. Other molecules are also useful in this study; in a ground-based survey of 18 different molecular species, Aladro et al. [2] also found that some molecules trace different temperature components than others and that the different chemical abundances in M82 and NGC253 may indicate different evolutionary stages of starbursts.

The *Herschel Space Observatory* [134] is the unique facility that can measure the submillimeter properties of nearby galaxies in a frequency range that cannot be observed from the ground. As one of the brightest extragalactic submillimeter sources, M82 has been studied extensively with *Herschel*. For example, the imaging photometer of the Spectral and Photometric Imaging REceiver [SPIRE, 66] has been used to study the cool dust of M82, revealing wind/halo temperatures that decrease with distance from the center with warmer starburst-like filaments between dust spurs [147]. The tidal interaction with M81 was likely very effective in removing cold interstellar dust from the disk; more than two thirds of the extraplanar dust follows the tidal streams. Panuzzo et al. [125] used the SPIRE Fourier-Transform Spectrometer (FTS) to study a single spectrum of the ^{12}CO emission from $J = 4 \rightarrow 3$ to $J = 13 \rightarrow 12$ to find that these higher-J CO lines likely trace a $\sim$ 500 K gas component not seen in the $\sim$ 30 K component that can be observed from ground-based studies. Also on-board *Herschel* is the Heterodyne Instrument for the Far Infrared (HIFI, de Graauw et al. [38]), which consists of a set of 7 heterodyne receivers with resolution of 125 kHz to 1 MHz for electronically tuneable frequency coverage of 2 x 4 GHz; it covers 480 - 1910 GHz.

HIFI found ionized water absorption from diffuse gas [181] and high-J transitions of the CO ladder. These CO transitions indicated a combination of one low and two high density gas components via comparison to PDR models [97].

We confirm the presence of multiple molecular hydrogen thermal components in M82 by performing a more in-depth modeling analysis on a deeper dataset as part of the *Herschel* Very Nearby Galaxies Survey. We add to existing data by using the SPIRE FTS mapping mode, providing spectroscopic imaging of a region approximately $3'$ x $3'$, which helps us confirm our source-beam coupling corrections. We also present a deep pointed spectrum [64 scans vs. 10 scans in 125] in order to detect fainter lines, such as ^{13}CO, H_2O, OH^+, HF, and more.

We add depth to the analysis by modeling both the cool and warm components of molecular gas, and simultaneously accounting for ^{12}CO, ^{13}CO, and [C I]. We also use [C I] emission as a separate estimate of total hydrogen mass and other absorption lines for column density estimates. We first analyze the CO excitation using likelihood analysis to determine the physical conditions, and then compare to possible energy sources. Our likelihoods test the uniqueness and uncertainty in the conditions, as has also been done in Naylor et al. [117], Kamenetzky et al. [79], Scott et al. [155], Bradford et al. [17], Panuzzo et al. [125], Rangwala et al. [139].

Our observations are described in Section 3.4. We describe the Bayesian likelihood analysis used to find the best physical properties of the molecular gas in Section 3.5 and present the results in Sections 3.6.1 and 3.6.2. In the remainder of Section 3.6, we discuss absorption results that are new to this study, possible excitation mechanisms of the warm gas, and comparisons to other galaxies. Conclusions are presented in Section 3.7.

3.4 Observations with SPIRE

3.4.1 The SPIRE Spectrometer

The SPIRE instrument [66] is on-board the *Herschel Space Observatory* [134]. It consists of a three-band imaging photometer (at 250, 350, and 500 μm) and an imaging Fourier-transform

spectrometer (FTS). We are presenting observations from the FTS, which operates in the range of 194-671 μm (447-1550 GHz). The bandwidth is split into two arrays of detectors: the Spectrometer Long Wave (SLW, 303-671 μm) and the Spectrometer Short Wave (SSW, 194-313 μm). The SPIRE spectrometer array consists of 7 (17) operational unvignetted bolometers for the SLW (SSW) detector, arranged in a hexagonal pattern. In the SLW, the beam FWHM is about 43″ at its largest, dropping to 30″ and then rising again to 35″ at higher frequency. The SSW beam is consistently around 19″.

Two SPIRE FTS observations from Operational Day 543 were utilized in this study: one long integration single pointing of 64 scans total ("deep", Observation ID 1342208389, 84 min [71 min integration time], AOR "SSpec-m82 -deep") and one fully-sampled map ("map", Observation ID 1342208388, $\sim$ 5 hrs, AOR "Sspec-m82"). The map observation was conducted in high-resolution (HR) mode and the deep observation was conducted in high+low-resolution (H+LR) mode. Both were processed in high-resolution mode ($\Delta\nu \sim 1.19$ GHz) with the *Herschel* Interactive Processing Environment (HIPE) 7.2.0 and the version 7.0 SPIRE calibration derived from Uranus [165, 60].

3.4.2 Spectral Map Making Procedure

In mapping mode, the SPIRE detector arrays are moved around the sky to 16 different jiggle positions, creating 112 and 272 spectra of 16 scans each for SLW and SSW, respectively, covering an area of the sky approximately 3 x 3 arcminutes. The positions of these scans on the sky are presented in Figure 3.1, with blue asterisks for SLW and red diamonds for SSW.

The recommended map making method bins the spectra into pixels approximately one half the FWHM of the beam for each detector, which are about 35″ for SLW and 19″ for SSW, leading to pixel sizes of 17.5″and 9.5″. We wrote a custom script to create the map, based largely on the NaiveProjection method described in the SPIRE documentation for HIPE. Each of the 256 scans per detector were processed individually. All scans for a given detector and jiggle position

[0] SPIRE Data Reduction Guide, http://herschel.esac.esa.int/hcss-doc-7.0/print/spire_dum/spire_dum.pdf, December 2, 2011.

falling within a given pixel were then averaged and an error bar for each wavenumber bin average is determined as the standard deviation of the scans divided by the square root of number of scans. All detector averaged spectra that fall into a pixel are then averaged using a weighted mean (where the weight is the inverse of the square of the error bar). We used the same 9.5″ grid for both bands.

Using a 9.5″ grid introduced more blank pixels in the SLW map, because the SLW map is more sparsely sampled because of its larger beam, as can be seen in Figure 3.1. However, this enabled the comparison of the same spectral locations across both bands (where the data were available), without averaging together spatially discrepant spectra in the SSW, as would happen if pixels were made larger. We emphasize that the blank pixels are somewhat artificial; the whole galaxy has been mapped, and the pixels locations are simply meant to indicate the central location of the detectors, though the beam size is larger than the pixel boundaries.

3.4.3 Line Fitting and Convolution Procedure

The mirror scan length determines the spectral resolution of the spectrum. Because the scan length is necessarily finite, the Fourier-Transformed spectrum contains ringing; therefore, the instrument's line profile is a sinc function, as can be clearly seen in Figures 3.3 and 3.4. The spectrum also contains the underlying continuum which must be removed before fitting the lines, which we do sequentially rather than simultaneously (see exceptions below). We isolate ± 25 GHz around the expected line center, and mask out the ± 6 GHz around the line center. We then fit the remaining signal with a second order polynomial fit to determine the continuum shape. After subtracting this continuum fit, we then use a Levenberg-Marquardt least-squares method to fit each line as a sinc function with the following free parameters: central frequency, line width, maximum amplitude, and residual (flat) baseline value. The baseline value stays around zero because the continuum has already been subtracted. The central frequency is limited such that the line center is no greater than ± 300 $\mathrm{km\,s^{-1}}$ from the expected frequency given the nominal redshift of M82. For comparison, the resolution varies from 230 to 810 $\mathrm{km\,s^{-1}}$, from the shorter to longer wavelength ends of the band.

For the deep spectrum, we detect weaker lines than in the map spectra. However, ringing from the strongest lines can interfere with the signal; therefore we first fit the strong lines (^{12}CO, [C I], and [N II]) using the procedure outlined above and subtract their fitted line profiles from the spectrum. After all of the ^{12}CO, [C I], and [N II] lines are fitted and subtracted from the spectrum, we then do a second pass to fit the weaker lines. An illustration of the difference this process can make for the ^{13}CO J$=5\rightarrow4$ line is in Figure 3.4.

In general, all of the lines are fit independently, with a few exceptions: the ^{12}CO J$=7\rightarrow6$ and [C I] J$=2\rightarrow1$ lines are a mere 2.7 GHz away in rest frequency, and ground state p-H_2O and o-H_2O^+ lines are separated by only 2 GHz. These two pairs must be fit simultaneously. Both are fit independently to supply initial guesses, which are then used to fit both lines as the sum of two sinc functions, each with their own central wavelength, width, and amplitude, but with one baseline value.

The integrated flux is simply the area under the fitted sinc function, which is proportional to the product of the amplitude and line width (converted to km/s). The error in the integrated flux is based on propagating the errors from the fitted parameters themselves. We note that the error estimation assumes all wavenumber bins are independent of one another, but that is in fact not entirely true in a FT spectrometer. Though lines that are separated spectrally do not affect one another greatly (hence why we fit most lines independently), within each line fit the data points used in the 50 GHz range around the line center are not independent.

The beam size of the SPIRE spectrometer varies between the two detector arrays. In addition, it varies across the spectral range of the SLW, as described in Section 3.4.1, and is not strictly proportional to wavenumber due to the presence of multiple modes in the SLW detectors [30]. When examining the spectral line energy distribution (SLED), it is imperative to scale all fluxes to a single beam size. For the map observation, we first fit the spectra as they were (with no correction factor). An example of integrated flux map, prior to any convolution or beam correction, is presented in Figure 3.2, with all other integrated flux maps available in the online version of the Journal. For the SLW detector, we present integrated flux maps using both 9.5″ and 17.5″ pixels.

The integrated flux maps for each line were then convolved with a kernel that matched the beams to the beam of the ^{12}CO J = 4 → 3 map, which has a FWHM of 43″. The kernel was created using a modified version of the procedure decribed by Bendo et al. [11] [see also 63]. However, instead of directly applying Equation 3 from Bendo et al. [11] to the images of the beams, we applied the equation to one-dimensional slices of the beams to create the radial profile of convolution kernels, which we then used to create two-dimensional kernels. The approach worked very effectively for creating kernels to match beams observed with SSW to the ^{12}CO J = 4 → 3 map. However, in cases where we created convolution kernels for matching beams measured at two different wavelengths by the SLW array, we needed to manually edit individual values in the kernel radial profiles to produce effective two dimensional kernels.

After the mathematical convolution of the integrated flux map with the kernel (resampled to match our map sizes), the fluxes were all converted to the units of Jy km s^{-1}/beam, referring to the ^{12}CO J = 4 → 3 beam. The ratio of beam areas was determined empirically by convolving the kernel with the smaller (observed) beam peak normalized to 1 and determining the ratio required to produce the larger $\Omega_{\mathrm{CO\,J=4\rightarrow3}}$ beam with the same peak (simulating the observation of a point source of 1 Jy km s^{-1}). To account for blank pixels, only the portion of Ω_{kernel} that encompasses data was used in the aforementioned conversion.

For the deep spectrum, we used the same source-beam coupling factor ($\eta_c(\nu)$) as in Panuzzo et al. [125], which was derived by convolving the M82 SPIRE photometer 250 μm map [147] with appropriate profiles to produce the continuum light distribution seen with the FTS. The deep spectrum was multiplied by this factor before the line fitting procedure. The deep spectrum is presented in four parts in Figure 3.3, and the measured lines fluxes ($\geq 3\sigma$) are in Table 3.1.

The central pixel of the convolved maps offers a direct comparison to the source-beam coupling corrected deep spectrum. In the SLW, these two SLEDS are within ± 16% of one another. Later, we assume calibration error of 20%, so these differences are within those bounds. There is greater variation in the SSW band, though this is the region in which the signal to noise of the lines greatly drops. When 20% calibration error is included, all the line measurements have overlapping error

bars with the exception of ^{12}CO J = 13 → 12, where the deep spectrum measurement is more than twice that of the map. The ^{12}CO J = 13 → 12 map, however, has a S/N of only 4 in the central pixel, with only 60/399 pixels having S/N greater than 3. We primarily use the deep spectrum for our likelihood analysis because of the higher S/N and access to more faint lines, but compare with using the convolved map central pixel in Section 3.6.2. The similarity of the two SLEDs, within error bars, using two independent methods (the derived $\eta_c(\nu)$ from photometry comparisons vs. map convolution) to account for source-beam coupling, indicates that both methods are robust.

Though the maps do not provide adequately high spatial/spectral resolution for a detailed study of the morphology of the emission, some qualitative assessments can be made. For example, the line centroids do trace the relative redshift/blueshift of the northeast and southwest components [$v_{hel} \sim 300$ km s^{-1} and 160 km s^{-1}, respectively, 97]. However, we do not resolve the two separate peaks in flux. The capabilities of these maps to resolve gradients in the physical parameters modeled in this work will be discussed in Section 3.6.2.

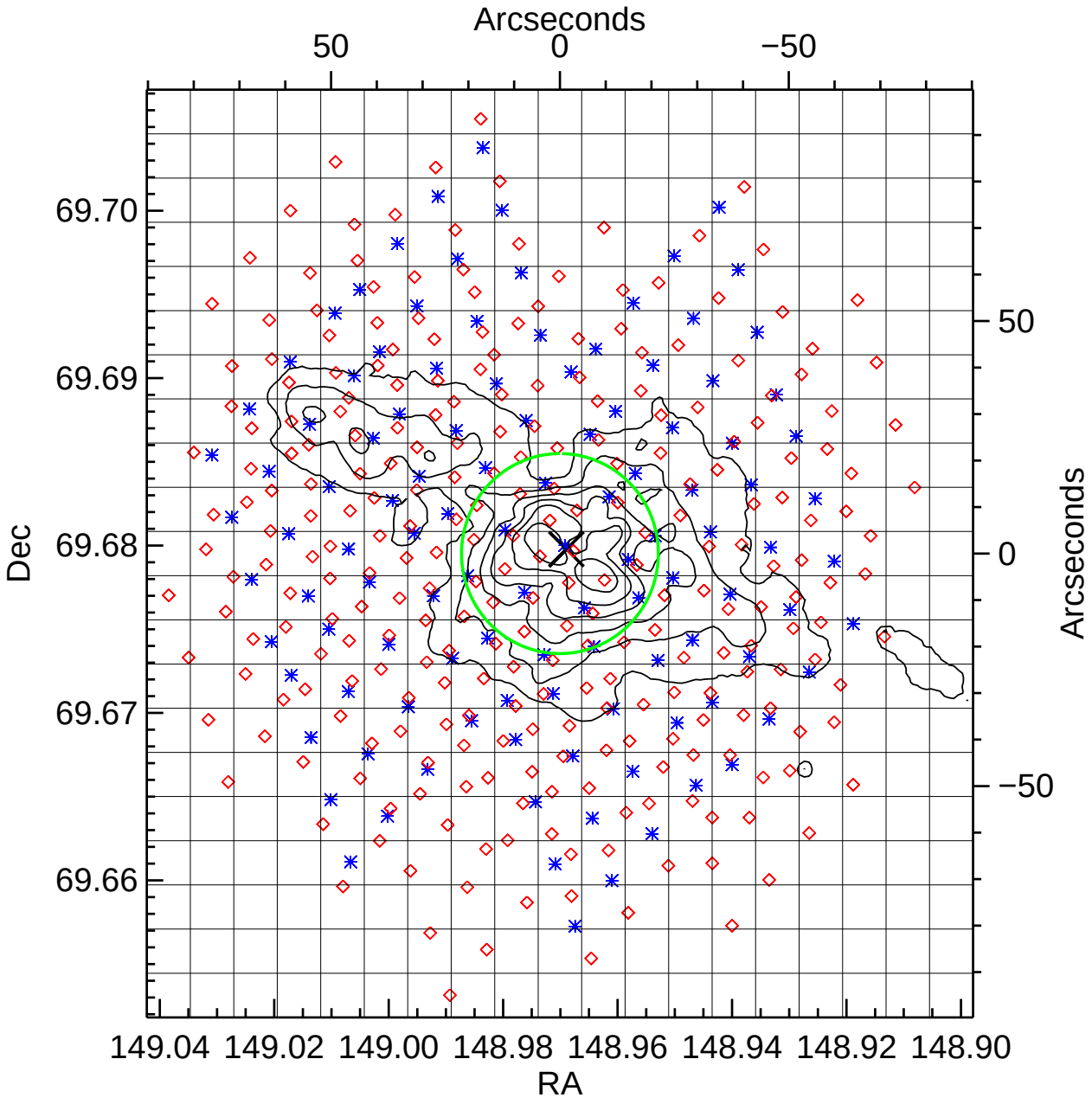

Figure 3.1 Spectrometer Mapping Point Locations. SLW spectra locations are indicated by blue asterisks, SSW by red diamonds. The pixel boundaries, spaced 9.5″ apart, are indicated by solid black lines. Hα contours are also plotted in black to indicate the orientation of the (nearly edge-on) galactic disk, from the Mount Laguna 40 inch telescope [31]. Contours are in decreasing intervals of 0.2 log(maximum), i.e. 10^{0}, $10^{-0.2}$, $10^{-0.4}$ ... $10^{-1.2}$. The green circle indicates the size of the ^{12}CO J$=4\rightarrow3$ 43″ beam FWHM. The black X marks the position of the single pointing ("deep") spectrum.

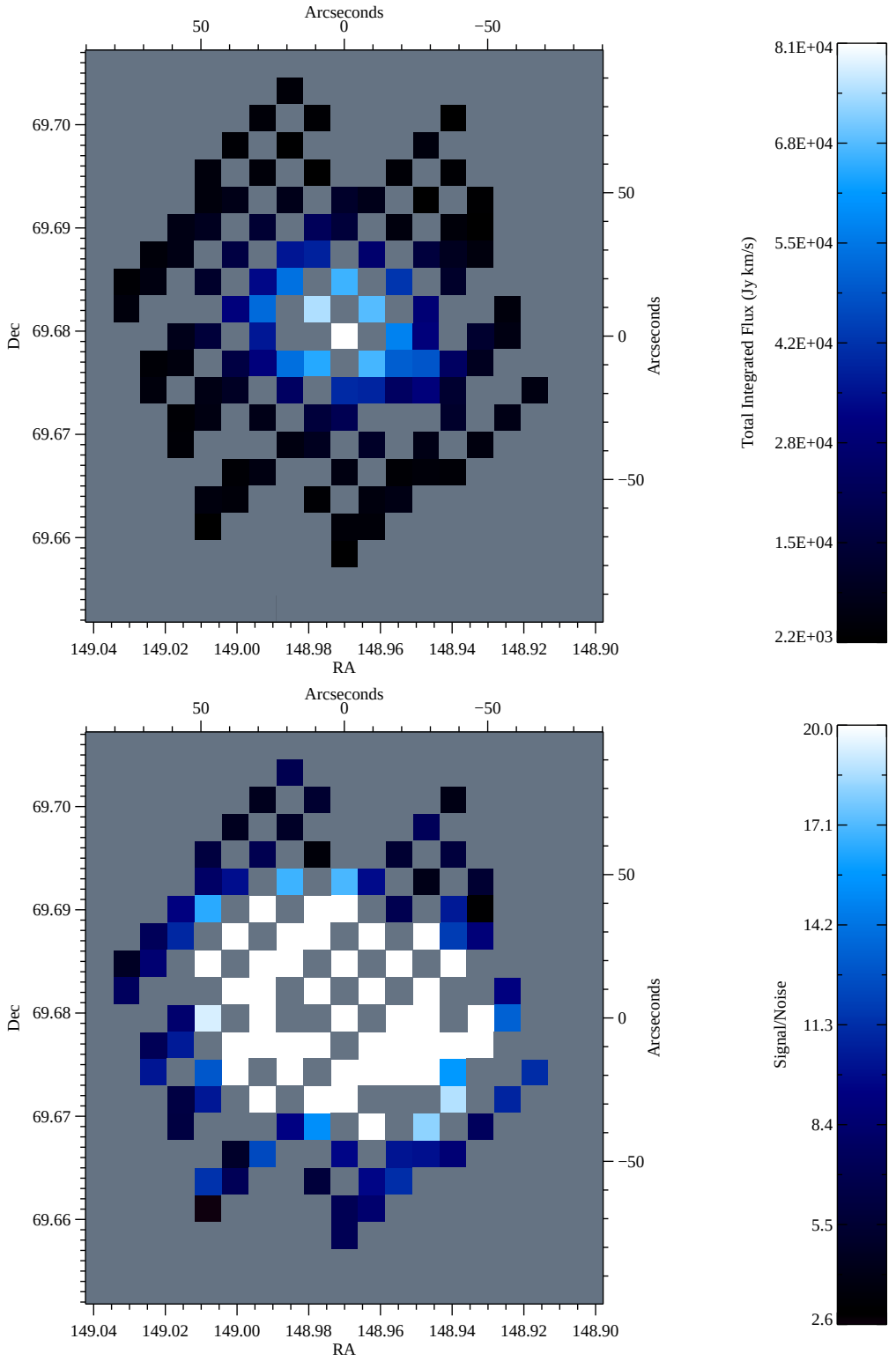

Figure 3.2 Integrated Flux (top) and Signal/Noise (bottom) maps for CO J = 4 → 3. Similar figures for other lines are in Appendix A. The top half includes no beam correction or convolution. Black corresponds to the lowest flux or zero if any fluxes are negative, at which point the colorbar becomes purple. The bottom half is a map of signal/noise, though the color bar tops out at 20 in order to better illustrate which pixels are near the threshold of detectability. On the color bar, black corresponds to the lowest signal/noise or three if any pixels have S/N less than three, at which point the colorbar becomes purple.

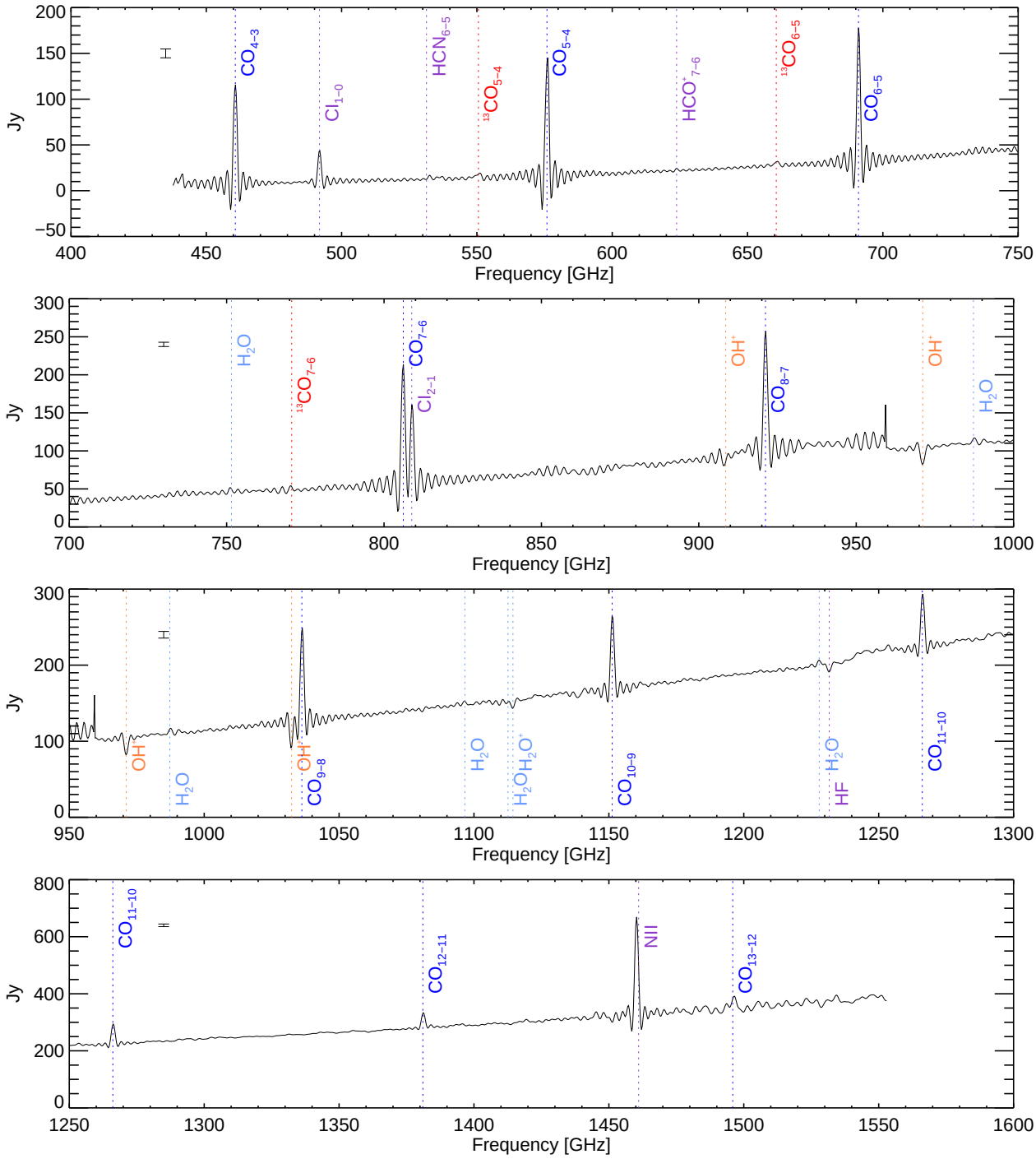

Figure 3.3 Deep Spectrum, split up by frequency. The switch from SLW to SSW bands occurs at approximately 950 GHz. Error bars are not shown on the spectrum for clarity, though the median error bar of each panel (times a factor of 20) is shown in the upper left corner. The spectrum contains ringing because the line profile of the FTS is a sinc function, as discussed in Section 3.4.3. Emission/absorption line locations are color-coded by molecular species: blue for ^{12}CO, red for ^{13}CO, light blue for water and its ion, orange for OH^+, and violet for all others.

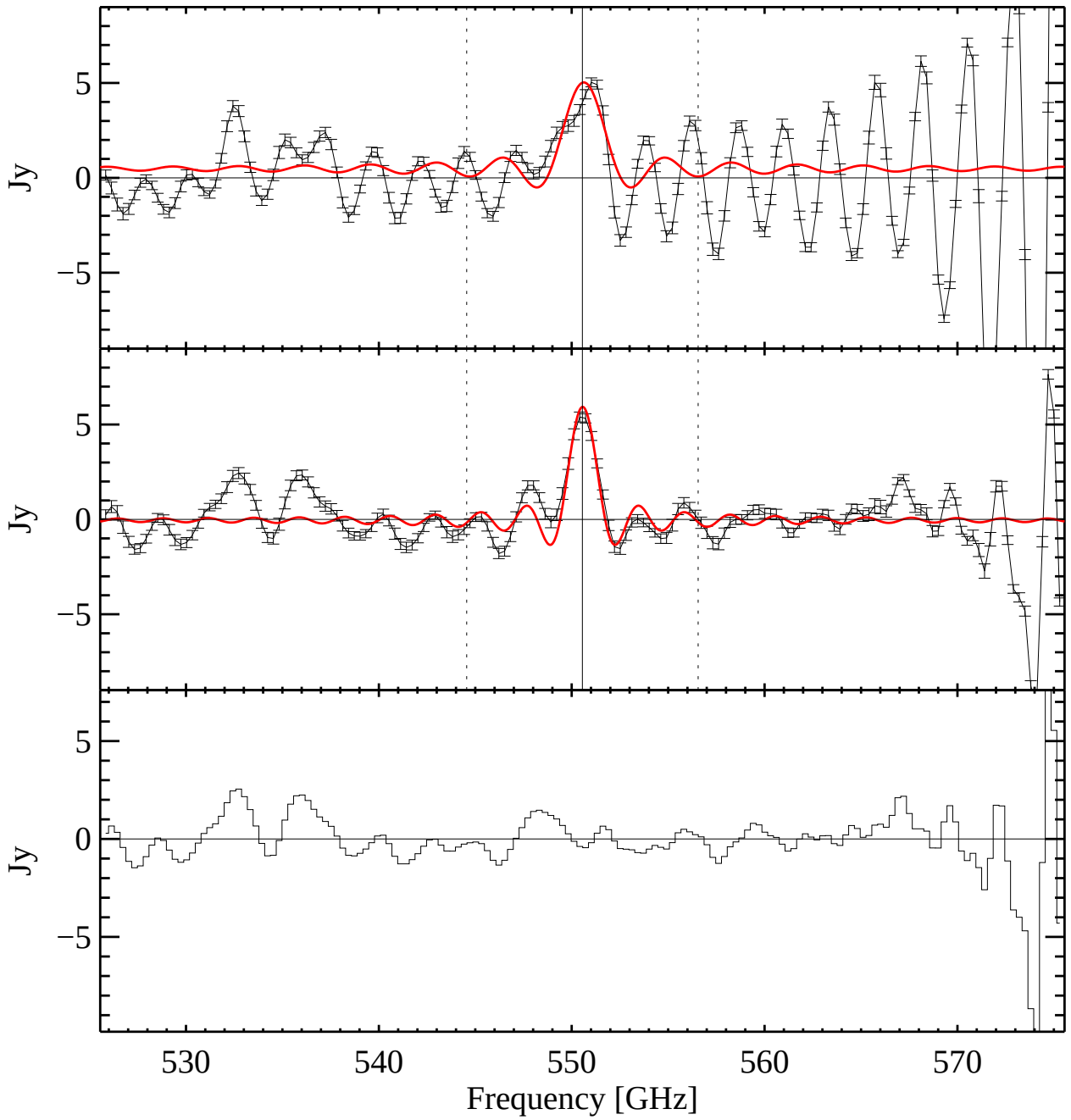

Figure 3.4 Example of line fit, using the ^{13}CO J=5→4 line. The top panel shows the continuum-subtracted spectrum (black); the ringing of the nearby ^{12}CO J=5→4 line is clearly visible on the right and interfering with the fit, overplotted in solid red. The middle panel shows the spectrum after subtracting out the strong ^{12}CO, [C I], and [N II] lines (though only the subtraction of the ^{12}CO J = 5 → 4 line is visible in this figure). In this example, the signal to noise ratio of the fit was improved from 1.1 to 6.6 (where the signal is the integrated flux and the noise is based on propagating the statistical errors of the fit parameters in the integrated flux calculation). The bottom panel is the residual of the fit. In all panels, a horizontal line indicates zero. In the top two panels, the solid vertical line indicates the expected line center, and the two dashed vertical lines demarcate the area within that was not used for fitting the continuum.

Table 3.1. Measured Fluxes of Detected Lines in Deep Spectrum

Transition	ν_{rest} [GHz]	$\int F_\nu dv$[a] [10^3 Jy km s^{-1}][b]
^{12}CO J=4→3	461.041	85.66 ± 0.90
^{12}CO J=5→4	576.268	79.44 ± 0.94
^{12}CO J=6→5	691.473	73.54 ± 0.44
^{12}CO J=7→6	806.652	66.04 ± 0.65
^{12}CO J=8→7	921.800	58.44 ± 0.87
^{12}CO J=9→8	1036.912	42.90 ± 0.74
^{12}CO J=10→9	1151.985	29.60 ± 0.41
^{12}CO J=11→10	1267.014	19.35 ± 0.33
^{12}CO J=12→11	1381.995	13.25 ± 0.35
^{12}CO J=13→12	1496.923	10.4 ± 1.1
[CI] ^{3}P$_1$→^{3}P$_0$	492.161	23.93 ± 0.55
[CI] ^{3}P$_2$→^{3}P$_1$	809.342	38.88 ± 0.58
[NII] ^{3}P$_1$→^{3}P$_0$	1462.000	82.4 ± 1.2
^{13}CO J=5→4	550.926	3.83 ± 0.58
^{13}CO J=6→5	661.067	3.02 ± 0.15
^{13}CO J=7→6	771.184	1.84 ± 0.31
^{13}CO J=8→7[c]	881.273	1.16 ± 0.45
HCN J=6→5[c]	531.716	1.15 ± 0.42
HCO$^+$ J=7→6	624.208	1.08 ± 0.17
OH$^+$ N=1→0, J=0→1	909.159	-5.2 ± 1.1
OH$^+$ N=1→0, J=2→1	971.805	-8.88 ± 0.41
OH$^+$ N=1→0, J=1→1	1033.118	-9.94 ± 0.39
HF J=1→0	1232.476	-3.64 ± 0.34
o-H$_2$O 3_{12}→3_{03}	1097.365	1.39 ± 0.30
o-H$_2$O 3_{12}→2_{21}	1153.127	2.57 ± 0.37
p-H$_2$O 2_{11}→2_{02}	752.033	1.86 ± 0.36

Table 3.1 (cont'd)

Transition	ν_{rest} [GHz]	$\int F_\nu dv$[a] [10^3 Jy km s^{-1}][b]
p-H_2O $2_{02} \rightarrow 1_{11}$	987.927	3.09 ± 0.56
p-H_2O $1_{11} \rightarrow 0_{00}$	1113.343	-2.69 ± 0.44
p-H_2O $2_{20} \rightarrow 2_{11}$	1228.789	2.01 ± 0.34
o-H_2O^+ $1_{11} \rightarrow 0_{00}$	1115.204	-2.82 ± 0.42

[a]All fits have been referenced to the 43″ beam of ^{12}CO J = 4 → 3, as described in Section 3.4.3. Uncertainties do not include calibration error.

[b]To convert to other units, we use these equations. L [$L_\odot$] = $\int F_\nu dv$ [Jy km s^{-1}] × 0.012 ν_{GHz}. $\int T dv$ [K km s^{-1}] = $\int F_\nu dv$ [Jy km s^{-1}] 660.8 ν_{GHz}^{-2}. F [W/m^2] = $\int F_\nu dv$ [Jy km s^{-1}] × 3.3 ×10^{-23} ν_{GHz}.

[c]The ^{13}CO J = 8 → 7 and HCN J = 6 → 5 lines are detected at slightly less than S/N of 3; 2-σ upper limits would be 9.0 and 8.4 × 10^2 Jy km s^{-1}, respectively.

3.5 Bayesian Likelihood Analysis

We follow the method described in Ward et al. [179] for the ^{12}CO J = 6 → 5 map of M82, used frequently in the analysis of ground based molecular observations of galaxies [e.g. the Z-spec collaboration, 117, 79, 155, 17] and also of the single pointing SPIRE spectrum of M82 [125] and Arp220 [139]. The goal of our Bayesian likelihood analysis is to map the relative probabilities of physical conditions over a large parameter space; this provides a more complete statistical analysis of the physical conditions as opposed to simply finding one best-fit solution.

For each molecular species, we first calculate a grid of expected line emission temperatures for various combinations of temperature ($T_{\rm kin}$), density ($n(H_2)$), and column density per unit linewidth ($N_{^{12}CO}/dv$) using RADEX [171]. We use the uniform sphere approximation for calculating the escape probabilities; the actual morphology in M82 shows a more complex velocity structure, therefore this approximation is considered an average of the bulk properties of the gas (and the results are not sensitive to uniform sphere vs. LVG approximation). RADEX performs statistical equilibrium calculations of the level populations, including the effects of radiative trapping, for a specified gas temperature, density, and column density per unit linewidth. The resulting solutions are output in the form of background-subtracted Rayleigh-Jeans equivalent line radiation temperatures.

We use a 2.73 K blackbody to represent the cosmic microwave background (CMB). We also experimented with using the continuum flux measured in our deep spectrum as a background; we fit the continuum in Jy across both bands, masking out the lines, with a third-order polynomial. The choice of this fit was to accurately represent the continuum background as a function of frequency; it was not meant to represent any physical conditions. Because the relevant radiation background is the specific intensity (Jy/sr), we divide our continuum by the area corresponding to a 43″ beam (as the entire deep spectrum has been corrected to that). Such a background is in fact orders of magnitude higher than the CMB at the highest frequencies that we are modeling. However, a grid with this background vs. the CMB produces the same likelihood results. This is because at a kinetic temperature of ∼ 500 K (the warm component we will model), collisional excitation

Table 3.2. RADEX Model Parameters and Ranges

Parameter	Range	# of Points
T_{kin} [K]	$10^{0.7} - 10^{3.7}$	61
$n(H_2)$ [cm^{-3}]	$10^2 - 10^6$	41
$N_{^{12}CO}/\Delta V$ [cm^{-2}]	$10^{14} - 10^{18}$	41
Φ_A	$10^{-3} - 10^0$	41
$X_{^{13}CO}/X_{^{12}CO}$	$10^{-2} - 10^{-1}$	11
$X_{[CI]}/X_{^{12}CO}$	$10^{-2} - 10^2$	11
ΔV [km s^{-1}]	1.0	fixed
$T_{background}$ [K]	2.73	fixed

Note. — All parameters are sampled evenly in log space. Velocity is fixed because all modeling is column per unit linewidth.

greatly dominates over radiative excitation. In other words, at high temperatures, the modeled line intensities do not depend on the background radiation field. The cool component we will model is traced by low-J lines, whose background is not as affected, and so this component also finds the same results with either background. Therefore we are presenting results using the CMB background.

In addition to ^{12}CO, we also model ^{13}CO and [C I] as a function of the same temperatures, densities, and column density of ^{12}CO. For those molecular/atomic species, we also add the parameter of the relative abundance, e.g. [^{13}CO]/[^{12}CO] or $X_{^{13}CO}/X_{^{12}CO}$. When modeling the intensity, the column density of ^{13}CO is simply that of ^{12}CO times the relative abundance. [C I] is modeled with the parameter of [C I]/[^{12}CO]. Finally, we introduce one more parameter, the area fractional filling factor Φ_A. The modeled emission may not entirely fill the beam, so the flux may be reduced by this factor. All model grid points are therefore multiplied by each value of Φ_A. The ranges of parameters, as well as the number of grid points, are presented in Table 3.2.

The RADEX grid gives us a set of line intensities as a function of model parameters $\boldsymbol{p} = (N_{^{12}CO}/dv, n(H_2), T_{\rm kin}, \Phi_A, \boldsymbol{X}_{mol}/\boldsymbol{X}_{^{12}CO})$, which we then compare to our measured intensities $\boldsymbol{x}$.

To compare to column density per unit linewidth, we divide the measured intensities by 180 $\mathrm{km\,s^{-1}}$, so that they are also per unit linewidth. The optical depth, and in turn the RADEX results, depend only on the ratio of column density to line width. Ward et al. [179] found linewidths of 180 $\mathrm{km\,s^{-1}}$ for the NE component and 160 $\mathrm{km\,s^{-1}}$ for the SW by resolving the structure in position-velocity diagrams for their study from CO $\mathrm{J} = 1 \rightarrow 0$ to $\mathrm{J} = 7 \rightarrow 6$, but we do not resolve the difference between the two and so we use the larger value. The Bayesian likelihood of the model parameters given the measurements is

$$P(\boldsymbol{p}|\boldsymbol{x}) = \frac{P(\boldsymbol{p})P(\boldsymbol{x}|\boldsymbol{p})}{P(\boldsymbol{x})}, \tag{3.1}$$

where $P(\boldsymbol{p})$ is the prior probability of the model parameters (see Section 3.5.2), $P(\boldsymbol{x})$ is for normalization, and $P(\boldsymbol{x}|\boldsymbol{p})$ is the probability of obtaining the observed data set given that the source follows the model described by $\boldsymbol{p}$. $P(\boldsymbol{x}|\boldsymbol{p})$ is the product of Gaussian distributions in each observation,

$$P(\boldsymbol{x}|\boldsymbol{p}) = \prod_i \frac{1}{\sqrt{2\pi\sigma_i^2}} \exp\left[- \frac{(x_i - I_i(p))^2}{2\sigma_i^2} \right] \tag{3.2}$$

where σ_i is the standard deviation of the observational measurement for transition i and $I_i(\mathbf{p})$ is the RADEX-predicted line intensity for that transition and model. For the total uncertainty, we take the statistical uncertainty in the total integrated intensity from the line fitting procedure and add 20%/10% calibration error for SSW/SLW in quadrature. To find the likelihood distribution of one parameter out of all of $\boldsymbol{p}$, we integrate over all other parameters to find, for example, $P(T_{kin})$.

3.5.1 Separate Components

We divide the lines fluxes into two components, one warmer and one cooler. Panuzzo et al. [125] already showed that the high-J lines of ^{12}CO trace a warmer component than those transitions available from the ground. However, some of the mid-J lines (especially CO $\mathrm{J} = 4 \rightarrow 3$) may have significant contributions from both components. To separate the ^{12}CO fluxes from each component,

we follow an iterative procedure. We first model the lowest three ^{12}CO lines from Ward et al. [179]; we take the sum of their measurements for the two observed lobes and scale the result by the ratio of their beam area to our 43″ beam. The best-fit SLED is then subtracted from our SPIRE measurements, producing the black triangles in Figures 3.5 and 3.6. These triangles comprise the "warm component." The best fit warm SLED is then subtracted from the low-J lines, producing the asterisks in the aforementioned figure. These fluxes are refit to produce our results for the "cool component."

We present a two-component model using just ^{12}CO, as well as one including our high-J lines of ^{13}CO along with the warm component. We did not model the low-J ^{13}CO lines reported in Ward et al. [179] due to the uncertainties presented in their Table 2 footnotes. We instead predicted the ^{13}CO spectrum of the cool component, given its best fit results and a ^{12}CO/^{13}CO ratio of of 35 [inbetween previously found 30 to 40 179], and found a very small contribution to the higher-J lines we are modeling. These small contributions are subtracted from the warm component, as with ^{12}CO in the previous paragraph.

We also sought to include [C I], which was assumed to be associated with the cool component, due to the low excitation temperature ($\sim$ 30 K) derived from the line ratios ($n_u/n_l = g_u/g_l \exp(-\Delta T/T_{ex})$, $n_i \propto I_i\,[\mathrm{W/cm^2}]/(A_i\nu_i)$). Here, we use $\Delta T = 38.84$, $g_u = 5$, $g_l = 3$, $A_u = 2.65 \times 10^{-7}$ s^{-1}, $A_l = 7.88 \times 10^{-8}$ s^{-1}. See Table 3.1 for the frequencies and unit conversion. However, this model produced some unphysical situations. We discuss our findings and implications of them in Section 3.6.1.

This analysis necessarily assumes that all of the line emission for a given component is coming from one portion of gas described in bulk by the model parameters. In reality, there is likely a variety of physical conditions, existing in a continuum of parameters. However, the high-J SPIRE data does not provide justification for modeling more than one warm component because the SLEDs are well-described by one component. We did attempt a procedure to model multiple warm components of CO by first fitting the highest-J lines and subtracting the predicted line fluxes for the mid-J lines. Such a procedure has been used in Rangwala et al. [139], for example. However, the predictions for

Table 3.3. Likelihood Parameters Used

Parameter	Value[a]	Units
Line width[b]	180	[km s^{-1}]
Abundance ($X_{^{12}CO}/X_{H_2}$)	3.0 $\times 10^{-4}$	
Angular Size Scale[c]	17	[pc/″]
Emission Size	43.0	[″]
Length Limit	900	[pc]
Dynamical Mass Limit	2 $\times 10^9$	[$M_\odot$]

[a]Citations for parameters are in Section 3.5.2.

[b]Used for scaling the line intensities. All other parameters used for prior probabilities.

[c]$A_{region} = \pi$ (Angular Size Scale [pc/″] $\times$ Source Size [″] / 2)^2

the mid-J lines either matched or were an overestimate of the observed fluxes, leaving no second component to be modeled. A range of conditions is definitely present in the molecular gas, yet these two (warm and cool) components are dominating the emission, within the observational and modeling uncertainties. We note that, with regards to the different molecules/atoms being modeled here, all three species have similar profiles, as shown from the HIFI (higher spectral resolution) spectra in Loenen et al. [97].

3.5.2 Prior Probabilities

We use a binary prior probability, $P(\boldsymbol{p})$, to indicate either a physically allowed scenario ($P(p)$=1) or an unphysical and thus not allowed scenario ($P(p)$=0). In other words, all combinations of parameters that are deemed physical based on the following three conditions were given equal prior probability, and all others are given zero prior probability. The conditions are as follows:

(1) The total length of the column (L_{col}) cannot exceed the length of the entire region. This assumes the length in the plane of the sky is the same as that orthogonal to the plane of the sky; we chose an upper-limit to the length of 900 pc because of the observed size [179].

This is the most significant of all the priors, placing an upper limit on the column density and a lower limit on the density. This prior can be stated as

$$\frac{N_{^{12}CO}}{n(H_2)\sqrt{\Phi_A}X_{^{12}CO}} \leq 900\,\mathrm{pc}. \tag{3.3}$$

For the relative abundance $X_{^{12}CO}$ to molecular hydrogen, we assume 3.0 $\times 10^{-4}$ [179].

(2) The total mass in the emission region (M_{region}) cannot exceed the dynamical mass of the galaxy. We use the expression

$$M_{region} = \frac{A_{region}N_{^{12}CO}\Phi_A 1.5 m_{H_2}}{X_{^{12}CO}} \tag{3.4}$$

to calculate the mass in the emission region, where the 1.5 accounts for helium and other heavy elements, and Φ_A is the filling factor. We estimate the dynamical mass to be 2×10^9 $M_\odot$ [179, 117], calculated using rotational velocity and radius. The other assumed parameters in the above expression are listed in Table 3.3.

(3) The optical depth of a line must be less than 100, as recommended by the RADEX documentation. The cloud excitation temperature can become too dependent on optical depth at high column densities, and so very high optical depths can lead to unreliable temperatures. We found that in the presence of the other priors, this limit does not affect the likelihood results.

3.5.3 Likelihood Analysis of the Map

We run each map pixel through the aforementioned likelihood analysis independently. (Note that due to the beam size being larger than the pixels themselves, each pixel's data are not independent of its neighbors). We only model ^{12}CO in the spectral maps because they are of lower integration time and ^{13}CO cannot be reliably measured. We also cannot account for cool emission at different locations in our map.

To be run through the likelihood analysis, a pixel was required to have both an SLW and SSW spectrum and at least 5 ^{12}CO lines with S/N $\geq$ 10 (the convolution tends to increase the signal/noise of each pixel). 90 pixels met this requirement (98 pixels would meet the requirement of 5 ^{12}CO lines with S/N $\geq$ 3, so little would be gained by going to lower S/N). Additionally, we do not find statistically significantly different results requiring only 3 lines, the minimum with which we could reasonably model the emission; to some extent, this requires at minimum the J = 6 $\rightarrow$ 5 transition, which means we will be tracing higher temperatures.

3.6 Modeling Results and Discussion

3.6.1 Physical Conditions: Deep Spectrum

We present two different versions of our likelihood analysis for the deep spectrum: one using only ^{12}CO, and one using ^{12}CO and ^{13}CO ("multiple molecule"). The motivation behind this is to investigate two questions: does the addition of different species change the modeled parameters of the gas, and/or does it better constrain the parameters? Both versions contain a warm and cool component. The modeling assumes all of the emission in a given component is coming from the same homogeneous gas, and by comparing these models we will investigate the validity of this assumption in this subsection.

The results for each of these versions are presented in Tables 3.4 and 3.5 respectively. Figures 3.5 and 3.6 show the input SLED as well as the best-fit model results. The primary results (temperature, density, column density, and filling factor) are displayed graphically in Figures 3.7 and 3.8. Secondary parameters, which are calculated from the aforementioned primary results, are displayed in Figures 3.9 and 3.10. These include the pressure (the product of temperature and density) and the beam-averaged column density ($\langle N_{^{12}\mathrm{CO}} \rangle$, the product of column density and filling factor). We note that in the results, the parameters of the most likely grid point ("4D Max") is not necessarily the same as the median or the mode ("1D Max") of the integrated likelihood distributions. The "4D Max" is describing one specific point, but the median, 1D Max, and associated error range are

Table 3.4. Likelihood Results: ^{12}CO Only

	Integrated Likelihood: Cool			4D Max	Units
	Median	1 Sigma Range	1D Max		
$T_{\rm kin}$	40	12 − 472	13	63	[K]
$n(\rm H_2)$	$10^{3.23}$	$10^{2.36} - 10^{4.81}$	$10^{2.20}$	$10^{3.40}$	[cm^{-3}]
N_{co}	$10^{19.03}$	$10^{18.38} - 10^{19.56}$	$10^{19.36}$	$10^{18.56}$	[cm^{-2}]
$\Phi_{\rm A}$	$10^{-0.92}$	$10^{-1.22} - 10^{-0.57}$	$10^{-0.97}$	$10^{-0.90}$	
P	$10^{5.11}$	$10^{4.55} - 10^{5.76}$	$10^{5.24}$	$10^{5.24}$	[K cm^{-2}]
$< N_{\rm co} >$	$10^{18.15}$	$10^{17.63} - 10^{18.84}$	$10^{17.78}$	$10^{17.78}$	[cm^{-2}]
Mass	$10^{7.67}$	$10^{7.16} - 10^{8.36}$	$10^{7.31}$	$10^{7.31}$	[M$_\odot$]
	Integrated Likelihood: Warm				
$T_{\rm kin}$	414	335 − 518	447	447	[K]
$n(\rm H_2)$	$10^{3.98}$	$10^{3.53} - 10^{4.21}$	$10^{4.10}$	$10^{4.10}$	[cm^{-3}]
N_{co}	$10^{18.12}$	$10^{17.06} - 10^{19.09}$	$10^{18.56}$	$10^{17.96}$	[cm^{-2}]
$\Phi_{\rm A}$	$10^{-1.50}$	$10^{-1.96} - 10^{-0.52}$	$10^{-1.88}$	$10^{-1.28}$	
P	$10^{6.61}$	$10^{6.16} - 10^{6.80}$	$10^{6.75}$	$10^{6.75}$	[K cm^{-2}]
$< N_{\rm co} >$	$10^{16.67}$	$10^{16.44} - 10^{17.20}$	$10^{16.58}$	$10^{16.58}$	[cm^{-2}]
Mass	$10^{6.20}$	$10^{5.97} - 10^{6.72}$	$10^{6.11}$	$10^{6.11}$	[M$_\odot$]

Note. — 1D Max refers to the maximum likelihood of that parameter after integrated over all the other parameters (the mode of the likelihood distributions). 4D Max refers to the single most probable grid point (mode of the entire multi-dimensional distribution). Median, 1 sigma lower and upper values refer to the integrated distribution, when the cumulative distribution function equals 0.5, ~ 0.16 and ~ 0.84, respectively. Note that the 1D Max may be outside the 1 sigma range because of asymmetry in the integrated likelihood. P and $\langle N_{^{12}\rm CO} \rangle$ are calculated from the 2D distribution of $T_{\rm kin}$ and $n(\rm H_2)$ (or $\Phi_{\rm A}$ and $N_{^{12}\rm CO}$) , which is why we give the same value in both the 1D Max and 4D Max columns.

Table 3.5. Likelihood Results: ^{12}CO and ^{13}CO

	Integrated Likelihood: Cool			4D Max	Units
	Median	1 Sigma Range	1D Max		
$T_{\rm kin}$	35	12 − 385	14	158	[K]
$n(H_2)$	$10^{3.44}$	$10^{2.48} - 10^{5.15}$	$10^{3.00}$	$10^{3.10}$	[cm^{-3}]
N_{co}	$10^{19.25}$	$10^{18.69} - 10^{19.70}$	$10^{19.36}$	$10^{18.96}$	[cm^{-2}]
$\Phi_{\rm A}$	$10^{-1.19}$	$10^{-1.52} - 10^{-0.83}$	$10^{-1.28}$	$10^{-1.35}$	
P	$10^{5.24}$	$10^{4.73} - 10^{6.18}$	$10^{5.24}$	$10^{5.24}$	[K cm^{-2}]
$< N_{\rm co} >$	$10^{18.09}$	$10^{17.59} - 10^{18.71}$	$10^{17.78}$	$10^{17.78}$	[cm^{-2}]
Mass	$10^{7.62}$	$10^{7.11} - 10^{8.23}$	$10^{7.31}$	$10^{7.31}$	[M$_\odot$]
Integrated Likelihood: Warm					
$T_{\rm kin}$	436	344 − 548	447	501	[K]
$n(H_2)$	$10^{3.58}$	$10^{3.17} - 10^{3.96}$	$10^{3.80}$	$10^{3.40}$	[cm^{-3}]
N_{co}	$10^{19.02}$	$10^{18.19} - 10^{19.51}$	$10^{19.16}$	$10^{19.26}$	[cm^{-2}]
$\Phi_{\rm A}$	$10^{-1.88}$	$10^{-2.06} - 10^{-1.50}$	$10^{-1.88}$	$10^{-1.88}$	
P	$10^{6.23}$	$10^{5.80} - 10^{6.60}$	$10^{6.61}$	$10^{6.61}$	[K cm^{-2}]
$< N_{\rm co} >$	$10^{17.12}$	$10^{16.69} - 10^{17.59}$	$10^{16.76}$	$10^{16.76}$	[cm^{-2}]
Mass	$10^{6.65}$	$10^{6.22} - 10^{7.12}$	$10^{6.28}$	$10^{6.28}$	[M$_\odot$]
$X_{\rm 13co}/X_{\rm co}$	$10^{-1.58}$	$10^{-1.70} - 10^{-1.46}$	$10^{-1.50}$	$10^{-1.50}$	
$N_{\rm 13co}$	$10^{17.44}$	$10^{16.62} - 10^{17.92}$	$10^{17.62}$	$10^{17.62}$	[cm^{-2}]

Note. — See Table 3.4 for more explanation.

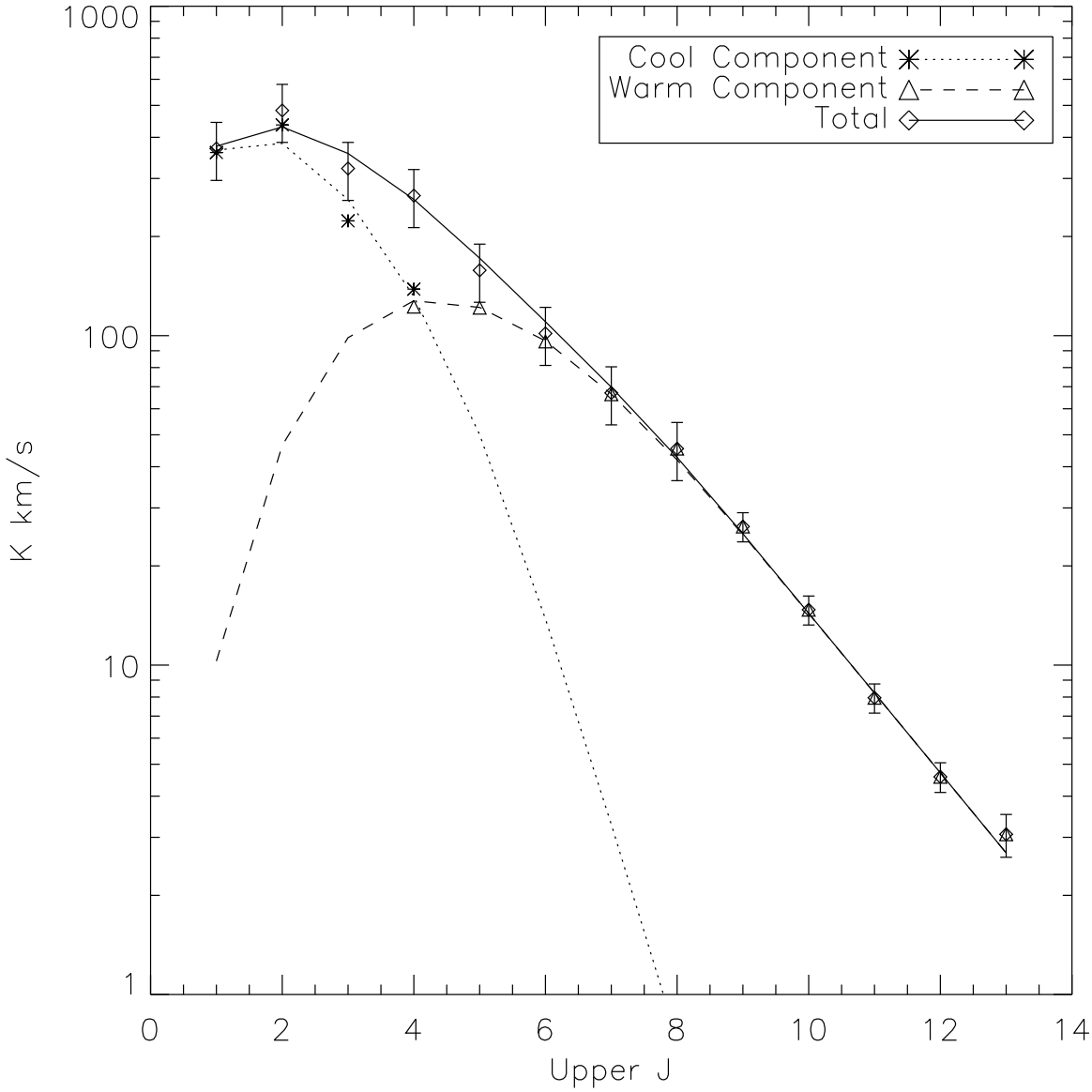

Figure 3.5 Bayesian Likelihood Analysis, Spectral Line Energy Distributions, ^{12}CO Only. Asterisks represent the cool component, with its best fit SLED ("4D Max" column in Table 3.4) shown by a dotted line. Triangles represent the warm component, with its best fit SLED shown by a dashed line. The total measurements are shown with diamonds with their associated error bars. The total of both components is the solid line.

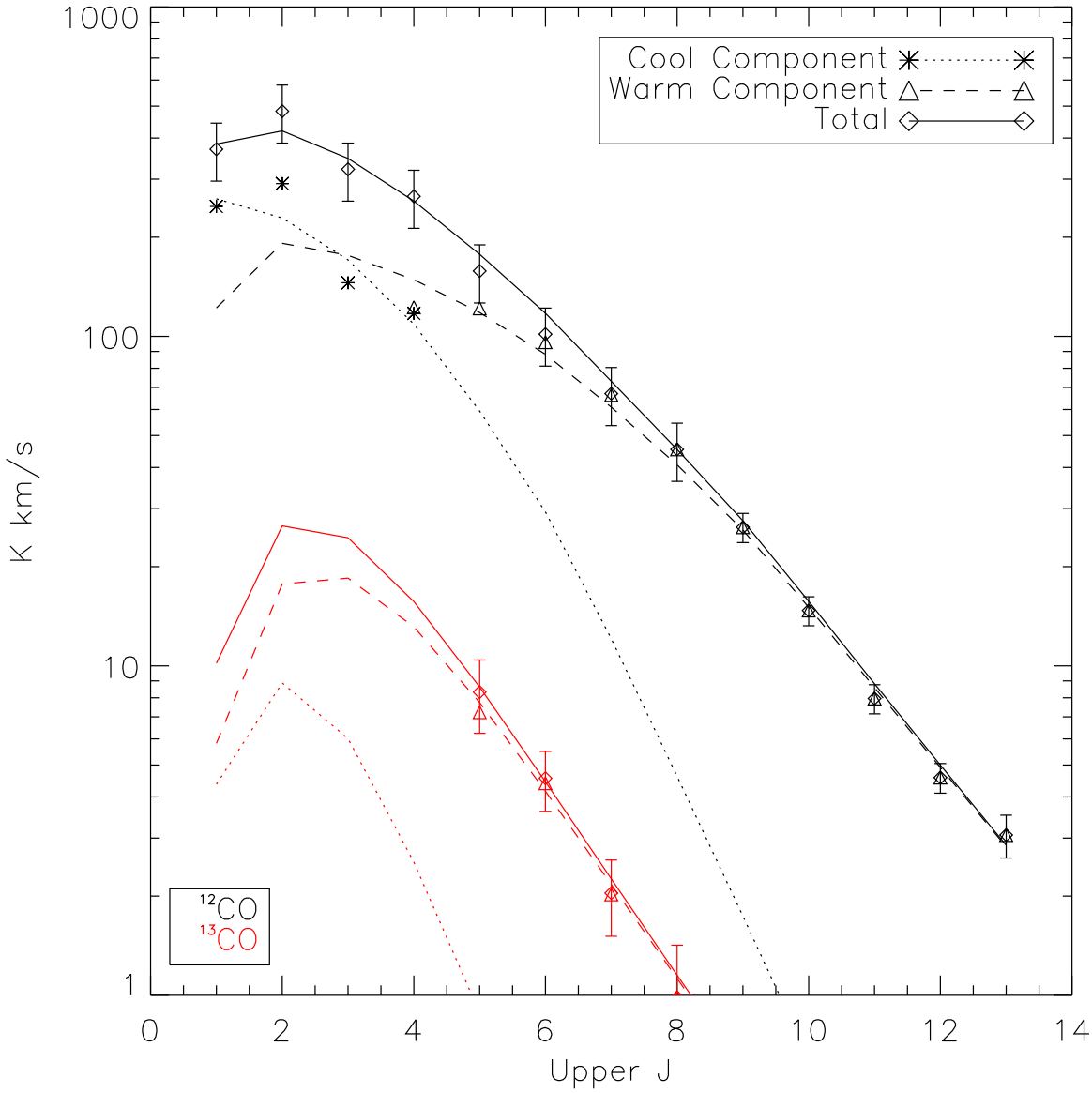

Figure 3.6 Bayesian Likelihood Analysis, Spectral Line Energy Distributions, including ^{13}CO. Each color is a separate species: black for ^{12}CO, red for ^{13}CO (only warm component). The total fluxes are shown by diamonds, but their separate components are in asterisks/triangles for the cool/warm components. Best fit SLEDs ("4D Max" column in Table 3.5) are shown with dotted/dashed lines for cool/warm components. The total SLED, shown with a solid line, is the sum of the two components.

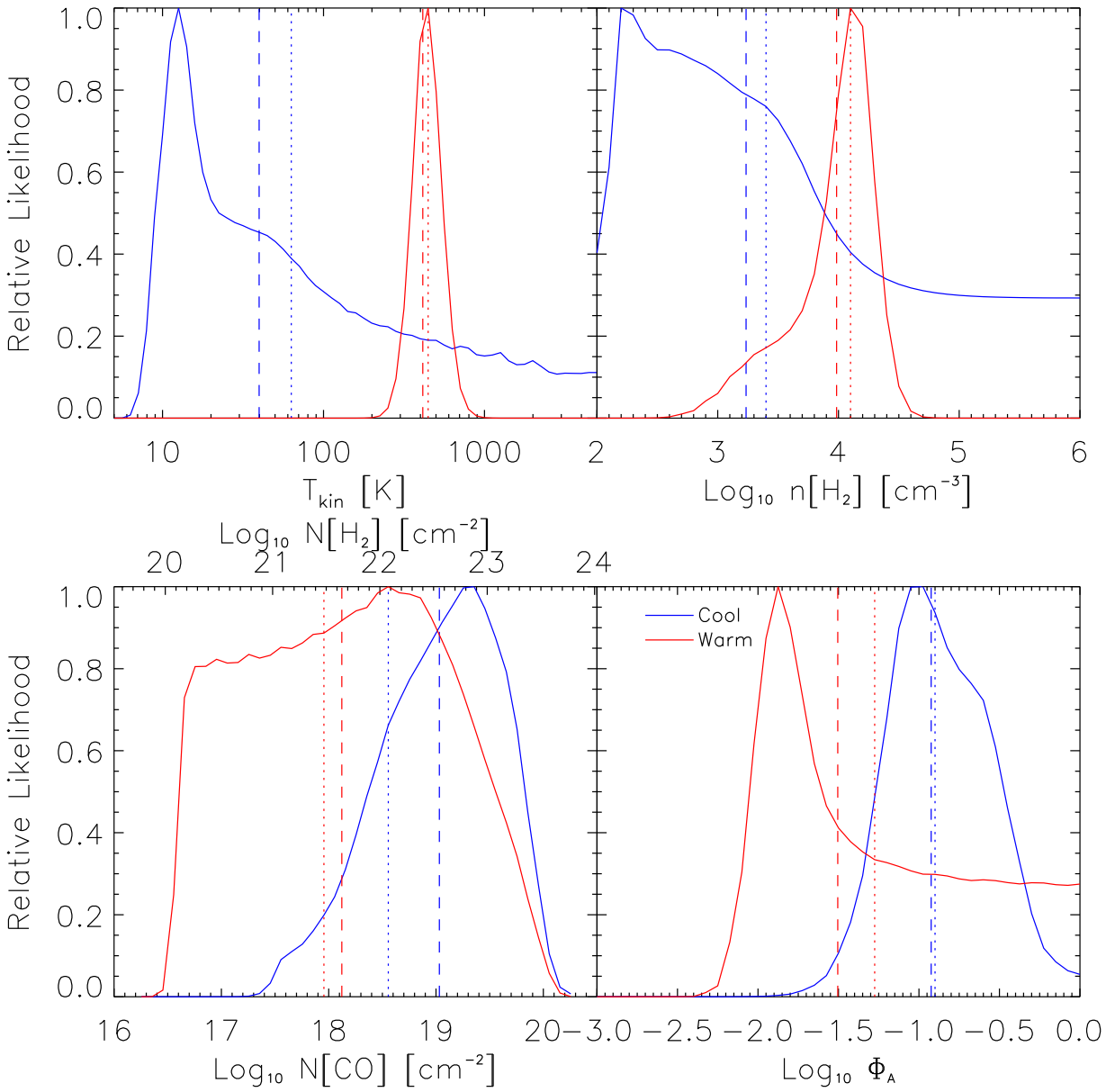

Figure 3.7 Bayesian Likelihood Analysis, Primary Parameter Results, ^{12}CO only. Each color represents a separate component; blue for cool, red for warm (see Section 3.5). Dashed/dotted vertical lines indicate the median/4D maximum of the distribution (see Table 3.4).

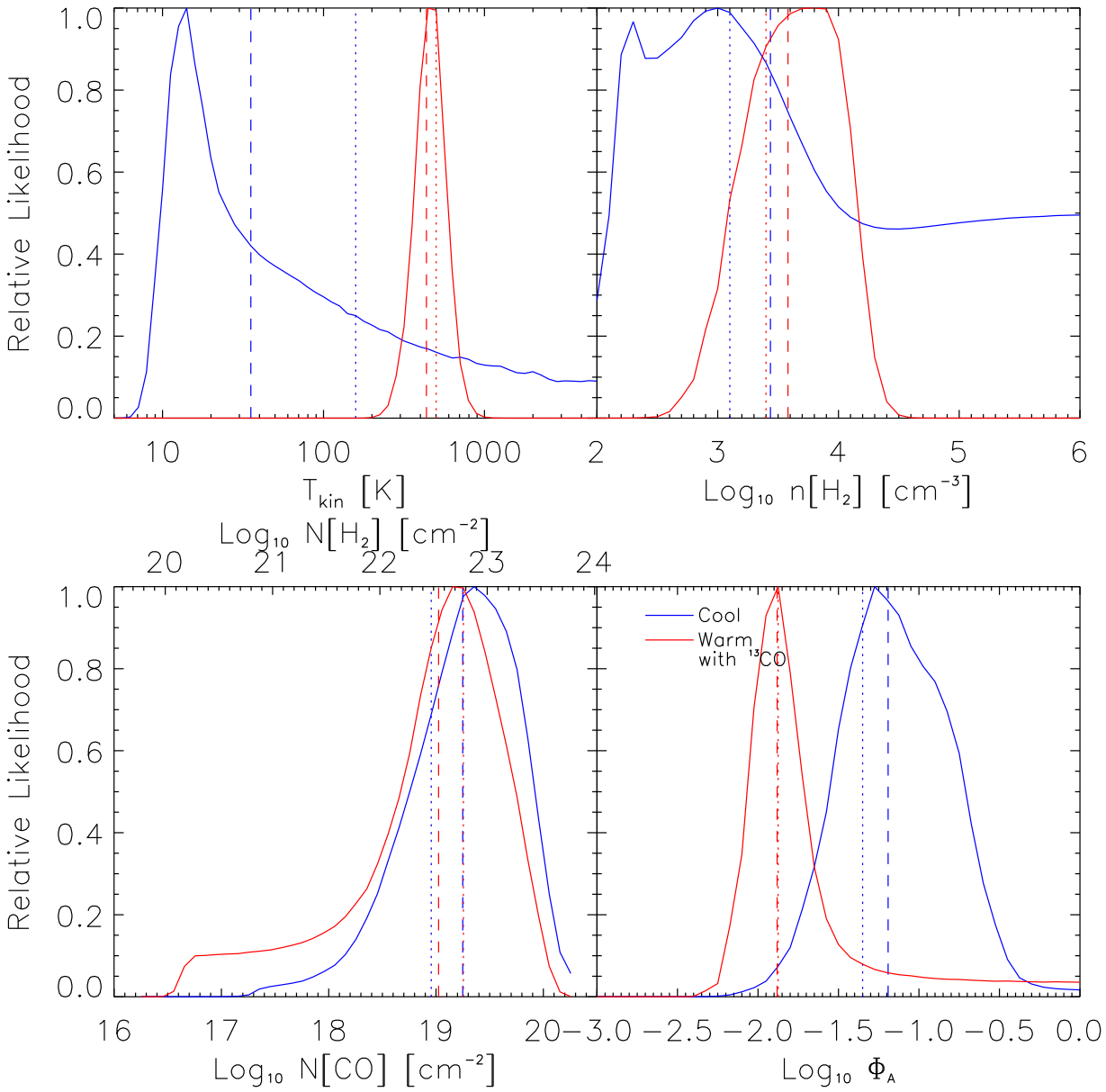

Figure 3.8 Bayesian Likelihood Analysis, Primary Parameter Results, including ^{13}CO. Each color represents a separate component; blue for cool, red for warm (see Section 3.5). Dashed/dotted vertical lines indicate the median/4D maximum of the distribution (see Table 3.4).

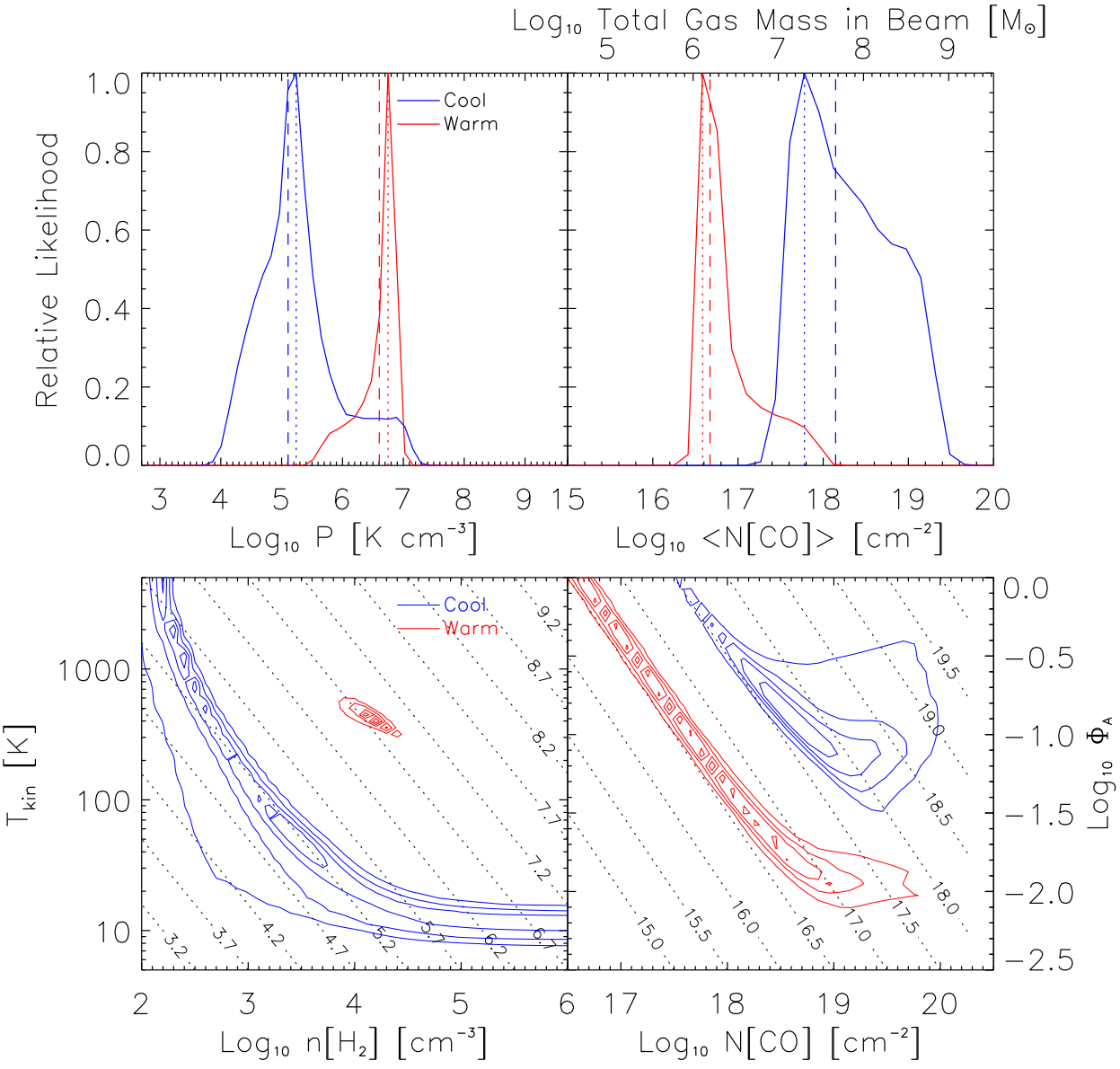

Figure 3.9 Bayesian Likelihood Analysis, Secondary Parameter Results, ^{12}CO only. Top: Each color represents a separate component; blue for cool, red for warm (see Section 3.5) Dashed/dotted vertical lines indicate the median/4D maximum of the distribution (see Table 3.4). Bottom: 2D distributions for the pairs of primary parameters from which the secondary parameters (top) were derived; colors correspond to component. Diagonal lines indicate values of the top parameters (pressure on left and beam-averaged column density on right). Contour levels are 20, 40, 60, and 80% of the maximum likelihood.

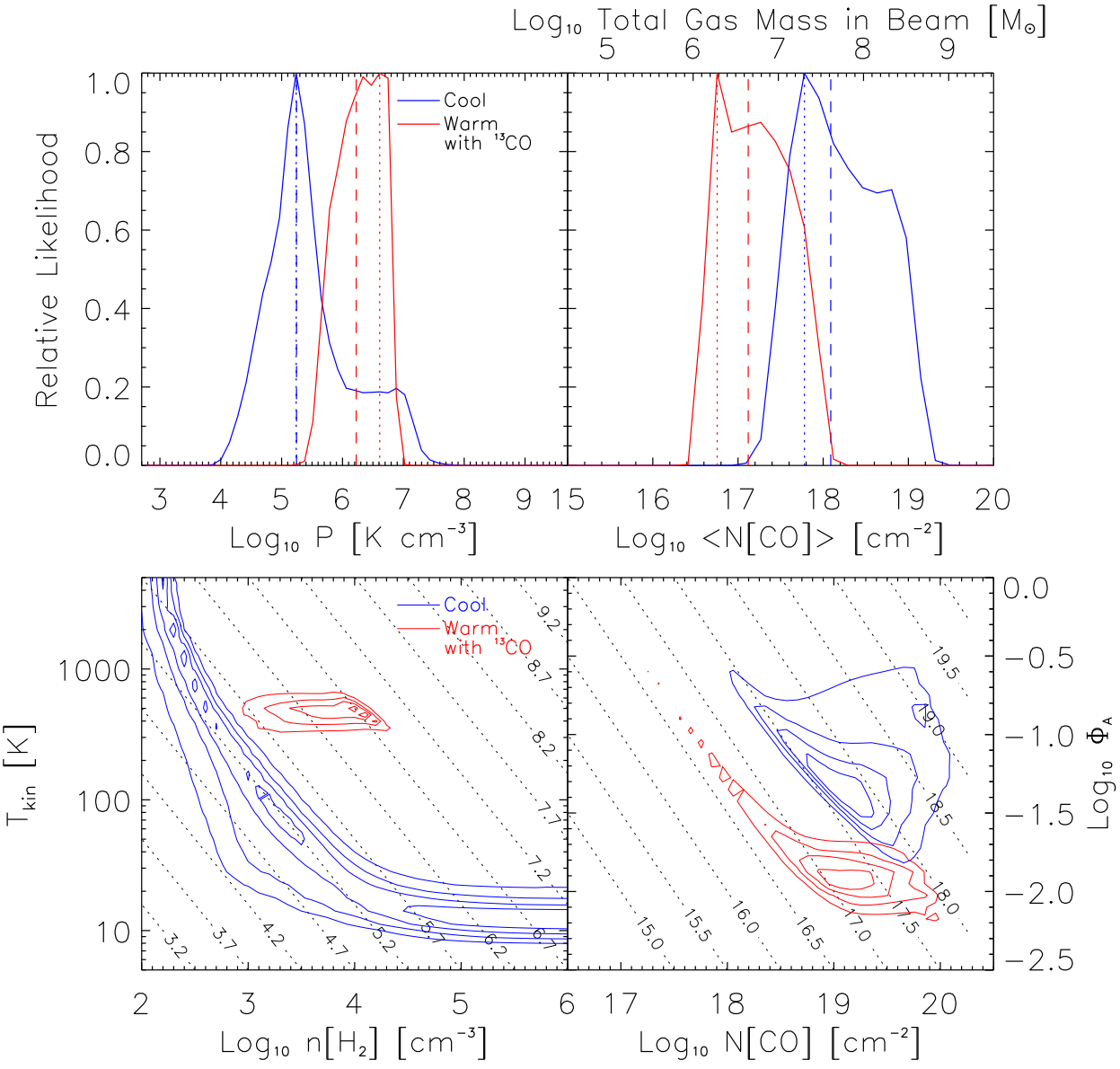

Figure 3.10 Bayesian Likelihood Analysis, Secondary Parameter Results, including ^{13}CO. Top: Each color represents a separate component; blue for cool, red for warm (see Section 3.5) Dashed/dotted vertical lines indicate the median/4D maximum of the distribution (see Table 3.4). Bottom: 2D distributions for the pairs of primary parameters from which the secondary parameters (top) were derived; colors correspond to component. Diagonal lines indicate values of the top parameters (pressure on left and beam-averaged column density on right). Contour levels are 20, 40, 60, and 80% of the maximum likelihood.

representative of the larger likelihood across all other parameters in the grid.

We first compare our two models, ^{12}CO only vs. multiple molecule. These are Tables 3.4 vs. 3.5, Figures 3.7 vs. 3.8, and Figures 3.9 vs. 3.10.

The addition of ^{13}CO to the warm component does not significantly change the temperature, but it does increase the likelihood of lower densities. It also decreases the likelihood of lower column densities. The consequences of these changes can be seen in the pressure and mass distributions in Figures 3.9 and 3.10. Adding ^{13}CO increased the likelihoods of the "shoulders" of these distributions; the lower half of pressure, and the upper half of mass. An examination of the contour plots in the bottom half of these figures illustrates why, statistically. In the ^{12}CO only model, though column density and filling factor are not well constrained independently, they are highly correlated; their contours run along an almost constant line of beam-averaged column density. Adding ^{13}CO introduced the $X_{^{13}CO}/X_{^{12}CO}$ parameter, which also impacts the absolute flux level of the models, like column density and filling factor. The result are likelihoods that are more constrained but not as highly correlated with one another. Therefore the mass distribution is wider. In the ^{12}CO-only model, the mass of the warm component is about 3.4/6.3% (median/4D Max) the mass of the cool component. Rigopoulou et al. [144] noted that "warm" gas is generally around 1 to 10% of total gas mass for starburst galaxies, so this is about as expected. The addition of ^{13}CO creates somewhat overlapping likelihood distributions for mass (the 1-sigma ranges are just touching), but the median and 4D Max now warm/cool ratios of 11% and 9%, respectively. One factor that may contribute to wider distributions is overestimated error; the error bars are dominated by our 20% calibration error, not statistical error.

After this point, we compare frequently to Panuzzo et al. [125]. The major factor responsible for the differences, just modeling ^{12}CO alone, is the shape of the CO SLED at those lines with upper rotational number greater than J=8. We also explicitely subtracted the cool component's contribution from ^{12}CO $\mathrm{J} = 4 \rightarrow 3$, whereas Panuzzo et al. [125] simply underpredicted the total flux. We will also compare with Loenen et al. [97], another high-J CO study of M82, in Section 3.6.4.

Our results are similar to Panuzzo et al. [125], who found that these high-J CO lines trace a very warm gas component that is separate from the cold molecular gas traced by those lines below $J = 4 \rightarrow 3$. Our best-fit temperature of the ^{12}CO only model (at 447 K, Table 3.4) is close to their value at 545 K, but the overall likelihood for temperature, integrated over all parameters, yields a slightly lower 414 K. Given the size of the uncertainty (335-518 K) in the parameter, the two distributions are very similar, and therefore the result is not significantly different. Such warm gas has also been traced in the S(1) and S(2) transitions of H_2, at 450 K with the Infrared Space Observatory [144] and 536 K with the Spitzer Infrared Spectrograph [10].

We do find a slightly higher density than Panuzzo et al. [125], with our best-fit value of $10^{4.1}$ compared to $10^{3.7}$ cm^{-3}, though the integrated likelihood distributions do overlap (see Figure 3.7). However, the temperature and density are degenerate; higher temperatures and lower densities may produce the same fluxes as lower temperatures and higher densities. Their product, the pressure, is better constrained. We seem to have collapsed/constrained the pressure distribution to the upper half of that presented in Panuzzo et al. [125].

The column density is not as well constrained as presented in Panuzzo et al. [125]; we found that they had an error in calculating the expected fluxes of the higher-J lines for lower column density values. We have recalculated the fluxes for those column densities, and we find that in fact when properly calculated these column densities have a non-zero likelihood. In the ^{12}CO only model, the column density itself is not constrained. However, the column density and filling factor are degenerate, so it is their product (beam-averaged column density, $\langle N_{\rm co} \rangle$) that is better constrained. Our best-fit value is $10^{16.6}$ cm^{-2}.

The total mass in the beam can be calculated using Equation 3.4 (and is presented as the top y-axis in Figures 3.9 and 3.10, upper right). As previously discussed, the ^{12}CO only model produces the expected result of less gas mass in the warm component. In the cool component we find a best-fit mass of 2.0 $\times 10^7$ M$_\odot$ (median 4.7 $\times 10^7$ M$_\odot$). This is smaller than the 2.0 $\times 10^8$ M$_\odot$ traced by the LVG analysis of Ward et al. [179] with lower-J CO lines. This difference is due to the fact that we subtract the contribution to the low-J flux from the warm component; in our initial

modeling of the cold component, before this subtraction, our best-fit mass is 9.8 $\times 10^7$ $M_\odot$ (with a range from 0.2 to 2.2 $\times 10^8$ $M_\odot$). The warm component is a smaller fraction of the gas, with a best-fit of 1.3 $\times 10^6$ $M_\odot$, about 6.3% the mass of the cool component.

The ^{12}CO/^{13}CO relative abundance is also a free parameter in our multi-species model; we find a best-fit value of about 32, similar to the 40 and 30 found previously for the NE and SW lobes, respectively [179].

As mentioned in Section 3.5.1, we also attempted to include our two [C I] lines with the cool component. We do not present the tables for this model because the mass distributions of the warm and cool components became overlapping, indicating the same amount of mass in both components, an unphysical situation. Additionally, the derived relative abundance of [C I] to ^{12}CO was unusually high. We found a ratio of 0.48 to 3.3, which is higher than White et al. [183, average value $\sim$ 0.5], Schilke et al. [153, 0.1-0.3], and Stutzki et al. [163, 0.5] using other methods. Before subtracting the warm component's contribution to the ^{12}CO flux (when we just fit all of the low-J ^{12}CO flux and [C I]), we find ratios more consistent with these values (best-fit 0.4, range 0.09 to 1.23). These two problems could be indicating that the assumption of CO and [C I] coming from the same component is flawed. The column density, temperature, and mass developed somewhat of a double-peaked structure; specifically, the addition of [C I] increases the likelihood of lower column densities and masses, but does not eliminiate the previous likelihood peak.

It is unclear how much of the molecular CO and atomic C are truly cospatial and therefore how physical our results for modeling them all together as one bulk gas component may be. Papadopoulos et al. [130] presented results which argue that [C I] and CO are cospatial and trace the same hydrogen gas mass ([C I] doing so better than CO in many conditions). This conflicts with the theoretical picture of gas clouds (especially in PDRs) as a structured transition between molecular, atomic, and ionized gas, but new observational and theoretical evidence indicates the types of gas are not so distinct [see references within 130]. For example, Howe et al. [73] and Li et al. [94] have found [C I] to trace ^{13}CO well. If the ISM is clumpy, well mixed, and dynamic, the [C I] and CO may be cospatial averaged over large scales. Strong stellar winds (and possibly the interaction with

M81) could be contributing to the dynamic nature of the gas, so it is not unreasonable to believe that the gas has not achieved the simple layered pattern. Though the SPIRE FTS cannot resolve the two separate velocity components of M82, HIFI can, and observations of these two [C I] lines indicate a generally similar shape to the CO lines, namely two Gaussians with the SW component demonstrating higher flux [97].

Wolfire et al. [189] presented a model PDR which shows a cloud layer traced by atomic (not-yet-ionized) [C I] where the hydrogen is still molecular due to self-shielding effects. This "dark molecular gas" (called so because it is not traced by CO) would be less-shielded and at a warmer temperature than the inner-most cloud layer of CO. It is possible that [C I] and CO are somewhat cospatial yet somewhat segregated as in the "dark molecular gas model." Our analysis is consistent with a picture in which the [C I] and ^{12}CO do not completely overlap spatially.

The [C I] J = 1 → 0 emission can also be used to estimate the total hydrogen mass using Equation 12 of Papadopoulos et al. [130]. Using the median $X_{[CI]}/X_{H_2}$ of 1.5 $\times 10^{-4}$ from $X_{[CI]}/X_{^{12}CO}$ = 0.5 [183, 163] and our assumed $X_{^{12}CO}/X_{H_2}$, we find a total gas mass of $4.4 \times 10^7 Q_{10}^{-1}$ $M_\odot$. Q_{10} is the ratio of the column of the J = 1 → 0 emission to the total [C I] column [see Appendix A of 130], which depends on the excitation conditions of the gas; for $Q_{10} \sim 0.5$ [127], the gas mass is 8.8×10^7 $M_\odot$ but is uncertain by modeled uncertainty in $X_{[CI]}$ alone. This method of estimating the mass is higher than total mass estimate of the cool component described earlier in this section. [C I] may be coming from a range of temperatures, but with only two lines, we cannot sort that out.

3.6.2 Physical Conditions: Map

Results for all of the same parameters for the deep spectrum were produced for each of the pixels in the map (that met the criteria in Section 3.5.3). We find that the beam size of SPIRE cannot resolve the structure in M82 as has been done with interferometric maps or high spectral resolution observations (which can resolve the velocity components of the NE and SW lobes). Because of the degeneracy between temperature/density and column density/filling factor,

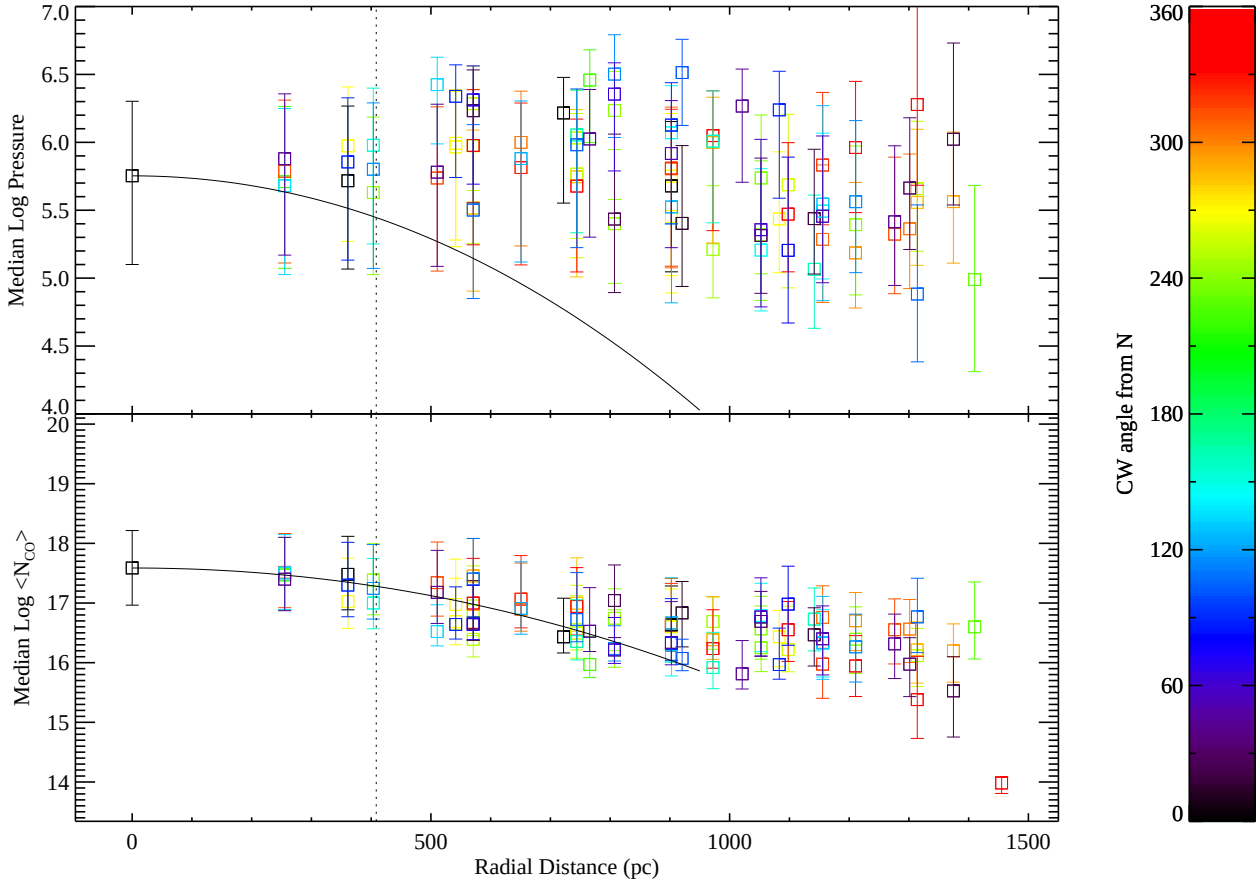

Figure 3.11 Bayesian Likelihood Analysis for Mapping Observation. The x-axis is the map pixel's radial distance (in pc) from the central detector's position, with its clockwise angle (meaning degrees from north through west) represented by the colorbar on the right. The y-axis is the median value (after integrating over all other parameters) and associated 68% error bars. The solid line represents the logarithm of the ^{12}CO $J = 4 \rightarrow 3$ beam profile such that the peak corresponds with the result at the central pixel; it is only plotted to $50''$ from the center because of uncertainties in the profile beyond this region. The dashed line represents one half the beam FWHM.

we present results of their products, pressure and beam-averaged column density in Figure 3.11. $\langle N_{^{12}\mathrm{CO}} \rangle$ shows a radially decreasing trend, roughly corresponding to the decrease in the beam profile (plotted with a solid black line), implying an observational effect due to source-beam coupling. We would expect an off-centered beam to be able to probe the pressure of the central region (because the relative ratios of the SLED would be preserved), so the lack of a radial trend also implies that we are not measuring different areas of M82 in each map pixel. This indicates that the SPIRE FTS map cannot resolve M82's structure, and therefore the single "deep" spectrum is an adequate representation of the galaxy as a whole. Our results in Section 3.6.1 are descriptive of the bulk properties of the galaxy and we do not see trends on the scale of our map. This analysis is separate from the dust temperature gradients (which we also see in the continuum gradients of our map spectra) found in M82 by Roussel et al. [147] and indicates that the dust and molecular gas are not coupled.

One difficulty with the map is it has lower signal/noise; it must also be convolved up the largest beam size (43″, like the deep spectrum). However, as mentioned in Section 3.6.1, it is the highest-J fluxes in the SSW detector that largely constrain the results of the likelihood for the deep spectrum. Therefore, we also attempted to model the map with just those lines with upper-J level of 9 or higher, without convolving. These lines all were measured with a beam FWHM of $\sim 19''$, offering higher resolution. However, these lines are also weaker, and with fewer, lower signal/noise lines this method does not constrain any parameters as well.

Though the off-axis pixels may not provide new information about the physical trends of the galaxy, we can compare the deep spectrum to the center pixel of our map as a test of the source-beam coupling corrections (see Section 3.4.2). The results of the central pixel are very similar to those presented in Section 3.6.1, though the integrated likelihoods are generally wider (the parameters are less constrained). This is partially, but not entirely, due to larger error bars on the SSW lines.

3.6.3 Molecular Line Absorption

In addition to the Bayesian likelihood modeling, we can also briefly discuss the absorption lines presented in Table 3.1.

3.6.3.1 Hydrogen Fluoride (HF)

Hydrogen fluoride (HF) is potentially a sensitive probe of total molecular gas column, because the HF/H_2 ratio is more reliably constant than ^{12}CO/H_2 because the formation of HF is dominated by a reaction of F with H_2 [114]. Furthermore, HF J = 1 → 0 is generally seen in absorption because of its high A-coefficient, 2.42 $\times 10^{-2}$ s^{-1} [114]. Assuming all HF molecules are in the ground state [generally true in the diffuse and dense ISM, 114], the HF J = 1 → 0 line yields the optical depth simply as $\tau = -ln(F_l/F_c)$, where F_l/F_c is the line-to-continuum ratio. In the case of HF, we mask out a nearby water emission line (1226 to 1229 GHz), though because the signal in each wavenumber bin is not independent due to the ringing, this can introduce added uncertainty. Therefore the following discussion is meant to be approximate. We estimate the HF column density using

$$\int \tau dv = \frac{A_{ul} g_u \lambda^3}{8\pi g_l} N(HF), \tag{3.5}$$

where $g_u = 3$ and $g_l = 1$. This implies $\int \tau dv = 4.16 \times 10^{-13} N(HF)\,\mathrm{cm}^2$ km s^{-1}. The HF line occurs in a part of our spectrum with some noticeable structure in the continuum (see Figure 3.3, third panel, around 1250 GHz). If we only integrate the 6 GHz surrounding the line, we find a column density of HF of 6.61 $\times 10^{13}$ cm^{-2}. Expanding the range over which we integrate increases the derived column density, but this may be due to other features in the spectrum, and so we consider our derived value a lower limit. Assuming a predicted abundance of HF of 3.6×10^{-8} [114], this corresponds to a molecular hydrogen column density of 1.84×10^{21} cm^{-2}. The column density derived from this line is similar to that of $\langle N \rangle$ of the cool component of ^{12}CO. However, there are still some uncertainties to this calculation. We are only able to see the HF in front of the continuum emission, and therefore we are not probing the total column density. Higher spectral

resolution could reveal the extent of spatial colocation of HF with CO. There are also uncertainties associated with either molecular abundance assumed and whether or not all HF molecules are truly in the ground state.

3.6.3.2 Water and Water Ion ($H_2O^{(+)}$)

Water is fundamental to the energy balance of collapsing clouds and the subsequent formation of stars, planets, and life. Many *Herschel* key programs are currently studying water and chemically related molecular species in a variety of conditions. An excellent summary of water chemistry in star forming regions is available in van Dishoeck et al. [175].

Weißet al. [181] studied the low-level water transitions in M82, and they detect the ground-state o-H_2O emission in two clearly resolved components, which we do not. With the $41''$ beam, the two components add to 370 ± 44 Jy km/s beam^{-1}, well below our threshold of detection, as can be seen by examining Table 3.1. Though we do not detect that line, we do detect four new water lines in addition to those presented in Weißet al. [181]: two p-H_2O (752 and 1229 GHz) and two o-H_2O (1097 and 1153 GHz). Combined with their ground-state transition of o-H_2O, we add to the picture of the water excitation in M82.

Our ground-state lines indicate similar column densities as Weißet al. [181], within a factor of 2. Using Equation 3.5 (low-excitation approximation), we find column densities of p-H_2O and o-H_2O^+ of $\sim 4 \times 10^{13}$ cm^{-2}, whereas Weißet al. [181] finds 9.0 and 2.2 $\times 10^{13}$ cm^{-2}, respectively. They found that the water absorption comes from a region northeast of the central CO peak; shocks related to the bar structure of M82 could be releasing water into the gas phase at such a location. The fact that the water comes from a lower column density region seems to contradict the existence of a PDR, which would require high column densities to shield water from UV dissociation; however, the relative strength and similarity of absorption profiles of o-H_2O^+ compared to p-H_2O indicates some ionizing photons (see their work for complete interpretation). Though these transitions are tracing a different region than CO, they add to the picture of a complicated mix of energy sources present in the gas, as addressed in Section 3.6.4. Models of water emission from shocks have been

investigated by others [i.e. 58], but detailed modeling of the water spectrum of M82 is outside the scope of this work.

3.6.4 Gas Excitation

At the high temperature of the warm component, the cooling will be dominated by hydrogen. Le Bourlot et al. [92] modeled the cooling rates for H_2, and made their tabulated rates available with an interpolation routine for desired values of density, temperature, ortho- to para-H_2 ratio, and H to H_2 density ratio[1] . For our best-fit temperature and density, assuming $n(H)/n(H_2) = 1$ [recommended by 92, for PDRs], this corresponds to a cooling rate of $10^{-22.54}$ erg s^{-1} per molecule, or 3 $L_\odot/M_\odot$(using o/p $H_2 = 1$, though the number is only $\sim 3\%$ lower for o/p $H_2 = 3$). Given the warm mass of 1.3×10^6 $M_\odot$ (using the ^{12}CO model for the rest of this section), that implies a hydrogen luminosity of 3.9×10^6 $L_\odot$. The total observed hydrogen luminosity thus far has been higher than this number; adding the luminosities presented in Rigopoulou et al. [144] and correcting for extinction as in Draine [44], we find a total of 1.2×10^7 $L_\odot$in the (0-0)S(0)-S(3), S(5), S(7), and (1-0)Q(3) lines. However, some of these hydrogen lines are tracing lower or higher temperature gas. We note that the mass range within one standard deviation of our likelihood results for the warm component is 0.93-5.2 $\times 10^6$ $M_\odot$, which corresponds to a predicted luminosity of 0.28-1.6 $\times 10^7$ $L_\odot$, encompassing the measured hydrogen luminosity.

There are a few possibilities for the source of the excitation of the gas: X-ray photons, cosmic rays, UV excitation of PDRs and shocks/collisional excitation. Hard X-rays from an AGN have already been ruled out by others in the literature due to the lack of evidence for a strong AGN and low X-ray luminosity [1.1 $\times 10^6$ $L_\odot$, 162].

The CO emission from M82 has previously been interpreted using PDR models. Beirão et al. [10] noted with the Spitzer Infrared Spectrograph that the H_2 emission is correlated with PAH emission, indicating that it is mainly excited by UV radiation in PDRs. Loenen et al. [97] combined HIFI data with ground based detections in order to model ^{12}CO J=1→0 to J=13→12

[1] http://ccp7.dur.ac.uk/cooling_by_h2/

and ^{13}CO J = 1 → 0 to J = 8 → 7. They reproduced the measured SLEDs with one low-density ($\log(n(H_2))$=3) and two high-density ($\log(n(H_2))$=5,6) components with relative proportions of 70%, 29%, and 1%, respectively. The low-density component is largely responsible for the low-J emission, while the highest-density component is responsible for the highest-J emission. These high densities are not consistent with the results of our likelihood analysis detailed in Section 3.6.1; the likelihood of solutions for the warm component at $\log(n(H_2))$>5 is essentially zero. We note that Loenen et al. [97]'s Figure 3 shows the consistency between HIFI and SPIRE fluxes from Panuzzo et al. [125]. In other words, the difference is not due to discrepant line fluxes, but different models (PDR vs. CO likelihood analysis).

There are two major differences in the approach of this work and Loenen et al. [97]. First, the order in which we approach the problem is different. We first analyze the CO excitation using likelihood analysis to determine the physical conditions. Once we have these conditions, we then look to the possible energy sources **based on** the conditions we have already derived, instead of first seeing under which conditions a certain energy source fits. Second, we look beyond the one best fit solution: in addition to presenting the best-fit solution, our likelihoods analyze the relative probabilities for a larger parameter space.

We also attempted to reproduce our deep SLED with various PDR models. Meijerink et al. [111] have added to their PDR and XDR models to include enhanced cosmic rays (at a rate of 5 $\times 10^{-15}$ s^{-1}), near our assumed rate discussed later in this section. Such models are currently available for incident flux of $\log(G_0)$ of 2-4 (G_0 = 1.6 $\times 10^{-3}$ erg cm^{-2} s^{-1}) for $\log(n(H_2))$=3 and $\log(G_0)$ of 3-5 for $\log(n(H_2))$ of 4 and 5. By examining the ratios of ^{12}CO J=9→8 with all higher-J lines (those largely driving the likelihood results, and also measured from similar beam sizes), none of the available 9 PDR models are an ideal match, but the PDR scenario for $\log(n(H_2))$=3, $\log(G_0)$=3 is the best match. Figure 3.12 compares the predicted and observed ratios. The ratios used are without source-beam coupling correction because the SSW already has similar beam sizes, but the ratios with beam correction are within 4-8% of those presented in Figure 3.12.

Additionally, we used a higher-resolution (in density and incident flux) grid of ^{12}CO PDR

models [189]. The same line ratios previously discussed (those shown in Figure 3.12) can only be reproduced by higher densities. For $(J=9\rightarrow8)/(J=10\rightarrow9)$, the observed ratio is only found for $\log(n(H_2)) > 4.5$, $\log(G_0) > 2$, and by $(J=9\rightarrow8)/(J=13\rightarrow12)$, only for $\log(n(H_2)) > 5$, $\log(G_0) > 2.5$.

To summarize, current PDR models can only explain the observed high-J ^{12}CO emission with densities higher than those indicated by the likelihood analysis (even when all priors are excluded). The cosmic-ray enhanced PDR models, though sparse, can come closer to reproducing the high-J line ratios at a lower density, though these are also below our likelihoods. There is also evidence that shocks enhance high-J lines far more than PDRs [137]. In their models, almost all of the emission from the lowest-J lines came from unshocked gas, and most of the emission above $J=7\rightarrow6$ was from shocked gas. The combination of shocks and PDRs could be responsible for the high-J CO lines observed, while PDRs alone are adequate to explain the lower-J CO lines and PAH emission. In summary, these high-J lines are not consistent with current PDR models, but improved modeling of shocks and the effects of cosmic rays on PDRs may help explain their emission.

Cosmic rays (CRs) are another possibility for the excitation. The Very Energetic Radiation Imaging Telescope Array System (VERITAS) Collaboration recently reported that the cosmic-ray density in M82 is about 500 times the average Galactic (Milky Way) density [176]. By using the cosmic ray ionization rate of the Galaxy [2-7 $\times10^{-17}$ s^{-1}, 62, 173], multiplied by 500, and then multiplied by the average energy per ionization (20 eV), one finds an energy deposition rate of 2-7 $\times10^{-13}$ eV/s per H_2 molecule in M82. This implies a heating rate of 0.03 to 0.12 $L_\odot/M_\odot$, less than 5% of the required molecular hydrogen cooling rate. Thus, cosmic rays alone cannot excite the molecular gas.

Turbulent heating mechanisms may also play a role in M82. From Bradford et al. [18], the turbulent heating per unit mass can be expressed in $L_\odot/M_\odot$ as

$$1.10\left(\frac{v_{rms}}{25\,\mathrm{km\ s^{-1}}}\right)^3\left(\frac{1\,\mathrm{pc}}{\Lambda_d}\right) \tag{3.6}$$

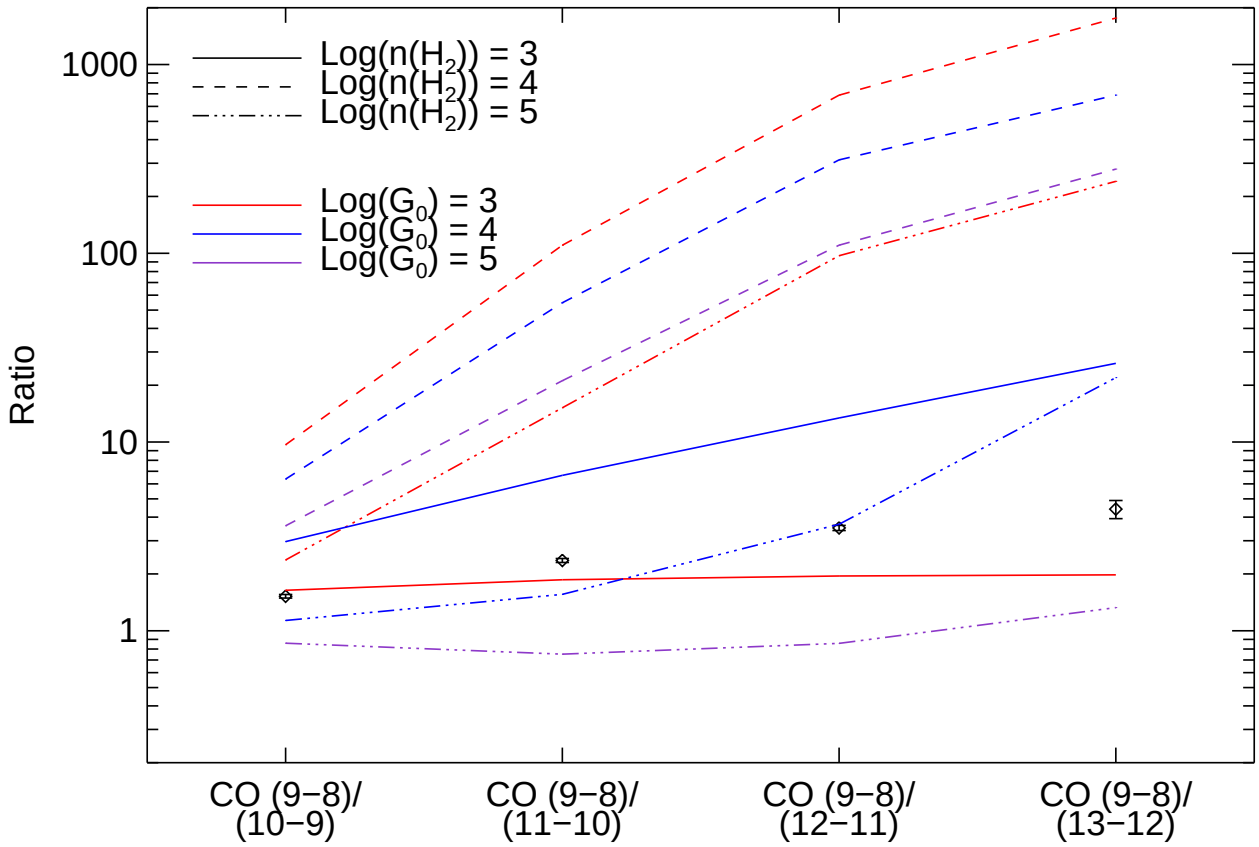

Figure 3.12 Enhanced Cosmic Ray PDR Models. The observed ratios are black diamonds. For the models, the line style indicates gas density and the line color indicates incident flux. Log(G_0)=2 is not plotted because the highest-J line fluxes are not reported for that model.

where v_{rms} is the turbulent velocity and Λ_d is the typical size scale of turbulent structures. We use the Jeans length for this size scale, calculated from the parameters of the likelihood results (Section 3.6.1), which is 0.9 pc. Given this size scale, the observed cooling rate could be replicated with a turbulent velocity of 33.7 $\mathrm{km\,s^{-1}}$. This would imply a velocity gradient of approximately 37.5 $\mathrm{km\,s^{-1}\,pc^{-1}}$. When we calculate the velocity gradient using our model results ($dv/dr = \Delta v\ n(H_2)/N(H_2)$), we find a 68% confidence lower limit of 16 $\mathrm{km\,s^{-1}\,pc^{-1}}$] (4 $\mathrm{km\,s^{-1}\,pc^{-1}}$ if we use the model with ^{13}CO) , but the upper limit is unphysically high. The velocity required for turbulent heating seems reasonable in context of our likelihood results. Panuzzo et al. [125] used their calculated velocity gradient of 35 $\mathrm{km\,s^{-1}\,pc^{-1}}$ to determine that they could match the heating required with a sizescale of 0.3 to 1.6 pc. These velocity gradients seem large compared to Galactic star-forming sites [e.g. 74], but M82 is known to have powerful stellar winds. According to Beirão et al. [10], the starburst activity has decreased in the past few Myr, and this appears to be evidence of negative feedback (by stellar winds and supernovae), because M82 still has a large reservoir of gas available for star formation. Therefore, there is evidence for turbulent heating mechanisms being in place. Additionally, Downes & Solomon [43] found high turbulent velocities (30-140 $\mathrm{km\,s^{-1}}$) in models of extreme star-forming galaxies.

None of the possibilities described seem to provide enough heating by themselves, with the exception of turbulent heating, which is based on a few approximations and assumptions. Likely, there is a combination of factors, namely PDRs and shocks/turbulent mechanisms. Such a situation has also been seen in other submillimeter-bright galaxies, discussed next. Interestingly, even a more quiescent galaxy like NGC 891 requires a combination of PDRs and shocks to explain mid-J CO transitions [J = 6 → 5, J = 7 → 6, 119].

3.6.5 Comparison to Other Starburst and Submillimeter Galaxies

Because only the first few lines in the CO ladder are easily visible from the ground for nearby galaxies, the high-J lines detected by *Herschel* represent new territory. Therefore, while adequate diagnostics of high-J CO lines are still being developed, it is useful to compare to other

submillimeter-bright galaxies.

Mrk 231 contains a luminous (Seyfert 1) AGN. It also shows a strong high-J CO ladder, such that only the emission up to $J = 8 \rightarrow 7$ is explained by UV irradiation from star formation. Their high-J CO luminosity SLED however, is flat (though ours for M82 are stronger than predicted, they are still decreasing with higher-J). van der Werf et al. [172] can explain this trend with either an XDR or a dense PDR. An additional difference between M82 and Mrk 231 is that OH^+ and H_2O^+ are both seen in strong emission in Mrk 231 (instead of absorption), indicative of X-ray driven chemistry. Mrk 231 is also more face-on than M82.

The FTS spectrum of Arp 220 has many features not present in M82, such as strong HCN absorption, P-Cygni profiles of OH^+, H_2O^+ and H_2O, and evidence for an AGN [139]. CO modeling, similar to the procedure done in this work, also indicates that the high-J lines trace a warmer component than low-J lines ($\sim$ 1350 K). Mechanical energy likely plays a large role in the heating of this merger galaxy as well. Though M82 has an outflow, it is not detected in P-Cygni profiles of the aforementioned lines.

The redshift of HLSW-01 [34] allows the CO $J = 7 \rightarrow 6$ to $J = 10 \rightarrow 9$ lines to be observed from the ground, as has been done with Z-Spec [155]. Unlike M82 (and others), the known CO SLED from $J = 1 \rightarrow 0$ and up can be described by a single component at 227 K (1.2×10^3 cm^{-3} density). If the velocity gradient is not constrained to be greater than or equal to that corresponding to virialized motion, the best fit solution becomes 566 K (0.3×10^3 cm^{-3} density), closer to our temperature. We chose to exclude this prior due to uncertainties in the calculation of velocity gradient related to M82's turbulent morphology. HLSW-01 appears to be unique in that a cold gas component is not required to fit the lower-J lines of the SLED, though two-component models can find a best-fit solution with a cold component.

In summary, M82 (like Arp 220 and HLSW-01) does not have the high CO excitation dominated by an AGN as seen in Mrk 231. Therefore, in addition to distinguishing between PDRs and shocks, high-J CO lines may also be used to indicate XDRs.

3.7 Conclusions

We have presented a multitude of molecular and atomic lines from M82 in the wavelength range (194-671 μm) accessible by the *Herschel*-SPIRE FTS (Table 3.1). After modeling ^{12}CO, ^{13}CO and [C I], we find support for the high-temperature molecular gas component presented in the results of Panuzzo et al. [125]. The temperature traced by the warm component of ^{12}CO is quite high (335-518 K), and the addition of ^{13}CO slightly expands the likelihood ranges. The addition of [C I] produced results that indicate that these atom is not entirely tracing the same region as ^{12}CO. Some of the emission from these molecules (especially [C I]) are likely tracing more diffuse gas less shielded from UV radiation.

The mapping observations did not resolve any significant gradients in physical parameters (except evidence for a slight drop-off in beam-averaged column density, consistent with the beam profile) indicating that the single "deep" spectrum is an adequate representation of the galaxy when limited by our beam size. However, the mapping observations were important in confirming the source-beam coupling factor utilized in Panuzzo et al. [125] and here, because through convolution of the maps we were able to confirm the central pixel's results matched with the deep spectrum.

Molecular absorption traces lower column regions of the disk than those traced by CO emission, but contribute to the interpretation of the molecular gas of M82 being excited by a combination of sources. Despite the enhanced cosmic ray density in M82, we do not find evidence that cosmic rays alone are sufficient to heat the gas enough to match the modeled hydrogen cooling rate. PDR models can only replicate the high-J CO line emission at high densities incompatible with those indicated by the likelihood analysis, though cosmic-ray enhanced PDRs may be a closer match at lower densities. Turbulent heating from stellar winds and supernovae likely play a large role in the heating. More specifically, shocks are required to explain bright high-J line emission [137].

Like other submillimeter bright galaxies, *Herschel* has opened up new opportunities and questions about molecular and atomic lines that have never been observed before. Because of this, the diagnostic power of high-J CO lines is still in development, and newer models currently being

developed may be able to explain the emission seen from M82 and other extreme environments.

Acknowledgments SPIRE has been developed by a consortium of institutes led by Cardiff Univ. (UK) and including: Univ. Lethbridge (Canada); NAOC (China); CEA, LAM (France); IFSI, Univ. Padua (Italy); IAC (Spain); Stockholm Observatory (Sweden); Imperial College London, RAL, UCL-MSSL, UKATC, Univ. Sussex (UK); and Caltech, JPL, NHSC, Univ. Colorado (USA). This development has been supported by national funding agencies: CSA (Canada); NAOC (China); CEA, CNES, CNRS (France); ASI (Italy); MCINN (Spain); SNSB (Sweden); STFC, UKSA (UK); and NASA (USA). J.K. also acknowledges the funding sources from the NSF GRFP. The research of C.D.W. is supported by grants from the Natural Sciences and Engineering Research Council of Canada. Thank you to the anonymous referee for comments which significantly improved this work.

Chapter 4

Survey of Molecular ISM Properties of Nearby Galaxies: Observations and Methods

4.1 Preface

The next two chapters together compose a paper currently being submitted for publication; this chapter outlines the observations and methodology, while the next presents the discussion and interpretation. It applies the methods presented in the previous chapter (and others) to a larger sample of galaxies, using only single-beam observations.

4.2 Abstract

The ^{12}CO J = 4 → 3 to J = 13 → 12 lines of the interstellar medium (ISM) from nearby galaxies, newly observable with the *Herschel* SPIRE Fourier Transform Spectrometer (FTS), offer an opportunity to study warmer, more luminous molecular gas than that traced by ^{12}CO J=1→0. Here we present a survey of 17 infrared-luminous galaxy systems (21 pointings) observed by the FTS. In addition to photometric modeling of the dust masses/luminosities and star formation rates, we modeled full ^{12}CO spectral line energy distributions from J = 1 → 0 to J = 13 → 12 with two components of warm and cool CO gas. We supplemented these models with LTE analysis of [CI], [CII], [NII], and H_2 lines. CO is emitted from a low-pressure/high-mass component traced by the low-J lines and a high-pressure/low-mass component which dominates the luminosity. We provide an in-depth discussion of the systematic effects of two-component CO modeling (e.g. model fits without J > 3 lines overestimate gas pressure by ∼ 0.5 dex), as well as comparisons of our results to

high-redshift galaxies and star-forming regions in the Galaxy. There is a shallow correlation between the warm gas pressure (but not cold gas pressure) and $L_{\rm FIR}$; the molecular interstellar medium of starburst galaxies is not simply an ensemble of Galactic-type GMCs. This work represents the development of a pipeline that will be applied to a larger number of galaxies observed with *Herschel*.

4.3 Introduction

Cool molecular gas in the interstellar medium (ISM) is the raw material out of which stars will form. The carbon monoxide molecule (^{12}CO, henceforth CO) is known to be an excellent tracer of the total molecular hydrogen in the ISM, especially at the ground-state rotational transition of $J = 1 \rightarrow 0$. For many prominent nearby galaxies, such as M82, Arp 220, and NGC 1068, the emission from the higher-J lines of CO has proven to be far more luminous than would have been predicted from ground-based observations restricted to low-J lines [e.g. 125, 80, 139, 161, 143, 133]. It is already well-established that the ISM is comprised of a multitude of constituents, both in composition (ionized, atomic, molecular) and physical conditions (temperatures, densities). High-J lines of CO offer a new opportunity to study the relatively warm (compared to low-J CO), yet still molecular, ISM. This warmer CO is notable because of its much large luminosity, representing a much greater role in the total energy budget of the molecular gas. Therefore, to study the ongoing questions regarding the feedback interactions between different energy sources (cosmic rays, ultraviolet light from stars, X-rays from AGN, or mechanical heating from turbulence, winds, shocks, etc.), one must specifically examine the warmer CO via high-J transitions.

In general, due to atmospheric water absorption, only the lowest-J lines of CO can be observed from the ground. However, the launch of the *Herschel* Space Observatory [134] offered a unique opportunity to observe at higher frequencies.[1] The Spectral and Photometric Imaging REceiver (SPIRE) instrument [66] consisted of a three-band imaging photometer and an imaging Fourier transform spectrometer (FTS). The FTS simultaneously observed spectra from 447-1550 GHz,

[1] Herschel is an ESA space observatory with science instruments provided by European-led Principal Investigator consortia and with important participation from NASA.

which for nearby galaxies, encompasses the ^{12}CO J=4→3 to J=13→12 transitions, among other molecular and atomic fine structure lines.

Herschel's mission has come to an end because of its finite supply of cryogens, but it has left behind an impressive legacy of observations. Approximately 300 galaxies have been observed in point-source mode with the FTS, with spectra of varying quality. In this paper, we establish a uniform pipeline for analysis of FTS spectra of galaxies, from the raw observations to the determination of the physical parameters of the cool and warm emitting CO gas. We present initial results for 21 pointings of 17 unique galaxy systems, most of which have been well-studied in the past. The motivation for this survey is to understand the physical parameters (e.g. pressure and mass) which describe warm CO emission and determine how the parameters vary with galaxy type, total infrared luminosity, etc. Studying the physical parameters of the gas provides necessary information to interpret the energy budget and physical processes acting on the gas. Additionally, it informs the analysis of high-redshift submillimeter galaxies with fewer observed lines. This paper represents a sub-sample of a planned archival study of the molecular gas and dust in as many galaxies as possible observed with the FTS.

Section 4.4 describes how the *Herschel* observations were utilized, including sample selection, source-beam coupling correction and spectral line fitting. Section 4.5 details our modeling methodology: dust and CO likelihood analysis with Multinest[55], stellar population modeling with MAGPHYS [35], and LTE analysis of H_2, [CI], [CII], and [NII]. A flowchart in Figure 4.1 should help the reader understand the many types of data and modeling utilized in this work. Section 5.1 summarizes our findings for this sample of galaxies, including a discussion of systematic effects of two-component likelihood modeling of physical properties, the calculation of the CO luminosity to mass conversion factor and gas to dust mass, and comparisons among our galaxies, Galactic star-forming regions, and high-redshift galaxies. Finally, we present conclusions and future plans in Section 5.2.

Table 4.1. *Herschel*-SPIRE Observation Numbers for Galaxies in Sample

FTS Name	Type	FTS RA	FTS Dec	FTS ObsID	Phot ObsID	D_L	L_{FIR}	Order
NGC 253	SB	0h47m33.12s	-25d17m17.6s	1342210847	1342199424	3.4	10.52	19
NGC 1068	AGN	2h42m40.71s	-0d00m47.8s	1342213445	1342189440	16.1	11.40	11
NGC 1222	Early	3h08m56.74s	-2d57m18.5s	1342239354	1342239232	34.6	10.66	17
NGC 1266	Early	3h16m00.70s	-2d25m38.0s	1342239338	1342189440	30.6	10.44	20
NGC 1365-SW	AGN	3h33m35.90s	-36d08m35.0s	1342204021	1342201472	20.7	11.11	12
NGC 1365-NE	AGN	3h33m36.60s	-36d08m20.0s	1342204020	1342201472	20.7	11.11	13
IRAS 09022-3615	ULIRG	9h04m12.72s	-36d27m01.3s	1342231063	1342230784	261.7	12.21	3
UGC 05101	AGN	9h35m51.65s	+61d21m11.3s	1342209278	1342204928	176.4	11.95	6
M82	SB	9h55m52.22s	+69d40m46.9s	1342208389	1342185600	3.7	10.79	16
Arp 299-B	SB	11h28m31.00s	+58d33m41.0s	1342199249	1342199296	49.3	11.74	9
Arp 299-C	SB	11h28m31.00s	+58d33m50.0s	1342199250	1342199296	49.3	11.74	8
Arp 299-A	SB	11h28m33.63s	+58d33m47.0s	1342199248	1342199296	49.3	11.74	10
NGC 4038	SB	12h01m53.00s	-18d52m01.0s	1342210860	1342188672	23.0	10.90	14
NGC 4038 (Overlap)	SB	12h01m54.90s	-18d52m46.0s	1342210859	1342188672	23.0	10.90	15
Mrk 231	AGN	12h56m14.23s	+56d52m25.2s	1342210493	1342201216	187.9	12.41	1
Cen A	AGN	13h25m27.61s	-43d01m08.8s	1342204037	1342188672	3.6	9.93	21
M83	SB	13h37m00.92s	-29d51m56.7s	1342212345	1342188672	6.1	10.53	18
Mrk 273	AGN	13h44m42.11s	+55d53m12.7s	1342209850	1342201216	167.6	12.13	5
Arp 220	ULIRG	15h34m57.12s	+23d30m11.5s	1342190674	1342188672	81.4	12.14	4
NGC 6240	SB	16h52m58.89s	+2d24m03.4s	1342214831	1342203648	108.0	11.83	7
IRAS F17207-0014	ULIRG	17h23m21.96s	-0d17m00.9s	1342192829	1342203648	189.8	12.34	2

Note. — In this table only, sources are sorted by RA; in subsequent tables, sources will be sorted by $L_{\rm FIR}$, in the order given in the rightmost column. For example, Mrk 231 has the highest $L_{\rm FIR}$, so it is first in subsequent tables, IRAS F17207-0014 is second, etc. FTS/Phot ObsID are the observation IDs for the FTS spectrometer/photometer. D_L is the luminosity distance in Mpc and $L_{\rm FIR}$ is in $\log(L_\odot)$, both from HyperLeda[2] . The category given in the Type column is not necessarily exclusive to other types (SB = Starburst, Early = early type).

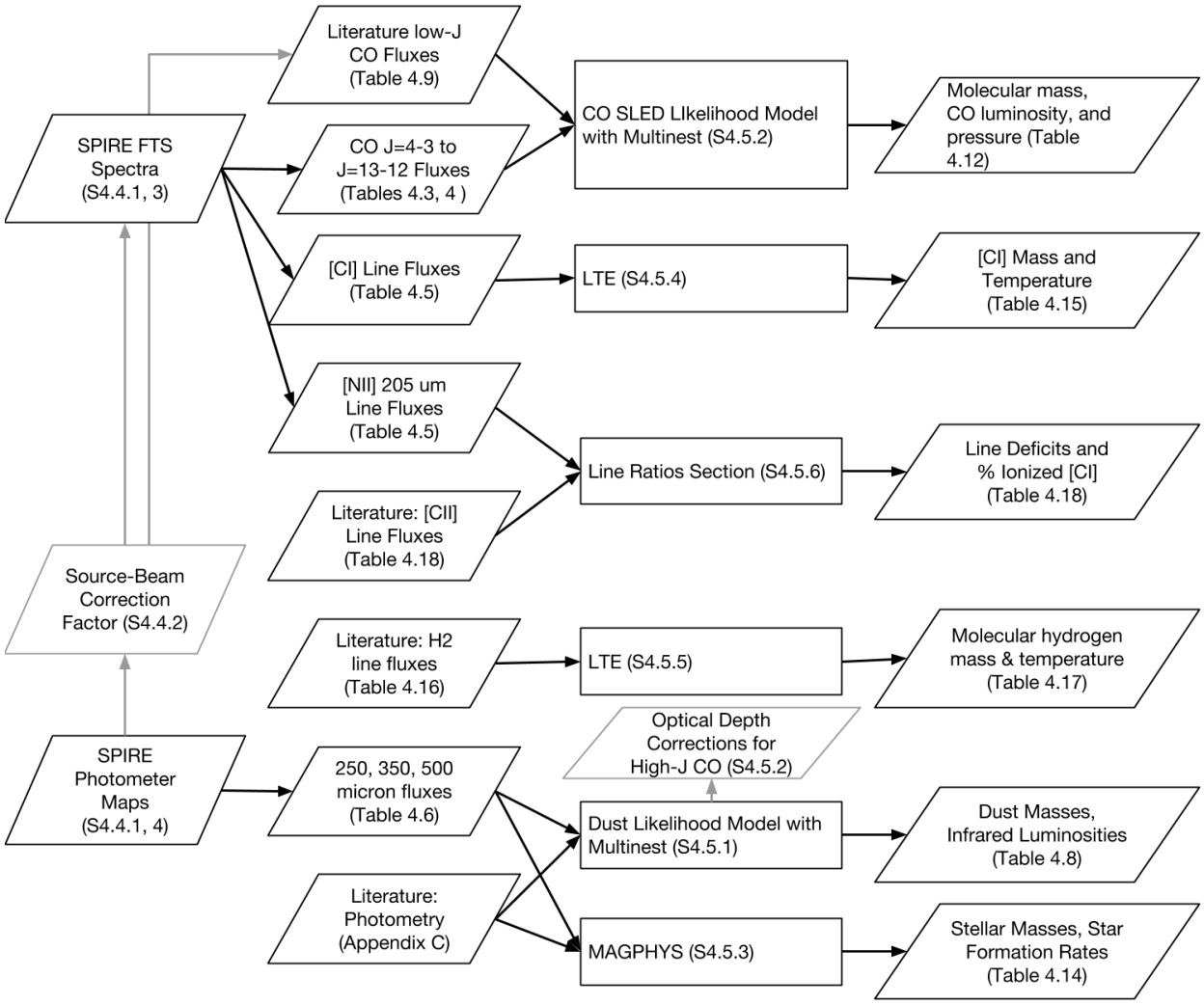

Figure 4.1 Flowchart of Data Analysis.

4.4 Observations

4.4.1 Sample Selection

This paper utilizes publicly available data from both the SPIRE spectrometer (FTS) and photometer, downloaded from the Herschel Science Archive. The 21 pointings in Table 4.1 represent 17 unique galaxy systems. This table lists both the observation IDs, coordinates and some basic properties of the sample galaxies; they are presented in order by RA in this table only, and will subsequently be presented in order of far infrared luminosity, $L_{\rm FIR}$ (the last column, "Order," can help the reader find each galaxy in subsequent tables and figures).[3] Some of the interacting galaxies with separated nuclei had FTS observations centered at each nucleus: there are two separate pointings within the Antennae (NGC 4038 and the Overlap region), two within NGC 1365, and three within Arp 299. Appendix B includes additional information on how these and other extended galaxies were handled.

These specific galaxies were chosen because they are relatively nearby (10 within 50 Mpc, all within $\sim$ 260 Mpc) and their spectra showed measurable, bright CO emission. Six are identified as AGN (UGC 05101, NGC 1068, Cen A, NGC 1365, Mrk 273, Mrk 231), three as ULIRGS (Arp 220 [which may also have an AGN, e.g., Rangwala et al. [139]], IRAS F17207-0014, IRAS 09022-3615), two as early-type galaxies (NGC 1266, NGC 1222), and the remaining six as starbursts (NGC 4038/4039, M82, M83, NGC 6240, Arp 299, NGC 253). The aforementioned categories are not mutually exclusive or necessarily complete.

The SPIRE photometer bands are 250, 350, and 500 μm for the Photometer Short/Medium/Long Wave (PSW, PMW, PLW), respectively. The photometer maps were all used as downloaded, as processed with Standard Product Generation (SPG) v8.2.1 and calibration `spire_cal_8_1`. The Fourier transform spectrometer (FTS) contains two arrays of detectors: the lowest frequencies are captured by the Spectrometer Long Wave (SLW, 303-671 μm) and the higher frequencies by the Spectrometer Short Wave (SSW, 194-313 μm). The FTS spectra were, in general, single(sparse)-

[3] Throughout this work, we use $L_{\rm FIR}$ to refer to the integrated flux from 8-1000 μm; definitions vary in the literature.

pointed observations downloaded as SPG v6.1.0 and reprocessed with HIPE v9 and `spire_cal_9_1`.[4] We used smooth off-axis background subtraction for UGC 05101 and Mrk 231 (see Appendix B) and daily dark background subtraction for NGC 1222, IRAS 09022-3615, and NGC 6240. The exceptions to the HIPE v9 reprocessing were NGC 4038 and its Overlap region, which were extracted from a mapping observation [154], as was M83 [191] and provided via private communication - see Appendix B for more information on these extended galaxies. IRAS F17207-0014 and Mrk 273 were reprocessed using HIPE v10 because the detector temperatures were abnormally low for those particular observations and standard telescope background subtraction available in v9 was inadequate.

4.4.2 Source-Beam Correction of Semi-Extended Sources

The emission we measured in the FTS (F') was produced by the multiplication of the (generally-non-Gaussian) source and beam. The beam size, $\Omega(\nu)_b$, varied from b (effective Gaussian FWHM) $\sim 45''$ to $17''$ across both bands ($\Omega_b = 1.133b^2$). For a point source ($\Omega_b \gg \Omega_s$), the FTS measured the total flux in Jy at all wavelengths. For a uniformly extended source ($\Omega_b \ll \Omega_s$), the flux density scaled with Ω_b, i.e. $(F'_{\Omega_1}/F'_{\Omega_2}) = \Omega_1/\Omega_2$. Many of the sources in this sample are semi-extended, meaning their source size is comparable to the beam size of the FTS. In this case, $(F'_{\Omega_1}/F'_{\Omega_2}) = \eta_{1,2}$, where $\eta_{1,2}$ will be between Ω_1/Ω_2 (uniform extended) and 1 (point source). We use a two-step procedure to correct the spectra for source-beam coupling effects: 1) derive $\eta_{1,2}$ from photometry maps and use it to scale all fluxes to a $43\farcs5$ beam, and 2) scale the resulting spectrum to match the total photometer fluxes. The final spectrum is as if it were observed by an instrument with a constant beam size.

Proper modeling of $\eta_{1,2}$ is necessary to compare flux densities measured at different frequencies of the FTS band as well as those measured from other telescopes. For this we follow a similar procedure to that used in Panuzzo et al. [125] using the Photometer Short Wave (PSW, 250 μm)

[4] HCSS, HSpot, and HIPE are joint developments by the Herschel Science Ground Segment Consortium, consisting of ESA, the NASA Herschel Science Center, and the HIFI, PACS and SPIRE consortia.

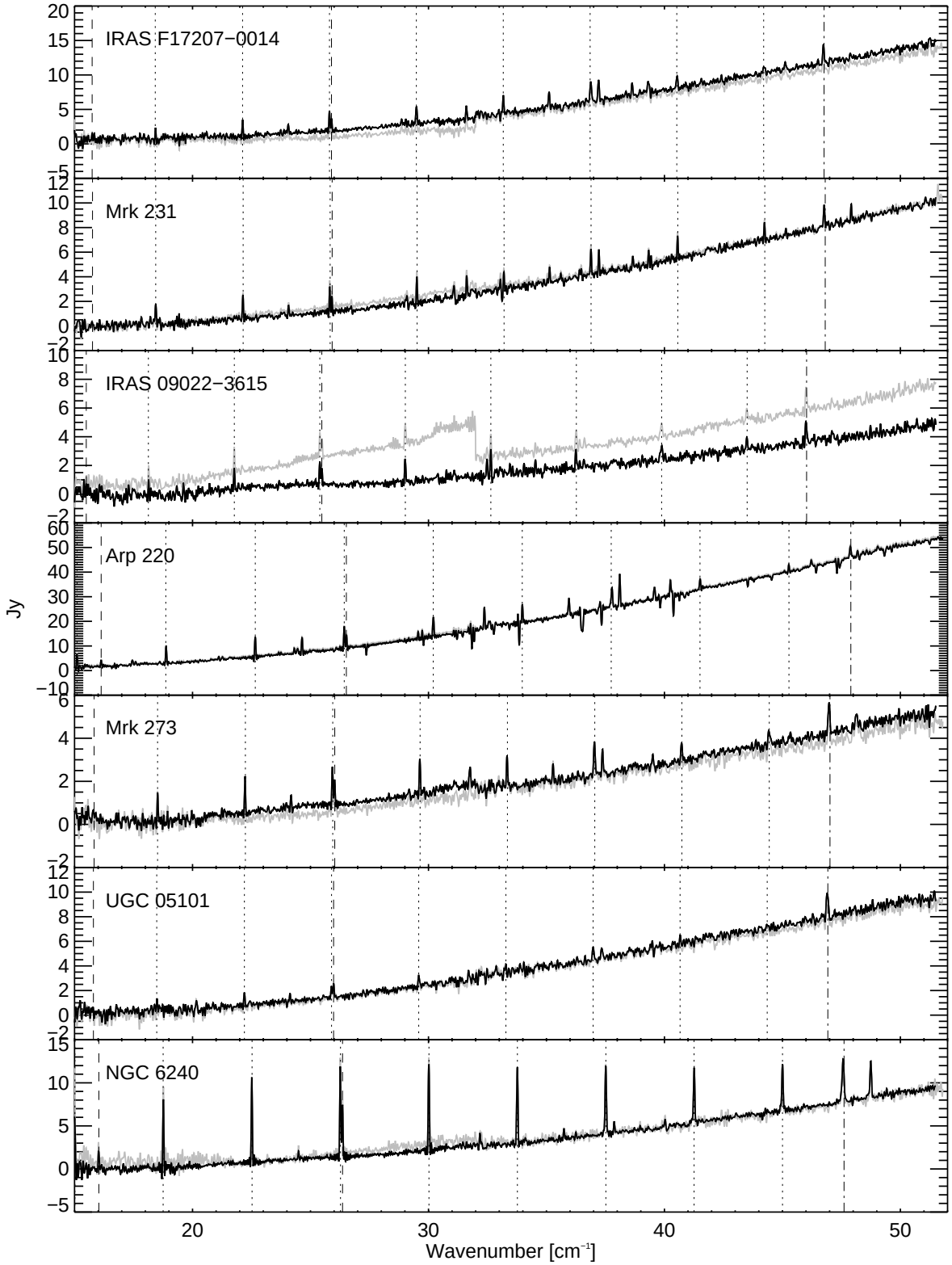

Figure 4.2 Source-Beam Coupling Corrected FTS Spectra 1 of 3. The galaxies, starting with this figure, are in order of decreasing far-infrared luminosity. The uncorrected spectra are shown in gray, the corrected spectra (as described in Section 4.4.2) are plotted over top in black. For point-source-like spectra, e.g. UGC 05101, the correction may be unnoticeable. The redshifted locations of the ^{12}CO, [CI], and [NII] lines are shown with dotted, dashed, and dash-dotted lines, respectively.

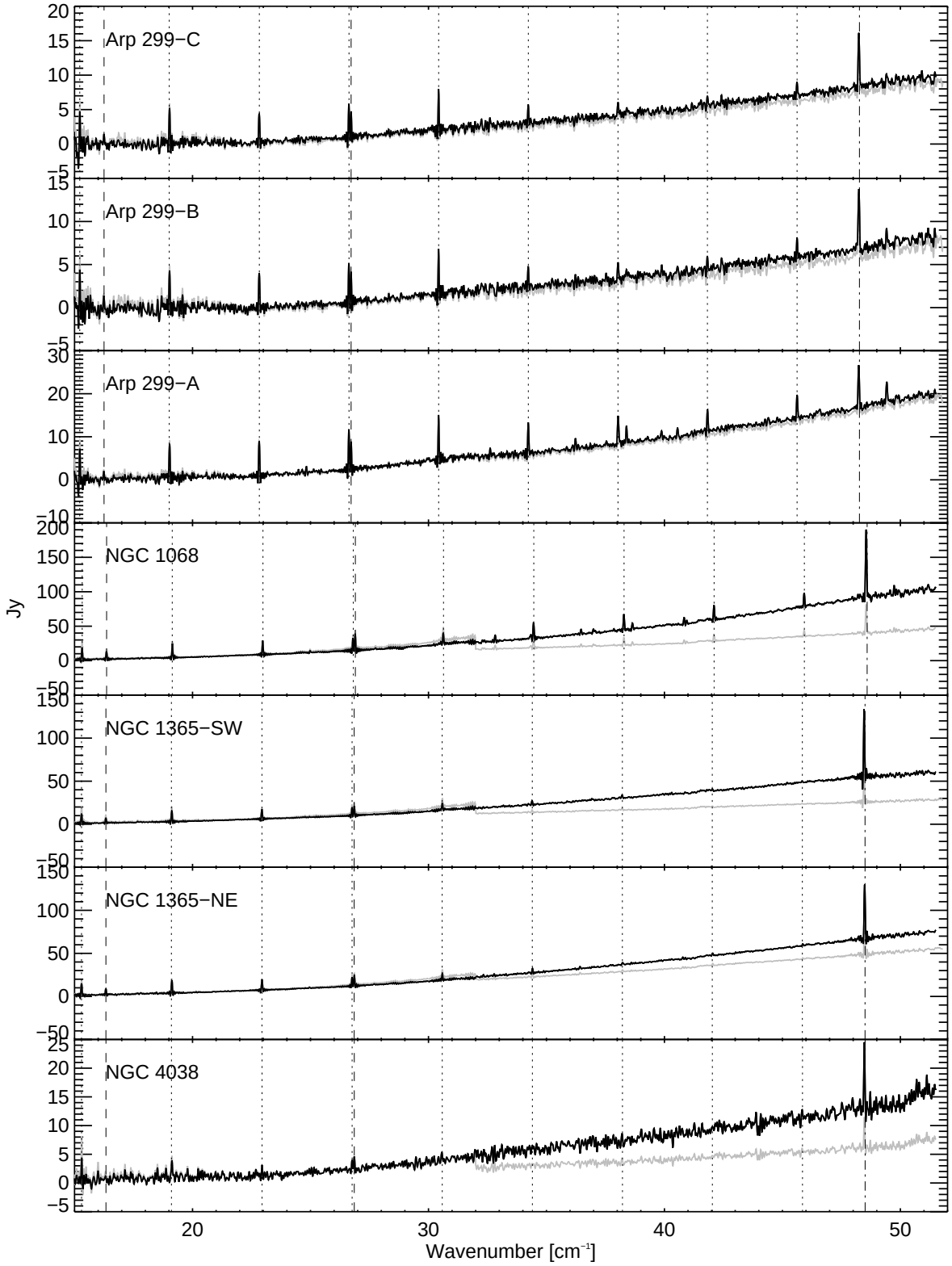

Figure 4.3 Source-Beam Coupling Corrected FTS Spectra 2 of 3. See Figure 4.2 caption for more information.

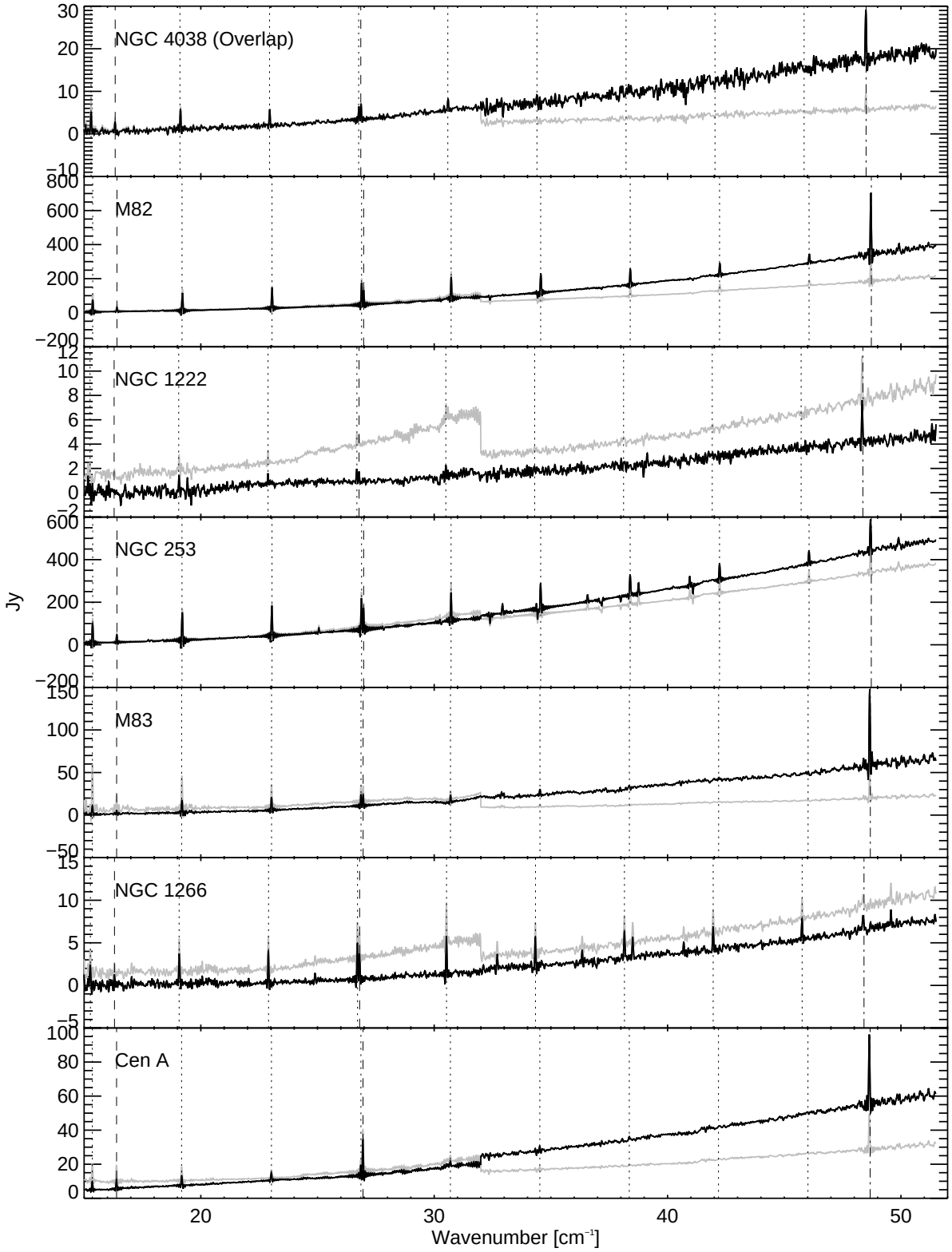

Figure 4.4 Source-Beam Coupling Corrected FTS Spectra 3 of 3. See Figure 4.2 caption for more information.

Table 4.2. Source/Beam Correction Parameters

FTS Name	$\eta(\Omega, 43.5) = a + b\Omega + c\Omega^2 + d\Omega^3$				$\eta(15, 43.5)$
	a $\times 10^1$	b $\times 10^2$	c $\times 10^4$	d $\times 10^6$	
Mrk 231	7.3	1.3	-2.4	1.9	0.88
IRAS F17207-0014	8.1	0.92	-1.8	1.5	0.91
IRAS 09022-3615	7.0	1.6	-2.9	2.1	0.88
Arp 220	6.6	1.6	-2.9	2.2	0.85
Mrk 273	7.8	1.1	-2.0	1.7	0.90
UGC 05101	8.2	0.88	-1.7	1.5	0.92
NGC 6240	4.3	2.5	-4.0	2.7	0.73
Arp 299-C	-3.7	4.7	-4.6	2.1	0.25
Arp 299-B	-4.0	4.7	-4.1	1.7	0.21
Arp 299-A	0.45	3.8	-4.9	2.9	0.51
NGC 1068	-4.7	5.7	-7.3	4.2	0.24
NGC 1365-SW	-4.7	5.8	-7.4	4.2	0.25
NGC 1365-NE	-0.042	4.4	-6.6	4.1	0.52
NGC 4038	1.8	0.54	3.7	-1.4	0.34
NGC 4038 (Overlap)	-2.7	4.3	-4.6	3.4	0.28
M82	-2.9	5.2	-6.9	4.1	0.35
NGC 1222	1.3	3.9	-6.1	3.8	0.60
M83	-1.7	4.4	-5.5	3.6	0.38
NGC 253	1.9	3.4	-5.0	3.5	0.60
NGC 1266	5.2	2.3	-3.8	2.7	0.78
Cen A	-0.012	2.2	-0.34	1.2	0.33

maps. Because $\Omega_{PSW} = 423$ arcsec^2, the effective FWHM of the PSW beam is $19\farcs32$. To determine the light distribution at a given beam size Ω_b ($> \Omega_{PSW}$), we convolve the PSW map with a Gaussian kernel of size $\Omega_{kernel} = \Omega_b - \Omega_{PSW}$. This procedure thus relies on two assumptions: that the distribution of the molecular gas follows the same spatial distribution as the 250 μm dust emission, and that the beams are roughly Gaussian.

We wish to obtain the spectrum measured within a $43\farcs5$ beam, as this is the largest size we require, at the CO J=4-3 line. We divide the flux convolved to Ω_b by that convolved to $\Omega_{43.5}$ to find $\eta(\Omega_b, \Omega_{43.5})$ for various beams from 20 to 43 arcseconds. We fit the resultant curve as a third order polynomial, the parameters for which are given in Table 4.2. The last column shows $\eta_{15,43.5}$ as an example. For M82, a telescope with a $15''$ beam (pointed at the same location as the FTS) would only measure 35% of the emission measured in a $43\farcs5$ beam. UGC 05101, in contrast, is extremely point like; a $15''$ beam would measure 91% of the flux despite having only 12% of the beam area. Knowing the beam size at each frequency, we divide the entire spectrum by the appropriate $\eta(\nu)$ for those galaxies whose $\eta_{20,43.5}$ is less than 90% (where we expect to be measuring real signal above a conservative 10% calibration error). This step removes the discontinuity between SLW and SSW, which indicates that we have correctly stitched together the flux over the discontinuity in beam sizes.

The second step is an additional calibration to match the absolute flux to that of the SPIRE photometer maps. We convolve each map by a kernel $\Omega_{kernel} = \Omega_{43.5} - \Omega_{phot}$ to match $43\farcs5$. Ω_{phot} is 423, 751, and 1587 square arcseconds for PSW, PMW, and PLW, respectively. We then measure the flux in Jy/Beam$_{43.5}$ at the point where the FTS beam is pointing, which is F$''$(PSW), for example. We compare this flux to that from the FTS spectrum ($S(\nu)$), considering the (unweighted) photometer response function, $R(\nu)$, which is $\hat{F}(\hat{\lambda_j}) = \frac{\int_0^\infty R(\nu)S(\nu)d\nu}{\int_0^\infty R(\nu)d\nu}$. For the SSW band, we multiply by the ratio $X_{SSW} = F''(PSW)/\hat{F}(PSW)$. There are two photometer bands (PMW and PLW) which overlap with the SLW band, so we define a line that connects those two ratios, thus dividing by $X_{SLW}(\nu)$. Often, the first step (η) overestimates the total flux in the SSW especially, and the second step (absolute flux calibration) reduces the overestimation.

Therefore the final corrected spectrum for SLW/SSW is $F_c(\nu) = X_{\rm SLW/SSW} F'(\nu)/\eta(\nu)$. The spectra are shown in Figures 4.2, 4.3, and 4.4. The empirical fits for $\eta(\Omega_b, \Omega_{43.5})$ from Table 4.2 were also used to correct fluxes from the literature for CO modeling (see Section 4.5.2.1).

4.4.3 FTS Spectral Line Fitting

To fit the CO, [CI], and [NII] lines, we used the FTFitter code from the University of Lethbridge.[5] Some of our spectra contain many more lines [for example, Arp 220, 139], but we do not fit them here in the interest of establishing a consistent pipeline for the brightest lines in all galaxies. For one detector (SLW or SSW) at a time, we first determine a polynomial fit to the baseline and then fit unresolved lines at the expected frequencies given the known redshifts. Some of our spectra contain many more lines [e.g. Arp 220, 139]; we do not fit them here in the interest of establishing a consistent pipeline for the brightest lines. The code utilizes the instrumental line profile to determine the area underneath each line in Jy cm^{-1}.

Most of the lines in this sample are unresolved; however, the velocity resolution improves at the highest frequencies, and the highest-J CO lines and [NII] line are sometimes resolved. These lines do not show the characteristic ringing of the sinc function, which is the expected line profile for a Fourier transform spectrometer. By visual inspection, we determined which lines were clearly resolved and refit them as a Gaussian convolved with the instrumental line profile. Though the code cannot break the degeneracy between the Gaussian amplitude and width, the area is well constrained. The [NII] line, the highest frequency line in our spectrum, was resolved in the following 11 galaxies: UGC 05101, NGC 1068, Arp 220, Mrk 273, Mrk 231, NGC 6240, Arp 299-A, -B, -C, NGC 1266, and IRAS 09022-3615. Two of these galaxies showed resolved line structure for multiple lines. All lines at and above CO J = 9 → 8 were resolved for Mrk 273, and all lines at and above CO J = 6 → 5 were resolved for NGC 6240. Additionally, the CO J = 7 → 6 and [CI] J = 2 → 1 lines are very close to one another; for three of the spectra (UGC 05101, Cen A, Arp 220), we manually fitted variable-width sinc functions to the lines when the FTFitter code could not properly fit the

[5] `https://www.uleth.ca/phy/naylor/index.php?page=ftfitter`

Table 4.3. Integrated Fluxes in 10^2 Jy km s^{-1}: CO

FTS Name	J=4→3		J=5→4		J=6→5		J=7→6		J=8→7	
	$I\Delta v$	σ	$I\Delta v$	σ	$I\Delta v$	σ	$I\Delta v$	σ	$I\Delta v$	σ
Mrk 231	...	...	10.0	0.96	9.77	0.49	9.04	0.29	8.15	0.36
IRAS F17207-0014	...	...	9.71	1.5	12.1	0.70	12.4	0.45	10.4	0.49
IRAS 09022-3615	...	...	5.99	0.98	7.27	0.55	8.19	0.34	6.55	0.36
Arp 220	...	...	41.0	4.7	43.1	1.8	38.0	1.7	33.7	1.8
Mrk 273	...	...	7.77	0.81	8.53	0.38	8.33	0.21	6.17	0.30
UGC 05101	...	...	6.31	0.91	5.84	0.43	4.33	0.36	3.66	0.35
NGC 6240	48.6	2.2	48.7	0.90	63.1	1.4	64.0	1.3	59.3	1.4
Arp 299-C	34.2	3.2	32.9	1.3	22.1	0.58	20.1	0.46	20.9	0.72
Arp 299-B	31.4	3.3	27.9	1.4	21.4	0.56	19.0	0.49	18.5	0.83
Arp 299-A	51.5	4.1	48.8	1.8	42.5	0.62	38.6	0.57	36.4	0.89
NGC 1068	129	8.6	111	5.2	99.9	2.3	69.3	1.3	59.7	2.0
NGC 1365-SW	86.3	3.9	77.1	2.2	58.6	0.94	34.4	0.69	32.3	1.1
NGC 1365-NE	104	4.8	90.2	2.4	64.0	0.89	38.6	0.65	29.2	1.0
NGC 4038	28.3	3.5	19.0	1.8	8.85	1.0	6.51	0.81	5.47	0.74
NGC 4038 (Overlap)	35.5	1.8	28.5	1.4	19.5	0.62	12.3	0.46	10.1	0.68
M82	583	22	625	12	607	5.1	537	4.3	482	5.1
NGC 1222	6.89	2.5	6.79	1.2	4.41	0.47	4.15	0.29	3.43	0.50
M83	74.9	4.6	101	3.0	80.6	1.3	53.9	0.85	25.8	1.1
NGC 253	750.	34	842	19	725	7.3	605	7.0	495	7.6
NGC 1266	17.8	2.4	21.9	0.99	18.7	0.42	17.9	0.32	16.7	0.51
Cen A	39.4	3.0	37.0	2.1	25.2	0.93	17.4	0.54	13.5	1.0

Note. — Some galaxies are missing measurements for J = 4 → 3 because the line falls outside the band or very close to the edge. Errors are one sigma. Lines were fit as unresolved, using instrumental line sinc profiles, unless otherwise specified in Section 4.4.3.

Table 4.4. Integrated Fluxes in 10^2 Jy km s^{-1}: CO, Continued

FTS Name	J=9→8		J=10→9		J=11→10		J=12→11		J=13→12	
	$I\Delta v$	σ	$I\Delta v$	σ	$I\Delta v$	σ	$I\Delta v$	σ	$I\Delta v$	σ
Mrk 231	5.00	0.48	6.53	0.35	5.14	0.33	3.80	0.27	3.31	0.27
IRAS F17207-0014	9.45	0.87	9.04	0.53	4.77	0.57	2.39	0.45	1.65	0.44
IRAS 09022-3615	6.27	0.50	4.11	0.30	2.80	0.28	2.45	0.27	1.42	0.24
Arp 220	25.6	2.6	24.4	2.1	12.6	2.2	7.23	1.8	5.47	1.7
Mrk 273	7.85	0.95	9.33	0.68	4.19	0.67	4.23	0.65	4.42	0.66
UGC 05101	2.51	0.45	3.08	0.31	2.13	0.34	0.734	0.27	1.10	0.25
NGC 6240	49.2	1.3	43.5	0.92	31.2	0.95	24.4	0.78	20.2	0.81
Arp 299-C	9.20	0.60	5.74	0.48	3.93	0.49	4.79	0.41	3.15	0.40
Arp 299-B	8.15	0.60	5.85	0.49	4.15	0.46	5.88	0.42	4.41	0.43
Arp 299-A	24.5	0.78	19.8	0.71	14.2	0.69	13.6	0.60	10.8	0.64
NGC 1068	75.2	2.5	69.1	2.2	56.8	2.1	50.8	2.0	27.7	2.1
NGC 1365-SW	15.3	1.6	10.2	1.5	4.83	1.5	3.94	1.3	...	...
NGC 1365-NE	16.6	1.6	6.58	1.5	7.13	1.3	4.33	1.0	5.52	1.4
NGC 4038	2.30	1.2	3.52	0.93	1.46	0.99	3.36	0.89	3.29	0.97
NGC 4038 (Overlap)	6.68	1.3	3.58	1.4	...	...	...	...	...	...
M82	394	6.4	289	6.9	188	7.6	136	6.4	88.1	6.2
NGC 1222	1.56	0.40	0.861	0.38	1.02	0.37	0.277	0.29	1.05	0.33
M83	21.8	2.7	10.0	2.7	11.4	2.8	...	...	...	...
NGC 253	416	11	291	12	216	14	155	15	91.3	17
NGC 1266	11.9	0.48	9.62	0.42	7.47	0.41	6.32	0.36	4.35	0.38
Cen A	9.20	1.2	5.81	1.1	2.13	1.2	2.90	0.97	5.62	1.2

Note. — See Table 4.3 for more information.

Table 4.5. Integrated Fluxes in 10^2 Jy km s^{-1}: [C I] and [N II]

FTS Name	[CI] 1-0		[CI] 2-1		[NII]	
	$I\Delta v$	σ	$I\Delta v$	σ	$I\Delta v$	σ
Mrk 231	3.12	1.5	5.00	0.30	6.42	0.83
IRAS F17207-0014	6.17	1.9	6.88	0.45	6.67	0.49
IRAS 09022-3615	7.46	1.8	5.65	0.30	7.26	0.74
Arp 220	18.9	5.8	19.5	1.6	23.6	5.1
Mrk 273	5.05	0.97	5.03	0.22	7.88	0.58
UGC 05101	3.45	1.2	5.44	0.34	12.3	0.89
NGC 6240	16.7	1.4	34.9	1.3	33.2	0.86
Arp 299-C	10.6	2.0	14.3	0.41	30.7	1.2
Arp 299-B	10.6	2.0	13.5	0.38	28.6	1.2
Arp 299-A	13.4	2.5	23.9	0.54	36.2	2.0
NGC 1068	81.1	5.0	101	1.4	358	7.7
NGC 1365-SW	39.9	2.3	43.1	0.70	192	1.4
NGC 1365-NE	47.2	3.0	48.4	0.68	156	1.3
NGC 4038	5.44	1.8	9.02	0.81	27.6	0.96
NGC 4038 (Overlap)	15.8	1.3	14.9	0.51	27.5	1.8
M82	175	16	315	3.7	867	6.2
NGC 1222	2.25	1.4	2.96	0.30	8.34	0.30
M83	27.7	2.7	51.9	1.2	219	2.2
NGC 253	262	21	387	5.8	357	18
NGC 1266	7.97	1.4	11.4	0.31	7.51	1.0
Cen A	39.4	2.1	93.8	0.57	102	1.0

Note. — See Table 4.3 for more information.

Table 4.6. Photometry Flux Densities in Jy: SPIRE Photometer

Galaxy	250 μm F_ν	σ_{tot}	350 μm F_ν	σ_{tot}	500 μm F_ν	σ_{tot}
Mrk 231	5.40	0.878	1.92	0.354	0.567	0.238
IRAS F17207-0014	7.67	1.29	2.84	0.451	0.944	0.284
IRAS 09022-3615	2.48	0.399	0.732	0.470	0.197	0.321
Arp 220	32.6	3.76	11.7	0.955	4.01	0.421
Mrk 273	4.27	0.822	1.49	0.225	0.491	0.139
UGC 05101	5.77	0.941	2.23	0.322	0.687	0.166
NGC 6240	6.82	0.877	2.64	0.370	0.815	0.246
Arp 299-A	22.0	1.96	7.60	0.721	2.36	0.325
NGC 1068	103	6.12	41.3	2.69	14.0	1.04
NGC 4038 (Overlap)	37.8	2.50	14.9	0.984	5.04	0.464
NGC 1222	3.65	0.387	1.43	0.319	0.446	0.202
NGC 1266	3.71	0.522	1.30	0.201	0.411	0.147
Cen A	271	60.0	110.	17.6	44.9	5.12

Note. — All are from this work, see Section 4.4.4.

two.

The integrated fluxes are shown in Tables 4.3, 4.4, 4.5. Our most luminous galaxies are distant enough that the CO J = 4 → 3 line is either completely redshifted out of the band, or extremely close to the edge. Fluxes are not reported in those cases.

In Figure 4.5, we show the CO spectral line energy distributions (SLEDs), all scaled such that the luminosity of J=1→0 line matches that of Mrk 231 (see Section 4.5.2.1 for how the low-J line fluxes were acquired from the literature). This figure illustrates just how varied the shapes of the CO SLEDs become at higher-J, and includes comparisons to Galactic sources, which will be discussed in Section 5.1.8.

4.4.4 Photometry

In addition to using the SPIRE photometry maps to determine the source-beam coupling correction, we also performed aperture photometry to obtain galaxy-integrated fluxes to supplement the dust modeling. Results are in Table 4.6. A circular aperture was centered on the FTS pointing location of the dust map, and a radius (r_a) was chosen to encompass all of the measured flux. The sky background is calculated from an annulus with inner radius r_a to outer radius r_a + 10 pixels.

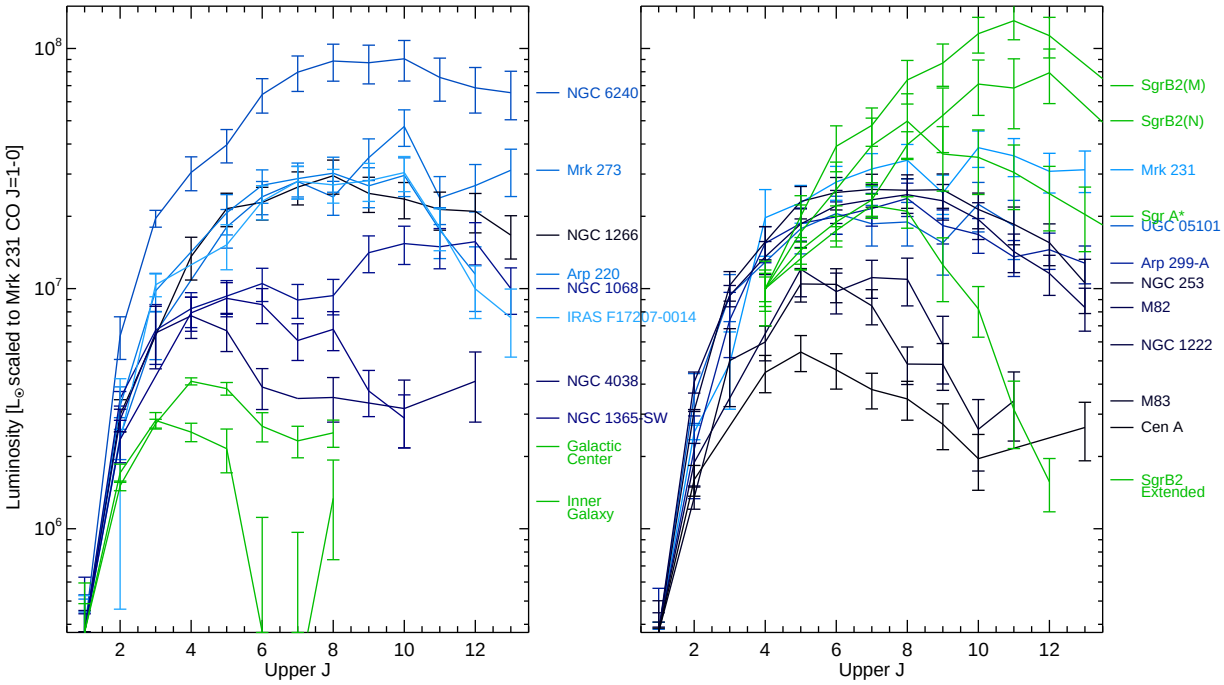

Figure 4.5 Normalized CO SLEDS. All J = 1 → 0 luminosities are scaled to match that of Mrk 231 (3.7×10^5 $L_\odot$). SLEDs are colored to indicate increasing $L_{\rm FIR}$ with increasing lightness. Placement in the left or right panel is for clarity only. On the left panel, the SLEDs of the Galactic center ($|l| < 2.^\circ5$) and the Inner Galaxy ($2.^\circ5 < |l| < 32.^\circ5$), also normalized, are shown in green for comparison [57]. On the right panel, we show the SLEDs of two star-forming cores and the extended envelope of Sgr B2 [53] and that of Sgr A* [61]. Because these SLEDs begin at J = 4 → 3, we scale J = 4 → 3 to 10^7 $L_\odot$ for visual comparison of the shapes. None of the SLEDs are corrected for dust extinction.

The sky is calculated as the median value of the data (Jy/beam) divided by (beam/pixel) times the area contained in the annulus (in pixels). For all points within r_a, the flux is the total of the data divided by beam/pixel minus the sky.

4.5 Analysis

For both dust and CO modeling, we utilize the nested sampling algorithm MultiNest [55] and its Python wrapper, PyMultiNest [24].[6] As stated in Feroz et al. [55], nested sampling "is a Monte Carlo technique aimed at efficient evaluation of the Bayesian evidence, but also produces posterior inferences as a by-product." The evidence in this context is the average likelihood of a model over its prior probability space. The algorithm "nests inwards" to subsequently smaller regions of high-likelihood parameter space. Unlike calculating the likelihood using a grid method, the algorithm can focus on high likelihood regions and thus estimate parameter constraints more efficiently.

In both cases (dust and CO), described in their respective sections (4.5.1 and 4.5.2), we have a set of measurements $\boldsymbol{x}$ with errors $\boldsymbol{\sigma}$, a model described by parameters $\boldsymbol{p}$ with predicted fluxes $I(\boldsymbol{p})$. For a Gaussian probability, the natural log of the likelihood is $-0.5(\boldsymbol{x} - \boldsymbol{I}(\boldsymbol{p}))^T \mathrm{Cov}^{(-1)}(\boldsymbol{x} - \boldsymbol{I}(\boldsymbol{p}))$. The covariance matrix is fully described for the dust modeling in Section 4.5.1. For the CO modeling, we use zero covariance between data points, simplifying the probability to $\prod_i (2\pi\sigma_i^2)^{-2} \exp(-0.5(x_i - I_i(\boldsymbol{p}))^2 \sigma_i^{-2})$, where i represents each data point (integrated flux). The natural log of the probability is $-\sum_i 0.5\ln(2\pi) + \ln(\sigma_i) + 0.5(x_i - I_i(\boldsymbol{p}))^2 \sigma_i^{-2}$.

We can determine the probability distribution for any one parameter by marginalizing the full distribution over all other parameters. There are different statistics that can be used to describe a parameter. The best-fit set of parameters is the combination that produced the highest likelihood. In the case of a very simple parameter space, where the solution is clustered in a Gaussian fashion in one area, the best-fit will likely coincide with the statistical mean of each parameter. This was the case for the dust modeling. However, the parameter space may not be so simply described,

[6] `https://github.com/JohannesBuchner/PyMultiNest`

which we will demonstrate for the CO modeling. This mode of parameter estimation is designed to focus on the whole probability density function (PDF), not to refine the best fit. We present the best-fit in our tables, as it is used in the plots of best-fit spectral (line) energy distributions, but we focus our discussion on the marginalized likelihoods.

In the case of a complicated parameter space, there can be multiple "modes," or islands in parameter space, as was sometimes the case for the CO modeling. The MultiNest algorithm partitions the posterior likelihood space into ellipsoids, which may overlap. Non-overlapping ellipsoids can be separated into separate modes, with a separate "local" evidence. In our cases, all posterior distributions with multiple likelihoods had one mode stand out as containing more posterior mass than others; we focus our parameter estimation on this most-likely mode, and present its statistical mean and standard deviation. This is as opposed to the mean that one would calculate considering the entire posterior distribution, which would be weighted towards other, less-likely modes. The extent of that weighting would depend on the ratio of the different local evidence.

4.5.1 Dust Modeling Likelihood with Multinest

In addition to SPIRE photometer observations (250, 350, 500 μm), we also used fluxes from the literature, those listed in Appendix C above 10 μm. These are galaxy-integrated fluxes; we only modeled once per galaxy with multiple FTS pointings (NGC 4038, NGC 1365, Arp 299), because fluxes separated into individual components were often not available. We used the dust model as in Casey [27], which is the sum of a greybody and a powerlaw with exponential drop-off:

$$S(\lambda) = N_{bb}\frac{(1-e^{-(\lambda_0/\lambda)^\beta})(c/\lambda)^3}{e^{hc/(\lambda kT)}-1} + N_{pl}\lambda^\alpha e^{-(\lambda/\lambda_c)^2}. \quad (4.1)$$

In Equation 4.1, the free parameters are T (temperature, K), β (emissivity index), λ_0 (wavelength at which optical depth is unity, μm), and α (slope of the mid-IR powerlaw). N_{bb}, the normalization in Jy for the greybody component, is fixed at the best-fit value for any given combination of the previous parameters. λ_c and N_{pl} are tied to the other parameters as in Casey [27, , Table 1]. In calculating the likelihood of the dust parameters, we assume that calibration errors

Table 4.7. Dust Fitting Results: Model Parameters

FTS Name	λ_0 [μm]			β			T [K]			α		
	Mean	σ	Best	Mean	σ	Best	Mean	σ	Best	Mean	σ	Best
Mrk 231	231	24	242	1.82	0.12	1.85	79.6	2.3	81.3	3.07	0.34	3.45
IRAS F17207-0014	96	24	120	1.48	0.11	1.46	48.8	3.0	52.3	3.27	0.16	3.49
IRAS 09022-3615	176	53	161	1.69	0.57	1.37	62.6	4.7	65.2	2.91	0.41	3.32
Arp 220	187	27	193	1.54	0.09	1.54	55.5	1.7	56.4	3.38	0.11	3.49
Mrk 273	115	25	136	1.58	0.07	1.60	58.5	5.0	63.5	2.89	0.36	3.41
UGC 05101	225	50	225	1.94	0.42	1.87	46.2	3.8	45.7	2.43	0.16	2.36
NGC 6240	226	46	212	1.65	0.25	1.60	57.6	4.8	56.0	1.98	0.31	1.80
Arp 299-A	120	30	140	1.26	0.08	1.28	58.6	2.7	60.9	3.23	0.20	3.48
NGC 1068	244	34	251	1.80	0.09	1.82	39.5	3.0	40.1	0.60	0.05	0.59
NGC 1365-NE	181	64	61	1.45	0.08	1.39	38.6	3.9	31.6	1.76	0.09	1.66
NGC 4038 (Overlap)	219	31	220	1.87	0.11	1.88	38.0	2.3	37.9	1.85	0.05	1.85
M82	137	44	100	1.30	0.06	1.30	55.6	7.3	49.3	1.48	0.37	1.25
NGC 1222	205	49	226	1.48	0.17	1.49	64.8	6.0	68.1	2.65	0.53	2.93
M83	213	49	211	1.59	0.09	1.60	37.1	2.8	36.9	1.70	0.07	1.71
NGC 253	267	28	294	1.46	0.07	1.50	45.0	2.5	46.3	1.64	0.10	1.66
NGC 1266	206	25	214	2.00	0.29	2.04	56.1	2.8	57.4	3.08	0.26	3.24
Cen A	187	66	64	0.71	0.10	0.68	38.8	1.8	36.5	1.91	0.09	1.88

are 50% correlated between measurements from the same instruments. We expect some degree of correlation, but too far above 50% in the covariance matrix can drive the best fit very far away from the data points of other instruments.

The results are shown in Figures 4.6 (histogram of best-fit parameters) and 4.7 (best-fit SEDs). The individual parameter results are in Table 4.7. In all cases, only one mode in likelihood space was found, and the resulting likelihood distributions were very well defined by Gaussians (the best-fit and the mode and median of the resulting marginalized parameters all aligned).

Table 4.8 also lists the results for parameters which can be derived from the model above: the optical depth at 100 μm (τ_{100}), the dust mass (M_{dust}), and the far-infrared luminosity from 8 to 1000 μm ($L_{8-1000\mu m}$ or $L_{\rm FIR}$). To calculate the dust mass, we utilize $\kappa_{125\mu m} = 2.64\,{\rm m}^2/{\rm kg}$ [48] and $M_d = \frac{S_\nu D_L^2}{\kappa_\nu B_\nu(T)}$. The values of $L_{\rm FIR}$ we find when modeling the full SED ($L = 4\pi D_L^2 \int_{8\mu m}^{1000\mu m} S_\nu d\nu$) are slightly higher than those derived from utilizing only the 60 and 100 μm fluxes (e.g. those presented in Table 4.1 from Hyperleda), by about a factor of 1.7 ± 0.5.

Casey [27] modeled 65 local LIRGS and ULIRGS, fixing $\lambda_0 = 200\mu$m and finding a mean $\beta = 1.60 \pm 0.38$ and $\alpha = 2.0 \pm 0.5$. We find, in Figure 4.6 that β and α can vary significantly, but cluster around similar values. When left to vary, λ_0 can often be higher than 200 μm.

Table 4.8. Dust Fitting Results: Derived Parameters

FTS Name	τ_{100}			Log $M_{\rm dust}$ [$M_\odot$]			Log $L_{8-1000\mu m}$ [$L_\odot$]		
	Mean	σ	Best	Mean	σ	Best	Mean	σ	Best
Mrk 231	5.18	1.46	5.57	7.80	0.02	7.80	12.41	0.02	12.40
IRAS F17207-0014	1.04	0.42	1.39	8.32	0.05	8.28	12.34	0.01	12.34
IRAS 09022-3615	4.08	3.61	2.09	7.96	0.07	7.90	12.21	0.02	12.23
Arp 220	2.80	0.79	2.85	8.08	0.02	8.07	12.14	0.02	12.14
Mrk 273	1.36	0.47	1.75	7.77	0.06	7.71	12.13	0.01	12.13
UGC 05101	6.78	4.58	4.91	8.27	0.07	8.27	11.95	0.02	11.96
NGC 6240	4.55	2.34	3.49	7.69	0.06	7.71	11.83	0.02	11.84
Arp 299-A	1.31	0.45	1.56	7.46	0.03	7.44	11.74	0.02	11.74
NGC 1068	5.22	1.46	5.41	7.49	0.07	7.48	11.40	0.02	11.41
NGC 1365-NE	2.56	1.34	0.51	7.56	0.09	7.72	11.11	0.02	11.12
NGC 4038 (Overlap)	4.59	1.45	4.47	7.43	0.06	7.43	10.90	0.02	10.90
M82	1.56	0.68	1.00	6.45	0.09	6.53	10.79	0.03	10.80
NGC 1222	3.18	1.38	3.45	6.31	0.06	6.27	10.66	0.02	10.65
M83	3.52	1.35	3.31	7.07	0.07	7.08	10.53	0.02	10.53
NGC 253	4.28	0.77	5.05	6.78	0.06	6.77	10.52	0.02	10.52
NGC 1266	4.69	1.94	4.82	6.34	0.04	6.33	10.44	0.01	10.45
Cen A	1.57	0.46	0.75	6.51	0.05	6.56	9.93	0.02	9.94

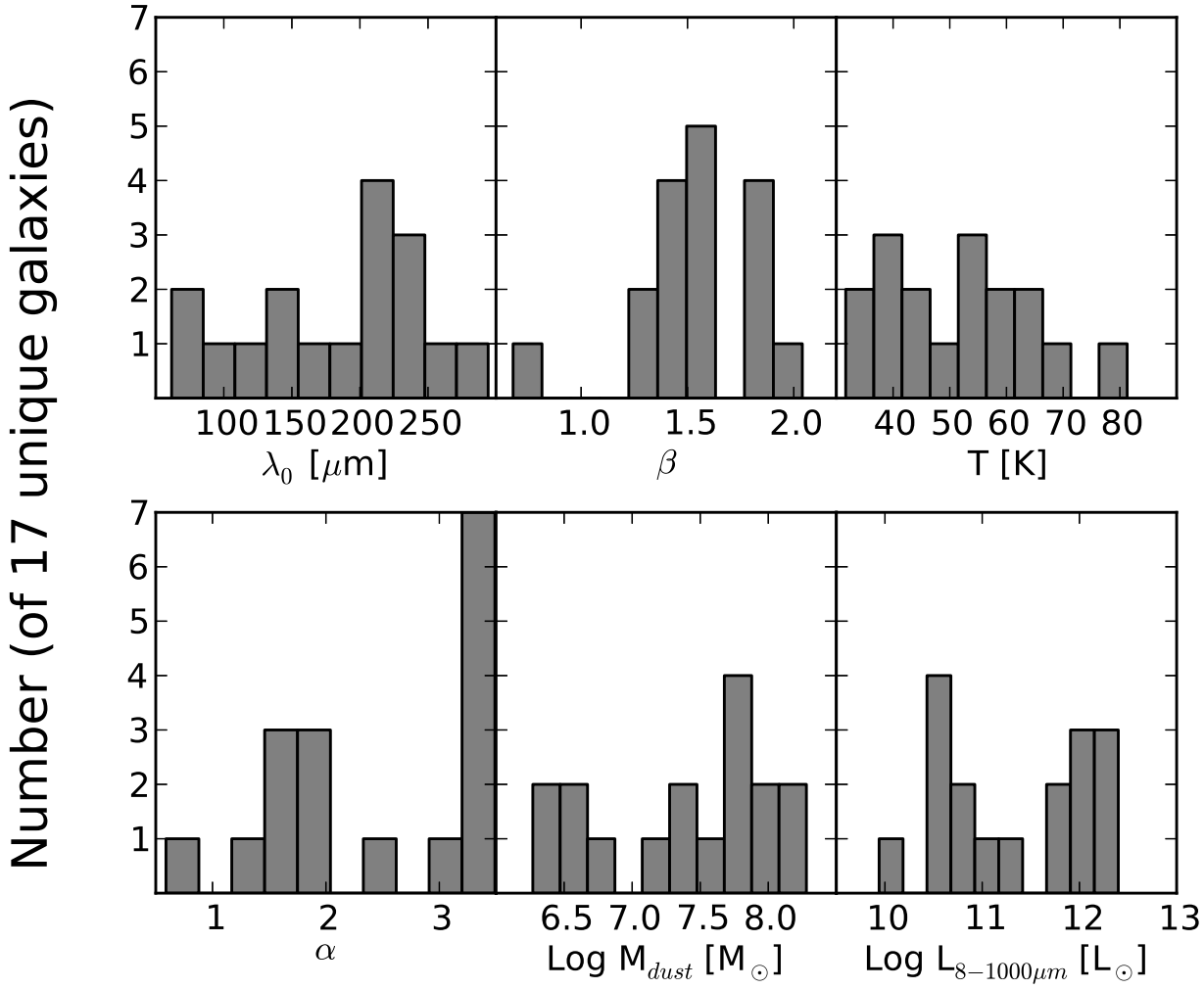

Figure 4.6 Dust modeling histogram results. See Section 4.5.1.

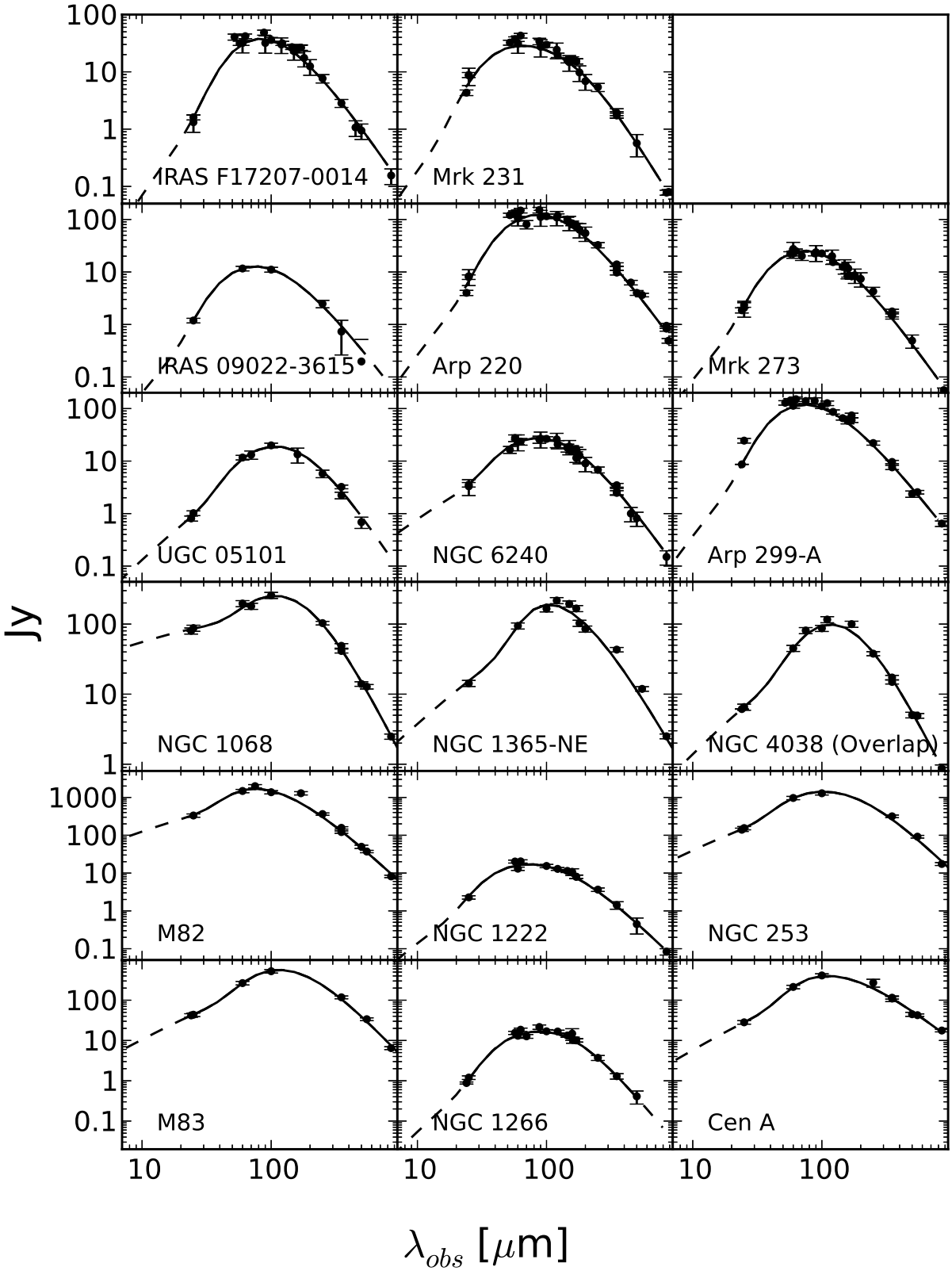

Figure 4.7 Dust modeling spectral energy distributions. The maximum likelihood solution is shown as a black line, solid in the wavelength range containing data, and dashed for the regions where the solution is an extrapolation outside the modeled data range.

4.5.2 CO Modeling Likelihood with Multinest

4.5.2.1 Measurements from the Literature and Dust Optical Depth Correction

As discussed in Section 4.3, previous work has shown that the high-J lines detected by the FTS are often emitted by a warmer component of gas than the low-J lines. To accurately model both components of gas, we supplemented our FTS line fluxes with measurements of $J = 1 \rightarrow 0$, $J = 2 \rightarrow 1$, and $J = 3 \rightarrow 2$ with instruments from the ground.

Table 4.9. CO Additional Line Measurements in Jy km s^{-1}

J_{up}	$I\Delta v$	σ	$\eta(\Omega)$	Ref	J_{up}	$I\Delta v$	σ	$\eta(\Omega)$	Ref	J_{up}	$I\Delta v$	σ	$\eta(\Omega)$	Ref
	UGC 05101					**Arp 220**					**NGC 6240**			
1	73.5	15	1.00	1	1	403	22	1.00	7	1	239	29	1.01	7
1	70.3	18	1.00	2	1	609	120	0.90	1	1	413	82	0.82	1
1	73.6	15	1.00	3	1	283	56	1.04	14	1	261	52	1.07	14
2	350.	81	1.00	2	1	520.	57	1.04	15	2	2210	430	0.81	16
3	609	130	1.00	2	2	1780	350	0.89	16	3	4710	900	0.72	16
	NGC 4038 (Overlap)				3	3970	760	0.84	16	3	4210	1200	0.82	6
1	851	170	0.99	4	3	3050	880	0.90	6		**IRAS F17207-0014**			
2	2930	320	0.70	5		**NGC 1365-NE**				1	93.2	19	1.00	1
3	5380	780	0.99	4	1	1840	360	1.11	17	1	161	29	1.00	2
3	8190	2400	0.49	6	1	2330	460	1.00	18	1	178	36	1.00	3
3	5610	630	0.49	5	1	2210	35	1.00	19	2	695	150	1.00	2
	NGC 4038				1	1440	140	1.11	15	2	330.	66	1.00	3
1	468	93	0.98	4	1	2160	440	1.01	3	3	1220	260	1.00	2
1	651	72	1.04	7	2	6670	1300	0.75	18	3	1050	310	1.00	6
2	2230	230	0.65	5	3	12100	1100	0.52	20		**Arp 299-A**			
3	2830	410	0.98	4		**NGC 1365-SW**				1	785	160	1.12	14
3	4600	1300	0.46	6	1	1500	300	1.18	17	1	442	88	0.65	3
3	3870	410	0.46	5	1	1860	370	1.01	18	2	1990	290	1.00	22
	M82				1	2140	430	1.02	3	2	1200	230	0.46	3
1	7060	700	0.62	8	2	5550	1100	0.58	18	3	3480	1000	0.67	6
1	6600	650	1.02	7		**Mrk 273**					**Arp 299-B**			
2	37400	3600	0.62	8	1	90.0	18	1.00	1	1	394	86	0.75	3
3	57200	5500	0.62	8	1	68.1	14	1.00	14	2	1690	250	1.00	22
6	68200	7800	0.19	5	1	82.3	15	1.00	2	3	3930	1200	0.44	6
	NGC 1068				1	112	28	1.00	21		**Arp 299-C**			
1	2260	330	1.03	7	1	97.6	19	1.00	3	1	385	84	0.77	3
1	4240	840	0.45	3	2	273	54	1.00	2	2	1710	250	1.00	22
2	11700	1100	0.74	9	3	491	110	1.00	2		**NGC 253**			
2	12600	2500	0.16	3		**Mrk 231**				1	10800	1100	1.01	7
3	17800	3000	1.00	10	1	90.4	13	1.00	7	1	7200	640	0.75	23
3	11800	3400	0.48	6	1	103	20.	1.00	1	2	33800	3200	0.89	24

Table 4.9 (cont'd)

J_{up}	$I\Delta v$	σ	$\eta(\Omega)$	Ref	J_{up}	$I\Delta v$	σ	$\eta(\Omega)$	Ref	J_{up}	$I\Delta v$	σ	$\eta(\Omega)$	Ref
		Cen A			1	88.5	16	1.00	2	2	34300	3600	0.75	23
1	1540	290	1.01	11	1	97.0	24	1.00	21	3	75300	9700	0.75	23
1	1620	170	1.04	12	1	83.7	12	1.00	15			**NGC 1266**		
2	3440	430	0.48	12	1	104	21	1.00	3	1	204	33	0.86	25
		M83			2	321	56	1.00	2	1	204	41	0.86	26
1	2020	200	1.02	7	2	292	72	1.00	21	2	906	140	0.74	25
2	3660	370	0.76	5	3	592	120	1.00	2	2	727	140	0.72	26
3	10500	2300	0.54	13	3	354	110	1.00	6			**NGC 1222**		
3	13400	3800	0.57	6	3	376	46	1.00	5	1	119	24	0.73	26
3	8680	830	0.57	5	4	1210	350	1.00	2	2	301	59	0.49	26

Note. — **References.** (1) Solomon et al. [160]; (2) Papadopoulos et al. [131]; (3) Baan et al. [7]; (4) Schirm et al. [154]; (5) Bayet et al. [9]; (6) Mao et al. [102]; (7) Young et al. [194]; (8) Ward et al. [179]; (9) Kamenetzky et al. [79]; (10) Spinoglio et al. [161]; (11) Wild & Eckart [185]; (12) Eckart et al. [49]; (13) Mauersberger et al. [106]; (14) Sanders et al. [150]; (15) Maiolino et al. [99]; (16) Greve et al. [65]; (17) Papadopoulos & Seaquist [128]; (18) Sandqvist et al. [152]; (19) Elfhag et al. [51]; (20) Sandqvist [151]; (21) Albrecht et al. [4]; (22) Sliwa et al. [158]; (23) Harrison et al. [70]; (24) Z-Spec; (25) Alatalo et al. [3]; (26) Young et al. [195]

The measurements used for this survey are presented in Table 4.9. We first utilized large surveys for consistent data; some galaxies had multiple measurements for the same line because of overlaps of the surveys. When surveys alone did not have enough lines for a particular galaxy, we sought out individual measurements in the literature. For the cases of semi-extended sources which may have multiple pointings, see Appendix B for more information on how these were handled. No ground-based measurements for IRAS 09022-3615 were available, so only the warm, high-J component of gas was modeled for this galaxy.

The low-J line measurements came from a variety of telescopes with different beam sizes. We divided all flux densities in Jy km/s by the appropriate $\eta(\Omega_b, \Omega_{43.5})$ from Table 4.2 to refer all fluxes to our beam size of $43\farcs5$ (see Section 4.4.2). The specific value used for each line flux in the last column of Table 4.9. In same cases, we gathered multiple transitions of the same line, and only discarded measurements which were wildly discrepant from the rest of the SLED.

We additionally corrected the line fluxes for obscuration by dust. At higher frequencies, the optical depth is not negligible. We corrected the lines by dividing by this factor for a mixed dust model, in which the line-emitting gas and the dust are assumed to be spatially co-extensive:

$$\frac{1 - e^{-\tau_\lambda}}{\tau_\lambda}, \tag{4.2}$$

where τ_λ for a given line was calculated by $(\lambda_0/\lambda)^\beta$, using the λ_0 and β from the dust model results in Table 4.7. We propagated the uncertainties in both parameters into the correction and resulting line fluxes; the correction was highest for the high-J lines. The correction did not significantly modify the resulting likelihood distribution, other than slight increases in the warm gas pressure and luminosity, as one would expect by changing the shape of the SLED in this fashion. To be explicit, the best-fit solution often moves, but the marginalized parameter distributions shift an insignificant amount compared to their large uncertainties. This is further discussed in Section 5.1.1.

4.5.2.2 Model Description

To model the CO fluxes, we use a custom version of the non-LTE code RADEX described in van der Tak et al. [171]. The input parameters to this model are kinetic temperature, T [K], column density of CO per unit linewidth, $N_{CO}/\Delta V$ [cm^{-2} / (km s^{-1})], and density of the colliding partner (molecular hydrogen, n_{H2} [cm^{-3}]). Additionally, we allowed the resultant fluxes to scale uniformly lower by an area filling factor $\Phi_A \leq 1$.

RADEX uses an escape probability method to perform statistical equilibrium calculations, first populating the rotational levels in the optically thin limit, then calculating the optical depths for the lines. The code continues calculating new level populations using new optical depth values until the two converge on a consistent solution. The line intensities are output as background-subtracted Rayleigh-Jeans equivalent radiation temperatures. We use the CMB (2.73 K at $z = 0$) as the radiation background, because we have found that the solution is generally not sensitive to the radiation background temperature for these types of galaxies [79, 80]. Previous work has shown that the high-J lines detected by the FTS are often emitted by a warmer component of gas which is typically 10% or less of the total CO mass. Therefore we simultaneously model two components of gas, described by eight parameters, $\mathbf{p} = (n_1, T_1, N_1/\Delta V, \Phi_1, n_2, T_2, N_2/\Delta V, \Phi_2)$, four for each

component.

In addition to these basic parameters which fully describe the model, we calculated other properties and their likelihood, some of which were better constrained than the formal parameters. The product of the temperature and density is the thermal pressure (P), and the product of the column density and filling factor ($< N_{CO} >$) is proportional to the total molecular gas mass,

$$M = A\Phi_A N_{CO} 1.4\, \mathrm{m_{H_2}} X_{^{12}\mathrm{CO}}^{-1} \tag{4.3}$$

where A is the area of the region, calculated from the luminosity distance, where $A = \frac{\pi}{4}s^2$ pc^2 and s is a diameter given by $s = 2 \times 10^6 \sqrt{\Omega_s/\pi} D_L (1+z)^{-2}$ [pc]. Note that both A and Φ_A, the area filling factor, are present in this equation, which accounts for beam dilution for the many sources that are less than $43\farcs5$ across. The factor of 1.4 accounts for helium and other heavy elements, and $X_{^{12}CO}$ is the abundance ratio of ^{12}CO to H_2: we use 2×10^{-4}. We also calculated the probabilities of the total CO luminosity in each component from RADEX, which may include contributions from higher-J lines other than those modeled here. Finally, we also determined the likelihood for the ratio of warm to cold properties (e.g. M_1/M_2).

The temperature and density are degenerate; even when one might not individually be well determined, their product (thermal pressure, henceforth simply "pressure") is better constrained, because the two properties are anti-correlated. Likewise, the column density and filling factor are degenerate, and it is their product (proportional to mass) that is better determined. However, it is important to note that these two parameters are not perfectly degenerate. Pressure is largely responsible for the shape of the SLED, and mass for the absolute flux scaling. However, optical depth effects can still change the shape of the SLED with increasing column density, and filling factor only linearly scales the entire SLED downwards. Thus, we modeled both column density and filling factor, and used $\Omega_s = 1.133 \times 43.5^2$ sq arcsec, allowing Φ_A to account for emission less than the extent of the beam.

Table 4.10. CO Likelihood Parameters

FTS Name	Linewidth [$\mathrm{km\,s^{-1}}$]	Length Max [pc]	Mass Max [10^8 $M_\odot$]
Mrk 231	198	1415	65
IRAS F17207-0014	373	5384	869
IRAS 09022-3615	547	5650	1961
Arp 220	428	4739	1008
Mrk 273	265	5090	417
UGC 05101	350	3955	562
NGC 6240	370	8770	1399
Arp 299-C	80	6351	47
Arp 299-B	155	6353	177
Arp 299-A	282	6349	586
NGC 1068	254	3454	258
NGC 1365-SW	250	2567	136
NGC 1365-NE	250	2564	135
NGC 4038	133	4900	101
NGC 4038 (Overlap)	166	5922	189
M82	174	850	30
NGC 1222	80	2703	20
M83	102	1169	14
NGC 253	220	402	23
NGC 1266	239	576	38
Cen A	150	1998	52

Note. — See Section 4.5.2.3. The CO likelihood also depends on the luminosity distance, given in Table 4.1, and the beam area. All are normalized to $\Omega_b = 5.04 \times 10^{-8}$ sr, see Section 4.4.2. Linewidths are the average of those reported from references in Table 4.9. No linewidths were available for NGC 1365-NE, NGC 1365-SW, NGC 1222, and IRAS 09022-3615; the v_{rot} from Hyperleda was used instead for the first three, and the [OIII] linewidth was used for the last from Lee et al. [93].

4.5.2.3 Model Constraints and Priors

RADEX calculates antenna temperatures in K, so we converted our data from Jy km/s to K km/s by multiplying by $646\nu^2_{\rm GHz}$ (assuming the aforementioned $43\farcs5$ beam). We then divided our integrated flux data into per unit linewidth units of temperature (K instead of K km/s) to directly compare to RADEX, assuming fixed linewidths. This is because the actual parameter we were testing was column density per unit linewidth; the modeled emission was simply multiplied by linewidth. Because the FTS did not resolve the widths of the lines, we relied on ground-based CO measurements for linewidths. The values used are in Table 4.10; many are medians of multiple CO linewidths from the literature, if more than one measurement was available. Our reported masses and luminosities scale linearly with linewidth.

Given the size of the eight dimensional parameter space, it was important to apply some physical constraints to limit the potential solutions to those that are physically meaningful. Some of these constraints were on the relationship between the two components: we required the first component to be cooler than the second (henceforth referred to as the "cool/cold" and "warm" components), and the cool component to contain more mass than the warm.

Two additional priors were used based on known physical constraints: the sum of the two components' mass could not exceed the dynamical mass of the galaxy, nor could either component's line-of-sight length be greater than the extent of the galaxy in the plane of the sky. The mass as a function of our parameters is that given in Equation 4.3; the dynamic mass sets a limit on the product of $\Phi_A \times N_{CO}$. The length as a function of our parameters is $N_{CO}(\sqrt{\Phi_A} n_{H2} X_{^{12}CO})^{-1}$.

The dynamical mass and length limits are presented in Table 4.10. The length upper limits were calculated by fitting a two dimensional Gaussian to the SPIRE PSW maps. This Gaussian was the convolution of the intrinsic source size and the PSW beam (FWHM = $19\farcs3$). We used the longest length of the Gaussian (g) and found the source size, $s = \sqrt{g^2 - 19.3^2}$. We utilized the largest-side-of-a-Gaussian approximation because we sought only an upper limit. The dynamical mass limit was determined from the linewidth (ΔV) and maximum length limit L, such that

$M_{max} = \Delta V^2 L/G$. If any of these constraints were violated, the likelihood for that set of parameters was not included.

Furthermore, any one line was not counted in the likelihood if its modeled optical depth was less than -0.9 or greater than 100. The upper limit of 100 was because the concept of a one-zone model breaks down at this point. The line center optical depths are so large that the measured excitation temperatures will vary strongly across the line profile, causing self-absorption. In other words, the escape probability method becomes invalid. We allowed a slightly negative lower limit because we found that, even given normal ISM conditions, the lowest population levels may be slightly inverted (resulting in negative optical depth). Again, the escape probability method can no longer be used with a strong maser.

Table 4.11. CO Fitting Results: Model Parameters

FTS Name	Log n_{H_2} [cm^{-3}]			Log T_{kin} [K]			Log N_{CO} [cm^{-2}]			Log Φ_A		
	Mean	σ	Best	Mean	σ	Best	Mean	σ	Best	Mean	σ	Best
Cool Component												
Mrk 231	3.6	1.3	5.4	1.4	0.6	0.8	17.4	0.8	16.4	-1.3	0.7	-0.3
IRAS F17207-0014	4.4	1.2	4.1	1.2	0.4	1.1	19.5	0.5	20.1	-2.6	0.3	-2.7
Arp 220	3.4	1.1	2.6	1.7	0.6	1.8	19.1	1.0	20.3	-2.0	0.7	-2.8
Mrk 273	3.5	1.3	5.4	1.5	0.6	0.8	18.4	1.1	18.8	-2.0	0.8	-2.2
UGC 05101	3.6	1.2	5.6	1.4	0.6	1.1	18.0	1.1	19.3	-1.9	0.9	-2.8
NGC 6240	4.3	1.0	5.8	1.7	0.5	1.2	17.8	0.8	18.0	-1.2	0.7	-1.4
Arp 299-C	3.6	1.3	5.9	1.5	0.6	1.1	19.0	0.5	18.9	-2.0	0.5	-1.7
Arp 299-B	3.6	1.3	5.8	1.1	0.5	1.1	18.7	0.8	19.4	-1.7	0.7	-2.1
Arp 299-A	3.2	1.1	3.8	1.2	0.5	0.5	18.2	0.9	17.6	-1.0	0.6	-0.3
NGC 1068	2.7	0.3	2.7	2.4	0.3	2.7	18.7	0.8	18.3	-1.0	0.5	-0.9
NGC 1365-SW	3.4	1.2	2.4	1.3	0.6	1.9	18.6	0.7	18.0	-0.9	0.5	-0.7
NGC 1365-NE	2.3	0.3	2.6	1.5	0.2	1.5	20.2	0.1	20.3	-1.8	0.1	-2.0
NGC 4038	2.6	0.9	2.1	2.1	0.5	2.6	19.0	0.5	19.1	-1.8	0.3	-1.8
NGC 4038 (Overlap)	3.5	1.2	3.8	1.6	0.7	0.9	18.7	0.6	19.4	-1.5	0.5	-1.4
M82	3.4	1.0	2.8	1.8	0.6	2.4	18.7	0.7	18.2	-0.6	0.5	-0.3
NGC 1222	3.6	1.3	5.5	1.2	0.5	1.0	17.9	0.9	19.4	-1.4	0.7	-2.0
M83	3.8	1.3	2.9	1.3	0.7	0.8	19.2	0.5	19.4	-1.7	0.5	-0.9
NGC 253	3.5	1.2	2.6	1.6	0.7	2.1	19.6	0.6	19.9	-1.2	0.5	-1.3
NGC 1266	3.4	1.2	2.2	1.5	0.6	2.2	18.5	1.0	19.3	-1.8	0.7	-2.5
Cen A	3.0	1.1	2.9	1.1	0.5	0.8	18.2	0.6	18.1	-0.5	0.4	-0.5
Warm Component												
Mrk 231	3.7	0.1	3.7	3.3	0.1	3.4	16.8	0.9	15.9	-1.5	0.9	-0.6
IRAS F17207-0014	4.9	0.5	4.7	2.4	0.2	2.5	16.7	0.9	17.4	-1.5	0.8	-2.2
IRAS 09022-3615	4.5	0.3	4.5	2.8	0.2	2.8	16.5	0.9	17.4	-1.5	0.9	-2.5
Arp 220	4.1	0.6	4.9	2.8	0.3	2.4	17.4	0.9	16.5	-1.5	0.8	-0.9
Mrk 273	3.8	0.2	3.7	3.3	0.1	3.4	16.7	0.9	15.2	-1.5	0.8	-0.0
UGC 05101	3.3	0.4	3.6	3.2	0.2	3.4	16.9	0.9	15.9	-1.5	0.9	-0.9
NGC 6240	4.1	0.3	4.1	3.0	0.2	3.1	17.4	0.9	16.3	-1.5	0.9	-0.4
Arp 299-C	2.3	0.2	2.1	3.3	0.1	3.4	18.7	1.0	19.7	-2.1	0.9	-3.0
Arp 299-B	2.5	0.3	2.7	3.4	0.1	3.5	17.9	0.9	18.2	-1.5	0.7	-2.0

Table 4.11 (cont'd)

FTS Name	Log n_{H_2} [cm^{-3}]			Log T$_{kin}$ [K]			Log N_{CO} [cm^{-2}]			Log Φ_A		
	Mean	σ	Best	Mean	σ	Best	Mean	σ	Best	Mean	σ	Best
Arp 299-A	3.3	0.2	3.1	3.2	0.1	3.2	17.5	0.8	18.0	-1.3	0.8	-1.7
NGC 1068	4.8	0.5	4.9	2.9	0.3	2.8	17.2	0.9	17.4	-1.5	0.9	-1.8
NGC 1365-SW	3.2	0.6	3.7	2.8	0.2	2.6	18.3	0.9	17.9	-1.5	0.7	-1.4
NGC 1365-NE	3.1	0.7	2.1	2.7	0.1	2.8	18.9	1.1	20.4	-2.1	0.8	-2.9
NGC 4038	4.6	1.2	5.5	3.0	0.3	3.0	16.3	1.2	15.0	-1.5	0.8	-0.9
NGC 4038 (Overlap)	3.3	0.9	3.1	2.9	0.2	2.9	17.4	1.1	18.4	-1.4	0.7	-2.1
M82	3.9	0.4	4.1	2.9	0.2	2.8	18.2	0.8	18.2	-1.1	0.6	-1.3
NGC 1222	4.2	0.5	4.3	2.4	0.2	2.4	16.7	0.9	15.7	-1.5	0.9	-0.7
M83	2.9	0.3	2.0	2.9	0.2	2.9	18.8	0.5	19.7	-1.9	0.5	-2.0
NGC 253	3.1	0.3	3.5	3.2	0.2	3.0	19.2	0.8	19.5	-1.7	0.8	-2.3
NGC 1266	3.6	0.3	3.7	3.2	0.1	3.2	17.1	0.8	16.0	-1.4	0.8	-0.5
Cen A	2.6	0.4	2.2	3.1	0.2	3.3	18.5	0.8	19.0	-1.8	0.6	-2.1

Table 4.12. CO Fitting Results: Derived Parameters

FTS Name	Log $L_{\rm CO}$ [erg s^{-1}]			Log P [K cm^{-3}]			Log $< N_{\rm CO} >$ [cm^{-2}]			Log $M_{\rm H_2}$ [M$_\odot$]		
	Mean	σ	Best	Mean	σ	Best	Mean	σ	Best	Mean	σ	Best
Cool Component												
Mrk 231	40.6	0.2	40.5	5.0	0.8	6.1	16.1	0.2	16.1	9.3	0.2	9.3
IRAS F17207-0014	41.2	0.2	41.2	5.6	1.0	5.2	16.9	0.4	17.3	10.1	0.4	10.5
Arp 220	41.0	0.4	41.3	5.0	0.8	4.4	17.1	0.4	17.5	9.6	0.4	10.0
Mrk 273	40.7	0.3	40.5	5.0	0.9	6.2	16.4	0.4	16.6	9.5	0.4	9.7
UGC 05101	40.5	0.4	41.0	5.0	1.0	6.6	16.2	0.4	16.5	9.3	0.4	9.6
NGC 6240	41.6	0.2	41.6	6.0	0.7	7.0	16.6	0.1	16.6	9.3	0.1	9.3
Arp 299-C	40.2	0.6	40.7	5.1	1.1	7.0	17.0	0.3	17.2	9.0	0.3	9.2
Arp 299-B	39.6	0.6	40.3	4.7	1.2	6.8	17.0	0.4	17.3	9.0	0.4	9.3
Arp 299-A	39.9	0.3	39.7	4.3	1.0	4.4	17.2	0.4	17.3	9.2	0.4	9.3
NGC 1068	40.8	0.1	41.0	5.0	0.4	5.4	17.6	0.3	17.4	8.8	0.3	8.5
NGC 1365-SW	40.0	0.4	40.2	4.6	1.0	4.3	17.6	0.4	17.3	9.1	0.4	8.8
NGC 1365-NE	40.4	0.2	40.5	3.8	0.2	4.0	18.4	0.1	18.3	9.9	0.1	9.8
NGC 4038	40.3	0.3	40.5	4.8	0.6	4.8	17.2	0.3	17.2	8.7	0.3	8.7
NGC 4038 (Overlap)	40.0	0.6	39.8	5.1	0.9	4.7	17.3	0.4	18.0	8.7	0.4	9.5
M82	39.6	0.5	39.9	5.2	0.7	5.3	18.1	0.3	17.9	7.9	0.3	7.7
NGC 1222	39.2	0.3	39.7	4.7	1.0	6.5	16.5	0.4	17.4	8.3	0.4	9.2
M83	38.6	0.9	38.7	5.1	1.1	3.7	17.6	0.5	18.6	8.0	0.5	9.1
NGC 253	39.3	1.0	40.0	5.0	0.9	4.6	18.5	0.4	18.6	8.3	0.4	8.4
NGC 1266	39.6	0.4	39.9	4.9	0.9	4.4	16.7	0.4	16.8	8.4	0.4	8.5
Cen A	38.7	0.3	38.5	4.1	0.9	3.7	17.7	0.5	17.6	8.2	0.5	8.2
Warm Component												
Mrk 231	42.59	0.06	42.66	7.0	0.1	7.1	15.3	0.1	15.3	8.4	0.1	8.5
IRAS F17207-0014	42.37	0.03	42.37	7.3	0.3	7.1	15.2	0.1	15.2	8.4	0.1	8.4
IRAS 09022-3615	42.63	0.04	42.62	7.3	0.1	7.3	14.9	0.1	14.9	8.4	0.1	8.4
Arp 220	42.23	0.07	42.16	6.9	0.3	7.3	15.9	0.2	15.6	8.4	0.2	8.1
Mrk 273	42.41	0.07	42.48	7.1	0.1	7.1	15.1	0.1	15.2	8.2	0.1	8.3
UGC 05101	42.10	0.06	42.23	6.5	0.3	7.0	15.4	0.3	15.0	8.5	0.3	8.2
NGC 6240	42.86	0.06	42.88	7.2	0.1	7.2	15.9	0.1	15.9	8.6	0.1	8.6
Arp 299-C	41.41	0.08	41.36	5.6	0.2	5.4	16.6	0.2	16.8	8.6	0.2	8.8
Arp 299-B	41.49	0.04	41.51	5.9	0.3	6.1	16.4	0.2	16.2	8.4	0.2	8.2

Table 4.12 (cont'd)

FTS Name	Log L_{CO} [erg s^{-1}]			Log P [K cm^{-3}]			Log $< N_{CO} >$ [cm^{-2}]			Log M_{H_2} [M$_\odot$]		
	Mean	σ	Best	Mean	σ	Best	Mean	σ	Best	Mean	σ	Best
Arp 299-A	41.86	0.04	41.87	6.5	0.2	6.4	16.2	0.1	16.3	8.2	0.1	8.4
NGC 1068	41.38	0.08	41.33	7.7	0.2	7.8	15.7	0.1	15.6	6.8	0.1	6.7
NGC 1365-SW	41.18	0.07	41.19	5.9	0.4	6.3	16.7	0.4	16.4	8.2	0.4	7.9
NGC 1365-NE	41.10	0.07	40.97	5.8	0.6	4.9	16.8	0.5	17.5	8.3	0.5	9.0
NGC 4038	40.62	0.37	40.79	7.5	1.1	8.5	14.8	0.8	14.1	6.2	0.8	5.6
NGC 4038 (Overlap)	40.69	0.44	40.79	6.2	0.9	6.0	15.9	1.0	16.3	7.4	1.0	7.8
M82	40.63	0.05	40.61	6.8	0.3	7.0	17.1	0.3	16.8	6.9	0.3	6.6
NGC 1222	40.44	0.11	40.43	6.6	0.3	6.8	15.1	0.3	14.9	7.0	0.3	6.8
M83	40.19	0.09	40.17	5.8	0.3	5.0	16.9	0.3	17.7	7.3	0.3	8.1
NGC 253	40.78	0.12	40.73	6.3	0.2	6.6	17.5	0.2	17.3	7.4	0.2	7.1
NGC 1266	41.25	0.05	41.22	6.8	0.2	6.9	15.6	0.2	15.5	7.4	0.2	7.2
Cen A	40.02	0.05	40.08	5.7	0.3	5.5	16.7	0.3	16.9	7.2	0.3	7.4

The results are presented in Figures 4.8, 4.9, 4.10, 4.11, 4.12, 4.13 and Tables 4.11, 4.12, 4.13. As with the dust modeling results in the previous section, we present the mode mean, mode sigma, and best-fit results (recall Section 4.5 for these terms). However, the likelihood distributions themselves (in the accompanying figures) are not as simply described as in the dust modeling case. In many instances, the best fit result (and the associated SLED illustrated in 4.8) does not correspond to the mean or mode of a marginalized parameter distribution. Additionally, the results for some galaxies included contributions from multiple modes, which can be thought of as separate islands in parameter space. The mode mean and sigma presented here are for that of the mode containing the highest integrated likelihood; this mode had an obvious distinction as the far more likely mode than any other ones found. The jaggedness of the lines should not be considered significant.

4.5.3 MAGPHYS

In addition to properties such as dust mass and luminosity, we also sought to compare galaxies by star formation rate (SFR) and specific star formation rate (sSFR), which requires stellar masses (M_*). We used MAGPHYS [35] and the same photometry as presented in Appendix C, now including those measurements below 10 μm, unlike in Section 4.5.1. MAGPHYS computes the spectral evolution of stellar populations [22], with dust attenuation due to a two-component

Table 4.13. CO Fitting Results: Derived Parameter Ratios

FTS Name	Log L_{warm}/L_{cool}			Log P_{warm}/P_{cool}			Log M_{warm}/M_{cool}		
	Mean	σ	Best	Mean	σ	Best	Mean	σ	Best
Mrk 231	1.9	0.2	2.1	2.0	0.9	1.0	-0.8	0.2	-0.8
IRAS F17207-0014	1.2	0.2	1.1	1.7	1.0	2.0	-1.7	0.4	-2.1
Arp 220	1.2	0.4	0.9	1.9	0.9	2.9	-1.2	0.5	-1.9
Mrk 273	1.7	0.3	2.0	2.0	0.9	0.9	-1.2	0.5	-1.4
UGC 05101	1.6	0.5	1.2	1.5	0.9	0.4	-0.8	0.5	-1.5
NGC 6240	1.2	0.2	1.3	1.2	0.7	0.1	-0.7	0.2	-0.7
Arp 299-C	1.2	0.6	0.7	0.5	1.1	-1.6	-0.4	0.3	-0.5
Arp 299-B	1.9	0.6	1.2	1.2	1.2	-0.7	-0.6	0.4	-1.1
Arp 299-A	2.0	0.3	2.1	2.2	0.9	2.0	-1.0	0.5	-1.0
NGC 1068	0.6	0.2	0.4	2.6	0.5	2.4	-1.9	0.3	-1.9
NGC 1365-SW	1.2	0.5	1.0	1.3	1.0	1.9	-0.9	0.5	-0.9
NGC 1365-NE	0.7	0.3	0.4	2.0	0.6	0.9	-1.5	0.6	-0.8
NGC 4038	0.4	0.4	0.3	2.7	1.3	3.7	-2.5	0.8	-3.1
NGC 4038 (Overlap)	0.7	0.9	1.0	1.1	1.2	1.2	-1.3	0.9	-1.7
M82	1.1	0.5	0.7	1.6	0.7	1.7	-1.1	0.4	-1.1
NGC 1222	1.3	0.4	0.7	1.9	1.0	0.3	-1.4	0.5	-2.5
M83	1.6	1.0	1.5	0.7	1.1	1.3	-0.7	0.4	-0.9
NGC 253	1.5	1.1	0.7	1.3	1.0	1.9	-0.9	0.5	-1.4
NGC 1266	1.6	0.4	1.3	1.9	0.9	2.5	-1.1	0.5	-1.3
Cen A	1.3	0.3	1.6	1.5	0.9	1.8	-1.0	0.5	-0.7
Weighted Average	1.2	0.1		1.8	0.2		-0.9	0.1	

Note. — IRAS 09022-3615 is not included because only one component was modeled.

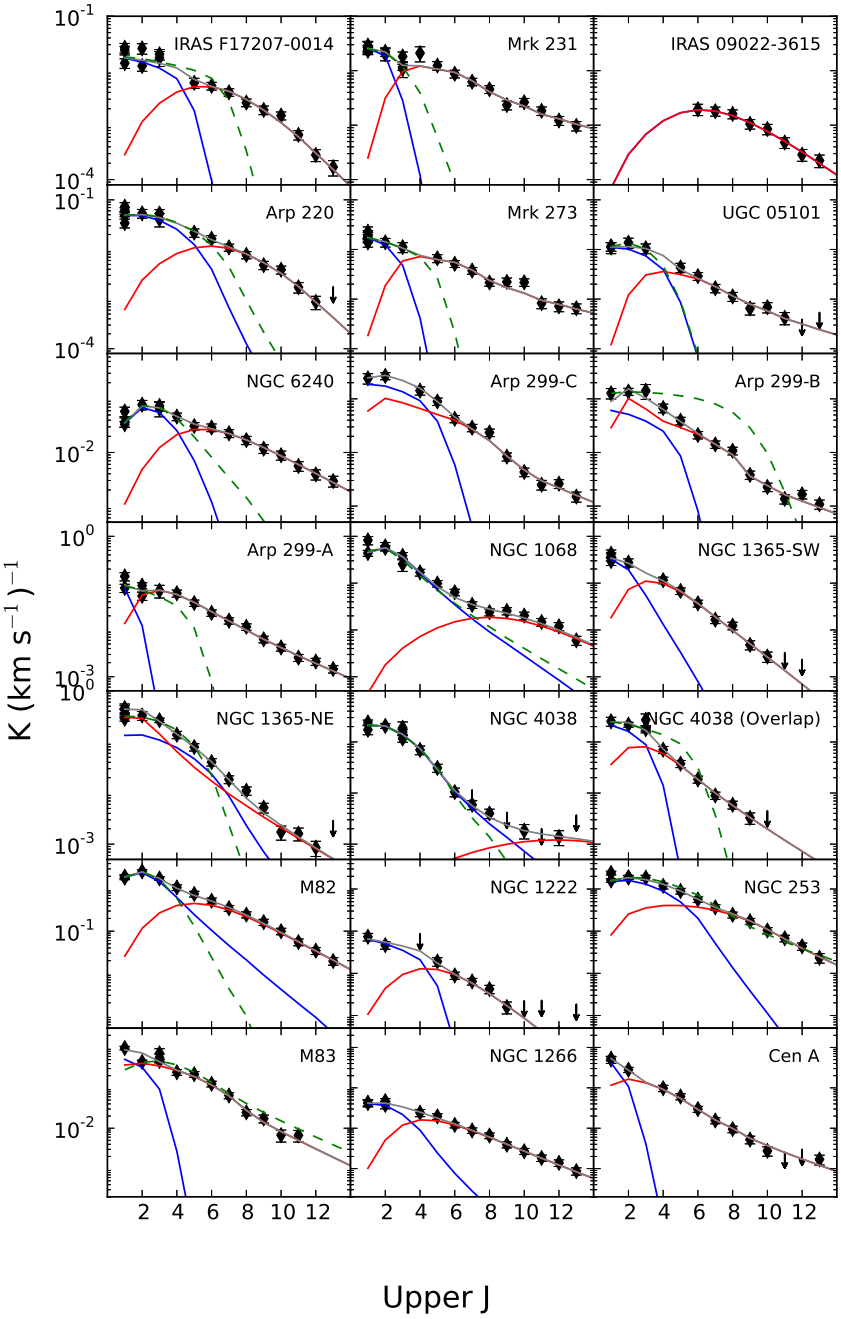

Figure 4.8 CO modeling spectral line energy distributions. The blue is the best-fit solution for the cold component, the red the best-fit solution for the warm, with their total in grey. Those galaxies that contain all three of the lowest-J transitions also have a green line (dashed), which is the fit to only those three lines.

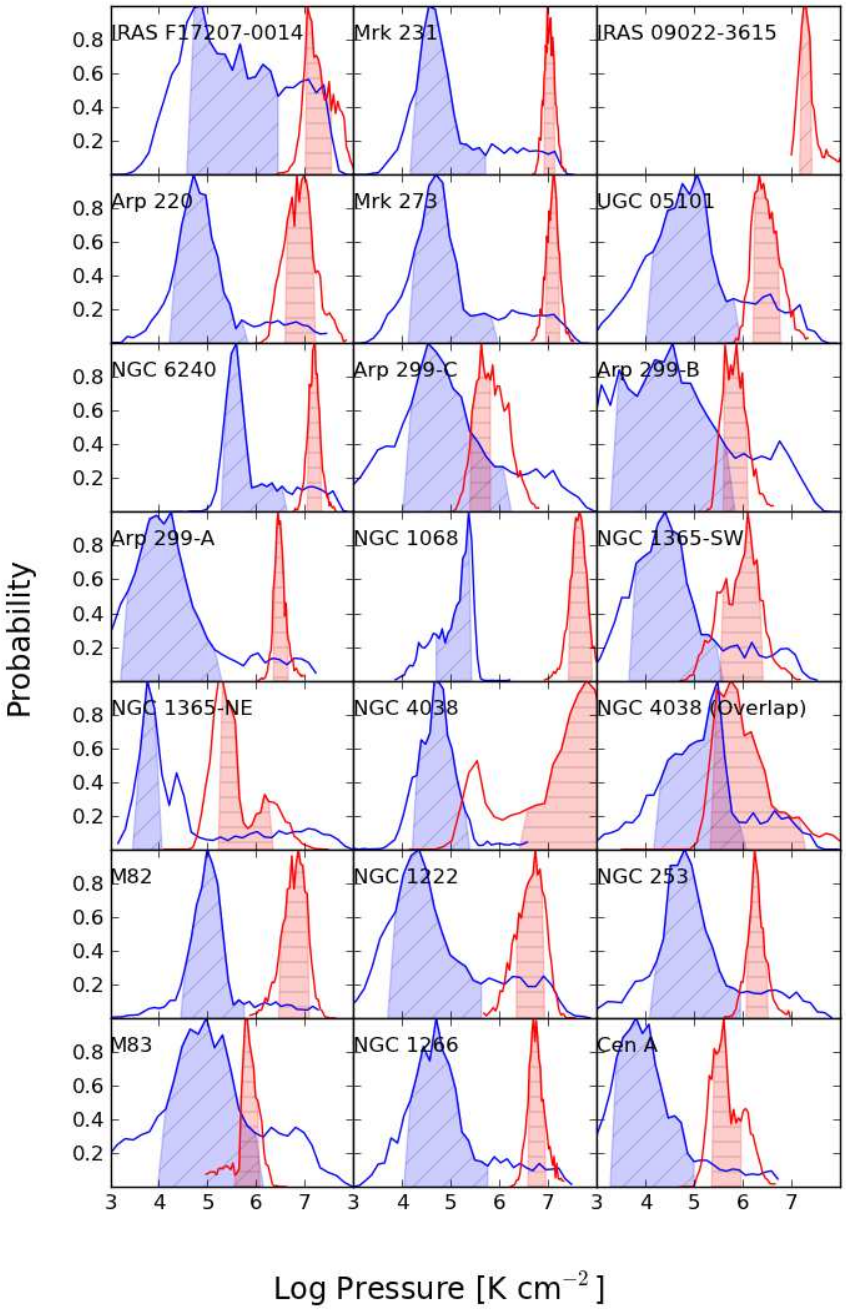

Figure 4.9 CO modeling likelihood results: pressure. Blue/red (diagonal/horizontal hatches) represent cool/warm components. Shaded areas indicate the 1σ uncertainty region, defined here as the mode median +/- the error (symmetric) on the parameter. Vertical lines represent the best-fit model parameter. IRAS F17207-0014 is an example of a galaxy with best-fit parameter values close to the median, whereas UGC 05101 is an example where the best-fit and median values do not align.

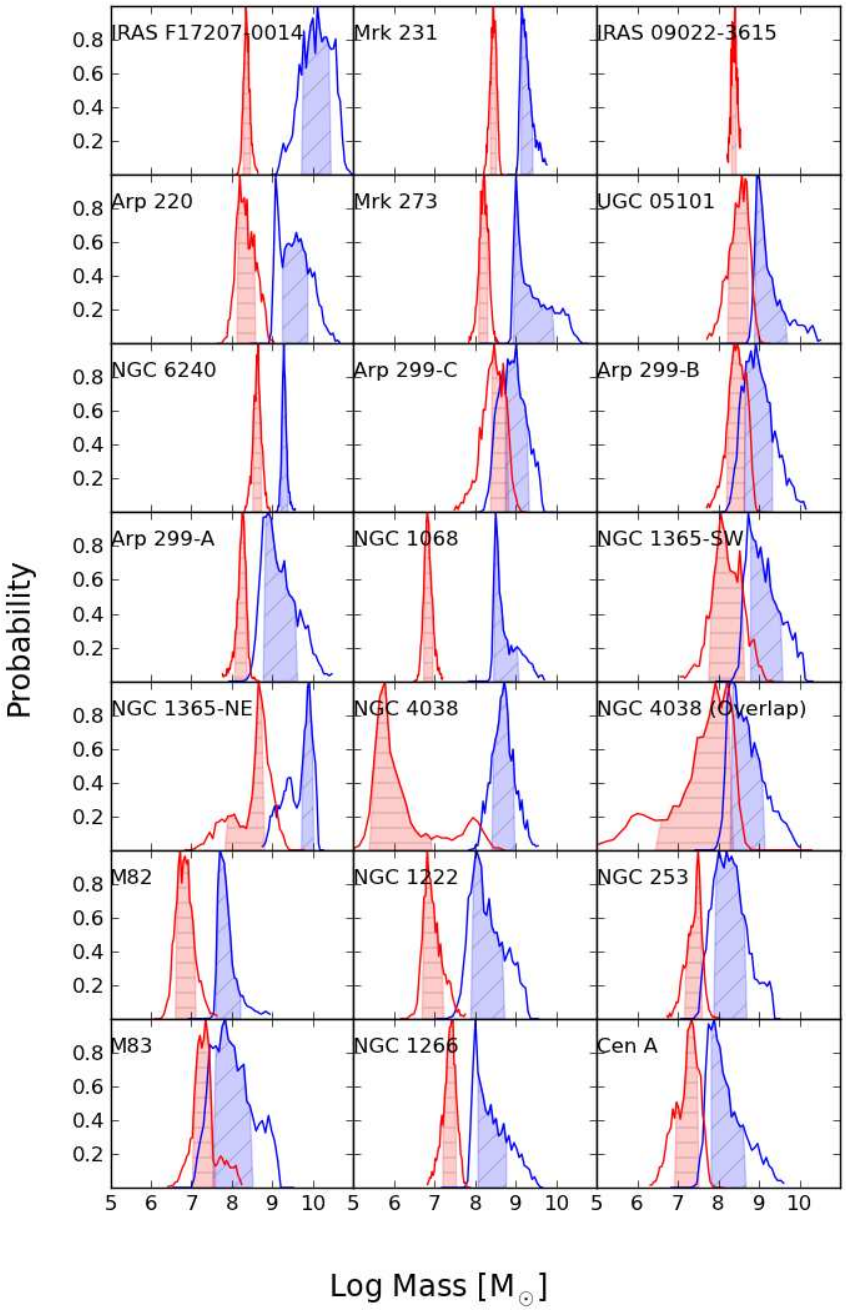

Figure 4.10 CO modeling likelihood results: mass. See Figure 4.9 for more information.

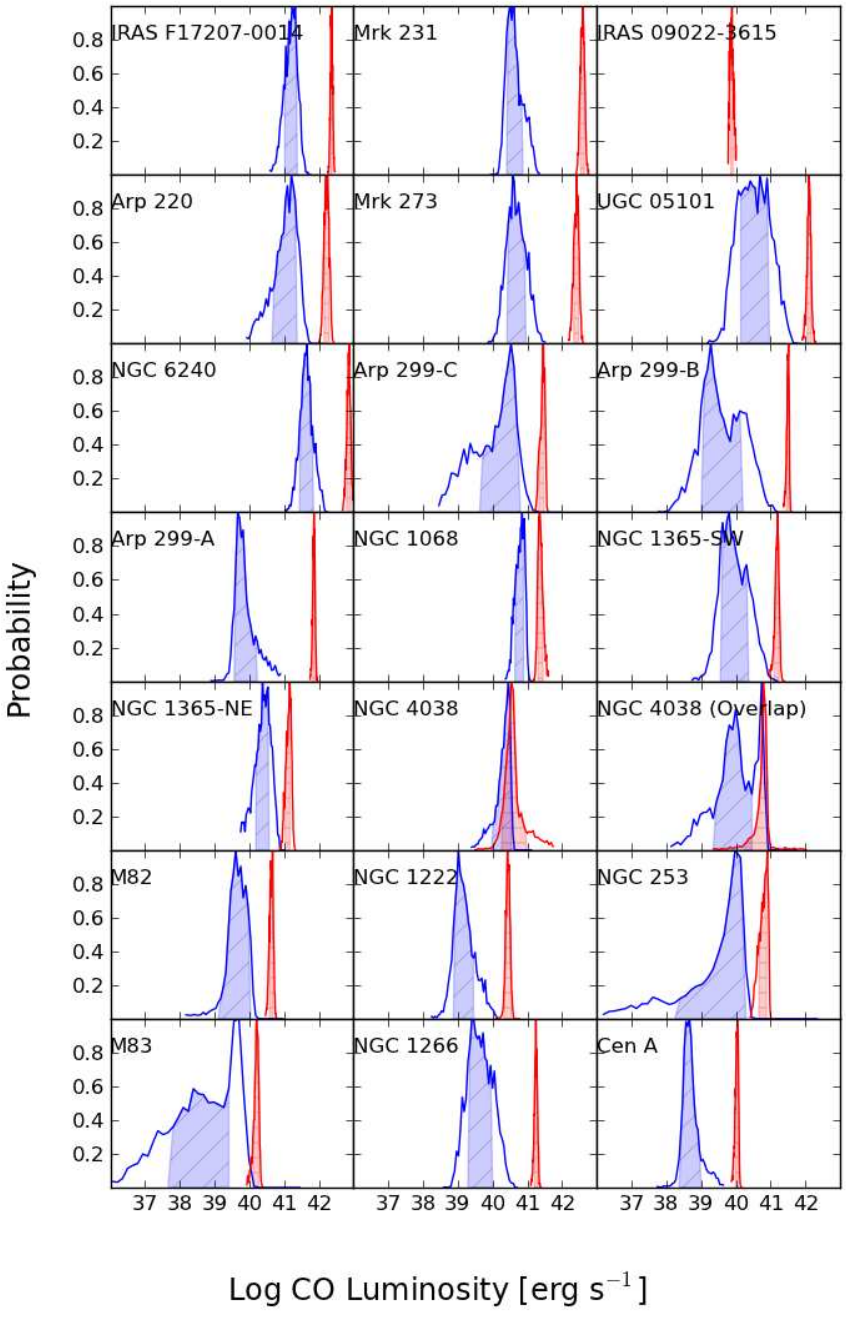

Figure 4.11 CO modeling likelihood results: luminosity. See Figure 4.9 for more information.

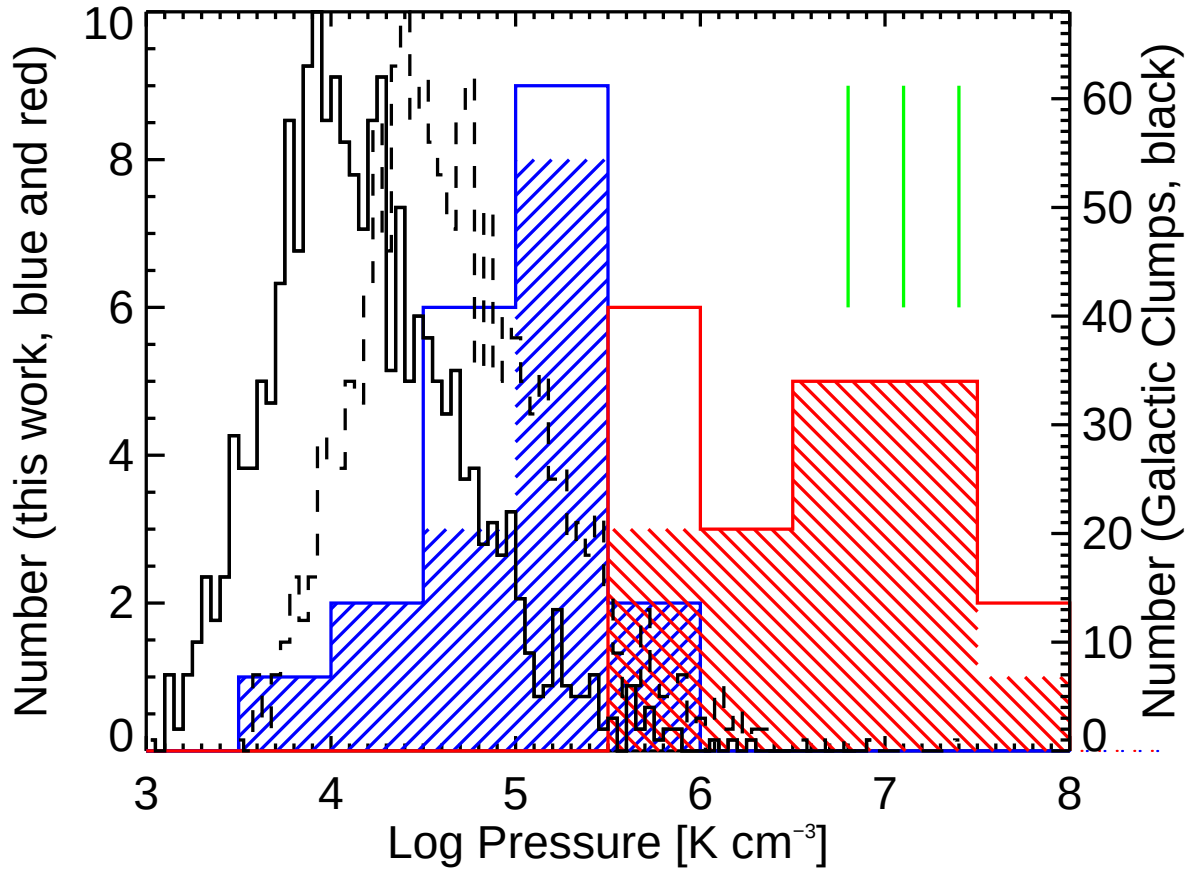

Figure 4.12 CO modeling histograms for pressure. Cold component is in blue (upward slant), warm component in red (downward slant). Duplicate pointings of galaxies are not filled in by diagonal lines. The black solid (dashed) histogram is the pressure of galactic molecular clumps at a temperature of 10 (30) K, based on densities determined by the Bolocam Galactic Plane Survey (BGPS, Ellsworth-Bowers et al., in prep). The temperature range is chosen from the 20 K mean gas kinetic temperature found for BGPS sources in Dunham et al. [46]. The y-axis on the left is the number for the distributions in this work, and the right axis is the number for the Galactic clumps. The vertical green lines indicate the pressures, from left to right, for the Sgr B2(N), Sgr A*, and Sgr B2(M) warm extended emission, discussed further in Section 5.1.8 [53, 61].

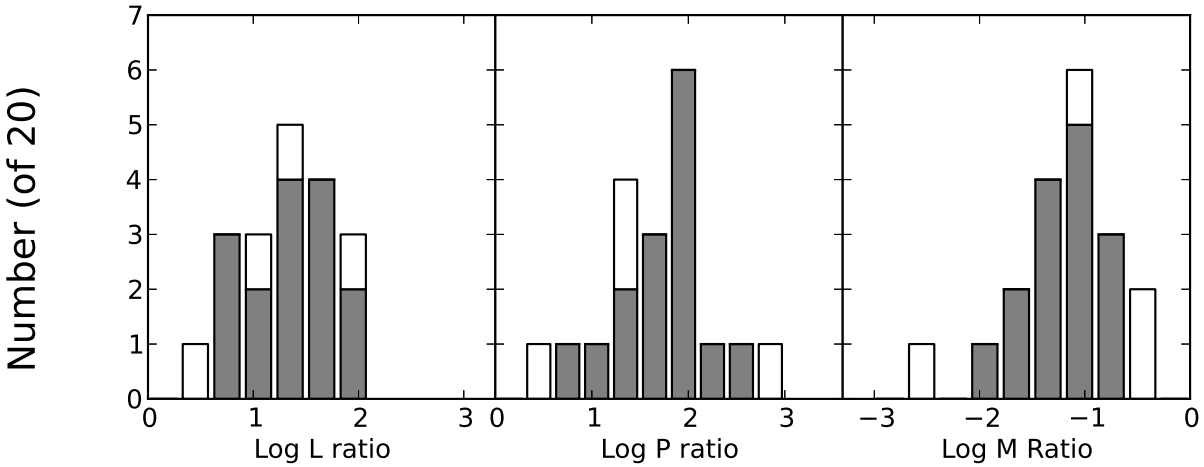

Figure 4.13 CO modeling histograms for derived parameter ratios. Duplicate pointings of galaxies are shown in white (one pointing per galaxy remains gray) and not used for fitting average values.

Table 4.14. MAGPHYS Results (Log)

FTS Name	M_* [$M_\odot$]	sSFR [yr^{-1}]	SFR[a] [$M_\odot yr^{-1}$]	SFR[b] [$M_\odot yr^{-1}$]
Mrk 231	10.2	-8.1	2.1	2.6
IRAS F17207-0014	10.2	-8.5	1.8	2.6
IRAS 09022-3615	10.8	-9.2	1.6	2.4
Arp 220	10.7	-9.4	1.3	2.4
Mrk 273	11.1	-9.7	1.4	2.4
UGC 05101	10.8	-9.0	1.7	2.2
NGC 6240	11.4	-10.3	1.1	2.1
Arp 299-A	10.5	-8.9	1.6	2.0
NGC 1068	11.0	-10.1	0.92	1.6
NGC 1365-NE	11.1	-10.4	0.75	1.3
NGC 4038 (Overlap)	10.4	-9.4	0.98	1.1
M82	9.8	-10.1	-0.28	1.0
NGC 1222	9.2	-9.0	0.23	0.89
M83	10.8	-10.1	0.70	0.76
NGC 253	10.2	-10.2	-0.0063	0.75
NGC 1266	9.8	-10.3	-0.47	0.67
Cen A	11.4	-11.5	-0.16	0.16

Note. — All columns are logarithms of the parameter in the units above. Three galaxies were not modeled with both GALEX UV bands, and should be treated with caution: Mrk 231, NGC 6240, IRAS F17207-0014. Additionally, the SFRs for the AGN should be treated as upper limits: UGC 05101, NGC 1068, Cen A, NGC 1365, Mrk 231, Mrk 273.

[a]From MAGPHYS.

[b]From 1.73×10^{-10} L_{FIR} [$L_\odot$], [82].

model [29] (giant molecular clouds and the diffuse ISM). This portion of the model absorbs UV and optical and is used to compute the infrared dust spectral energy distribution. MAGPHYS computes SEDs of stellar light re-radiated by dust as the sum of three components: polycyclic aromatic hydrocarbons (PAHs), a mid-infrared continuum from hot grains at 130-230 K, and grains at 30-60K. The relative proportions of these 3 components are fixed to reproduce the Milky Way, which is perhaps not an appropriate model for these galaxies.

The resulting best-fit parameters of interest (out of the 12 parameters in the model) are presented in Table 4.14. The uncertainties are not deducible due to the coarseness of the parameter grid, but we assume large uncertainties (0.5 dex) simply from the difficulties in SED modeling and the assumptions of the models. We found that the star formation rates are often much lower than those derived from the Kennicutt [82] starburst relationship with far-infrared luminosity, shown in the last column of Table 4.14. We also found the dust masses to be much lower than those calculated from our modeling in Section 4.5.1. Both of these properties are derived from the long-wavelength portion of the SED. The stellar mass, however, is derived from the short wavelength portion of the SED and matches well with comparisons (next paragraph), so we still use this value in order to calculate mass depletion timescales in Section 5.1.9.

We compared with other usages of MAGPHYS in the literature: five of our galaxies were modeled in U et al. [170], and three in Lanz et al. [90] (using MAGPHYS). We found very similar results for all properties with Lanz et al. [90] for NGC 4038 and Arp 299 (within half a dex). For M82, they used much fainter UV fluxes than those from NED, causing a significant difference in SFR (theirs was lower, at log(SFR) = -1.38 $M_{\odot}yr^{-1}$). U et al. [170] did not use MAGPHYS, though our results still matched well for UGC 05101 and Arp 299. For Arp 220 and Mrk 273, we found a lower sSFR, due mostly due to a lower SFR, not stellar mass. When we modeled their data with MAGPHYS, we found the same results as when modeling our data, indicating that the difference was due to the model, not the data. For Mrk 231, we found a higher sSFR (and lower M_*); however, the UV is not constrained for this galaxy and its results for the stellar population are thus not well constrained. This was also the case for IRAS F17207-0014 (no GALEX data available), and to a

lesser extent, NGC 6240 (only one of two GALEX bands available). To summarize, we do not use the star formation rates from MAGPHYS, because we found them to be too low. Instead we use SFRs from the Kennicutt relation [82] to be more comparable to the literature.

4.5.4 LTE Analysis of [CI]

Two forbidden lines of neutral carbon ([CI]) were present in our spectra. The ratios of the line intensities in Jy km s^{-1} (J=2→1/J=1→0) were used to derive excitation temperatures, equivalent to the kinetic temperatures of the [CI] emitting gas under the assumption of local thermodynamic equilibrium:

$$T_{ex} = E_{2-1}\left[\ln\left(\frac{g_2}{g_1}\frac{A_{2-1}S_{1-0}}{A_{1-0}S_{2-1}}\right)\right]^{-1}. \tag{4.4}$$

In the above equation, A is the Einstein A coefficient for each line, g the statistical weight of a level, E_{2-1} the difference in energy levels in K (as we will use through the remainder of the section), and S the flux in Jy km s^{-1}. (If using the ratio in K km s^{-1} or W m^{-2}, one must also include $\lambda_{1-0}/\lambda_{2-1}$ in the natural log term above.)

We corrected each flux to account for the absorption by dust as described in Section 4.5.2.1. Each integrated flux in LTE is proportional to the population level of the upper state of the line, where the total number of atoms or molecules in the state, N_j equals $L_{j\to i}/(A_{j\to i}h\nu_{j\to i})$. The total number of atoms or molecules can be found by dividing by the fraction of those in that state, where $f_i = g_i e^{-E_i/T_{ex}}/Z(T_{ex})$ and $Z(T_{ex})$ is the partition function, $Z(T_{ex}) = \sum_J g_J e^{-E_J/T_{ex}}$. The total mass is therefore mN_i/f_i, where m is the mass of the atom or molecule. Temperatures and masses (calculated from the J=2 energy level, as these lines have the lowest error in flux) are in Table 4.15. We further discuss these results in Section 5.1.7.

4.5.5 LTE Analysis of H_2

CO is used as a proxy for total molecular gas, most of which is molecular hydrogen. The electric quadrupole transitions of H_2 are difficult to observe, but were available for many of these

Table 4.15. [CI] LTE Temperatures

FTS Name	T_{ex} [K]	σ [K]	$M_{[CI]}$ [10^4 $M_\odot$]	σ [10^4 $M_\odot$]
Mrk 231	34	10	160	10
IRAS F17207-0014	24	5	350	30
IRAS 09022-3615	20.	3	800	70
Arp 220	24	5	190	20
Mrk 273	23	3	230	10
UGC 05101	33	10	160	10
NGC 6240	44	6	300	20
Arp 299-C	28	4	41	1
Arp 299-B	27	4	41	2
Arp 299-A	35	6	52	2
NGC 1068	28	1	31	0.9
NGC 1365-SW	25	1	27	1
NGC 1365-NE	24	1	32	1
NGC 4038	35	10	4.4	0.4
NGC 4038 (Overlap)	23	1	13	0.5
M82	36	3	3.9	0.1
NGC 1222	29	10	4.1	0.4
M83	39	4	1.6	0.07
NGC 253	33	2	4.5	0.1
NGC 1266	30.	4	11	0.4
Cen A	50.	6	0.86	0.05
Average	26	8		

Table 4.16. H_2 Line Measurements: 10^{-16} W m^{-2}

FTS Name	S(0)	σ	S(1)	σ	S(2)	σ	S(3)	σ	S(5)	σ	S(7)	σ	$\tau_{9.7}$	Ref
Mrk 231	< 67.5	...	1.14	0.28	0.39	0.14	0.43	0.10	...	...	< 122	...	0.8	1,2
IRAS F17207-0014	< 23.9	...	0.88	0.01	0.50	0.09	0.57	0.11	...	...	< 8.50	...	0.0	2
IRAS 09022-3615	< 3.30	...	0.12	0.01	< 0.20	...	< 0.20	...	...	...	< 0.04	...	0.0	2
Arp 220	< 97.0	...	1.86	0.17	0.98	0.13	0.73	0.02	...	...	1.29	0.38	3.3	2
Mrk 273	< 26.3	...	1.02	0.01	0.56	0.07	1.04	0.09	...	...	< 15.0	...	2.0	2
UGC 05101	< 10.0	...	0.50	0.05	0.27	0.05	0.28	0.03	...	...	< 19.5	...	1.6	2
NGC 6240	0.5	0.2	4.27	0.34	3.55	0.26	5.83	0.43	...	...	5.54	0.50	0.0	2
Arp 299-C	< 0.7	...	4.11	1.0	1.92	0.48	...	...	1.46	0.36	...	...	1.2	3
Arp 299-B	< 0.7	...	4.11	1.0	1.92	0.48	...	...	1.46	0.36	...	...	1.2	3
Arp 299-A	< 1.21	...	3.70	0.90	1.80	0.45	...	...	1.97	0.50	...	...	1.2	3
NGC 1068	< 1.87	...	6.50	1.6	< 8.00	...	5.76	1.4	6.40	1.6	3.50	0.87	0.5	3,4
NGC 1365-SW	1.59	0.1	5.69	1.4	< 3.13	...	...	...	2.01	0.50	...	...	0.2	3,5
NGC 1365-NE	1.59	0.1	5.69	1.4	< 3.13	...	...	...	2.01	0.50	...	...	0.2	3,5
NGC 4038	0.7	0.2	3.95	0.99	1.60	0.40	...	...	...	...	...	...	4.7	3,6
NGC 4038 (Overlap)	3.67	0.3	7.02	0.37	2.38	0.47	< 2.15	...	...	...	...	...	0.0	6
M82	7.80	1.9	15.0	3.8	12.0	3.0	...	...	11.5	2.9	4.80	1.2	1.8	3
NGC 1222	0.3	0.0	0.95	0.03	0.29	0.02	...	...	...	...	...	...	0.0	5
M83	< 1.04	...	7.29	1.8	...	...	...	...	2.84	0.70	...	...	0.3	3
NGC 253	2.13	0.5	19.6	4.9	12.0	3.0	...	...	11.5	2.9	8.40	2.1	1.8	3
NGC 1266	0.2	0.1	1.49	0.07	1.22	0.07	1.90	0.12	2.42	0.20	1.92	0.29	0.2	7
Cen A	2.51	0.6	8.64	2.2	5.40	1.4	5.81	1.5	4.54	1.1	3.26	0.80	1.8	3

Note. — See Appendix B for information about extended sources. **References.** (1) Armus et al. [6]; (2) Higdon et al. [71]; (3) Rigopoulou et al. [144]; (4) Lutz et al. [98]; (5) Bernard-Salas et al. [13]; (6) Brandl et al. [19]; (7) Roussel et al. [146]

bright galaxies. Here we consider the S(0), S(1), S(2), S(3), S(5), and S(7) transitions of H_2. The hydrogen fluxes and optical depths are in Table 4.16; see Appendix B for detailed information on extended galaxies. The derived temperatures and masses are in Table 4.17, with excitation diagrams in Figure 4.14.

With Equation 4.4, we calculated excitation temperatures for the S(1)-S(0) line, the S(3), S(2), and S(1) lines, and the S(7)-S(5) transitions, when available. We also corrected these lines for dust extinction, but in this portion of the spectrum the notable feature is the 9.7 μm silicate absorption feature. Based on the extinction models of Draine [44], we used $\tau_\lambda/\tau_{9.7} = 0.19, 0.35, 0.43, 0.99, 0.20, 0.30$ for S(0), S(1), S(2), S(3), S(5), and S(7), and $A_\lambda = 1.086\tau$, $A_V = 17\tau_{9.7}$. The values that we use for $\tau_{9.7}$ are listed in the last column of Table 4.17. In many cases, only an upper limit was available for S(0), meaning the S(1)-S(0) excitation temperature is a lower limit, and the S(0)-derived mass an upper limit.

One could calculate an excitation temperature from any pair of lines. The excitation temperature is the inverse of the slope of the lines presented in the excitation diagrams (Figure 4.14), which can be used to fit an excitation temperature to multiple lines, as we did with S(3), S(2), and S(1). One excitation temperature generally could not be fit for all lines from S(0) through S(7), which is why we present three. We did not calculate, for example, an excitation temperature from S(7)-S(3) when the S(5) line was unavailable, for consistency across the sample.

The extinction correction most dramatically increased the flux for the S(3) line, because of its alignment in wavelength with the silicate absorption feature. Cen A is a good example of a galaxy with high extinction and many lines measured. The extinction correction raised the three temperatures by 6, 39, and 50 K. If we calculated separate excitation temperatures S(2)-S(1) and S(3)-S(2), with no extinction correction we found 392 ± 82 and 300 ± 39 K. With extinction correction, the temperatures were 406 ± 88 and 351 ± 54 K. The correction had the effect of increasing the two temperatures, but more importantly, bringing these three mid-excitation lines into better alignment, giving us a better estimate of one middle excitation temperature. (Notice that the S(2)-S(1) and S(3)-S(2) temperatures quoted above are not distinguishable with the error bars.)

For the conditions studied here, the first 5 H_2 levels are likely in LTE, based on the collision rate coefficients in Le Bourlot et al. [92]. This assumption may become increasingly poor for the S(5) and S(7) lines, and the temperatures and masses from these lines should be treated as approximations.

4.5.6 [CII] and [NII] Line Ratios

Finally, we collected [CII] 158 μm fluxes for our sample of galaxies to compare to our FTS measured [NII] 205 μm line. The ratio of these two lines ([CII]/[NII]) from ionized gas is fairly constant, about 2.5 to 4.3, independent of ionized gas density [121]. This implies that ratios higher than this value indicate excess [CII] emission from other sources, especially PDRs. For example, a ratio of 30 indicates 8 to 14% of [CII] emission from ionized gas, hence 92 to 86% from other sources (for an assumed ionized ratio range of 2.5 to 4.3, respectively).

We present our results in Table 4.18, which includes the [CII] line fluxes used, and the percentage of emission from ionized gas. In most of our galaxies, the majority of [CII] emission is from PDRs and other non-ionized sources, ranging from 48% to 96%. We discuss the meaning of this in Section 5.1.7. The median is 75-85%.

Table 4.17. H_2 LTE Results

FTS Name		T_1 [K]	σ [K]	T_2 [K]	σ [K]	T_3 [K]	σ [K]	M_1 [10^6 $M_\odot$]	σ	M_2 [10^6 $M_\odot$]	σ	M_3 [10^3 $M_\odot$]	σ	$\tau_{9.7}$
Mrk 231	>	57	...	310	20	...	...	...	...	159	36	...	...	0.80
IRAS F17207-0014	>	63	...	340	10	...	...	...	...	94.6	7.1	...	...	0.00
IRAS 09022-3615	>	63	...	...	...	...	...	...	...	...	...	...	...	0.00
Arp 220	>	59	...	350	7	...	...	...	...	61.8	4.4	...	...	3.30
Mrk 273	>	64	...	420	9	...	...	...	...	81.3	2.8	...	...	2.00
UGC 05101	>	66	...	360	10	...	...	...	...	55.4	5.2	...	...	1.60
NGC 6240		200	40	400	10	...	...	786	470	119	8.2	...	...	0.00
Arp 299-C	>	180	...	340	60	...	...	...	...	35.6	14	...	...	1.18
Arp 299-B	>	180	...	340	60	...	...	...	...	35.6	14	...	...	1.18
Arp 299-A	>	140	...	350	60	...	...	...	...	30.7	12	...	...	1.18
NGC 1068	>	150	...	370	30	1110	170	...	...	4.56	1.2	77.7	35	0.47
NGC 1365-SW		150	10	...	...	...	...	168	36	...	...	...	...	0.15
NGC 1365-NE		150	10	...	...	...	...	168	36	...	...	...	...	0.15
NGC 4038		190	30	330	60	...	...	83.6	32	13.3	5.2	...	...	4.70
NGC 4038 (Overlap)		120	2	290	30	...	...	758	78	16.1	3.4	...	...	0.00
M82		130	10	480	100	1020	140	44.7	16	0.481	0.16	11.3	5.2	1.76
NGC 1222		140	4	280	7	...	...	111	15	5.53	0.39	...	...	0.00
M83	>	180	...	...	...	...	...	...	...	...	...	...	...	0.29
NGC 253		210	30	400	90	1310	230	3.47	1.2	0.676	0.25	4.69	2.0	1.76
NGC 1266		200	40	400	8	1320	110	20.1	12	3.25	0.14	66.0	13	0.24
Cen A		150	20	370	30	1300	220	8.97	3.2	0.396	0.089	2.12	0.87	1.76

Note. — T_1 is derived from the S(1)-S(0) lines, T_2 from the S(1), S(2), and S(3) lines, and T_3 from the S(7)-S(5) lines. Some values of T_1 are lower limits because the S(0) lines were upper limits. M_1 is derived from the S(0) line at T_1, M_2 from the S(1), S(2), or S(3) line using T_2, and M_3 from the S(5) or S(7) line and T_3. Note that the numbers in M_3 are presented as 3 orders of magnitude smaller than those in the other mass columns. See Section 4.5.5 for more explanation, and Table 4.16 for references for $\tau_{9.7}$.

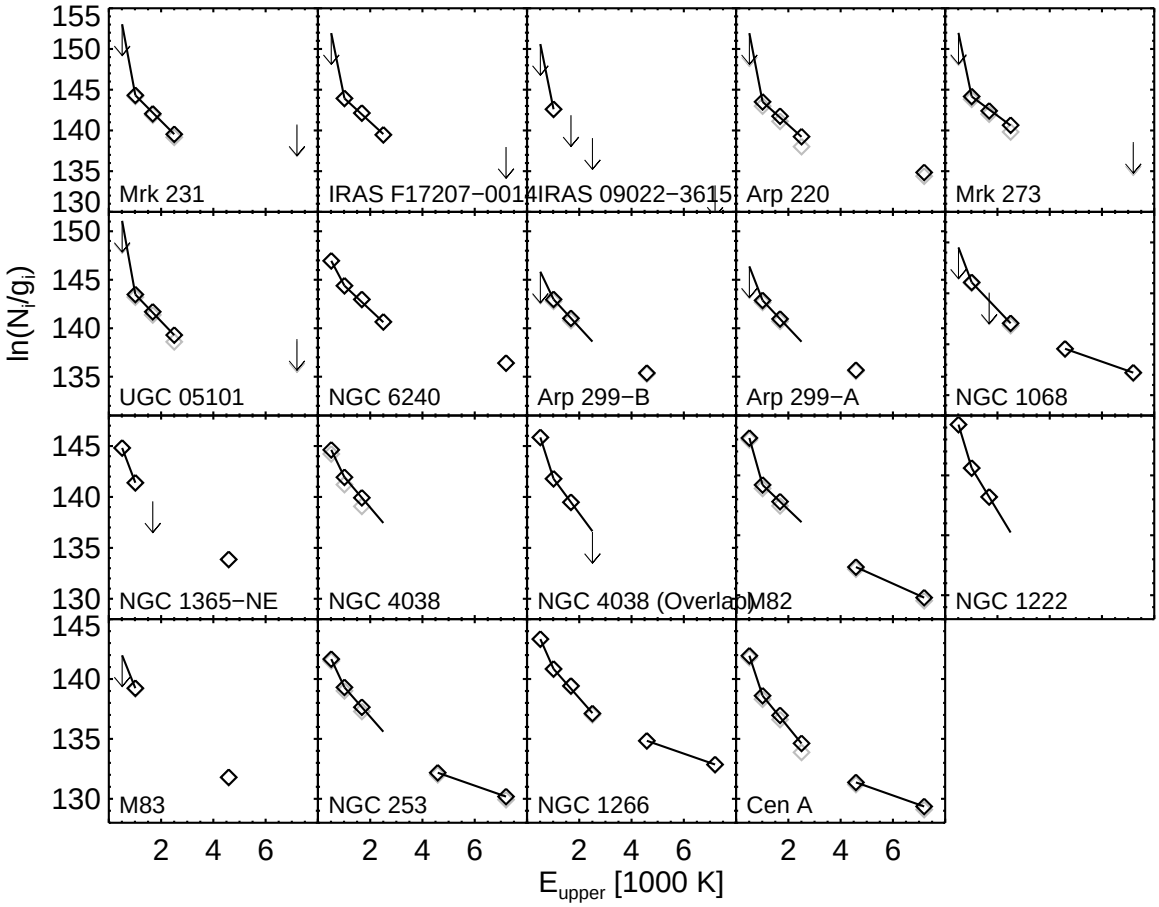

Figure 4.14 H_2 Excitation Diagrams. For each line flux available, the total number of molecules is calculated by the equations in 4.5.4. The inverse of the solid line slopes are the excitation temperatures; the S(3), S(2), and S(1) generally lie on a fairly constant line, but the higher and lower energy fluxes demonstrate a gradient in excitation temperatures. The non-extinction-corrected lines are shown in gray.

Table 4.18. [CII] Line Measurements: 10^{-16} W m^{-2}

FTS Name	[CII]	σ	% Ionized[a]	σ	% Ionized[b]	σ
Mrk 231	3.70	0.20	20.	3	35	5
IRAS F17207-0014	6.70	0.80	12	2	20.	3
IRAS 09022-3615	6.69	0.22	12	1	21	2
Arp 220	9.40	0.40	30.	7	52	10
Mrk 273	5.50	0.30	17	2	29	3
UGC 05101	5.59	0.28	26	2	44	4
NGC 6240	27.2	0.60	15	0.5	25	0.9
Arp 299-C	...	...	...	...	...	...
Arp 299-B	...	...	...	...	...	...
Arp 299-A	82.2	1.2	5.3	0.3	9.1	0.5
NGC 1068	214	1.7	20.	0.5	35	0.8
NGC 1365-SW	104	2.5	22	0.6	38	1
NGC 1365-NE	104	2.5	18	0.5	31	0.8
NGC 4038	50.2	1.3	6.7	0.3	11	0.5
NGC 4038 (Overlap)	...	...	...	...	...	...
M82	1320	4.3	8.0	0.06	14	0.1
NGC 1222	24.2	0.90	4.2	0.2	7.2	0.4
M83	181	3.5	15	0.3	25	0.6
NGC 253	499	5.2	8.7	0.5	15	0.8
NGC 1266	5.00	1.0	18	4	31	8
Cen A	295	2.1	4.2	0.05	7.2	0.09
Median			14		25	

Note. — All are from Brauher et al. [20] except UGC 05101 and IRAS 09022-3615 from Díaz-Santos et al. [41]. [NII] line fluxes were given in Table 4.5.

[a]Calculated using [CII]/[NII]ratio = 2.5 in ionized medium.

[b]Calculated using [CII]/[NII]ratio = 4.3 in ionized medium.

Chapter 5

Survey of Molecular ISM Properties of Nearby Galaxies: Discussion and Conclusions

5.1 Discussion

This survey sought to answer a variety of questions related to the molecular ISM in galaxies. The first three subsections here (Sections 5.1.1, 5.1.2, 5.1.3) address systematic effects of our modeling procedure, including aspects of two-component modeling that ought to be considered in future CO SLED modeling. The next two focus on two useful quantities derived from our data: the luminosity-to-mass conversion factor (Section 5.1.4) and gas-to-dust mass ratios (Section 5.1.5). Section 5.1.6 discusses trends in the molecular gas properties within our sample, and Section 5.1.7 specifically examines the difference in properties derived from C, C^+, and CO. Finally, Sections 5.1.8 and 5.1.9 compare the molecular gas properties to those of high-redshift SMGs and the Galactic center, respectively.

In the plots that follow, most parameters are plotted in log-log space, with a line fit presented, Log(y) = a×Log(x) + b. In the case of a slope a = 1, the relationship is simply y $\propto$ x. This is a small sample of diverse galaxies; the lines are meant to illustrate general trends, but should be interpreted with caution. In some cases, our primary interest is whether two parameters have a linear relationship or not; to robustly determine the uncertainties, we used a case re-sampling nonparametric bootstrap method. For n galaxies included in the fit, we drew n samples (allowing re-selection of the same sample) and fit a line 1000 times; the error was then the 68% interval of the probability density function of the resulting parameter fits.

5.1.1 Effects of Extinction Correction and Modeling Priors

The effects of extinction corrections for the [CI] and H_2 lines were discussed in Sections 4.5.4 and 4.5.5, respectively. Here were focus on the effects of extinction correction (Section 4.5.2.1) and modeling priors (Section 4.5.2.3) on our CO analysis. The extinction correction affected the high-J CO lines the most, increasing their fluxes more than low-J lines and thus affecting the shape of the SLED. The overall shape of the SLED is determined by the pressure, and we would therefore expect the warm component pressure to change the most.

In fact, when we conducted the same modeling procedures as in Section 4.5.2 with fluxes that were not extinction corrected, we found that the distribution of parameters were indistinguishable given the errors bars. The most noticeable difference, as predicted, was the warm pressure, which was only 0.1 dex higher when dust correction is included. The CO luminosity generally peaks at mid-J lines not as strongly affected by extinction (e.g. $J = 6 \rightarrow 5$). Even for the galaxy with the highest median optical depth at $J = 13 \rightarrow 12$, NGC 253 ($\tau_{200\,\mu\mathrm{m}} = 1.5$), the distributions were not significantly different. (We caution the reader that the uncertainty in the optical depth propagated from σ_{λ_0} and σ_β at 200 μm is quite large, and most of our galaxies have overlapping optical depth likelihood distributions, so we do not mean to imply that NGC 253 is in fact more optically thick than many of the other galaxies in the sample.)

Of the maximum mass and length priors, the length turned out to limit only a very small section of the allowed parameter space. The dynamical mass was the more restrictive prior. When modeled without the maximum mass and length priors, the marginalized parameter likelihoods for most of our galaxies were indistinguishable from modeling with the priors. This means they did not have a significant effect (i.e. the combinations of parameters violating these priors did not contribute significantly to the likelihood anyway due to poor match to the data). Only a few showed an appreciable difference: M82, Arp 220, and NGC 253. In the case of M82, removing the priors allows for a unconstrained shoulder of the cold component mass above $\sim 10^9$ $M_\odot$, but did not change the location of the mass peak around $10^{7.7}$ $M_\odot$. In Arp 220, removing the prior

increased the height of the cold component likelihood distribution relative to the sharp peak at 10^9 $M_\odot$ (Figure 4.10). For NGC 253, the (cold component) density distribution was modified as well as the mass, because a high-mass mode was associated with higher densities. Without the mass prior, densities above 10^4 cm^{-3} had a greater relative probability; as a result, higher temperatures had a lower relative probability. Without the priors, there was a noticeable shoulder of mass likelihood around $10^{9.5}$ $M_\odot$, but the large peak of the distribution was unchanged closer to 10^8 $M_\odot$.

In most cases, our use of extinction correction and mass and length priors did not significantly impact the results of the CO modeling, especially in the determination of the molecular mass, which will become important in the next section.

5.1.2 Assessment of the Simultaneous Two-Component Modeling Procedure, Compared to One-Component and Iterative Two-Component

Most previous studies of CO molecular gas properties were based on the few lines available in atmospheric windows. With three or four lines, only one component of cool molecular gas could be described with molecular excitation models such as RADEX, relying on four parameters. To place our study in context with the majority of the molecular gas literature, we first ask, "How does access to an additional 10 lines change our understanding of molecular gas excitation?" The first answer, immediately visible upon examination of the SLEDs (Figure 4.8) is that additional excitation is required to explain the high-J line fluxes. This point has already become noticeable in the past few years and was a major motivation for this study [e.g. 125, 80, 139, 161, 143, 68, 133].

The more in-depth question is: how does simultaneously modeling two components *change* our understanding of the cold component? To answer this, we also ran single-component likelihoods using only the J = 1 → 0, J = 2 → 1, and J = 3 → 2 lines, if all three were available in the literature (for 17 of our 21 pointings, those with green dashed SLEDs shown in Figure 4.8). Because we allowed multiple line measurements from the literature, our results are not necessarily as well constrained as those that rely only on one measurement of each line. We found that the luminosity of CO and thermal gas pressure in the cold component was overestimated when modeled alone by an average

of 0.5 and 0.6 dex, respectively. No effect on the temperature and density could be determined, because the two parameters were not as well constrained as the pressure (this is a consequence of their degeneracy in excitation modeling and not specific to the methods compared here). A good example of this is Mrk 273, where the shape of the cold SLED when modeled alone (green, Figure 4.8) must account for all flux in the first three lines, whereas when modeled with a warm component (blue and red), the warm component accounts for some flux in the $J = 3 \rightarrow 2$ line. Certainly, there are exceptions to this statement visible in Figure 4.8, such as M82. In all cases, modeling only the cold CO will severely underestimate the total CO luminosity, because the majority of the power is in the high-J lines. The parameter that was usually correctly determined is the CO mass, because it is most highly dependent on the J = 0, 1, and 2 population levels. This point will become very important when discussing luminosity to mass conversion factors in Section 5.1.4.

Having compared the difference between one and two components, it is also useful to examine the effect that simultaneous modeling of an 8-dimensional parameter space has compared to an iterative modeling approach, which has been used in the past [e.g. 80, 154]. This iterative modeling involves first modeling high-J lines alone, above some cutoff such as the $J = 6 \rightarrow 5$ line. The low-J line fluxes predicted by the best-fit model are then subtracted from the measured low-J line fluxes, and the remainder is modeled as the cold component. One can continue alternating between warm and cool components until the two solutions converge. This approach has three major issues. First, as discussed near the beginning of Section 4.5, most likelihood analysis codes suitable for a large number of parameters are not well designed to refine the best-fit solution, which can differ significantly from the median parameters. This means that the selection of the model flux to subtract from the measured fluxes for modeling the second component is not representative of the probability distribution function. Second, the choice of where to break the SLED apart for the two component modeling is somewhat arbitrary. Upon examining the SLEDs in Figure 4.8, it is clear that all lines above $J = 10 \rightarrow 9$ are entirely emitted from the warm component, but these lines are often fainter (and will have higher uncertainties), and one would ideally model more lines for determining the 4 parameters of the warm component. However, one could have a situation where

the best-fit warm component describes the emission down to $J = 3 \rightarrow 2$ (e.g. M83, Arp 299-A in Figure 4.8), or the warm component may drop off significantly below $J = 7 \rightarrow 6$ (e.g. NGC 253, Arp 220). By picking one cut-off line, an arbitrary prior, or restriction of parameter space, is introduced. Schirm et al. [154] illustrated the differences that can be caused by choosing different lines to break the spectrum; they found the statistical ranges of the parameters found for three different choices do not vary significantly in the case of the Antennae.

Third, as a consequence of the previous two drawbacks, iterative modeling uncouples the uncertainties and covariance of the warm and cool components, which falsely lifts some degeneracies in the analysis. For example, we found higher uncertainties in the mass of the warm component than the aforementioned Schirm et al. [154] paper. We believe that our parameter estimates and uncertainties are a more accurate description of a two-component model, and that future two-component modeling should allow for covariance between the components' parameters, as we do here. Specific comparisons of the results from iterative vs. simultaneous modeling are given in Appendix B for M82, Arp 220, and NGC 4038.

5.1.3 Assessment of the Simultaneous Two-Component Modeling Procedure, Compared to Three or More Components

Having examined the differences between 1 vs. 2 component modeling, and simultaneous vs. iterative modeling, we now address the question of why we modeled 2 components, and not 3 or more. The simplest answer is that the SLEDs were statistically well described by 8 parameters and hence there is no justification for adding a more complicated model. However, a more in-depth investigation is still interesting, especially given our understanding of the more complicated physical situation we are attempting to describe via a statistical investigation of these 8 parameters. We recognize that we are really measuring the sum of the emission from a wide distribution of molecular cloud properties. Discussing "cool" and "warm" gas is the minimum distinction we can make given the data, and as we show here, also the maximum.

We compared our CO results to the H_2 temperatures and masses presented in Table 4.17.

We first note that H_2 rotational lines are not sensitive to the coldest molecular gas; the J=2 state (upper level of S(0) transition) is 510 K above ground. Because most of the molecular mass resides at much cooler temperatures, the mass derived from the S(0) line will be an underestimate of the total molecular gas mass. The H_2 excitation ladders (Figure 4.14) clearly indicate a gradient in excitation temperatures. Higher lines of H_2 indicate higher temperatures and lower masses. In general, Table 4.17 shows that the mass in the few hundred K component (T_2) is 1-20% of that in the colder gas traced by S(0). The S(5) and S(7) lines, which trace > 1000 K gas, come from orders of magnitude smaller gas masses. In our two-component SLED modeling, we found 10% of the mass in very warm gas, but these two components are presumably sums over a range of gas conditions.

We therefore sought to investigate if we could model the temperature/mass components we see in H_2 (now referred to as Components I, II, and III) with the CO SLEDs. We used the same method as described in 4.5.2 (now requiring 12 free parameters) for two well-defined galaxy SLEDs (Arp 220 and M82). We applied some additional constraints: $T_{\rm I} < T_{\rm II} < T_{\rm III}$, $M_{\rm I} > M_{\rm II} > M_{\rm III}$, and we restricted the temperature ranges for each component, such that $0.5/2/2.3 < \mathrm{Log}(T_{\rm I}/T_{\rm II}/T_{\rm III}) < 2.3/3/3.5$. The same priors as previously used were applied for optical depths, maximum length of any one component, and maximum total mass (Section 4.5.2.3).

The resultant best fits were nearly identical with the 2-component fits, with Component I acting as the cool component and Component II as the warm. By this we mean that the pressure, luminosity, and mass distributions were significantly overlapping with our previous results (though discernible). We illustrate this in Appendix B for the case of Arp 220. Component III had negligible mass, negligible contribution to the total luminosity, and was poorly constrained otherwise. In other words, the CO SLEDs are not sensitive to the extremely low mass component derived from S(7)-S(5) hydrogen lines, *absent additional strict prior constraints on the parameter space*. Though one could exactly fix the mass and temperatures of each component to match that of hydrogen, we have no reason to believe that there is a one-to-one correspondence between the CO and H_2 components, in addition to doubts about the LTE approximation for the S(7) and S(5) lines, and

the knowledge that the H_2 cannot probe the coolest gas anyway. More importantly, fixing the mass of Component III orders of magnitude lower than the other components (to match H_2) would produce the same result: a SLED described by the other two components, where the temperature of Component II would simply move up or down (allowable due to the $n - T$ degeneracy) based on the imposed constraints to preserve the same pressure. This was our best-fit result *without* requiring that the M_{III} be orders of magnitude lower than M_{II}, only that it be lower. The best-fit SLED was statistically indistinguishable from the best-fit two-component SLED (same total χ^2), because the third component contributed negligible flux to each line.

We ran the 3-component fit again, this time *not* requiring that $M_{\rm III}$ be lower than the other masses (only that the sum be less than the dynamical mass prior, as before). We still found a two-component fit, with the remaining component contributing negligible mass and luminosity. The two components were still high-mass/low-pressure and low-mass/high-pressure, but this time, their comparable roles to the original two component fit were switched. Component III (the highest temperature one) shared the same low-pressure, high-mass likelihood distributions as our "cool" component model in the two-component fit. Likewise, Component I (the lowest temperature) shared the same high-pressure, lower-mass distributions as the "warm" component. They accomplished this "switch" in temperatures with different density distributions; recall that the temperature and density are inversely correlated. This illustrates the important role of the priors (and allowed parameter space): *the density distribution will be highly affected by priors placed on the temperature, and vice versa*. We know the low-pressure, high-mass component is actually cooler in temperature because of prior knowledge, it is *not* inherent to the statistical fitting. This is a fundamental basis of Bayesian analysis: more knowledge means better constraints. Furthermore, this experiment illustrates the robustness of our two-component solution.

The take-away message is that the CO SLEDs from $J = 1 \rightarrow 0$ to $J = 13 \rightarrow 12$ could only be described by 3 non-negligible temperature components if artificial constraints, not motivated by our current knowledge of CO emission, were imposed. The high-mass/low-pressure and low-mass/high-pressure components arise out of the fitting even if constraints on e.g. the temperature

or mass are modified. It is very likely that there are a continuum of conditions present, but more than two dominant components are not required to fit the SLEDs. In Section 5.1.8, we will discuss the observational evidence for such components in the giant molecular cloud Sgr B2. Numerical simulations of galaxies, coupled with radiative transfer, could potentially deepen our understanding of how a gradient of excitation conditions adds up to produce the total emission we can measure [e.g. 115]. Numerical models which distinguish multiple components could provide useful priors for modeling CO SLEDs; one cannot make those distinctions *from the modeling* of CO SLEDs.

The intention of this and the previous subsection was to discuss the place of two-component modeling in context with a field which has, due to atmospheric absorption, historically only had access to the measured emission from the lowest temperature component of molecular gas. We showed that masses derived from LVG models of the cool gas alone remain valid, but that the pressure (shape of the SLED extrapolated to higher-J values) will be overestimated by 0.6 dex. Simultaneous, as opposed to iterative, modeling more accurately characterizes the molecular gas properties and their uncertainties. Finally, though we recognize that our two-component models are simply approximations to describe the bulk emission of molecular gas in galaxies, they are statistically indiscernible from three-component models, given reasonable constraints.

5.1.4 Luminosity to Mass Conversion Factors

It is common to use an empirically measured value to convert from CO J=1→0 luminosity to total molecular mass. For Milky Way clouds, this is the "X-factor" in units of cm^{-2} (K km s^{-1}): $X(\mathrm{CO}) = N(\mathrm{H_2})/I(\mathrm{CO})$, where $I(\mathrm{CO}) = \int T dv$. For extragalactic work, one cannot resolve individual clouds, but an ensemble of emitting clouds would have a similar proportionality known as $\alpha_{\mathrm{CO}} = M/L'$ [$\mathrm{M}_\odot$(K km s^{-1} $\mathrm{pc}^2)^{-1}$] [42]. For simplicity, we do not include the units of α_{CO} and $X(\mathrm{CO})$ from now on. L' is the area-integrated source brightness temperature, $I(\mathrm{CO})$ times the area on the sky in pc^2. If neither (or both) factors take helium into account, then $X(\mathrm{CO}) = 6.6 \times 10^{19}\alpha$ (in the respective units given above). However, for an X-factor in terms of $N_{\mathrm{H_2}}$ (standard) and masses in total molecular gas (including He), the conversion is $X(\mathrm{CO}) = 4.5 \times 10^{19}\alpha$ due to the

factor of 1.4 in our Equation 4.3.

Bolatto et al. [16] discussed the theoretical basis for the CO-to-H_2 conversion and presented a comprehensive summary of the techniques and results of its measurement for Galactic and extra-galactic molecular clouds. A typical $X(\mathrm{CO})$ for the disk of the Milky Way is 2×10^{20} ($\alpha_{\mathrm{CO}} \approx 4$), but for the Galactic center, $X(\mathrm{CO})$ is 3-10 times lower. Normal spiral galaxies have values close to that of the Milky Way disk, whereas starburst galaxies and (U)LIRGS have values $X(\mathrm{CO}) < 1 \times 10^{20}$ ($\alpha_{\mathrm{CO}} < 2$). For these highly excited galaxies, the lower $X(\mathrm{CO})$ values are often attributed to higher gas temperatures and large velocity dispersions [in excess of self-gravity, see simulations by 116]. Additionally, if the CO emission is extended and not confined in self-gravitating molecular clouds, $X(\mathrm{CO})$ would also be lower, a condition that is likely present for ULIRGS [16]. Other factors may influence the CO-to-H_2 conversion factor, such as metallicity and gas-to-dust mass ratio. Lower metallicity or gas/dust ratios will decrease the depth of the CO-emitting layer in molecular clouds, decreasing the CO intensity and increasing $X(\mathrm{CO})$. Additionally, $X(\mathrm{CO})$ is only sensitive to CO-bright gas; we may be missing CO-faint H_2 reservoirs of H_2 where C^+ or C is the dominant form of carbon, instead of CO (see further discussion in Section 5.1.7). We will first present our derived values of α_{CO} and then discuss the systematic effects that could affect these values [see also 100].

The masses and luminosities used to derive α_{CO} are plotted in Figure 5.1, and resulting values in Table 5.1. When we collected multiple measurements of the $\mathrm{J}=1\rightarrow0$ line, we used a weighted average (after converting all to a $43.5''$ beam following Section 4.4.2). We used the total CO mass (cool and warm components), but point out that the conclusions are unchanged if only using cold CO mass, as the error is dominated by the error of the cold CO mass (because the warm mass is a relatively small fraction of the total). As discussed in the previous section, the mass estimate using only the first three lines of CO should be the same as our estimate derived from the entire SLED. This means we do not differ significantly from previous studies also using radiative transfer models to determine mass for this conversion factor.

The dotted lines in Figure 5.1 clearly demonstrate that we find $\alpha_{\mathrm{CO}} < 10$ in all cases, and in fact $\alpha_{\mathrm{CO}} \leq 1$ in all but two cases (both with $\alpha_{\mathrm{CO}} \approx 3$), Cen A and NGC 1365-NE. NGC 1365-

Table 5.1. Derived Values of α_{CO} [$M_\odot$(K km s^{-1} pc^2)$^{-1}$]

FTS Name	Log(α_{CO})	σ_{Log}	α_{CO}	σ
Mrk 231	-0.6	0.1	0.3	0.09
IRAS F17207-0014	0.05	0.4	1	1
IRAS 09022-3615	...	...	...	...
Arp 220	-0.3	0.4	0.6	0.5
Mrk 273	-0.3	0.4	0.5	0.5
UGC 05101	-0.4	0.4	0.4	0.3
NGC 6240	-0.5	0.2	0.3	0.1
Arp 299-C	-0.2	0.2	0.6	0.3
Arp 299-B	-0.3	0.3	0.5	0.4
Arp 299-A	-0.3	0.4	0.5	0.5
NGC 1068	-0.5	0.4	0.4	0.3
NGC 1365-SW	-0.1	0.4	0.8	0.7
NGC 1365-NE	0.5	0.2	3	1
NGC 4038	-0.2	0.3	0.6	0.4
NGC 4038 (Overlap)	-0.3	0.4	0.5	0.5
M82	-0.4	0.3	0.4	0.3
NGC 1222	-0.2	0.4	0.6	0.6
M83	-0.2	0.4	0.6	0.6
NGC 253	-0.05	0.4	0.9	0.8
NGC 1266	-0.2	0.4	0.6	0.5
Cen A	0.5	0.4	3	3
Average	-0.2	0.3	0.3	1.1

Note. — See Section 5.1.4. IRAS 09022-3615 is not included because the cold gas mass was not modeled. Averages do not include the following duplicate pointings: Arp 299-B, Arp 299-C, NGC 4038, NGC 1365-SW

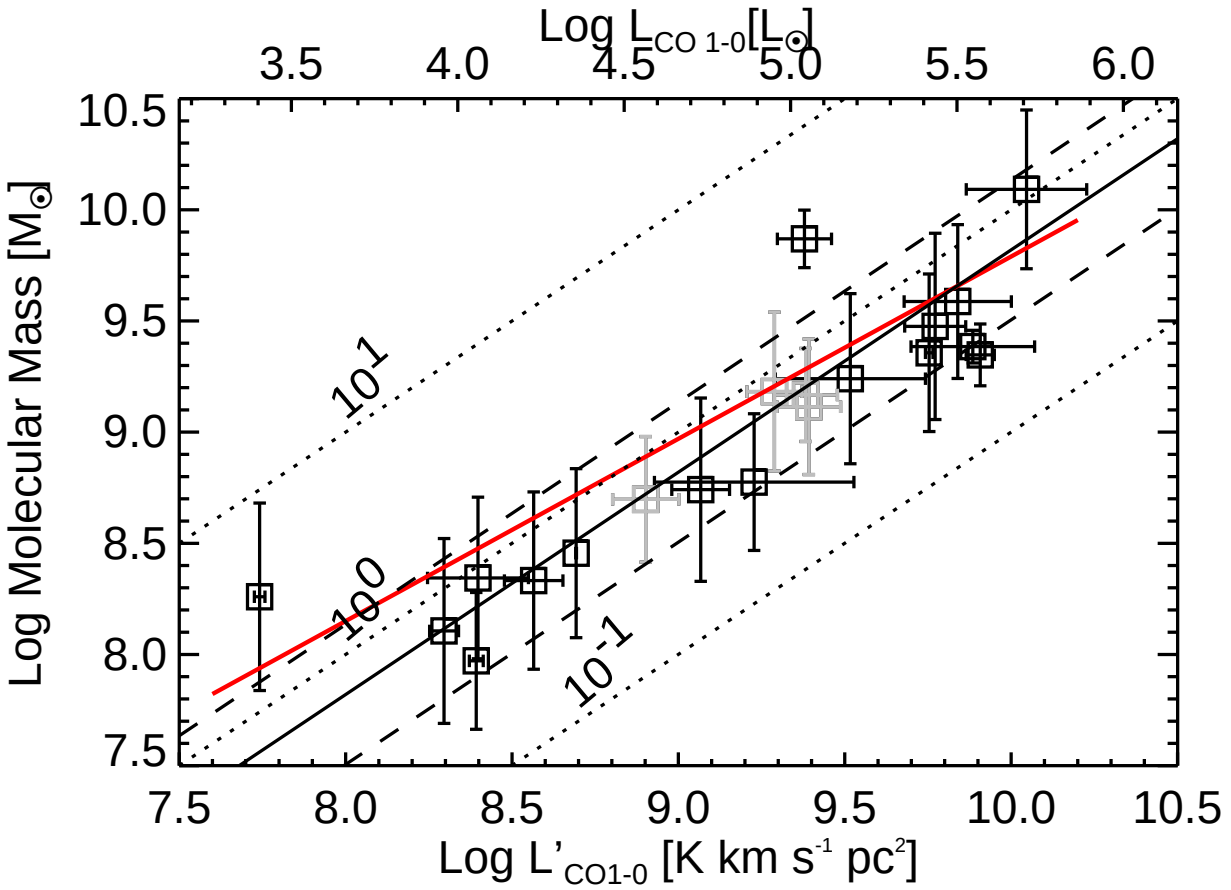

Figure 5.1 CO-to-H_2 Conversion Factor, α_{CO}. See Section 5.1.4. The x-axis is luminosity of CO J=1→0, averaged if multiple lines were available. The y-axis is the total molecular mas from the CO modeling. The dotted diagonal lines represent the slopes corresponding to α_{CO} =10, 1, and 0.1. The solid line is our best-fit ratio, excluding the gray duplicate galaxy points, Log(α_{CO}) = -0.2 ±0.3. Dashed lines indicate the ±1σ lines. Linearly this corresponds to $\alpha_{CO} = 0.7 \pm 0.5$. The solid red line is out best-fit when allowing for a nonlinear slope, $M = 40(L')^{0.82}$, excluding NGC 6240. Gray points are duplicate galaxy pointings excluded from line fitting.

SW, however, shows $\alpha_{\rm CO} = 0.8$, and we would not expect the two to be dramatically different (or particularly independent, given their close separation relative to the FTS beam size, see Appendix B). The discrepancy is due to the higher mass found for NGC 1365-NE. Cen A is often an outlier in this sample; its lower gas excitation and lower mass would in fact lead us to expect a higher $\alpha_{\rm CO}$ for reasons described below. Our derived values match well with those in the literature as summarized by Bolatto et al. [16], though generally on the lower end of ranges given, e.g. NGC 1068 [129], NGC 4038 [198], Arp 299 [158], Mrk 231, NGC 6240 [23]. We are somewhat lower for M82 [0.4 ± 0.3 vs. $1.2 - 2.4$ 184], NGC 4038 Overlap [0.5 ± 0.5 vs. $1.2 - 2.4$ 198], and Arp 220 [0.6 ± 0.5 vs. 2.4 156].

Even with the two outliers, our best-fit $\alpha_{\rm CO}$ is approximately 0.6 ± 0.5 ($X({\rm CO}) = 0.25 \pm 0.21 \times 10^{20}$). This is on the low, but overlapping end of the range of estimates by Yao et al. [193] for starburst galaxies ($X({\rm CO}) = 0.3 \pm 0.8 \times 10^{20}$) and Papadopoulos et al. [131] for LIRGS ($X({\rm CO}) = 0.3 \times 10^{20}$). If we instead fit a line to Figure 5.1, allow for slope not equal to one, we find $M = 2200(L')^{0.62}$, which corresponds to $\alpha_{\rm CO}$ from 2.0 to 0.4 over the approximate range of $L' = 10^8 - 10^{10}$ (K km s^{-1} pc^2). The bootstrapped estimate of the slope is 0.67 ± 0.20. This fit is largely fixed by the very low mass error bars on NGC 6240; excluding this point, the linear fit is $M = 40(L')^{0.82}$, $\alpha_{\rm CO}$ from $1.4 - 0.6$. Here the bootstrapped slope is 0.80 ± 0.20, so we cannot rule out a linear relationship.

A variety of systematic effects could change our derived $\alpha_{\rm CO}$. First, using a factor of 1.36 (correcting for helium only, as is often done), rather than 1.4 would lower $\alpha_{\rm CO}$ by only a few percent. A different value of the relative abundance of CO to H_2 (*not* the same as $X({\rm CO})$ in this section) would also modify our mass calculation. We use 3×10^{-4}; another commonly used value, 1×10^{-4}, would lower $\alpha_{\rm CO}$ by a factor of 3.

We confirm that a conversion factor $\alpha_{\rm CO} < 1$ is appropriate for CO J$=1\rightarrow0$ emission from LIRGs and other submillimeter-bright local galaxies. This factor may not scale linearly with CO J$=1\rightarrow0$ luminosity. We attempted to discern a similar relationship between the CO J$=6\rightarrow5$ emission and the warm molecular mass, but did not find one. This is not particularly surprising;

the theoretical basis for $\alpha_{\rm CO}$ relies on CO J=1→0 being thermalized and $T_{\rm kinetic}$ being the same in all sources [100]. We find very subthermal excitation in the J=6→5 line ($T_{\rm excitation} \ll T_{\rm kinetic}$). The best-fit excitation temperatures for the CO J = 6 → 5 line range from 3-30 K (with one, IRAS 09022-3615 at 140 K), while the kinetic temperatures are 200-3000 K, and the two are not correlated. Even if the J = 6 → 5 line were thermalized, the warm gas temperature varies in a non-systematic way from galaxy to galaxy. Thus, CO J = 6 → 5 is a poor tracer of mass (but a good tracer of warm component luminosity, as we show in Section 5.1.6).

5.1.5 Gas-to-Dust Mass Ratios

In Figure 5.2, we show the dust mass vs. the molecular gas mass (for both warm and cold components). For comparison, we also show the 1:1, 10:1, and 100:1 gas:dust mass ratios with dotted lines. Our mean results (for the cold component of CO) lie between the 10:1 and 100:1 lines; the blue best-fit line varies from a ratio of 76 at the lowest end to 42 at the higher end, but the uncertainty in the slope is high enough that we cannot rule out a constant ratio. (Recall that the warm mass is generally only 10% of the contribution to the total molecular gas, but that our conclusions utilizing the cold component below are uncertain by a larger factor.)

In a survey of 14 galaxies with the Submillimeter Array (half of which are in this sample), the average gas/dust ratio in the center of galaxies was found to be about 120 ± 28, though with large variation [187, W08]. The gas/dust mass ratios derived from total galaxy luminosities (comparable to this work) showed even greater variation, with ratios from 29 to 725. Our ratios vary from about 10 to 120, with considerable error bars, but we do not find ratios in the hundreds. Our estimates for the dust and gas mass are both calculated differently than in W08, where the gas mass was calculated from the CO J = 3 → 2 flux, assuming an area-integrated luminosity ratio of (J = 3 → 2/J = 1 → 0) of 0.5 and α = 0.8 (recall Section 5.1.4). For all our available (J=3→2/J=1→0) line ratios, we find a median of 0.7 and a standard deviation of 0.4. The dust mass in W08 was calculated by scaling the 850 or 800 μm fluxes to 880 μm using $\beta = 1.5 \pm 0.5$ and $\kappa = 0.9$ cm^2 g^{-1}. When our ratios of gas/dust are different, half the time it is due to the dust

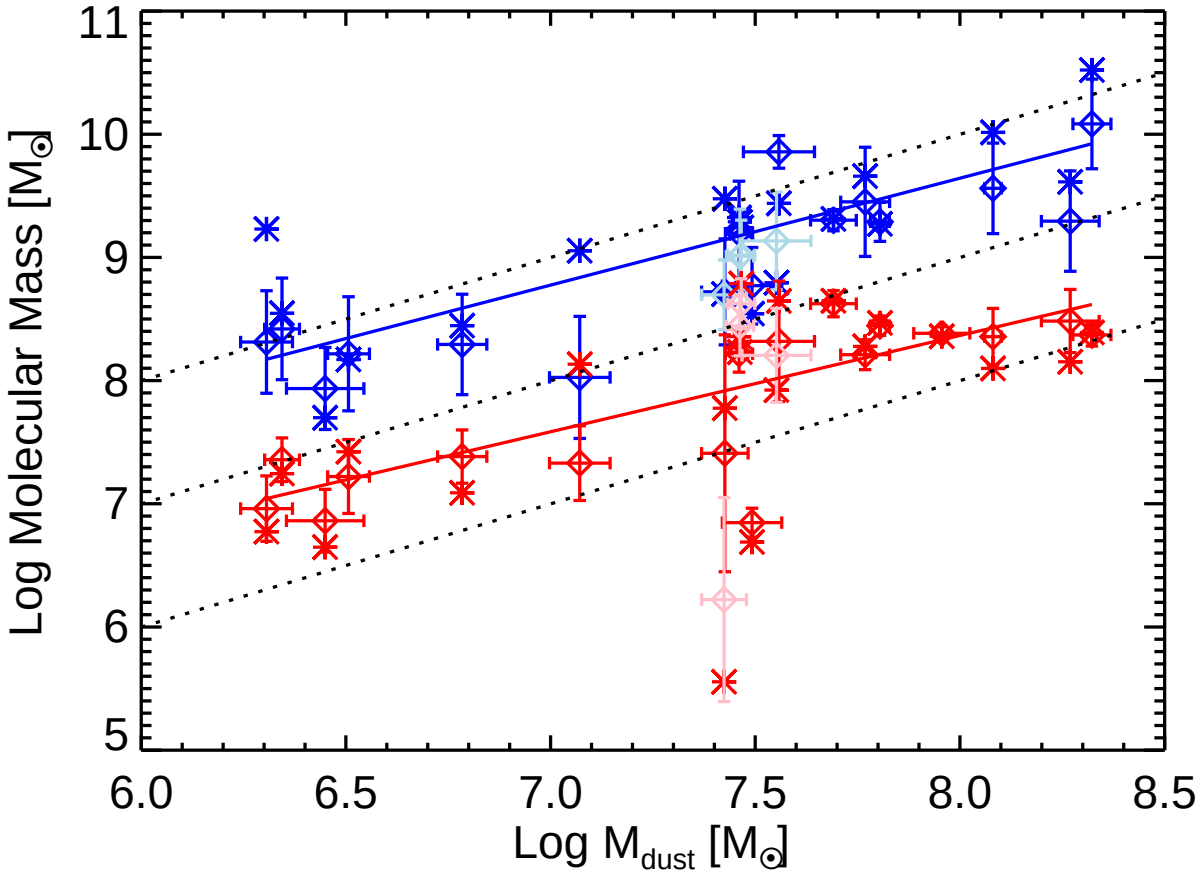

Figure 5.2 Gas vs. Dust Mass. $\mathrm{Log}(M_{H_2,cool}) = (0.87 \pm 0.1)\mathrm{Log}(M_d) + (2.7 \pm 1)$, $\mathrm{Log}(M_{H_2,warm}) = (0.78 \pm 0.07)\mathrm{Log}(M_d) + (2.1 \pm 0.5)$. The dotted lines correspond, from bottom to top, to the 1:1, 10:1, and 100:1 ratios. Diamonds are medians with one sigma error bars, asterisks are best-fit, red/blue represents warm/cool components, and lighter colored points are duplicate galaxy pointings excluded from line fitting.

mass being very different, and the other half of the time, the gas mass. Our molecular masses are determined by non-LTE modeling, and our dust masses from full SED modeling; we believe these methods to be more robust, and thus rule out gas/dust masses much greater than 120, our largest ratio. This is lower than that of the local region of the Milky Way [140, 45].

Rémy-Ruyer et al. [140] found that metallicity was the most important parameter in determining gas/dust mass ratios. According to their broken power law model, gas/dust ratios of 1, 10, and 100 correspond to metallicities of 2.2, 1.2, and 0.2 dex above solar. Gas/dust ratios above ~ 160 indicate sub-solar metallicity. Our ratios, ranging from 76 to 42, would correspond to metallicities of 0.3 to 0.6 dex above solar, increasing with far-infrared luminosity (and proportionally, star formation rate). Their relationship (which they note is derived from data with considerable scatter), and our data points, are not sufficient to determine the metallicity of individual galaxies with precision.

Tremonti & Heckman [169] established a correlation between stellar mass and metallicity for 53,000 galaxies from the Sloan Digital Sky Survey; using this relation for the stellar masses we find from MAGPHYS (Table 4.14), we would expect from 0 to 0.5 dex above solar, generally around 0.4. However, Rupke et al. [148] found that many (U)LIRGs have lower metallicities than expected from the typical mass-metallicity curve. This is attributed to radial inflow of gas into the galactic nuclei, where much of the star formation occurs and molecular emission originates. Without an independent estimate of metallicity, we cannot present our gas/dust ratios as diagnostic, but they are consistent with the literature, and our methods for determining gas and dust masses are more robust than those often used elsewhere.

5.1.6 Molecular Gas Properties in Context: Comparisons Among Galaxies

An examination of the SLED shapes in Figure 4.5 shows the variety of excitation conditions present in our sample. Some have bright mid-J excitation but turn over at high-J (e.g. M82, NGC 253). Others remain somewhat flat at high-J (e.g. Mrk 273, Mrk 231). On one extreme end, the CO $J=10\rightarrow9$ luminosity of NGC 6240 is over 240 times that of $J=1\rightarrow0$, while for Cen A, the

ratio is less than 6.

Having derived a variety of molecular gas properties for the warm and cool components (most reliably luminosity, pressure, and mass), we now examine which of those properties are shared among the sample and which vary with, for example, galaxy $L_{\rm FIR}$. To examine these relationships, we compared each likelihood parameter against the $L_{\rm FIR}$ derived from the dust modeling. No discernible relationships were found for temperature or density, but pressure is discussed below.

The warm and cold component CO luminosities and masses, perhaps not surprisingly, are proportional to $L_{\rm FIR}$ (Figures 5.3 and 5.4); massive/luminous galaxies tend to be more luminous across the electromagnetic spectrum. To determine if this were the only relation we were observing, we also examined the slope of the CO luminosity vs. mass for the cold (warm) component, finding a slope of 0.8 ± 0.3 (1.3 ± 0.2), consistent with unity. We also looked at the CO luminosity per unit mass for each component vs. $L_{\rm FIR}$, and found a slope of 0.4 ± 0.2 for the cold component, consistent with zero. For the warm component, we 0.3 ± 0.1, which may imply a non-zero relationship; that is, that the ratio of CO luminosity per mass in the warm component increases slightly with increasing $L_{\rm FIR}$. Note that in the two aforementioned figures, the cold and warm components are plotted separately; the *total* mass/luminosity is dominated by the cool/warm components, respectively. Given the large uncertainties in the slopes, we cannot discern a different relationship between mass (or luminosity) and $L_{\rm FIR}$ for the warm and cold components. The total CO luminosity is about 4 $\times 10^{-4}$ $L_{\rm FIR}$ (Figure 5.3). The luminosity in only the cold component is (2.3 - 5) $\times 10^{-5}$ $L_{\rm FIR}$. The total CO luminosity is also well correlated with the CO J$=6\rightarrow5$ line luminosity (Figure 5.5).

In Figure 4.12, we show histograms of the warm and cool component pressures in red and blue, respectively. We also plot the pressure histogram for molecular cloud clumps derived from the densities measured from the Bolocam Galactic Plane Survey (Ellsworth-Bowers et al., in prep), assuming a temperature of 10 K (solid line) or 30 K (dashed line). In addition to the temperature dependence, the BGPS distributions in Figure 4.12 also depend (linearly) on the dust opacity used to calculate the clump mass and density [122]. The warm component clearly has a higher pressure, independent of those assumptions, meaning it is not like most Galactic molecular clumps (though

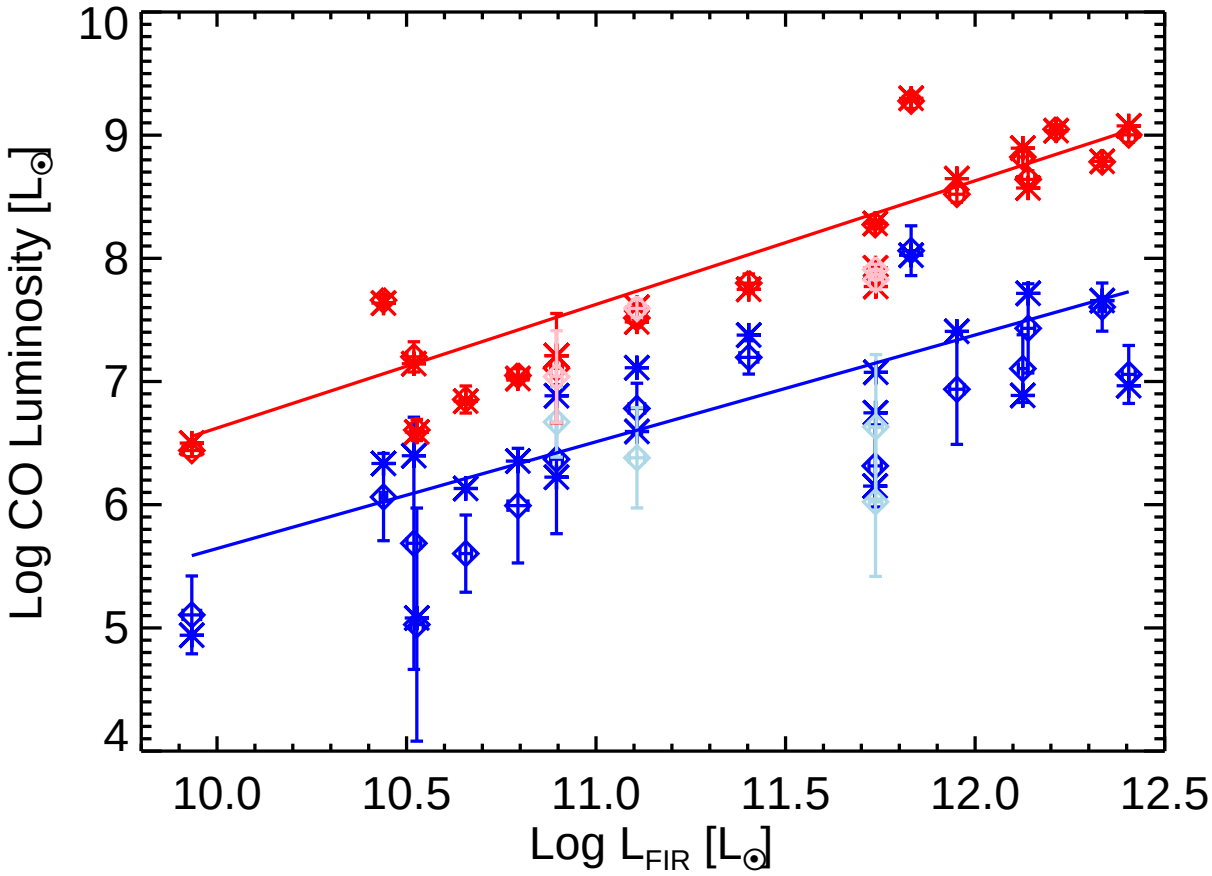

Figure 5.3 CO modeling likelihood results vs. $L_{\rm FIR}$: luminosity. $\mathrm{Log}(L_{CO,cool}) = (0.87 \pm 0.2)\mathrm{Log}(L_{FIR}) + (-3.0 \pm 2)$, $\mathrm{Log}(L_{CO,warm}) = (1.0 \pm 0.12)\mathrm{Log}(L_{FIR}) + (-3.4 \pm 2)$. Diamonds are medians with one sigma error bars, asterisks are best-fit, red/blue represents warm/cool components, and lighter colored points are duplicate galaxy pointings excluded from line fitting.

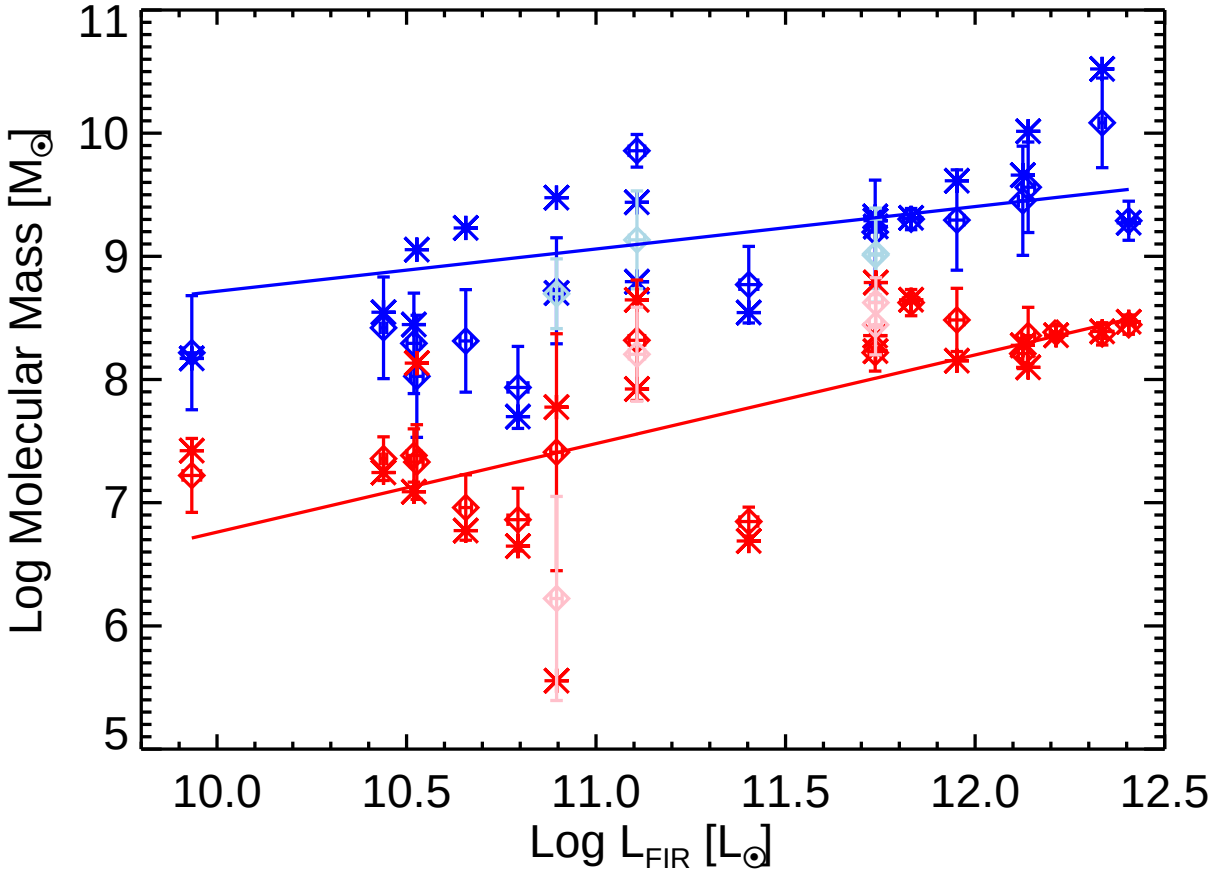

Figure 5.4 CO modeling likelihood results vs. $L_{\rm FIR}$: mass. $\mathrm{Log}(M_{H_2,cool}) = (0.34{\pm}0.3)\mathrm{Log}(L_{FIR}){+}$ (5.3 ± 4), $\mathrm{Log}(M_{H_2,warm}) = (0.70 \pm 0.1)\mathrm{Log}(L_{FIR}) + (-0.4 \pm 1.6)$. Diamonds are medians with one sigma error bars, asterisks are best-fit, red/blue represents warm/cool components, and lighter colored points are duplicate galaxy pointings excluded from line fitting.

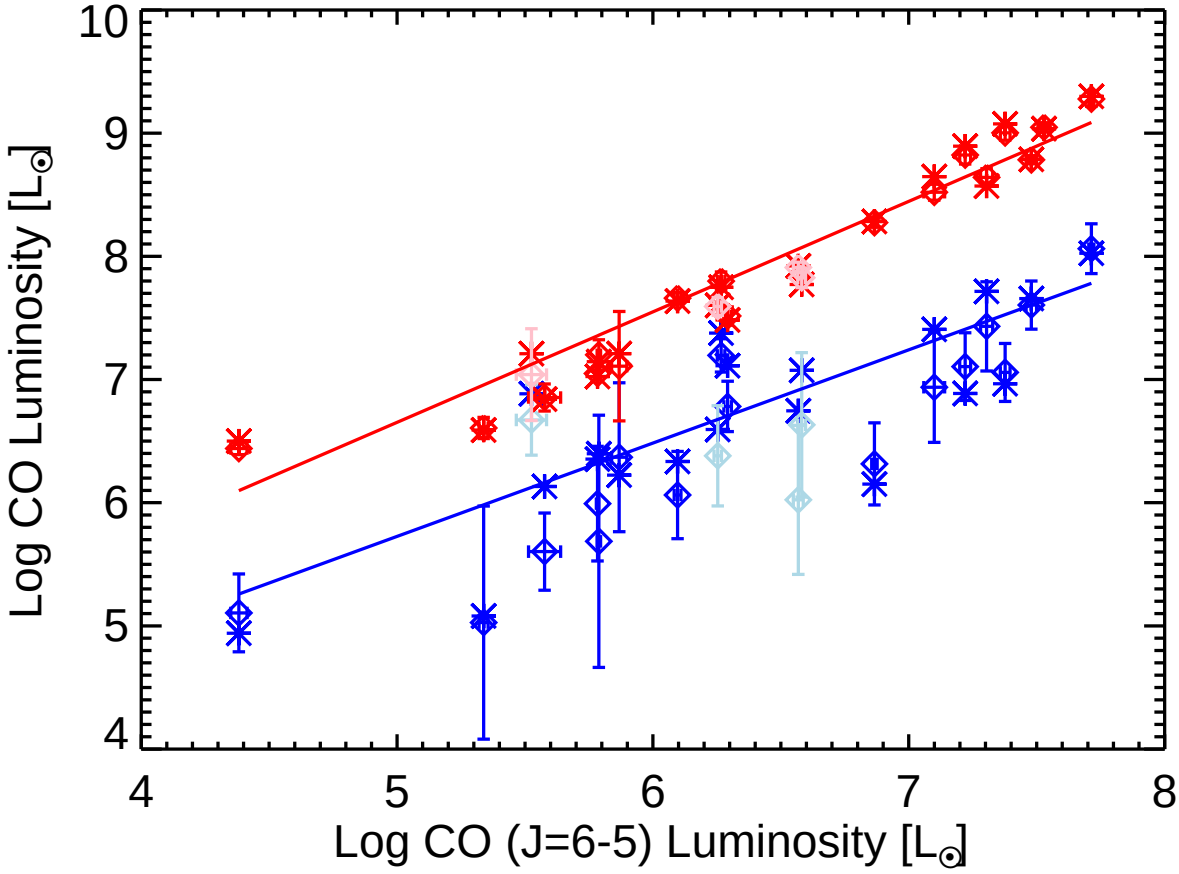

Figure 5.5 CO modeling likelihood results vs. $L_{CO_{6-5}}$: luminosity $\mathrm{Log}(L_{CO,cool}) = (0.76 \pm 0.13)\mathrm{Log}(L_{FIR}) + (1.9 \pm 1)$, $\mathrm{Log}(L_{CO,warm}) = (0.90 \pm 0.10)\mathrm{Log}(L_{FIR}) + (2.2 \pm 1)$. Diamonds are medians with one sigma error bars, asterisks are best-fit, red/blue represents warm/cool components, and lighter colored points are duplicate galaxy pointings excluded from line fitting.

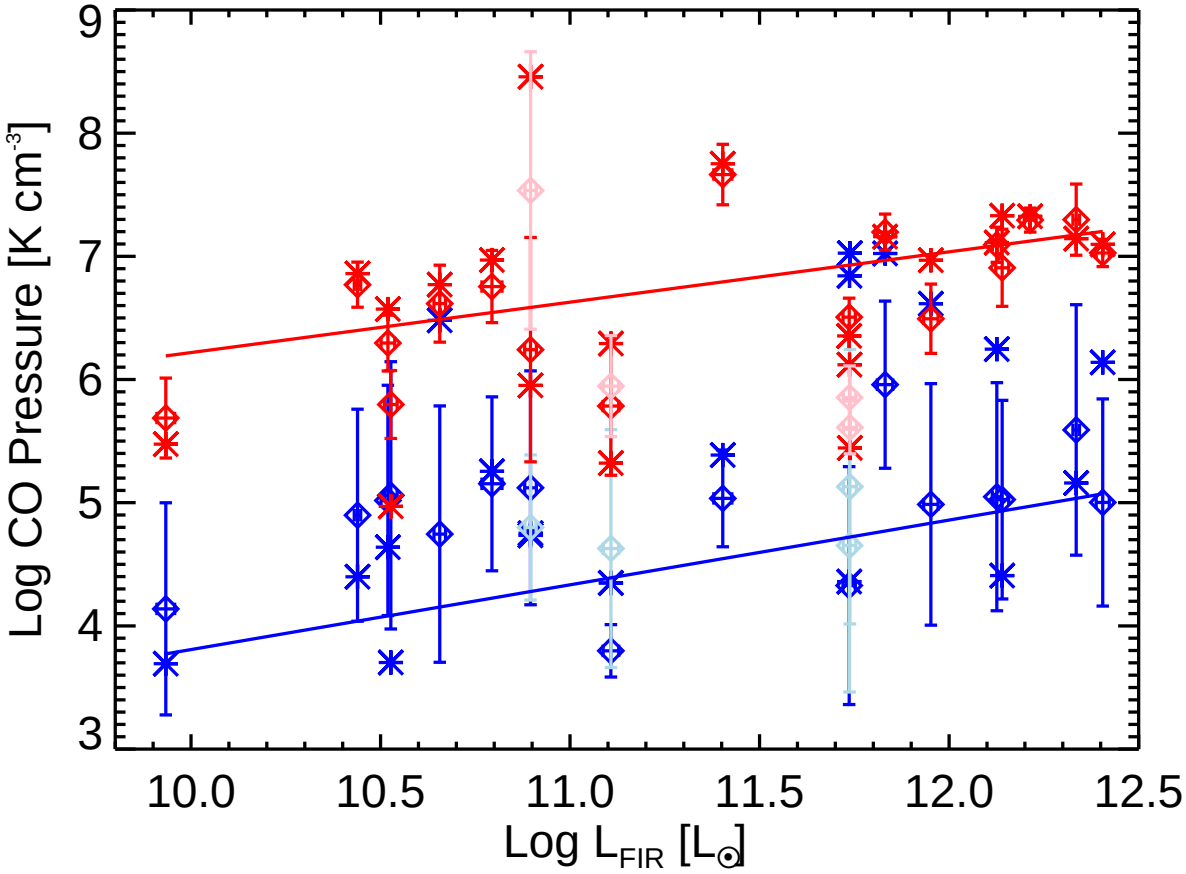

Figure 5.6 CO modeling likelihood results vs. $L_{\rm FIR}$: pressure. $\mathrm{Log}(P_{cool}) = (0.5 \pm 0.3)\mathrm{Log}(L_{FIR}) + (-1.4 \pm 3.4)$, $\mathrm{Log}(P_{warm}) = (0.4 \pm 0.1)\mathrm{Log}(L_{FIR}) + (2.1 \pm 1.4)$. Diamonds are medians with one sigma error bars, asterisks are best-fit, red/blue represents warm/cool components, and lighter colored points are duplicate galaxy pointings excluded from line fitting.

see the comparisons to Sgr B2 and Sgr A* in Section 5.1.8)

The bulk of the molecular mass in the Galaxy is in lower pressure ($\sim 10^4$ K cm^{-3}) clouds, not clumps. Were we to be simply "counting" Galactic-type giant molecular clouds in these galaxies, we would expect the cold CO pressures to be similar; instead, ours are higher. (Recall from Section 5.1.2, our cold pressure is 0.5 dex *lower* than if we modeled this component alone; simultaneous modeling is *not* the reason our pressure is *higher* than Galactic.) This means that the bulk of the molecular gas in this sample of galaxies is more energetic (higher thermal pressure, and hence greater thermal energy per unit volume) than the bulk of molecular gas in our Galaxy. Additionally, the bulk excitation may be similar to that of denser Galactic clumps, but this additional interpretation relies on the aforementioned assumptions.

One explanation could be the high cosmic-ray energy densities caused by the higher star formation rates in these galaxies [1]. Cosmic rays can volumetrically heat the gas, including the dense UV-shielded cores that set the initial conditions for star formation; cosmic-ray-dominated regions (CRDRs) heat the gas to 80-240 K in compact extreme starbursts, closer to the cold component temperatures we find here [126]. Even if cosmic rays do not dominate the heating, their influence will still heat the gas more than PDRs alone and will increase the Jeans mass, and hence the stellar initial mass function mass scale [126]. The higher temperatures in our cool gas component may be a direct feedback mechanism of star formation; not from the UV light of O and B stars, but from cosmic rays.

It could still be that we are "counting" molecular clouds that typically have higher pressures than Galactic clouds; in that case, we would expect the mass and luminosity to increase with increasing galaxy mass or luminosity, but the average pressure to remain the same. Though it is hard to discern a relationship between pressure and luminosity (Figure 5.6), we find a best-fit slope of 0.53 and 0.41 for the cool and warm components, respectively. The bootstrap method yields errors on these parameters of $\pm$ 0.27 and 0.12. For the cold component, we cannot exclude a zero slope at the 2σ level, but for the warm component, the bulk average pressure doesn't vary linearly with $L_{\rm FIR}$ nor is it independent. This implies that the energetics of the warm component in these

galaxies are different, not that we are just viewing "more" of the same molecular gas components with increased $L_{\rm FIR}$. The slight correlation between the luminosity/mass ratio and $L_{\rm FIR}$ for the warm component may also be indicative of this.

Other properties we sought to investigate were the relative *ratios* between the warm and cool component pressure, mass, and luminosity, shown in Figure 4.13. We did not detect any trend with $L_{\rm FIR}$ (or SFR), sSFR, the presence of an AGN, $L_{CO_{6-5}}$, or dust mass. On average, the log ratios of the warm/cold CO pressure, mass, and luminosity were 1.8 ± 0.2, -1.0 ± 0.08, and 1.2 ± 0.08. Linearly, these correspond to ratios of 60 ± 30, 0.11 ± 0.02, and 15.6 ± 2.7. The pressure is the least well determined ratio. It is dependent upon the relative shapes of the SLEDs of the two components; they can "trade off" a significant amount in the mid-J lines and still fit the overall shape. We find that the two components are not in pressure equilibrium; once equilibrium is not enforced, we have no expectation for what the ratio should be. Aside from the broad constraints that the gas be both dense enough and cool enough to be molecular, but not so dense and cold that the timescale for gravitational collapse is short compared to a dynamical time, there is no obvious limitations on the allowed ranges of n and T, so we might expect a broad distribution. Furthermore, if we see such different excitation among galaxies, as described in the previous paragraph, we would also expect different distributions of excitation mechanisms within galaxies. The mass and luminosity are global properties (a sum), whereas the pressure is a local quantity (here, an average). Mass and luminosity are anchored by the lowest-J (for cool) and highest-J (for warm) lines. This reaffirms previous conclusions in the literature, from studying individual galaxies, that the low-J CO dominates the mass and the high-J CO dominates the luminosity and hence the cooling [e.g. 80, 139, 161, 143].

5.1.7 Carbon in Various Forms: C, C^+, CO

Near newly formed, bright O and B stars, CO only exists where it is adequately shielded from dissociation by UV photons. In the traditional model of a molecular cloud, this will be in the interior of the cloud, surrounded by a transition layer in which carbon is mostly neutral and atomic,

but the hydrogen is still substantially molecular, and then another layer in which the carbon is mostly ionized and the hydrogen atomic [72]. The molecular gas in the transition layer will not be traced by CO emission, so it is referred to as "CO-dark." The PDR models of Wolfire et al. [189] indicate CO-dark gas may account for 30% of the molecular gas mass. New observations indicate that a significant fraction of molecular gas in the Milky Way is CO-dark [135]. Here we compare the view of galaxies studied with C, C^+, CO, and dust.

We first discuss the column density ratios (and overall relative abundances) of C, C^+, and CO. Our beam-averaged column densities for the cold and warm components of CO are presented in Table 4.12, and the total mass from [CI] in Table 4.15. Though we could not calculate excitation temperatures for [CII] to use in the equations in Section 4.5.4, we used 150 K which corresponds to a fraction of atoms in the upper state of 0.52 (the fraction approaches 2/3 for $T \gg 92$ K). Even with this assumption, the uncertainties in the column density ratios are dominated by the uncertainties in the CO column densities. The distributions are shown in Figure 5.7; we found a median $N_{\rm C}/N_{\rm CO} \sim 0.5$ and a median $N_{\rm C^+}/N_{\rm C} \sim 0.5$. Almost all $N_{\rm C}/N_{\rm CO}$ values are less than 1, in line with those reported in Wilson [186], except for NGC 6240, which appears to have [CI] emission even more abnormally luminous than its CO emission.

We next turn our attention to the temperatures derived from the two neutral atomic carbon lines in our spectra. The excitation temperatures of [CI], shown in Table 4.15 appear to be clustered between 20-40 K, regardless of galaxy, and are not correlated to other measures, such as total infrared luminosity or cold CO temperature. Without correcting fluxes for the dust absorption, which affects the $\rm J = 2 \rightarrow 1$ line slightly more than the $\rm J = 1 \rightarrow 0$, the derived temperatures would be about 0.5 to 5 K lower. We found an average temperature of 26.3 ± 8.8 K, in agreement with the 29.1 ± 6.3 K cited for a sample of high-z galaxies [177]. This indicates that neutral C is likely tracing the same cool component of gas across a range of galaxy luminosities and redshifts, and is therefore not a particularly good distinguisher of excitation conditions.

However, Papadopoulos & Greve [127] proposed using the [CI] $\rm J = 1 \rightarrow 0$ line to measure global molecular gas mass, finding good agreement with molecular mass measured by CO. We also

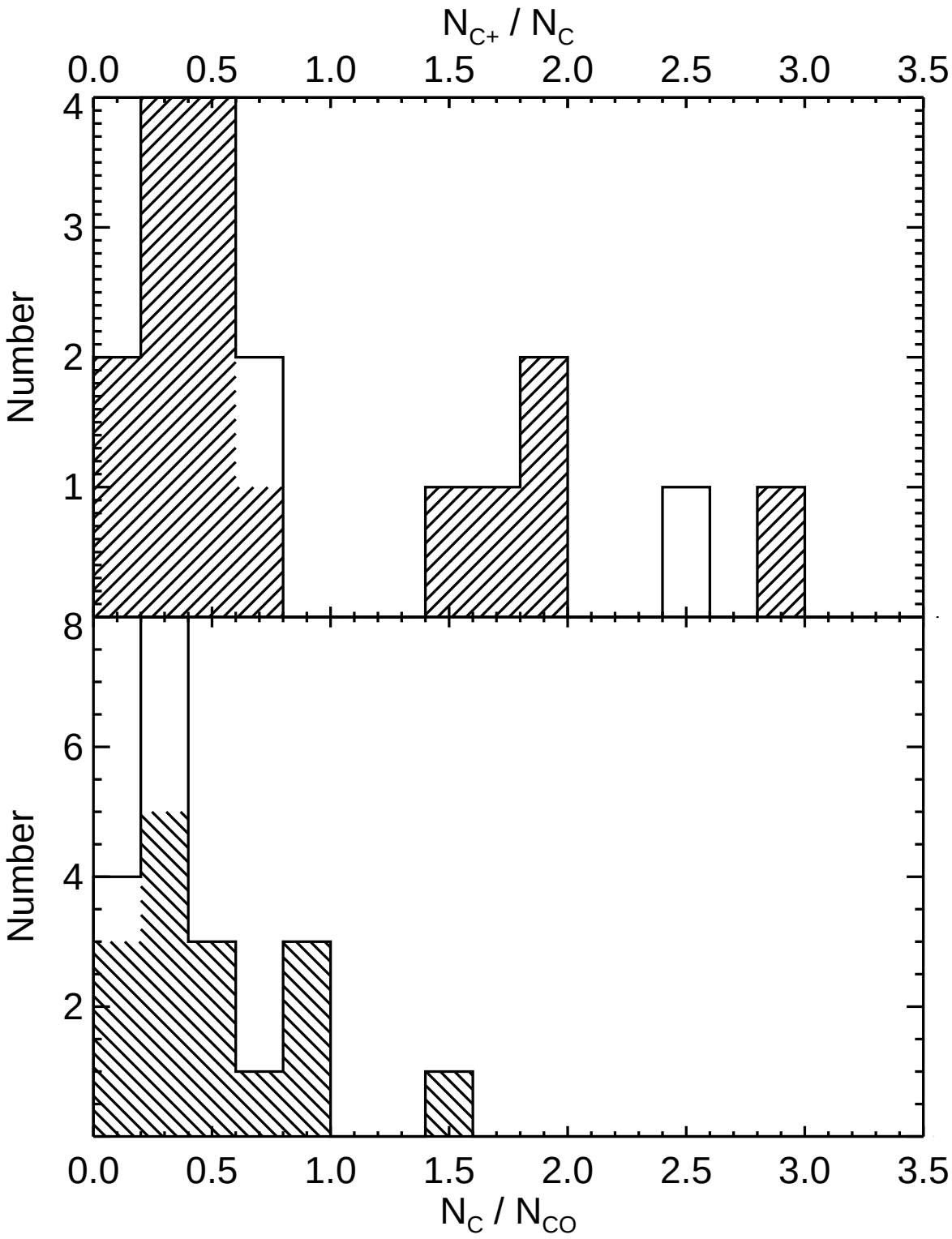

Figure 5.7 Column Density Ratios of C, C^+, CO. Top panel is the ratio of C^+ to C column density, bottom panel is ratio of C to CO column density. Duplicate pointings of galaxies are not filled in by diagonal lines. The only galaxy not included in the bottom plot is NGC 6240, with an abnormally high ratio of 38.

found a correlation between neutral C mass and molecular mass measured from CO, consistent with a linear relationship. They adopted a relative abundance $X_{\rm [CI]/H_2} = 3 \times 10^{-5}$. The weighted average abundance of $X_{\rm [CI]/H_2} = M_C/(M_{gas}/1.4) \times m_{H_2}/m_C$; using the gas mass derived from the cold component CO fitting (and therefore dependent upon X_{CO}), we found $\log(X_{\rm [CI]/H_2})$ = -4.1 $\pm$ 0.5. In a linear ratio, this is $8^{+17}_{-5} \times 10^{-5}$, a not particularly well constrained value but consistent with the values presented in Papadopoulos & Greve [127] for the Cloverleaf quasar, the Orion A and B clouds, and the nucleus of M82 (ranging from $1 - 5 \times 10^{-5}$), as well as with the mean of $8.4 \pm 3.5 \times 10^{-5}$ reported for high redshift galaxies in Carilli & Walter [26]. We required a higher average abundance of [CI] to match our CO-derived gas mass values than in Papadopoulos & Greve [127], and this discrepancy is almost entirely due to our higher measured [CI] fluxes for the three galaxies that our samples share (NGC 6240, Arp 220, and Mrk 231). We differed in how we determined the populations of the J levels: we used both [CI] lines, calculated an excitation temperature, and then used Boltzmann distributed populations, as opposed to using one line and an estimate based on the gas conditions as in Papadopoulos et al. [130]. In the end the population levels were roughly the same, but the different line fluxes caused the difference in [CI] mass. We confirm the conclusions of Papadopoulos & Greve [127]: [CI] is as good of a tracer of total molecular mass as radiative transfer modeling of CO, though further refinements of the value of $X_{\rm [CI]/H_2}$ will aid in its precision.

Our finding of differing temperatures between dust, [CI], and CO, is in line with the findings of others in the literature. For example, Mangum et al. [101] found the temperatures derived from ammonia (NH_3), a well-known kinetic temperature probe, differed from the dust temperatures for a sample of star-forming galaxies (seven of which are in our sample). We found higher dust temperatures by modeling the full SED instead of just using the 60 and 100 μm flux densities (6 to 11 K higher), but still confirm that $T_{\rm NH_3} > T_{\rm dust}$, and add $T_{\rm [CI]} < T_{\rm dust}$. They concluded that dust temperature should not be used as a proxy for gas temperature, and that higher gas temperatures of NH_3 may be caused by turbulence and/or cosmic ray heating, not just radiative processes. Carilli & Walter [26] also note that "the heating and cooling processes of the dust

and molecular gas phases are quite different, and therefore thermal balance is not required." We confirm these findings, and add the additional caution that gas temperatures from different atomic or molecular species are likely tracing different conditions. Specifically, [CI] is not tracing the higher temperature gas (certainly not that of high-J CO, and possibly not that of low-J CO). This means [CI] is likely measuring neutral atomic gas unaffected by star formation [26].

The picture becomes more complicated when considering the [CII] 158 μm line, which has been found to be emitted by from a variety of sources, and may be tracing the CO-dark H_2 gas described above. (Note that α_{CO} is not sensitive to reservoirs of H_2 where C^+ or C is the dominant form of carbon.) Pineda et al. [135] found, via a study of the Galactic center, that [CII] emission is produced by a combination of PDRs ($\sim$ 47%), CO-dark H_2 gas ($\sim$ 28%), cold atomic gas ($\sim$ 21%), and ionized gas ($\sim$ 4%). Langer et al. [89] also studied the column densities of CO-dark H_2 gas of individual clouds, a level of detail we do not have here. We have already discussed some differences between our galaxies and the Milky Way; can these distributions be valid in starburst galaxies? In Section 4.5.6 and Table 4.18, we presented the estimated percentage of C^+ emission from ionized gas using line ratios, and found that in most cases, the fractions are higher than 4%, with a median of 14-25%. They are not correlated with L_{FIR} or [CII]/L_{FIR}. This matches with the 27% (error range 19-46%) found for the Carina Nebula [121]. However, we cannot say anything about the distribution of the remaining source contributions, only that there is less (proportional) [CII] line emission from the sum of PDRs, CO-dark H_2 gas, and cold atomic gas in these galaxies than in the Milky Way. Pineda et al. [135] found that the fraction of mass from CO-dark H_2 increases with Galactocentric distance, from 20% at 4 kpc to 80% at 10 kpc . Because the emission from our galaxies is more akin to that of the Galactic center, we predict lower fractions of CO-dark H_2 gas than in the Milky Way as a whole. A study similar to that of Pineda et al. [135] and Langer et al. [89] could be conducted for the nearest galaxies or Milky Way satellites comparing the distribution of HI, C^+, ^{12}CO and ^{13}CO to test this prediction.

Even absent formal modeling of PDRs, we see a picture that contradicts traditional PDR models, even with additional heating from mechanical turbulence or enhanced cosmic rays [e.g.

189]. Detailed studies of individual galaxies have consistently found that PDR models cannot explain the large luminosities in the mid- to high-J CO lines: Arp 220 [139], M82 [80], M83 [191], NGC 6240 [110], Cen A [76], NGC 891 [119], and the Galactic center [18]. In only a few instances have PDRs been found to be adequate, namely the Antennae [154], IC324 [143], and the outer star-forming ring of NGC 1068 [161]. Additionally, the low $\alpha_{\rm CO}$ we find requires some combination of higher temperatures (thereby raising the emissivity provided the line remains optically thick) or non-virialized molecular clouds. Cosmic-ray dominated regions (CRDRs) could explain the elevated CO temperatures [126] or be combined with PDRs [112], which would imply a higher Jeans mass as a consequence. The concurrence of evidence presented here (and in the cited literature) confirms that *high-J CO emission is generally powered by non-radiative processes*, a conclusion which future models must take into account.

5.1.8 Comparison to the Galactic Center: Sgr A* and Sgr B2

We have already compared our pressure distributions to those of molecular clumps in the Galactic plane (Section 5.1.6). Two specific regions in the Galaxy are more comparable to the galaxies in our sample: the warm gas and dust heated and ionized by the massive stars orbiting Sgr A*, and the giant molecular cloud Sgr B2, approximately 120 pc away from Sgr A*. The CO SLEDs of these observations were included in Figure 4.5.

Goicoechea et al. [61] found the CO SLED from $J = 4 \rightarrow 3$ to $J = 24 \rightarrow 23$ in the warm gas within 1.5 pc of Sgr A* was consistent with either a single component of gas (T = $10^{3.1}$ K, n $\leq 10^4$ cm^{-3}, pressure $\leq 10^{7.1}$ K cm^{-3}) or multiple cooler components at higher density. In the single component case, this hot gas must fill a small fraction of the volume (not homogeneously distributed), and requires excitation in addition to PDRs. Despite its proximity to our Galaxy's central black hole, the X-ray luminosity is too low to create an XDR, and cosmic rays would only heat the gas to a few tens of K. The authors suggest low-density shocks contribute to the heating of this hot molecular gas, though it is unclear if they are from in-falling gas, clump-clump collisions, or outflows from stellar winds or protostars.

Etxaluze et al. [53] resolved the three main compact cores, Sgr B2(N), Sgr B2(M), and Sgr B2(S) from the extended envelope of the Sgr B2 molecular cloud in both dust and molecular line emission and absorption. In addition to determining the dust properties over a ~ 58 arcmin^2 map, they map the line emission from the CO $J = 4 \rightarrow 3$ to $J = 11 \rightarrow 10$ lines. While the $J = 6 \rightarrow 5$ warm gas emission is spread over the molecular cloud, that of $J = 11 \rightarrow 10$ is highly concentrated around the compact cores. They conduct non-LTE modeling of the CO emission for the B2(N) and B2(M) cores and require two components (starting from the $J = 4 \rightarrow 3$ line, not $J = 1 \rightarrow 0$), which they denote as warm extended emission (60 and 100 K) and hot compact emission associated with the cores (560 and 320 K). The log(pressure) for the warm components are 6.8 and 7.4, and for the hot components, 8.7 and 8.5, respectively, for B2(N) and B2(M). For our galaxy-averaged spectra, *the pressures for our warm component are consistent with those of the Sgr B2 extended molecular cloud emission*, and lower than that of the hot components.

While very high molecular gas temperatures are not found in the Galactic plane as a whole, they are found in Sgr B2 and Sgr A*. Though we cannot resolve molecular clouds in nearby galaxies, it is clear that the high-J lines are emitted from regions of highly excited gas. As one progresses from lower to higher J, the area filling factor of the emitted region becomes progressively smaller, as was demonstrated by Etxaluze et al. [53] for Sgr B2. The SLEDs of the Sgr B2 cores, shown in Figure 4.5, peak at higher-J than the mid-J peak of the extended Sgr B2 molecular cloud envelope (which is more similar to our galaxies). This means that our warm component emission is likely dominated by regions resembling the warm extended molecular cloud envelopes (whose pressure matches those we measure here), not star-forming cores (of a higher pressure). While such compact regions are undoubtedly present, it must be at a lower level, so the bulk of the emission we measure is from the extended molecular clouds, not cores. We tested this by examining the total integrated flux of the Sgr B2 SPIRE FTS map, as one would measure if it were a distant point-source. The resulting SLED is similar to that of the Sgr B2 molecular cloud, not the cores, despite their brightness in high-J lines. As extensively discussed in Section 5.1.3, we know there are gradients in physical conditions in our SLEDs, as we saw from LTE analysis of H_2 lines; the

emission from cores (the hottest material) contributes an undetectably small fraction of the total high-J CO emission over the whole galaxy. The broad implications for future modeling are clear: the excitation conditions and the geometries (filling factors) of the mid- to high-J lines must be treated distinctly from e.g., $J = 1 \rightarrow 0$. ALMA can achieve unprecedented spatial resolution in observations of the $J = 6 \rightarrow 5$ line; such information can be used to place further prior information on CO modeling and possibly disentangle the multiple components (e.g. the analogues to those seen in the Galactic plane, the Sgr B2 molecular cloud, and the Sgr B2 cores) within nearby galaxies.

5.1.9 Comparison to High-Redshift Galaxies

Cool gas is the direct fuel for star formation, and it is important to assess the gas content of galaxies and feedback from star formation at all redshifts, including the peak of star formation ($z \sim 1-3$). Elbaz et al. [50] developed the idea of a main sequence of galaxies, where most "normal" main sequence galaxies have a constant specific SFR, but some galaxies with higher star formation rates relative to their stellar masses lie above this relation. We plot our galaxies relative to this main sequence in Figure 5.8. The galaxies that lie above the galaxy main sequence in Figure 5.8 are often thought of as SMG analogues: Arp 299, UGC 05101, Arp 220, Mrk 273, IRAS 09022-3615, and possibly Mrk 231 and IRAS F17207-0014. These are our highest luminosity sources, with the exception of NGC 6240, which is anomalous in its exceptionally luminous CO emission [110]. Additionally, as previously noted, the lack of both GALEX UV bands makes its position on the diagram suspect; it has had a lower stellar mass estimated elsewhere [~ 1 dex lower for the sum of the north and south nuclei, 52]. However, it is likely that the star formation in these local galaxies is more nuclear and compact than in high-z SMGs, so though both these galaxies and SMGs lie above the main sequence, they are not completely comparable [113, 54]. Figure 5.9 also illustrates gas consumption timescales. For high-z galaxies, Carilli & Walter [26] report gas depletion timescales of 10^7 yr for SMGs and quasars, and 10^{8-9} yr for lower-excitation color-selected high-z galaxies. High-z SMGs may have cooler dust temperatures than similarly luminous galaxies at $z \sim 0$ [138], but this could be due to selection effects. Swinbank et al. [164] found SMGs with average dust

temperatures 32 ± 1 K, which they say is 3-5 K lower than comparable local galaxies. Our dust temperatures are much more than 3-5 K higher (from 37-80 K), but our methods are not entirely comparable, because we allow λ_0, β, and T to vary, instead of using template fitting where most such values are fixed.

This work illustrates the vast, though complicated, amount of information provided by CO SLEDs from $J = 1 \rightarrow 0$ through $J = 13 \rightarrow 12$. We have already shown that the gas consumption timescales of our highest-luminosity galaxies are comparable to high-z SMGs. High-redshift SMGs have rarely been detected in more than a few CO lines. Carilli & Walter [26] reviewed studies of cool molecular gas in high-z galaxies and found that quasars require a high-excitation component, related to the AGN, to explain mid-J line flux. We showed that even galaxies with no AGN require a high-excitation component. Furthermore, they note that SMGs (in contrast with quasars) demonstrate less excited molecular gas and excess emission in the CO $J=1\rightarrow0$ transition. We have demonstrated that the problem is perhaps best approached from another direction: the "excess" emission is not in the CO $J=1\rightarrow0$ transition. Instead, the CO $J=1\rightarrow0$ should be considered as entirely emitted by the coldest gas, and the real excess is in the mid-J lines, requiring the higher-excitation component. Just such a component was found using the $J=3\rightarrow2$ to $J=9\rightarrow8$ lines of the $z = 2.56$ Cloverleaf quasar [thermal pressure $> 10^6$ K cm^{-3}; 17]. One cannot disentangle this question without a more complete SLED, as we show here for a range of low-z galaxies (with and without AGN, with and without active starbursts). By more complete, we mean a good distribution of lines from $J=1\rightarrow0$ to $J=9\rightarrow8$ or higher. Moreover, the mass estimated from mid-J lines alone will be an underestimate of the total molecular mass if CO $J=1\rightarrow0$ is unavailable. We tested the extent of this effect by modeling only the $J=3\rightarrow2$ to $J=6\rightarrow5$ lines as one component of molecular gas. On average, the log of the ratio of cold component mass (from our two-component models) to these mid-J masses was 0.56 ± 0.34. This means masses using mid-J lines will be underestimated by a factor of 1.7 - 7.9, or 3.6 on average. For example, with ALMA, the $J=1\rightarrow0$ ($J=2\rightarrow1$) line is unavailable above $z = 0.4$ (1.7), so it will be difficult to accurately estimate molecular mass at high-redshift; dust emission may have to be relied upon more heavily for cold ISM mass measurements.

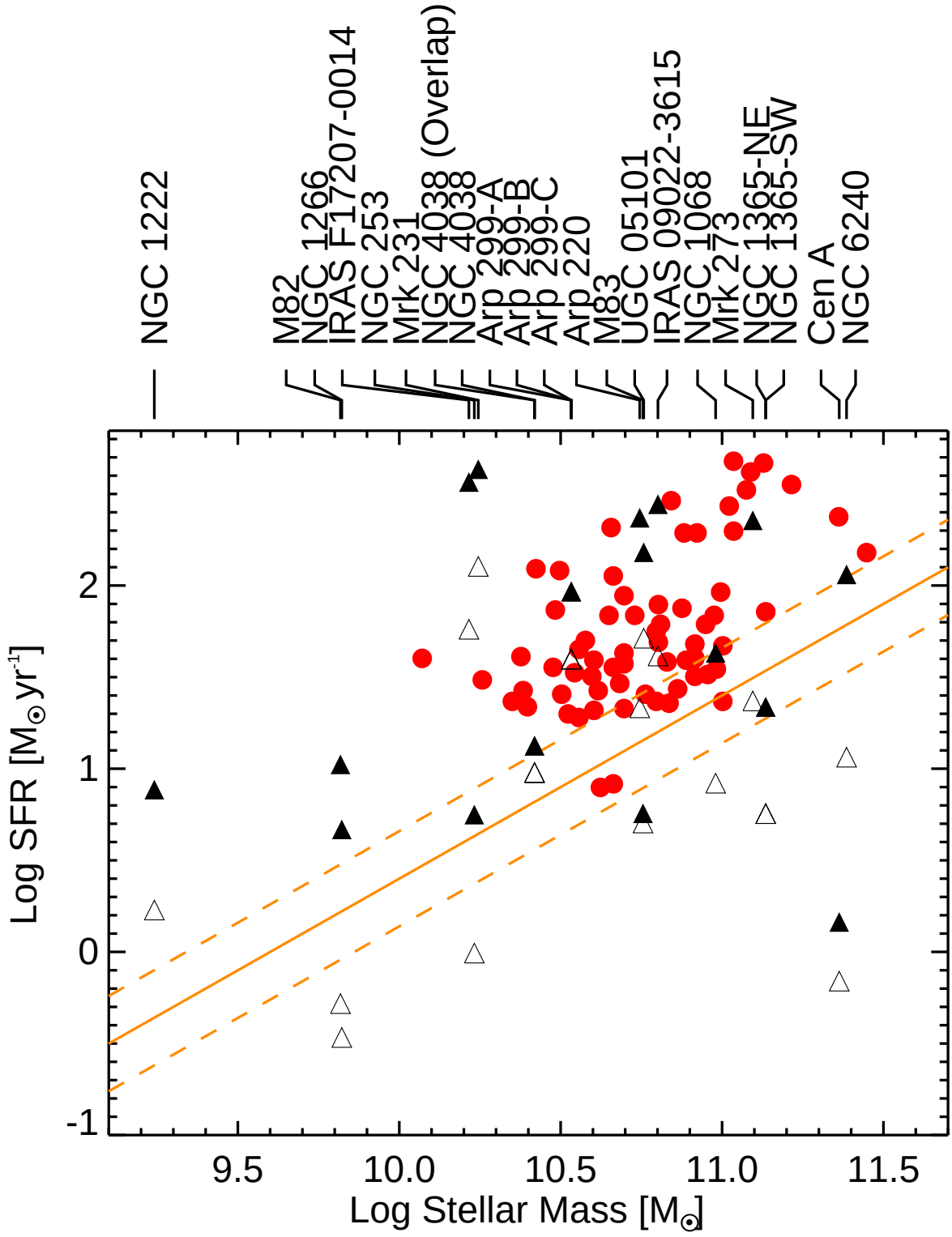

Figure 5.8 Star formation rate vs. Stellar Mass. The solid line denotes the galaxy "main sequence" presented in Elbaz et al. [50], with uncertainties bracketed by dashed lines. The red circles are the compact, "starbursty" galaxies in Figure 16 of Elbaz et al. [50], which reside above the main sequence relationship. The solid black triangles are our data, using star formation rates from the Kennicutt relation with $L_{\rm FIR}$. The open black triangles are those with SFR from MAGPHYS, which we believe to be too low but are presented here for comparison. Note that Mrk 231 and IRAS F17207-0014 do not have UV data and their outlying position should be treated with caution. Star formation rates are also upper limits for galaxies with AGN: UGC 05101, NGC 1068, Cen A, NGC 1365, Mrk 231, Mrk 273.

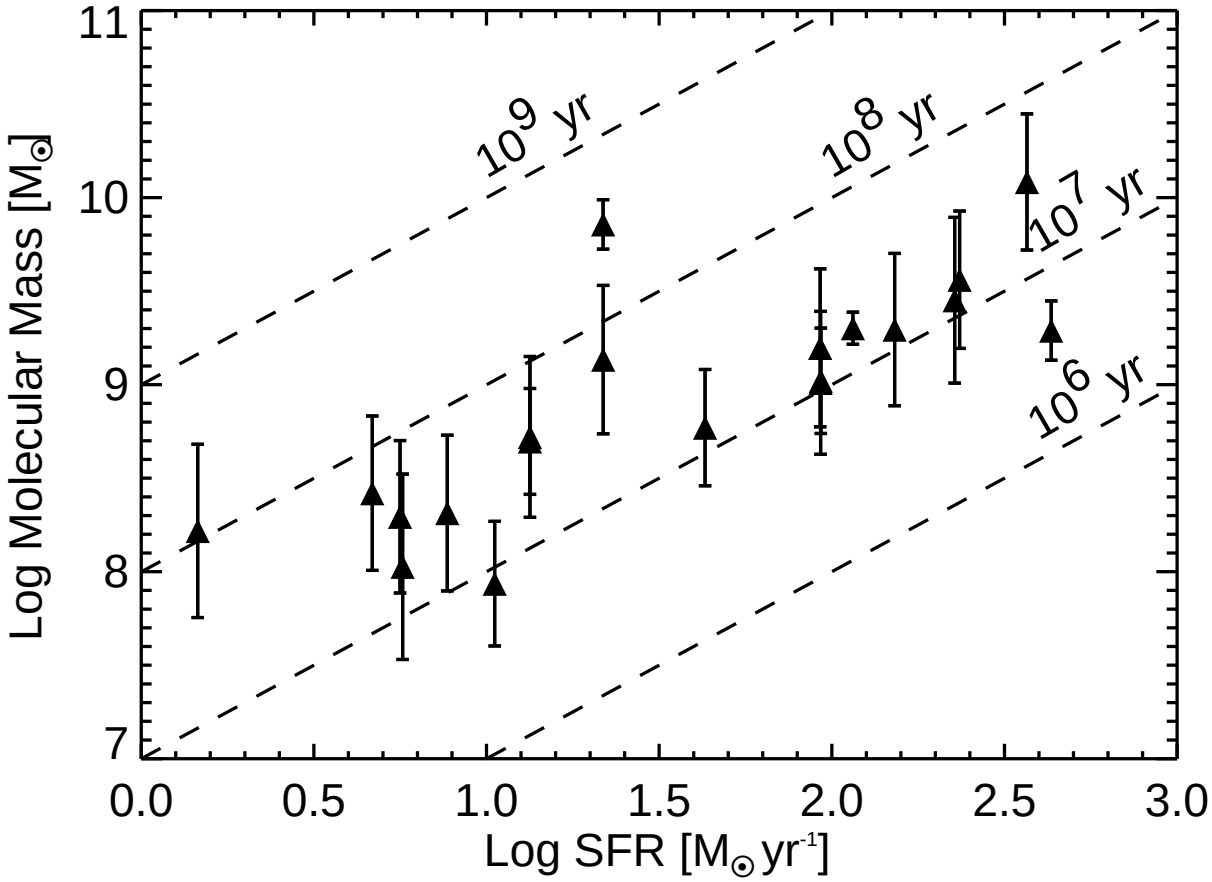

Figure 5.9 Molecular Mass vs. SFR. The y-axis divided by x-axis is an indication of the timescale for consumption of the molecular gas by star formation; dashed diagonal lines indicate constant consumption times. High-SFR galaxies are consistent with approximately 10^7 years, whereas lower SFR galaxies may follow a longer timescale relation.

The SLEDs shown here could also be used as analogues for missing lines in future high-z molecular gas modeling.

5.2 Conclusions

We presented spectra of 17 infrared-luminous galaxy systems at 21 different pointings observed with the *Herschel* FTS from 450-1550 GHz. We have created a uniform, consistent pipeline which can perform analysis of such spectra, including source-beam coupling corrections, line fitting, and an 8 parameter likelihood analysis of the warm and cool CO gas for each source. Such analysis for nearby galaxies can, at this time, only be performed with *Herschel* data, which contain enough CO lines to construct SLEDs up to J = 13 → 12. We supplemented this analysis with stellar population and dust modeling to discover potential correlations or diagnostic power in the total $L_{\rm FIR}$, specific star formation rate, etc. of these galaxies.

We found that high-excitation molecular gas is ubiquitous in this sample of galaxies with Log($L_{\rm FIR}$) from $\sim$ 10 to 12.5. We clearly distinguish a low-pressure/high-mass component traced by low-J lines from a high-pressure/low-mass component in all systems from their CO SLEDs. The ratios of the warm/cold pressure, mass, and CO luminosity were 60 ± 30, 0.11 ± 0.02, and 15.6 ± 2.7. Future interpretation of high-z CO emission, which often must be derived from just a few CO lines, should take these ratios into account. Though the mass and CO luminosity scale linearly with $L_{\rm FIR}$, the highly excited molecular gas pressure is proportional to ${L_{\rm FIR}}^{(0.4\pm0.1)}$, indicating higher excitation per bulk mass of molecular material.

The total mass of the low-pressure molecular gas is well-traced by the CO J = 1 → 0 line (and [CI]), but the pressure will be overestimated if not modeled simultaneously with the high-pressure component. We found a luminosity-to-mass conversion factor of $\alpha_{\rm CO} \approx 0.6$, consistent with higher temperatures and/or non-virialized gas motions *in this low-pressure gas component*. We measure gas-to-dust mass ratios of ≤ 120, though the CO gas and dust temperatures are not related. Cosmic rays may be responsible for heating the CO gas above the very cool temperatures found in PDR models, and above that of Galactic clouds.

Most of the CO luminosity is emitted from the warmer, high-pressure component; the total CO luminosity is about $4\times10^{-4}\ L_{\rm FIR}$, and is well-traced by the CO J$=6\rightarrow5$ line. The high-pressure molecular gas excitation is consistent with the extended molecular cloud emission of Sgr B2 [53]. The compact cores Sgr B2(N) and Sgr B2(M) are more highly excited than we measured in the extragalactic SLEDs; such emission is undoubtedly present, but being emitted from significantly smaller and lower mass regions, cannot be resolved by non-LTE modeling of the CO SLEDs. Numerical simulations could place useful priors on models to help distinguish the physical parameters of such highly excited molecular gas; such information will be necessary to fully understand the excitation and feedback mechanisms taking place in star-forming galaxies. Additionally, ALMA is now offering opportunities to spatially map the distribution of this warm molecular gas and complement our galaxy-integrated observations. In most of these galaxies, non-radiative processes, such as shocks, turbulence, and stellar winds are required for the high-pressure molecular gas excitation.

Acknowledgements: SPIRE has been developed by a consortium of institutes led by Cardiff University (UK) and including Univ. Lethbridge (Canada); NAOC (China); CEA, LAM (France); IFSI, Univ. Padua (Italy); IAC (Spain); Stockholm Observatory (Sweden); Imperial College London, RAL, UCL-MSSL, UKATC, Univ. Sussex (UK); and Caltech, JPL, NHSC, Univ. Colorado (USA). This development has been supported by national funding agencies: CSA (Canada); NAOC (China); CEA, CNES, CNRS (France); ASI (Italy); MCINN (Spain); SNSB (Sweden); STFC (UK); and NASA (USA). We would like to thank Rosalind Hopwood for HIPE reprocessing. This paper is based upon work supported by NASA under award number NNX13AL16G. John Bally provided excellent discussion which positively influenced the analysis of this work.

Chapter 6

Future Work

Herschel's groundbreaking work will continue to be analyzed in the coming years; here we preview the utility of applying this pipeline to all galaxies observed by the FTS, and further observations that can be made by ALMA to add spatially and spectrally resolved information about the warm CO.

6.1 Preview of the Full FTS CO Survey

The work in this thesis established a uniform pipeline to model the molecular gas conditions in any galaxy that has a *Herschel* SPIRE-FTS spectrum, using additional information gathered from the literature, when available. We presented only 17 unique galaxies, with 21 pointings. In total, the FTS was scheduled to observe 301 pointings of galaxies, both nearby and at high/unknown redshift (229 had publicly available redshifts prior to their observations, 200 of which are $z < 0.1$). 78 are known to contain AGN, 24 are categorized as ultra-luminous infrared galaxies, and 87 are luminous infrared galaxies. On October 29, 2013, the last of the proprietary *Herschel* data was made publicly available. At this time, 287 FTS observations of galaxies are available (14 approved observations were not observed, or failed and were not reobserved).

Here we preview the currently available FTS spectra. Upon initial line fitting, 167 of the spectra with known redshifts have a signal/noise ratio greater than three for a detection of CO $J = 6 \rightarrow 5$. For those galaxies for which this has been calculated with photometer data, most (185 of the 230) require more than a 10% source-beam correction for a $20''$ beam. We currently have

detections (S/N $\geq$ 3) of at least 8 lines of CO J = 4 $\rightarrow$ 3 to J = 13 $\rightarrow$ 12, [CI], and [NII] for 133 galaxies.

The low-J lines used to supplement the CO modeling in this work were drawn from a variety of surveys (see Appendix C). Of this current database, measurements of two or three of the first three lines are available for 78 of the SPIRE-FTS galaxies. These lines are necessary in order to model both components of the CO spectral line energy distribution. A further literature search may reveal more, but others will require follow-up observations from single dish radio telescopes, such as the Arizona Radio Observatory (ARO), the Atacama Pathfinder EXperiment (APEX), and the IRAM 30-m telescope. Of the 97 (54) with known redshifts but zero (one) detection(s) of the first three lines, 62 (42) are above -20° in declination, accessible by the ARO.

Completion of the full survey will provide the opportunity to make statistically significant comparisons of the ISM excitation conditions between galaxies of different types (e.g. those with an active galactic nucleus) and by other galactic properties, such as total FIR luminosity or specific star formation rate. We will be able to make a much more robust calculation of $\alpha_{\rm CO}$, the average gas-to-dust mass ratio, and the slope of the relationship between warm and cool pressure and $L_{\rm FIR}$. Such a comprehensive survey of CO emission up to J = 13 $\rightarrow$ 12 has not been published before. The publication of this survey, which will include a combination of derived photometry, spectral line fluxes, and modeled physical parameters, as well as a large collection of the same from the literature, will be a significant resource for all future studies of molecular gas in nearby and distant galaxies.

Furthermore, in this work we have not done a quantitative analysis of the excitation mechanisms in the gas (e.g. comparisons to PDR, XDR, or cosmic ray models). These mechanisms are more easily distinguished via molecules other than CO. For example, Meijerink et al. [112] found that HCN and HNC are useful diagnostics of mechanical heating, and H_2O^+ and other water-related ionized species (OH^+, H_3O^+) are powerful tracers of cosmic rays. These lines are only detected in the brightest spectra [see e.g. Arp 220, 139], but coaddition of multiple galaxy spectra could reveal such lines. Because the cosmic ray diagnostics are often degenerate with XDRs, we would conduct

this analysis only including galaxies without known AGN. This can test our proposed explanation of cosmic ray heating elevating the cool gas pressure above that of Galactic GMCs.

6.2 High-Resolution CO J = 6 → 5 Observations with ALMA

Herschel's bandwidth allowed us to construct full CO spectral line energy distributions up to J = 13 → 12. Unfortunately, the tradeoff for this ability is decreased spatial and spectral resolution. For the cool molecular gas, traced by CO J = 1 → 0, there is in fact more information available than presented here for these galaxies with regards to spatial extent, morphology, and kinematics. For the high-J lines, though, such information is lacking. The work in this thesis has demonstrated that the J = 6 → 5 line is a good proxy for the warm component of gas. ALMA will be able to observe the CO J = 6 → 5 transition at increasingly fine resolution (see Figure 6.1), allowing us to compare the morphology of the two ISM components and model the physical conditions (pressure, mass) as a function of spatial location. Such work will determine the physical extent of the high-J CO emission compared to the cool gas and dust. Also, ALMA maps could provide evidence for the turbulent motion and shock heating we believe is required to excite the CO. With better velocity resolution, we will be able to see how strong velocity gradients correspond to higher excitation, or perhaps outflowing material. Higher resolution will also allow us to make important comparisons between atomic and molecular species, such as [CI], [CII], ^{12}CO and ^{13}CO.

Few galaxies have been interferometrically mapped at J = 6 → 5 [e.g. Arp 220, VV 114, 104, 157]; the Submillimeter Array had this capability, but could not acheive the same resolution as ALMA can now, and that observing band may be discontinued soon. ALMA Cycle 1 observations of Arp 220 CO J = 6 → 5 show a spatial offset between warm gas and the dust continuum, as well as many interesting features that can only be discerned at high resolution (Rangwala et al. 2014, in prep). Our research group has received ALMA Cycle 2 time to map Arp 220 in CO J = 4 → 3 to complement the Cycle 1 observations, and NGC 6240 in J = 6 → 5 and J = 3 → 2 (P.I. Rangwala). The J = 4 → 3 line of NGC 6240 is in an atmospheric absorption band (Figure 6.1). In the coming years, we plan to observe more galaxies in CO J = 6 → 5, a good tracer of the total CO luminosity

and the warm gas. The total integration time for observations of CO J = 6 → 5 is about one hour per galaxy, because high signal-to-noise observations are required for self-calibration in Band 9.

6.3 Determination of CO Mass and Dynamics in SN1987A

We turn the reader's attention once again to the use of CO to determine molecular gas properties in a different environment, that of SN1987A (see Chapter 2). We were able to determine that the CO emission is confined to the inner debris left behind by the star (not the now-shocked ring of mass shed by the pre-SN progenitor star), but could not otherwise discern much of the dynamics or morphology with the relatively few telescopes available early in ALMA Cycle 0. Additionally, our observations serendipitously discovered SiO in the other sideband of our CO observations. Because we did not intend to observe that line, we were unable to view the complete line profile and determine a total integrated line flux.

The improved spatial resolution available since Cycle 0 and our discovery of SiO were two motivating factors in our ALMA Cycle 2 follow-up proposals. For the debris — a spherically expanding object — surfaces of constant Doppler shift are planar sections of the debris (planes perpendicular to our line of sight). This means that we will be able to image the debris of three dimensions using Doppler tomography. Such 3D maps have been created for lower-wavelength atomic lines in SN1987A and Cas A [75, 40, 91], but never for molecules. One Cycle 2 proposal (P.I. Indebetouw) will create such high-resolution ($< 0\farcs2$) maps for ^{12}CO J = 3 → 2 and J = 6 → 5, and ^{28}SiO J = 7 → 6 and J = 8 → 7. Our second proposal accepted for ALMA Cycle 2 (P.I. Matsuura) is an unbiased line survey of the molecular emission in Bands 6 and 7 (see Figure 6.1). We will compare maps of CO and SiO, which likely arise from separate clumps in the debris (due to the layered nucleosynthesis in the progenitor star's final stages), to determine the extent of the post-SN mixing. The extent of the chemical mixing can modify our understanding of the gas and dust formation/destruction processes.

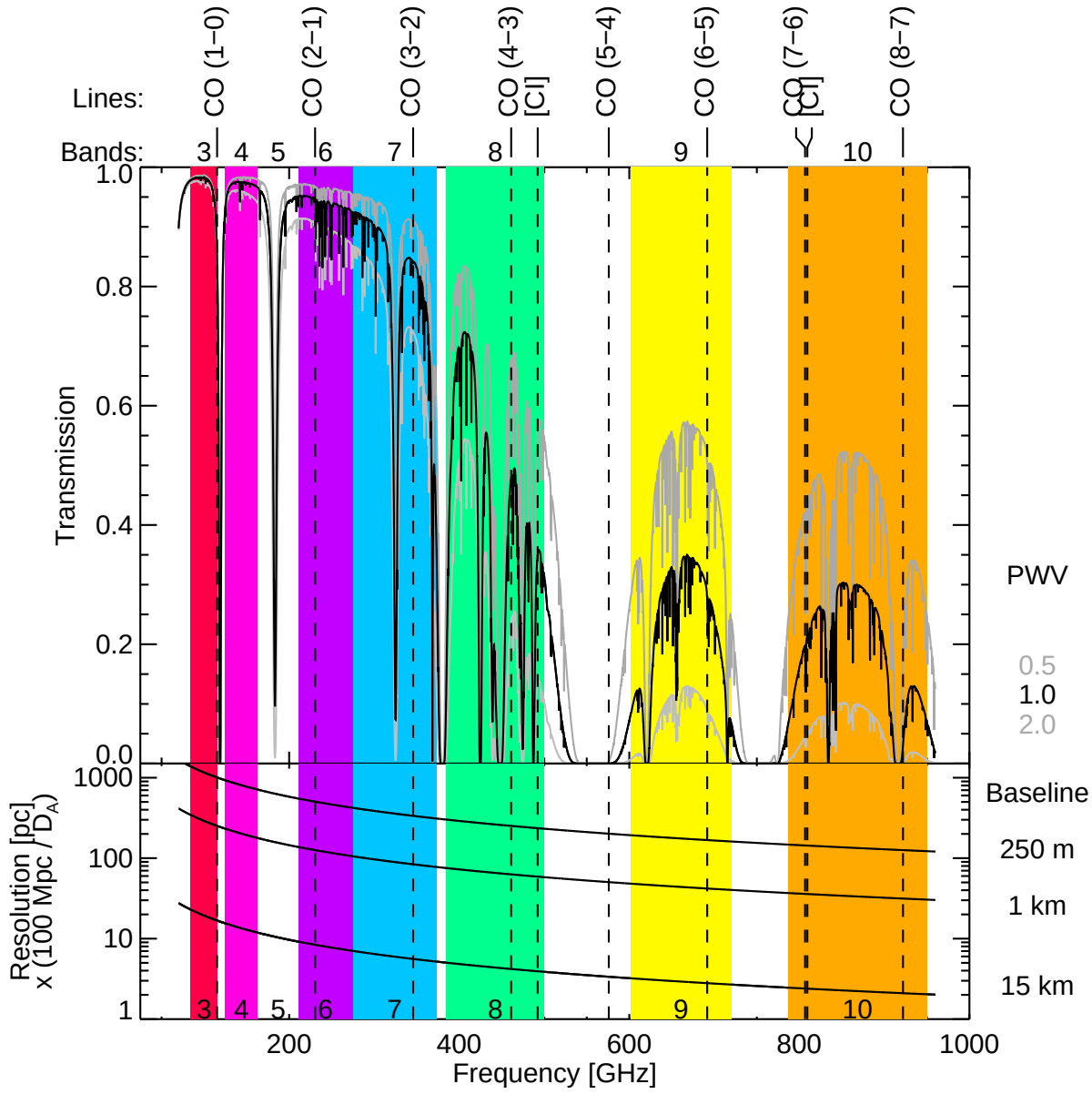

Figure 6.1 ALMA Transmission and Sensitivity by Bands. The frequency range of each ALMA band is indicated with a separate color; Band 10 is not complete, and Band 5 may not be built. The frequencies of the ^{12}CO and [CI] lines are indicated at the top of the plot and with vertical dashed lines. *Top:* atmospheric transmission vs. frequency in GHz for precipitable water vapor (PWV) of 0.5, 1.0, and 2.0 mm, from top to bottom. The weather conditions reach these levels 25%, 50%, and 65% of the time, respectively. *Bottom:* the maximum angular resolution achievable for a galaxy 100 Mpc away by frequency, for maximum baselines of 250 m (Early Science), 1 km (Cycle 2, for some bands), and 15 km (complete array). The resolution will scale with angular distance. For SN1987A, at a distance of 50 kpc, the resolution in pc is a factor of 2000 times higher.

Bibliography

[1] Abdo, A. A. et al. 2010, Astrophys. J., 709, L152

[2] Aladro, R., Martín, S., Martín-Pintado, J., Mauersberger, R., Henkel, C., Ocaña Flaquer, B., & Amo-Baladrón, M. 2011, Astron. Astrophys., 535, A84

[3] Alatalo, K. et al. 2011, Astrophys. J., 735, 88

[4] Albrecht, M., Krügel, E., & Chini, R. 2007, Astron. Astrophys., 462, 575

[5] Allen, C. W. & Cox, A. N. 2000, Allen's Astrophysical Quantities (Springer)

[6] Armus, L. et al. 2007, Astrophys. J., 656, 148

[7] Baan, W. A., Henkel, C., Loenen, A. F., Baudry, A., & Wiklind, T. 2008, Astron. Astrophys., 477, 747

[8] Balakrishnan, N., Yan, M., & Dalgarno, A. 2002, Astrophys. J., 568, 443

[9] Bayet, E., Gerin, M., Phillips, T. G., & Contursi, A. 2006, Astron. Astrophys., 460, 467

[10] Beirão, P. et al. 2008, Astrophys. J., 676, 304

[11] Bendo, G. J. et al. 2011, ArXiv e-prints

[12] Bergin, E. A. & Tafalla, M. 2007, Annu. Rev. Astron. Astrophys., 45, 339

[13] Bernard-Salas, J. et al. 2009, Astrophys. J. Suppl. Ser., 184, 230

[14] Bianchi, L., Herald, J., Efremova, B., Girardi, L., Zabot, A., Marigo, P., Conti, A., & Shiao, B. 2011, Astrophys. Space Sci., 335, 161

[15] Biermann, P. L., Chini, R., Haslam, C. G. T., Kreysa, E., Lemke, R., & Sievers, A. 1992, Astron. Astrophys., 255, L5

[16] Bolatto, A. D., Wolfire, M., & Leroy, A. K. 2013, Annu. Rev. Astron. Astrophys., 51, 207

[17] Bradford, C. M. et al. 2009, Astrophys. J., 705, 112

[18] Bradford, C. M. M., Stacey, G. J. J., Nikola, T., Bolatto, A. D. D., Jackson, J. M. M., Savage, M. L. L., & Davidson, J. A. A. 2005, Astrophys. J., 623, 866

[19] Brandl, B. R. et al. 2009, Astrophys. J., 699, 1982

[20] Brauher, J. R., Dale, D. A., & Helou, G. 2008, Astrophys. J. Suppl. Ser., 178, 280

[21] Briggs, D. S. 1995, PhD thesis, The New Mexico Institute of Mining and Technolog, New Mexico Institute of Mining and Technology

[22] Bruzual, G. & Charlot, S. 2003, Mon. Not. R. Astron. Soc., 344, 1000

[23] Bryant, P. M. & Scoville, N. Z. 1999, Astron. J., 117, 2632

[24] Buchner, J. et al. 2014, 28

[25] Bush, S. J., Wang, Z., Karovska, M., & Fazio, G. G. 2008, Astrophys. J., 688, 875

[26] Carilli, C. & Walter, F. 2013, Annu. Rev. Astron. Astrophys., 51, 105

[27] Casey, C. M. 2012, Mon. Not. R. Astron. Soc., 425, 3094

[28] Castor, J. 1970, Mon. Not. R. Astron. Soc., 149, 111

[29] Charlot, S. & Fall, S. M. 2000, Astrophys. J., 539, 718

[30] Chattopadhyay, G., Glenn, J., Bock, J. J., Rownd, B. K., Caldwell, M., & Griffin, M. J. 2003, IEEE Trans. Microw. Theory Tech., 51, 2139

[31] Cheng, K. P., Collins, N., Angione, R., Talbert, F., Hintzen, P., Smith, E. P., Stecher, T., & The UIT Team, eds. 1997, UV/Visible Sky Gallery on CDROM

[32] Cherchneff, I. & Dwek, E. 2009, Astrophys. J., 703, 642

[33] Cherchneff, I. & Sarangi, A. 2011, Proc. Int. Astron. Union, 7, 228

[34] Conley, A. et al. 2011, Astrophys. J., 732, L35

[35] da Cunha, E., Charlot, S., & Elbaz, D. 2008, Mon. Not. R. Astron. Soc., 388, 1595

[36] Dalcanton, J. J. et al. 2009, Astrophys. J. Suppl. Ser., 183, 67

[37] Dale, D. A. et al. 2007, Astrophys. J., 655, 863

[38] de Graauw, T. et al. 2010, Astron. Astrophys., 518, L6

[39] de Vaucouleurs, G., de Vaucouleurs, A., Corwin Jr., H. G., Buta, R. J., Paturel, G., & Fouque, P. 1991, Third Reference Catalogue of Bright Galaxies, ed. Roman, N.˜G., de Vaucouleurs, G., de Vaucouleurs, A., Corwin, H.˜G., Jr., Buta, R.˜J., Paturel, G., & Fouqué, P.

[40] DeLaney, T. et al. 2010, Astrophys. J., 725, 2038

[41] Díaz-Santos, T. et al. 2013, Astrophys. J., 774, 68

[42] Dickman, R. L., Snell, R. L., & Schloerb, F. P. 1986, Astrophys. J., 309, 326

[43] Downes, D. & Solomon, P. M. 1998, Astrophys. J., 507, 615

[44] Draine, B. T. 1989, ESA, 290, 93

[45] Draine, B. T. et al. 2007, Astrophys. J., 663, 866

[46] Dunham, M. K. et al. 2010, Astrophys. J., 717, 1157

[47] Dunne, L., Eales, S., Edmunds, M., Ivison, R. J., Alexander, P., & Clements, D. L. 2000, Mon. Not. R. Astron. Soc., 315, 115

[48] Dunne, L., Eales, S. A., & Edmunds, M. G. 2003, Mon. Not. R. Astron. Soc., 341, 589

[49] Eckart, A., Cameron, M., Rothermel, H., Wild, W., Zinnecker, H., Rydbeck, G., Olberg, M., & Wiklind, T. 1990, Astrophys. J., 363, 451

[50] Elbaz, D. et al. 2011, Astron. Astrophys., 533, A119

[51] Elfhag, T., Booth, R. S., Hoeglund, B., Johansson, L. E. B., & Sandqvist, A. 1996, Astron. Astrophys. Suppl., 115, 439

[52] Engel, H. et al. 2010, Astron. Astrophys., 524, A56

[53] Etxaluze, M. et al. 2013, Astron. Astrophys., 556, A137

[54] Farrah, D. et al. 2008, Astrophys. J., 677, 957

[55] Feroz, F., Hobson, M. P., & Bridges, M. 2009, Mon. Not. R. Astron. Soc., 398, 1601

[56] Ferrière, K. 2001, Rev. Mod. Phys., 73, 1031

[57] Fixsen, D. J., Bennett, C. L., & Mather, J. C. 1999, Astrophys. J., 526, 207

[58] Flower, D. R. & Pineau des Forêts, G. 2010, Mon. Not. R. Astron. Soc., 406, 1745

[59] Fransson, C. et al. 2013, Astrophys. J., 768, 88

[60] Fulton, T. R. et al. 2010, Sp. Telesc. Instrum. 2010 Opt., 7731, 99

[61] Goicoechea, J. R. et al. 2013, Astrophys. J., 769, L13

[62] Goldsmith, P. F. & Langer, W. D. 1978, Astrophys. J., 222, 881

[63] Gordon, K. D., Engelbracht, C. W., Rieke, G. H., Misselt, K. A., Smith, J.-D. T., & Kennicutt Jr., R. C. 2008, Astrophys. J., 682, 336

[64] Green, S. 1993, Astrophys. J., 412, 436

[65] Greve, T. R., Papadopoulos, P. P., Gao, Y., & Radford, S. J. E. 2009, Astrophys. J., 692, 1432

[66] Griffin, M. J. et al. 2010, Astron. Astrophys., 518, L3

[67] Groenewegen, M. et al. 2011, Astron. Astrophys., 526, A162

[68] Hailey-Dunsheath, S. et al. 2012, Astron. J., 755, 57

[69] Harris, A., Stutzki, J., Graf, U. U., Russell, A., & Genzel, R. 1991, Astrophys. J. Lett., 382, L75

[70] Harrison, A., Henkel, C., & Russell, A. 1999, Mon. Not. R. Astron. Soc., 303, 157

[71] Higdon, S., Armus, L., Higdon, J., Soifer, B., & Spoon, H. 2006, Astrophys. J., 648, 323

[72] Hollenbach, D. J. & Tielens, A. G. G. M. 1997, Annu. Rev. Astron. Astrophys., 35, 179

[73] Howe, J. E. et al. 2000, Astrophys. J., 539, L137

[74] Imara, N. & Blitz, L. 2011, Astrophys. J., 732, 78

[75] Isensee, K., Rudnick, L., DeLaney, T., Smith, J. D., Rho, J., Reach, W. T., Kozasa, T., & Gomez, H. 2010, Astrophys. J., 725, 2059

[76] Israel, F. P. et al. 2014, 14

[77] Janka, H.-T. 2012, Annu. Rev. Nucl. Part. Sci., 62, 407

[78] Jerkstrand, A., Fransson, C., & Kozma, C. 2011, Astron. Astrophys., 530, A45

[79] Kamenetzky, J. et al. 2011, Astrophys. J., 731, 83

[80] —. 2012, Astrophys. J., 753, 70

[81] —. 2013, Astrophys. J. Lett., 773, L34

[82] Kennicutt, R. C. 1998, Annu. Rev. Astron. Astrophys., 36, 189

[83] Kennicutt, R. C. & Evans, N. J. 2012, Annu. Rev. Astron. Astrophys., 50, 531

[84] Kjæ r, K., Leibundgut, B., Fransson, C., Jerkstrand, A., & Spyromilio, J. 2010, Astron. Astrophys., 517, A51

[85] Klaas, U. et al. 2001, Astron. Astrophys., 379, 823

[86] Kruegel, . & Siebenmorgen, . 1994, Astron. Astrophys.

[87] Lakićević, M., van Loon, J. T., Patat, F., Staveley-Smith, L., & Zanardo, G. 2011, Astron. Astrophys., 532, L8

[88] Lakićević, M., van Loon, J. T., Stanke, T., de Breuck, C., & Patat, F. 2012, Astron. Astrophys., 541, L1

[89] Langer, W. D., Velusamy, T., Pineda, J. L., Willacy, K., & Goldsmith, P. F. 2014, Astron. Astrophys., 561, A122

[90] Lanz, . et al. 2013, Astrophys. J., 768

[91] Larsson, J. et al. 2013, Astrophys. J., 768, 89

[92] Le Bourlot, J., Pineau des Forêts, G., & Flower, D. R. 1999, Mon. Not. R. Astron. Soc., 305, 802

[93] Lee, J. C., Hwang, H. S., Lee, M. G., Kim, M., & Kim, S. C. 2011, Mon. Not. R. Astron. Soc., 414, 702

[94] Li, D., Goldsmith, P. F., & Melnick, G. 2004, Milky W. Surv. Struct. Evol. our Galaxy, 317, 82

[95] Liu, W. & Dalgarno, A. 1995, Astrophys. J., 454, 472

[96] Liu, W., Dalgarno, A., & Lepp, S. 1992, Astrophys. J., 396, 679

[97] Loenen, A. F. et al. 2010, Astron. Astrophys., 521, L2

[98] Lutz, D., Sturm, E., Genzel, R., Moorwood, A. F. M., Alexander, T., Netzer, H., & Sternberg, A. 2000, Astrophys. J., 536, 697

[99] Maiolino, R., Ruiz, M., Rieke, G. H., & Papadopoulos, P. 1997, Astrophys. J., 485, 552

[100] Maloney, P. & Black, J. H. 1988, Astrophys. J., 325, 389

[101] Mangum, J. G., Darling, J., Henkel, C., Menten, K. M., MacGregor, M., Svoboda, B. E., & Schinnerer, E. 2013, Astrophys. J., 779, 33

[102] Mao, R., Schulz, A., Henkel, C., Mauersberger, R., Muders, D., & Dinh-V-Trung. 2010, Astrophys. J., 724, 1336

[103] Mao, R. Q., Henkel, C., Schulz, A., Zielinsky, M., Mauersberger, R., Störzer, H., Wilson, T. L., & Gensheimer, P. 2000, Astron. Astrophys., 358, 433

[104] Matsushita, S. et al. 2009, Astrophys. J., 693, 56

[105] Matsuura, M. et al. 2011, Science (80-.)., 333, 1258

[106] Mauersberger, R., Henkel, C., Walsh, W., & Schulz, A. 1999, Astron. Astrophys., 341, 256

[107] Mayya, Y. D., Carrasco, L., & Luna, A. 2005, Astrophys. J., 628, L33

[108] McCray, R. 1993, Annu. Rev. Astron. Astrophys., 31, 175

[109] McCray, R., Immler, S., & Weiler, K. 2007, in AIP Conf. Proc., Vol. 937 (AIP), 3–14

[110] Meijerink, R. et al. 2013, Astrophys. J., 762, L16

[111] Meijerink, R., Spaans, M., & Israel, F. P. 2006, Astrophys. J., 650, L103

[112] Meijerink, R., Spaans, M., Loenen, A. F., & van der Werf, P. P. 2011, Astron. Astrophys., 525, A119

[113] Menéndez-Delmestre, K. et al. 2009, Astrophys. J., 699, 667

[114] Monje, R. R. et al. 2011, Astrophys. J. Lett., 734, L23

[115] Narayanan, D. & Krumholz, M. 2014, 18

[116] Narayanan, D., Krumholz, M., Ostriker, E. C., & Hernquist, L. 2011, Mon. Not. R. Astron. Soc., 418, 664

[117] Naylor, B. J. et al. 2010, Astrophys. J., 722, 668

[118] Ng, C., Gaensler, B., Staveley-Smith, L., Manchester, R., Kesteven, M., Ball, L., & Tzioumis, A. 2008, Astrophys. J., 684, 481

[119] Nikola, T., Stacey, G. J., Brisbin, D., Ferkinhoff, C., Hailey-Dunsheath, S., Parshley, S., & Tucker, C. 2011, Astron. J., 742, 88

[120] Nyström, O. et al. 2009, J. Infrared, Millimeter, Terahertz Waves, 30, 746

[121] Oberst, T. E. et al. 2006, Astrophys. J., 652, L125

[122] Ossenkopf, . & Henning, . 1990, Phys. Compos. Interstellar Matter

[123] Panagia, N. 1999, Proceedings, 190, 549

[124] Panagia, N., Gilmozzi, R., Macchetto, F., Adorf, H., & Kirshner, R. P. 1991, Astrophys. J. Lett., 380, L23

[125] Panuzzo, P. et al. 2010, Astron. Astrophys., 518, L37

[126] Papadopoulos, P. P. 2010, Astrophys. J., 720, 226

[127] Papadopoulos, P. P. & Greve, T. R. 2004, Astrophys. J., 615, L29

[128] Papadopoulos, P. P. & Seaquist, E. R. 1998, Astrophys. J., 492, 521

[129] —. 1999, Astrophys. J., 516, 114

[130] Papadopoulos, P. P., Thi, W., & Viti, S. 2004, Mon. Not. R. Astron. Soc., 351, 147

[131] Papadopoulos, P. P., van der Werf, P. P., Xilouris, E. M., Isaak, K. G., Gao, Y., & Mühle, S. 2012, Mon. Not. R. Astron. Soc., 426, 2601

[132] Parkin, T. J. et al. 2014, Astrophys. J., 787, 16

[133] Pereira-Santaella, M. et al. 2013, Astrophys. J., 768, 55

[134] Pilbratt, G. L. et al. 2010, Astron. Astrophys., 518, L1

[135] Pineda, J. L., Langer, W. D., Velusamy, T., & Goldsmith, P. F. 2013, Astron. Astrophys., 554, A103

[136] Planck Collaboration et al. 2011, Astron. Astrophys., 536, 7

[137] Pon, A., Johnstone, D., & Kaufman, M. J. 2012, Astrophys. J., 748, 25

[138] Pope, A. et al. 2006, Mon. Not. R. Astron. Soc., 370, 1185

[139] Rangwala, N. et al. 2011, Astrophys. J., 743, 94

[140] Rémy-Ruyer, A. et al. 2014, Astron. Astrophys., 563, A31

[141] Rho, J., Onaka, T., Cami, J., & Reach, W. 2012, Astrophys. J., 747, L6

[142] Rickard, L. J., Palmer, P., Morris, M., Turner, B. E., & Zuckerman, B. 1975, Astrophys. J., 199, L75

[143] Rigopoulou, D. et al. 2013, Mon. Not. R. Astron. Soc., 434, 2051

[144] Rigopoulou, D., Kunze, D., Lutz, D., Genzel, R., & Moorwood, A. F. M. 2002, Astron. Astrophys., 389, 374

[145] Rodighiero, G. et al. 2011, Astrophys. J., 739, L40

[146] Roussel, H. et al. 2007, Astrophys. J., 669, 959

[147] —. 2010, Astron. Astrophys., 518, L66

[148] Rupke, D. S. N., Veilleux, S., & Baker, A. J. 2008, Astrophys. J., 674, 172

[149] Sanders, D. B., Mazzarella, J. M., Kim, D., Surace, J. A., & Soifer, B. T. 2003, Astron. J., 126, 1607

[150] Sanders, D. B., Scoville, N. Z., & Soifer, B. T. 1991, Astrophys. J., 370, 158

[151] Sandqvist, A. 1999, Astron. Astrophys.

[152] Sandqvist, ., Joersaeter, ., & Lindblad, . 1995, Astron. Astrophys.

[153] Schilke, P., Carlstrom, J. E., Keene, J., & Phillips, T. G. 1993, Astrophys. J. Lett., 417, L67

[154] Schirm, M. R. P. et al. 2014, Astrophys. J.

[155] Scott, K. S. et al. 2011, Astrophys. J., 733, 29

[156] Scoville, N. Z., Yun, M. S., & Bryant, P. M. 1997, Astrophys. J., 484, 702

[157] Sliwa, K. et al. 2013, Astrophys. J., 777, 126

[158] Sliwa, K., Wilson, C. D., Petitpas, G. R., Armus, L., Juvela, M., Matsushita, S., Peck, A. B., & Yun, M. S. 2012, arXiv, astro-ph.G

[159] Solomon, P. M. & de Zafra, R. 1975, Astrophys. J., 199, L79

[160] Solomon, P. M., Downes, D., Radford, S. J. E., & Barrett, J. W. 1997, Astrophys. J., 478, 144

[161] Spinoglio, L. et al. 2012, Astrophys. J., 758, 108

[162] Strickland, D. K. & Heckman, T. M. 2007, Astrophys. J., 658, 258

[163] Stutzki, J. et al. 1997, Astrophys. J. Lett., 477, L33

[164] Swinbank, A. M. et al. 2013, Mon. Not. R. Astron. Soc., 438, 1267

[165] Swinyard, B. M. et al. 2010, Astron. Astrophys., 518, L4

[166] Taylor, C. L., Walter, F., & Yun, M. S. 2001, Astrophys. J., 562, L43

[167] Temi, P., Brighenti, F., & Mathews, W. G. 2009, Astrophys. J., 707, 890

[168] Tielens, A. G. G. M. 2005, The Physics and Chemistry of the Interstellar Medium, 510

[169] Tremonti, C. & Heckman, T. 2004, Astrophys. J., 613, 898

[170] U, V. et al. 2012, Astrophys. J. Suppl. Ser., 203, 9

[171] van der Tak, F. F. S., Black, J. H., Schöier, F. L., Jansen, D. J., & van Dishoeck, E. F. 2007, Astron. Astrophys., 468, 627

[172] van der Werf, P. P. et al. 2010, Astron. Astrophys., 518, L42

[173] van Dishoeck, E. F. & Black, J. H. 1986, Astrophys. J. Suppl. Ser., 62, 109

[174] —. 1988, Astrophys. J., 334, 771

[175] van Dishoeck, E. F. et al. 2011, Publ. Astron. Soc. Pacific, 123, 138

[176] VERITAS Collaboration et al. 2009, Nature, 462, 770

[177] Walter, F., Weiß, A., Downes, D., Decarli, R., & Henkel, C. 2011, Astrophys. J., 730, 18

[178] Walter, F., Weiss, A., & Scoville, N. 2002, Astrophys. J., 580, L21

[179] Ward, J. S., Zmuidzinas, J., Harris, A. I., & Isaak, K. G. 2003, Astrophys. J., 587, 171

[180] Weiß, A., Neininger, N., Hüttemeister, S., & Klein, U. 2001, Astron. Astrophys., 365, 571

[181] Weiß, A. et al. 2010, Astron. Astrophys., 521, L1

[182] Weiß, A., Walter, F., & Scoville, N. Z. 2005, Astron. Astrophys., 438, 533

[183] White, G. J., Ellison, B., Claude, S., Dent, W. R. F., & Matheson, D. N. 1994, Astron. Astrophys., 284, L23

[184] Wild, W., Harris, A. I., Eckart, A., Genzel, R., Graf, U. U., Jackson, J. M., Russell, A. P. G., & Stutzki, J. 1992, Astron. Astrophys., 265, 447

[185] Wild, . & Eckart, . 2000, Astron. Astrophys.

[186] Wilson, C. D. 1997, Astrophys. J., 487, L49

[187] Wilson, C. D. et al. 2008, Astrophys. J. Suppl. Ser., 178, 189

[188] Wilson, R. W., Jefferts, K. B., & Penzias, A. A. 1970, Astrophys. J., 161, L43

[189] Wolfire, M. G., Hollenbach, D., & McKee, C. F. 2010, Astrophys. J., 716, 1191

[190] Woosley, S. E. 1988, Astrophys. J., 330, 218

[191] Wu, R. et al. 2014, 1

[192] Yang, B., Stancil, P., Balakrishnan, N., & Forrey, R. 2010, Astrophys. J., 718, 1062

[193] Yao, L., Seaquist, E. R., Kuno, N., & Dunne, L. 2003, Astrophys. J., 588, 771

[194] Young, J. S. et al. 1995, Astrophys. J. Suppl. Ser., 98, 219

[195] Young, L. M. et al. 2011, Mon. Not. R. Astron. Soc., 414, 940

[196] Yun, M. S., Ho, P. T. P., & Lo, K. Y. 1993, Astrophys. J., 411, L17

[197] Zanardo, G., Staveley-Smith, L., Ng, C., Gaensler, B., Potter, T., Manchester, R., & Tzioumis, A. 2013, arXiv

[198] Zhu, M., Seaquist, E. R., & Kuno, N. 2003, Astrophys. J., 588, 243

Appendix A

M82 Integrated Line Flux Maps

The following integrated flux maps of M82 are the complement to Figure 3.2. In that chapter, only the CO J$=4\rightarrow3$ line was shown, this appendix includes the maps of other lines. These maps do not include beam correction or convolution. Black corresponds to the lowest flux or zero if any fluxes are negative, at which point the colorbar becomes purple. The bottom half of each page is a map of signal/noise, though the color bar tops out at 20 in order to better illustrate which pixels are near the threshold of detectability. On the color bar, black corresponds to the lowest signal/noise or three if any pixels have S/N less than three, at which point the colorbar becomes purple.

Figures A.1 to Figures A.6 are those lines detected in the SLW for a pixel size of $9\farcs5$. Figures A.7 to Figures A.12 are SSW lines with $9\farcs5$ pixels. Finally, Figures A.13 to A.19 are SLW lines again with a pixel size of $19''$.

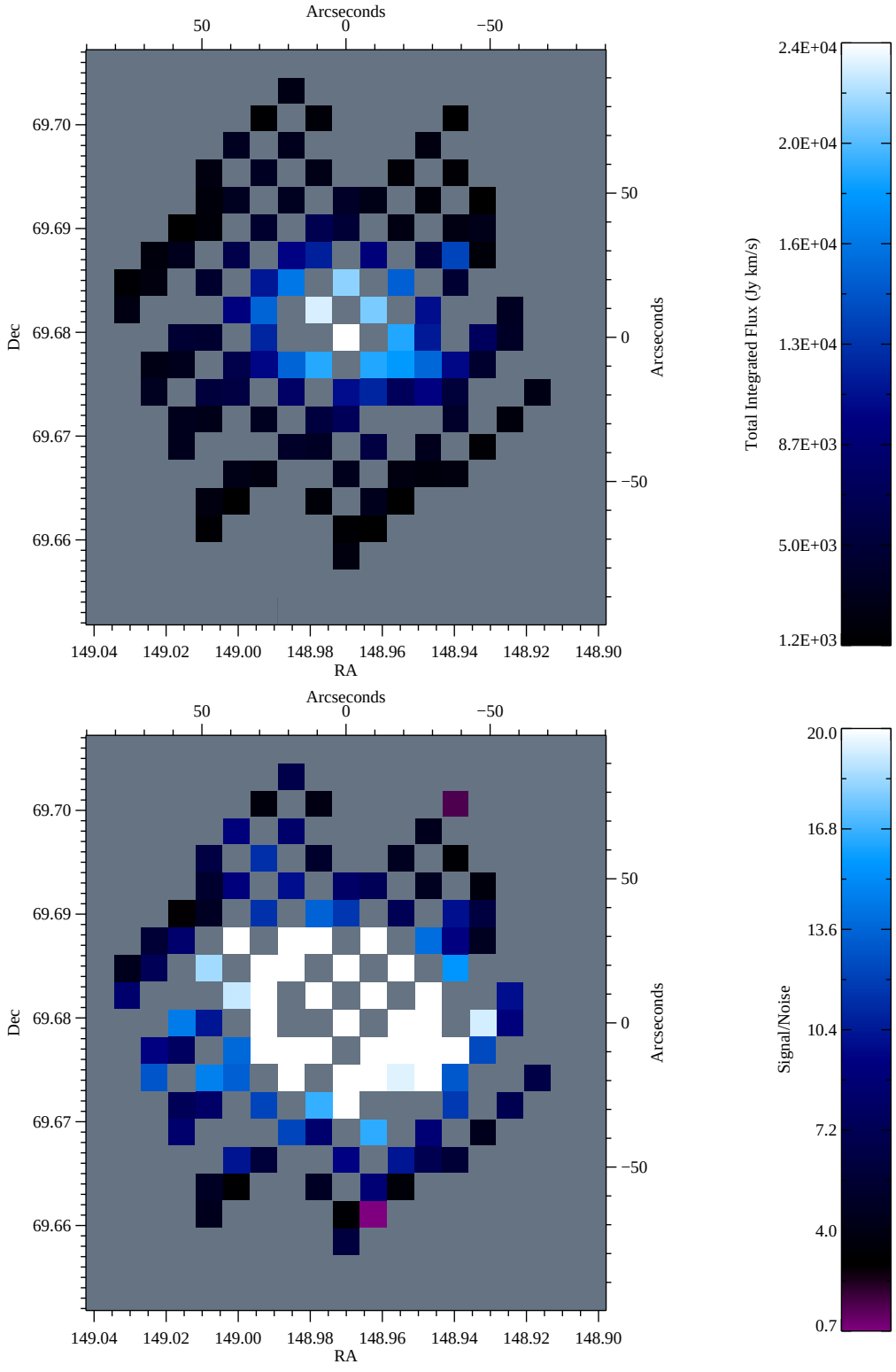

Figure A.1 Integrated Flux (top) and Signal/Noise (bottom) maps for CI J = 1 → 0.

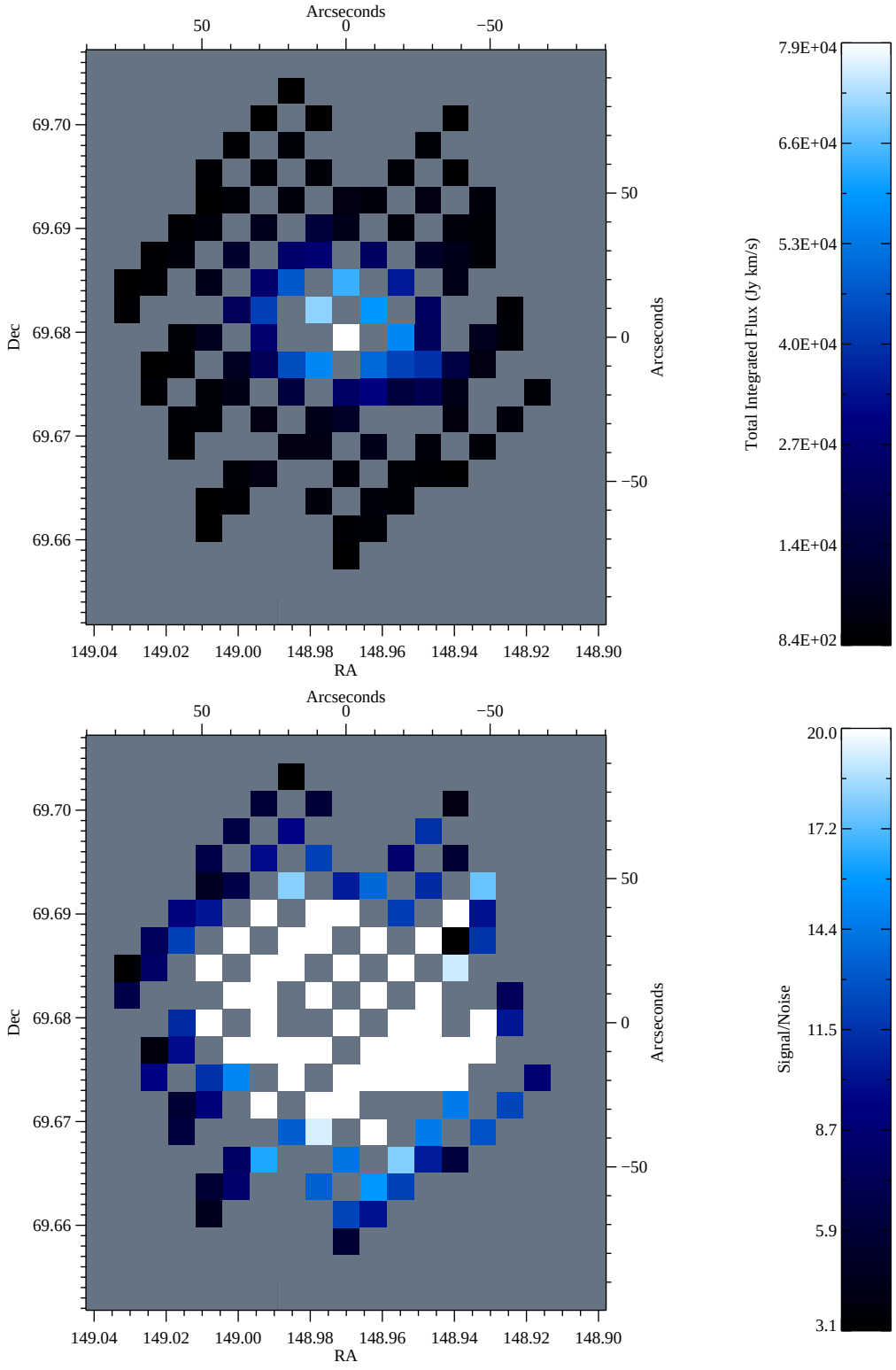

Figure A.2 Integrated Flux (top) and Signal/Noise (bottom) maps for CO J = 5 → 4.

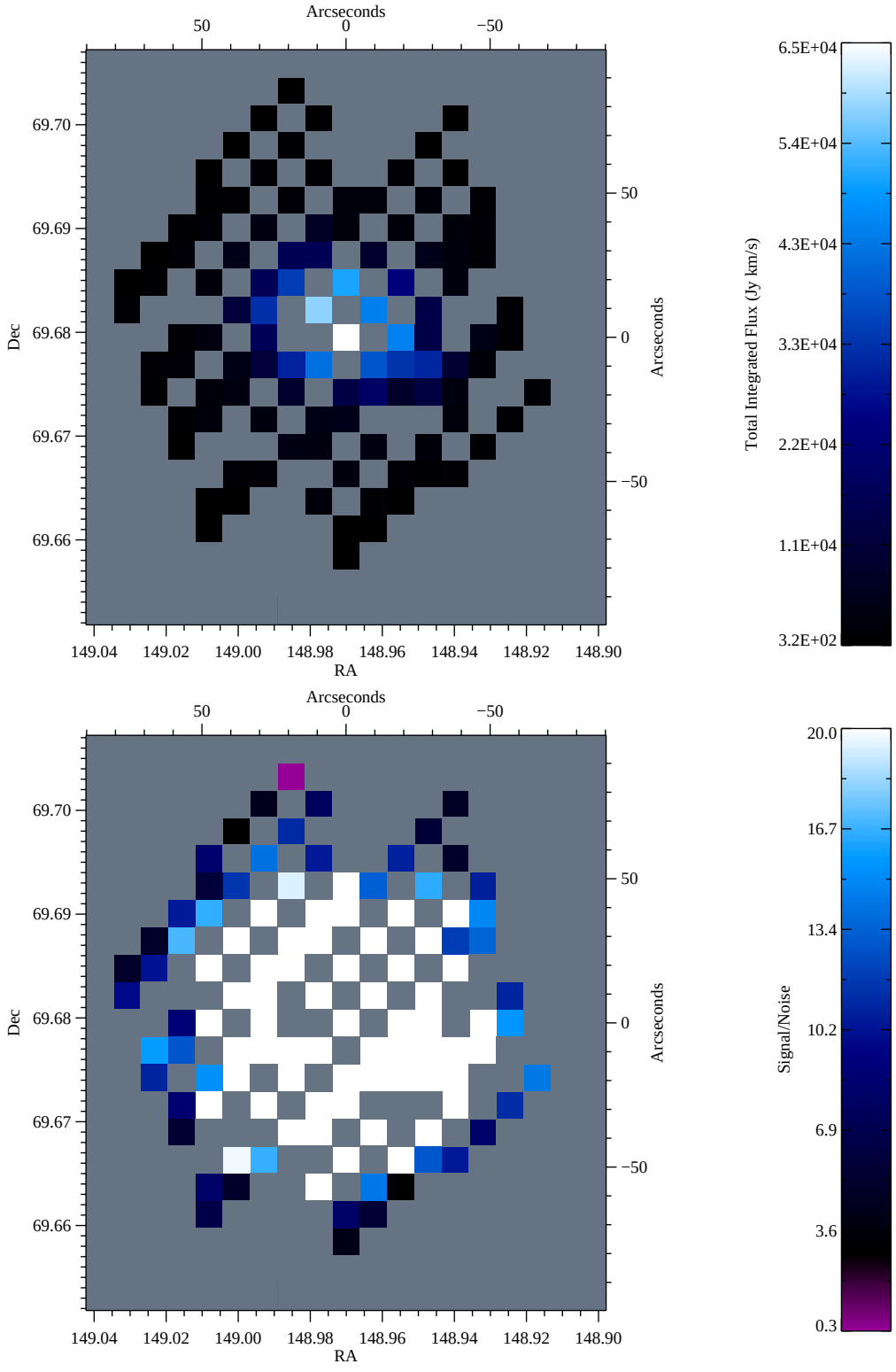

Figure A.3 Integrated Flux (top) and Signal/Noise (bottom) maps for CO J = 6 → 5.

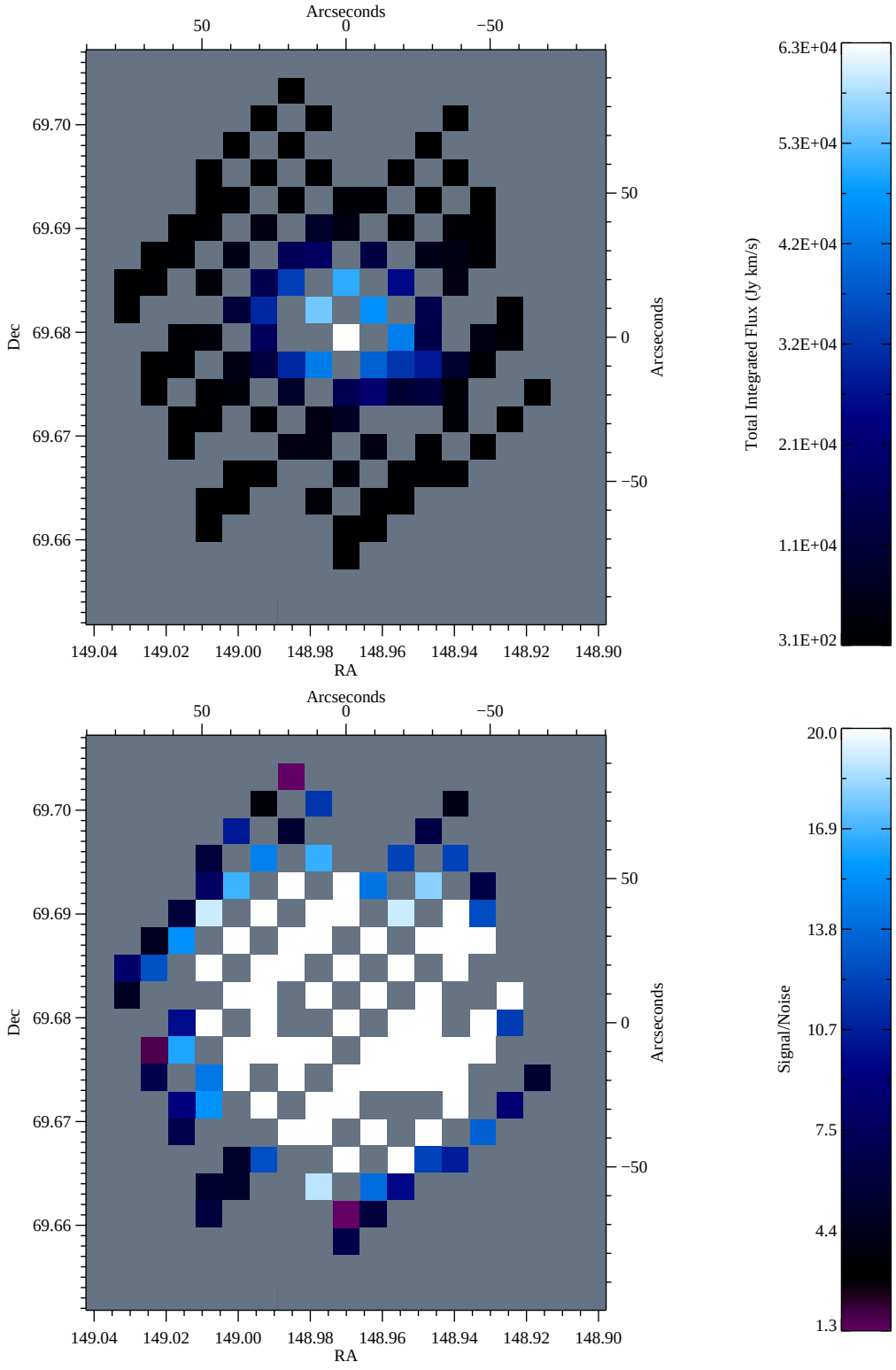

Figure A.4 Integrated Flux (top) and Signal/Noise (bottom) maps for CO J = 7 → 6.

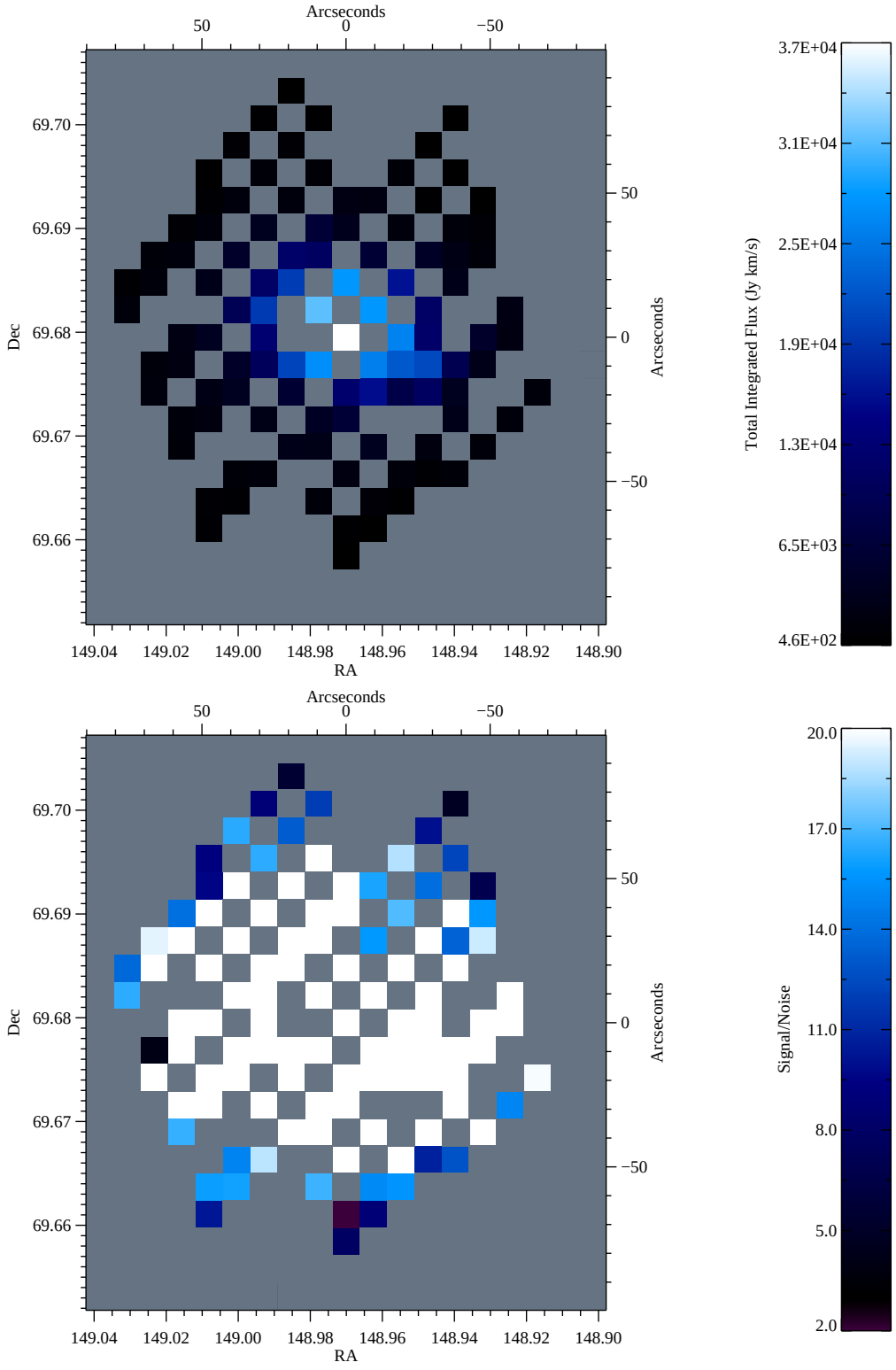

Figure A.5 Integrated Flux (top) and Signal/Noise (bottom) maps for CI J = 2 → 1.

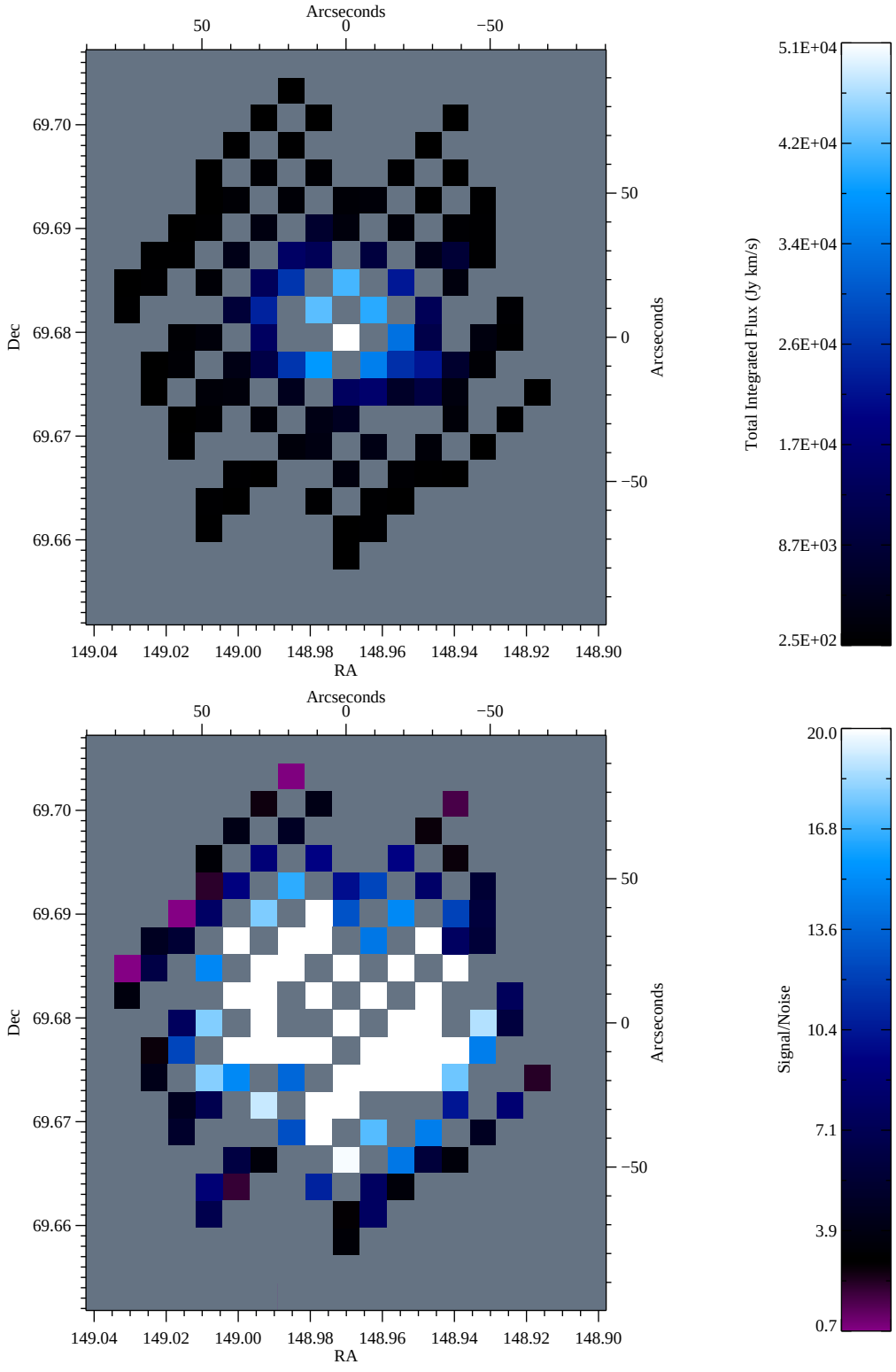

Figure A.6 Integrated Flux (top) and Signal/Noise (bottom) maps for CO J = 8 → 7.

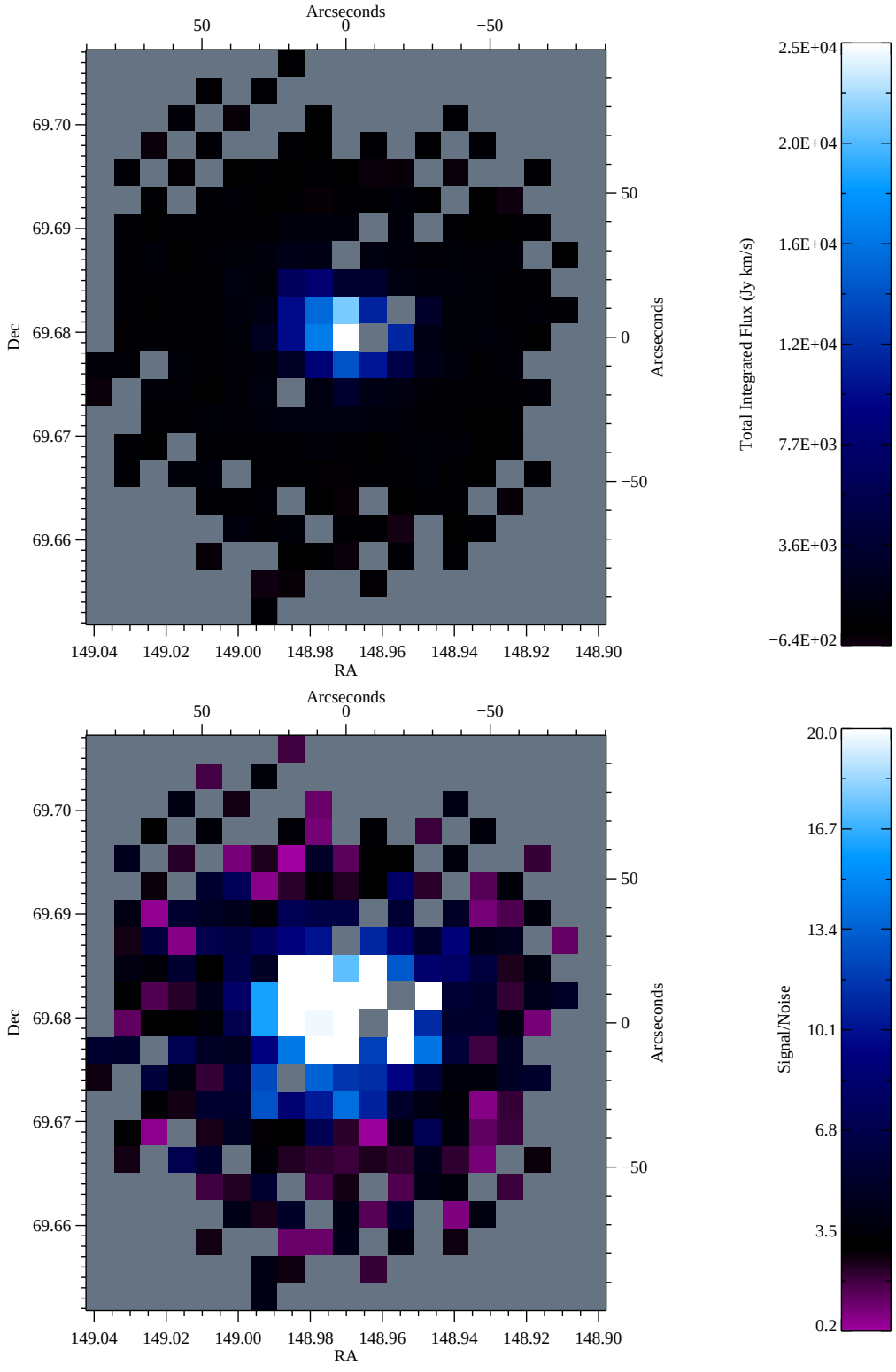

Figure A.7 Integrated Flux (top) and Signal/Noise (bottom) maps for CO J = 9 → 8.

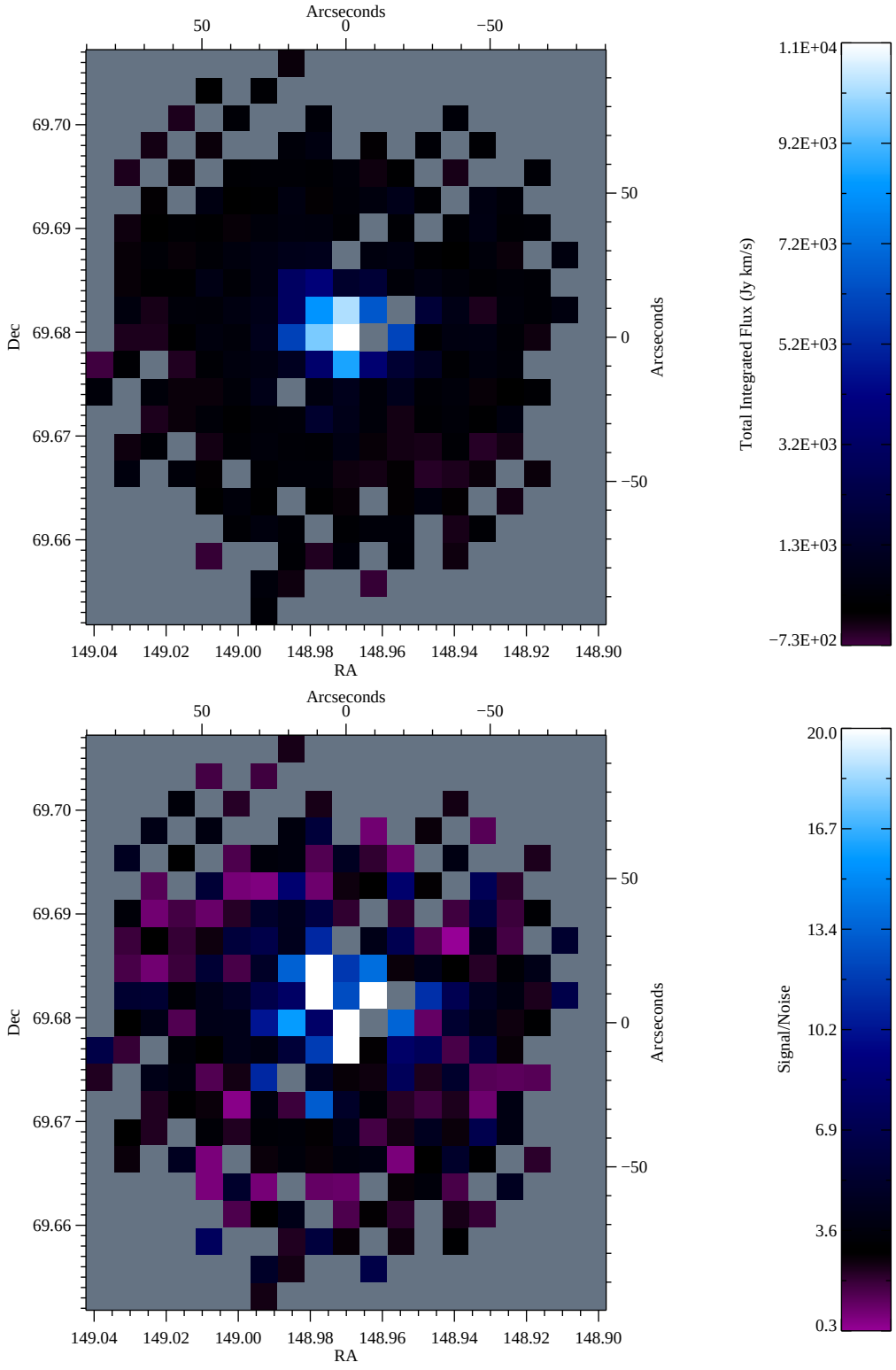

Figure A.8 Integrated Flux (top) and Signal/Noise (bottom) maps for CO J = 10 → 9.

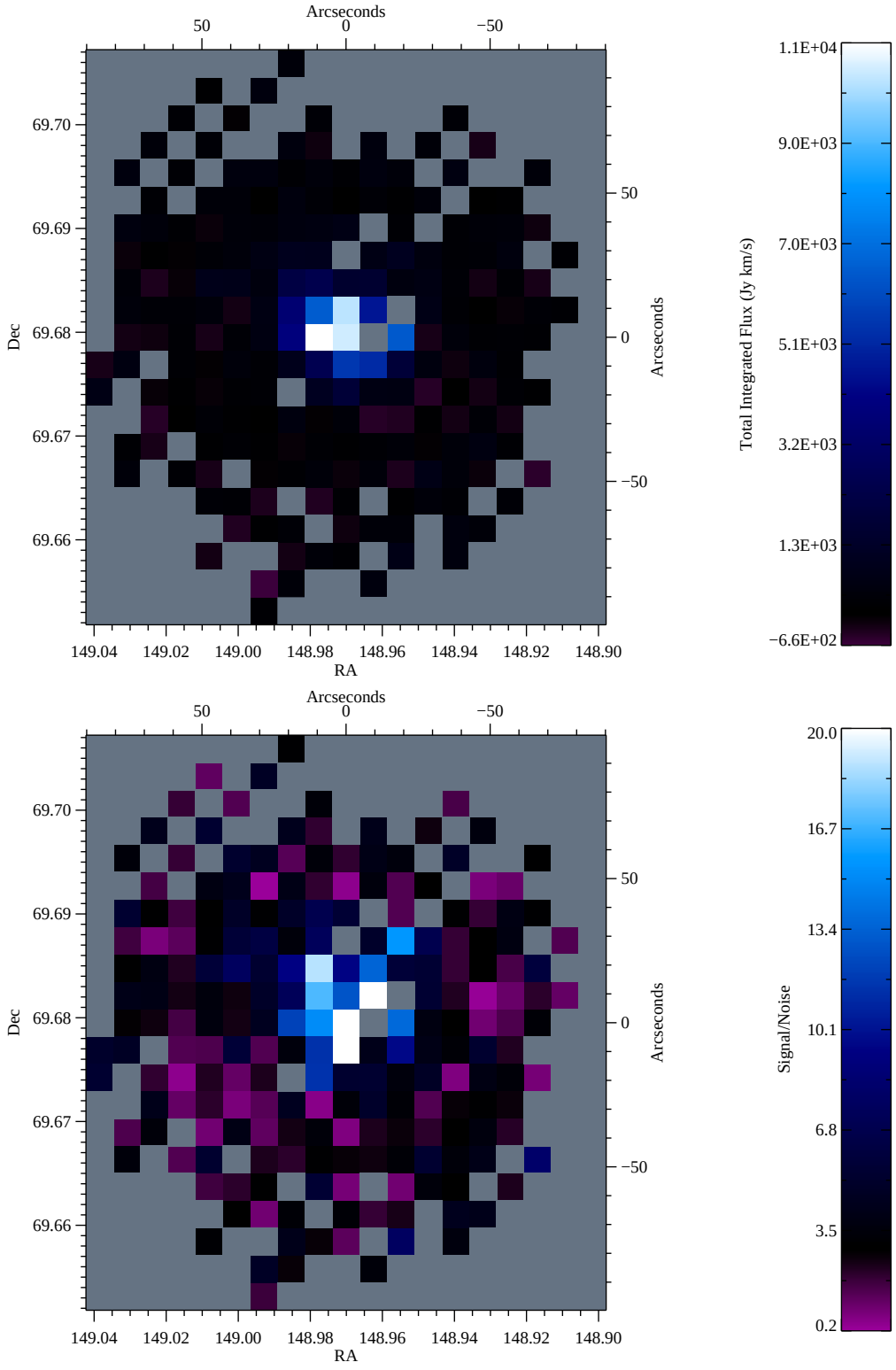

Figure A.9 Integrated Flux (top) and Signal/Noise (bottom) maps for CO J = 11 → 10.

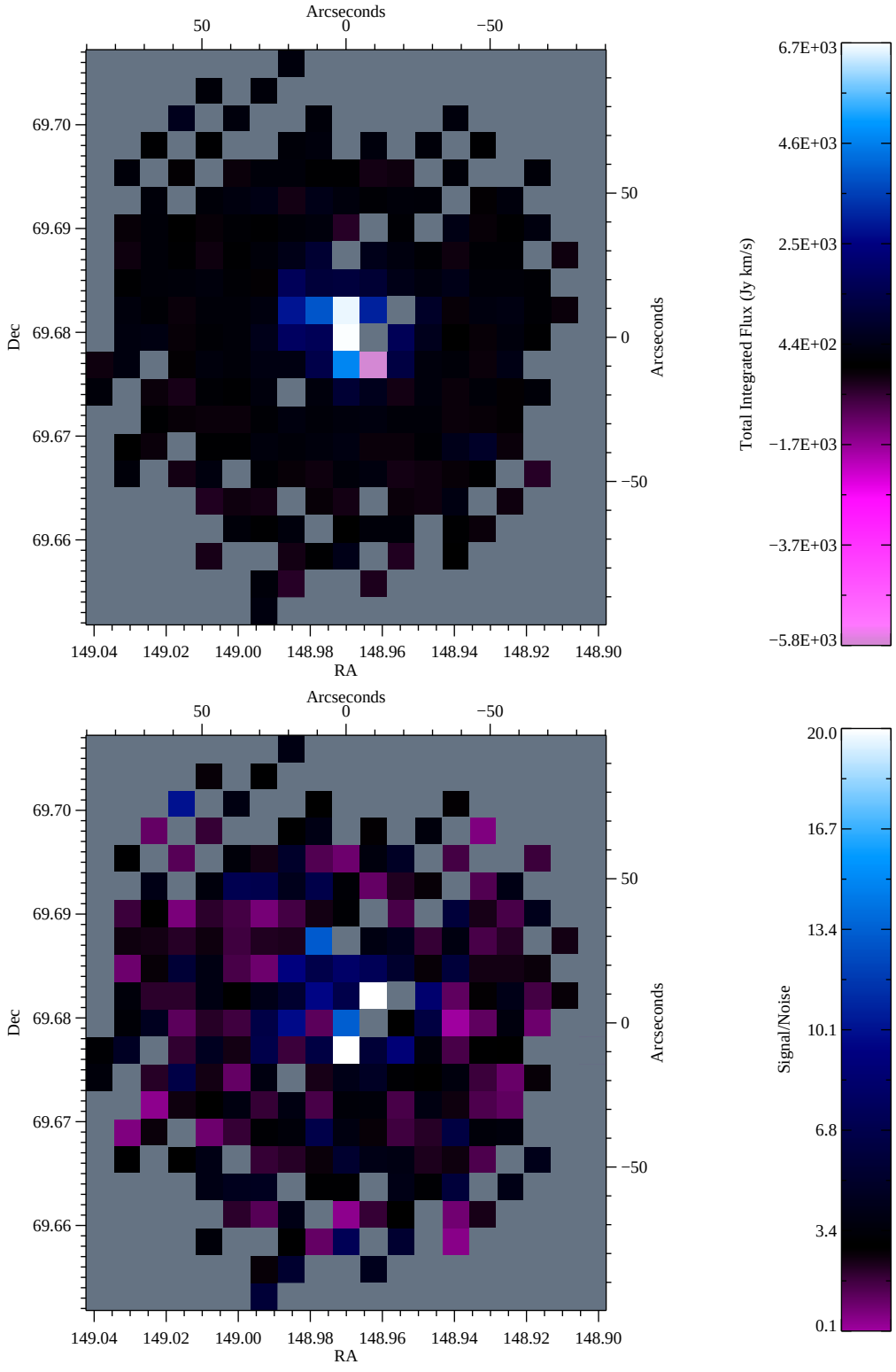

Figure A.10 Integrated Flux (top) and Signal/Noise (bottom) maps for CO J = 12 → 11.

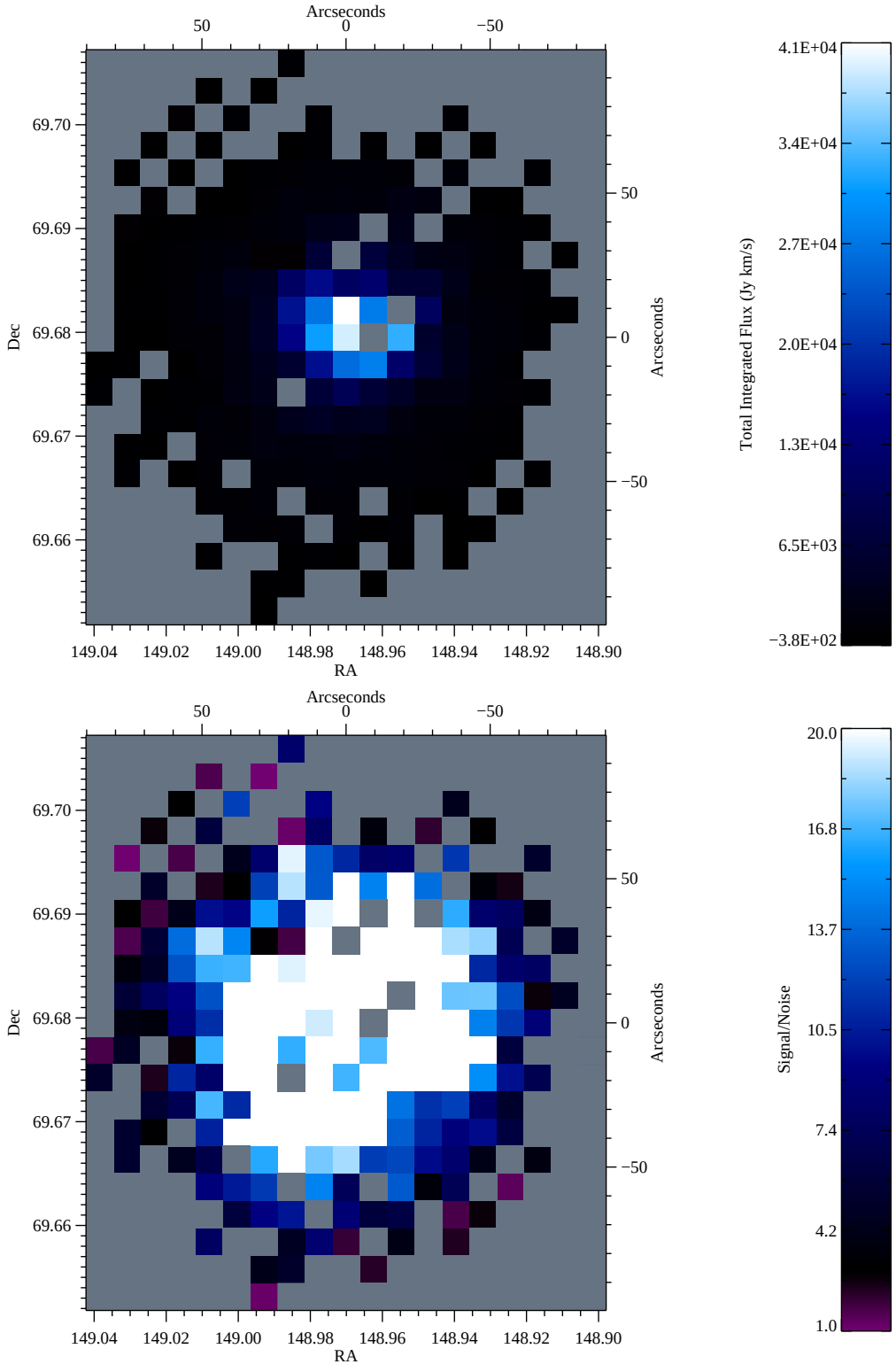

Figure A.11 Integrated Flux (top) and Signal/Noise (bottom) maps for NII.

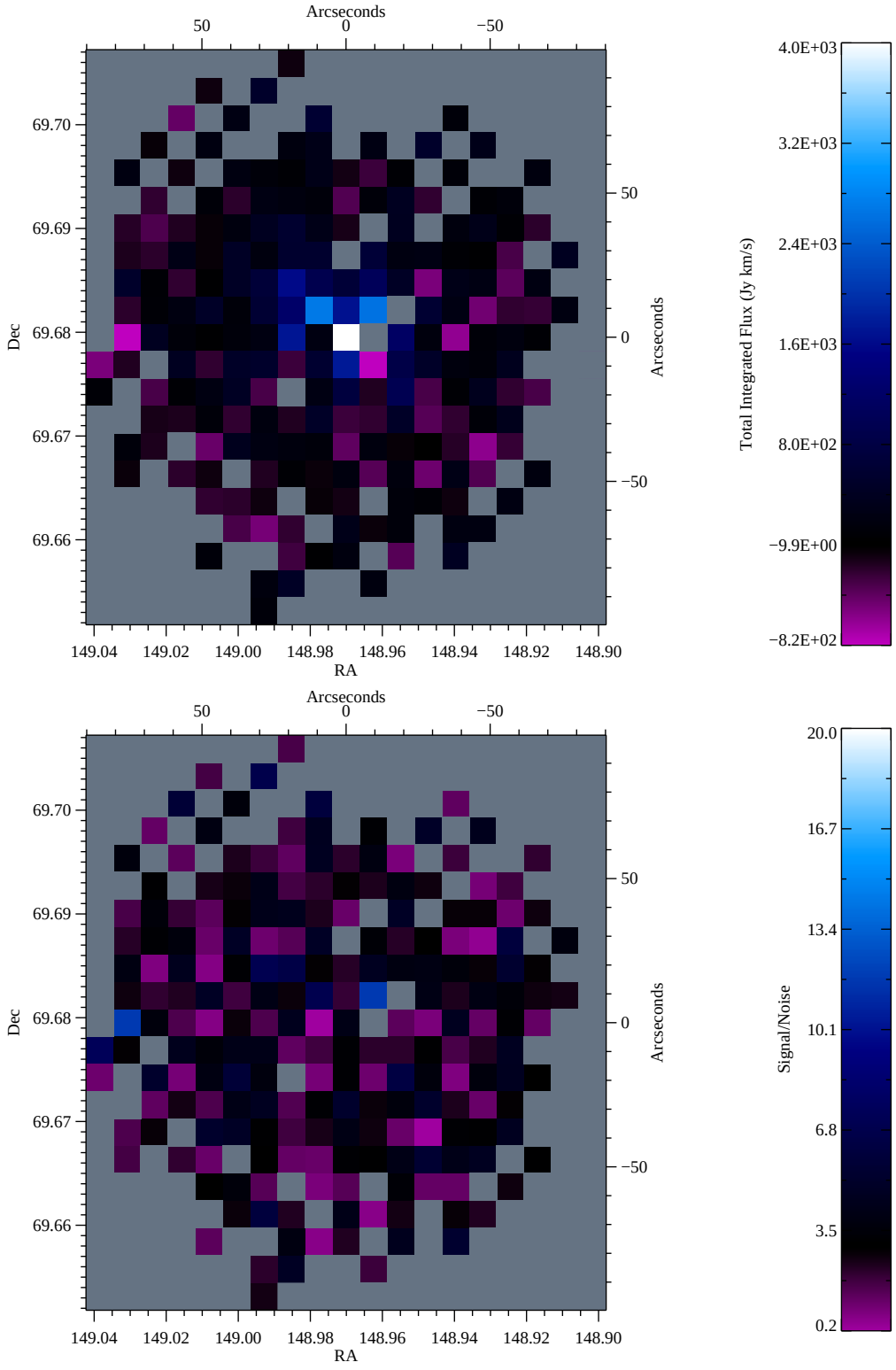

Figure A.12 Integrated Flux (top) and Signal/Noise (bottom) maps for CO J = 13 → 12.

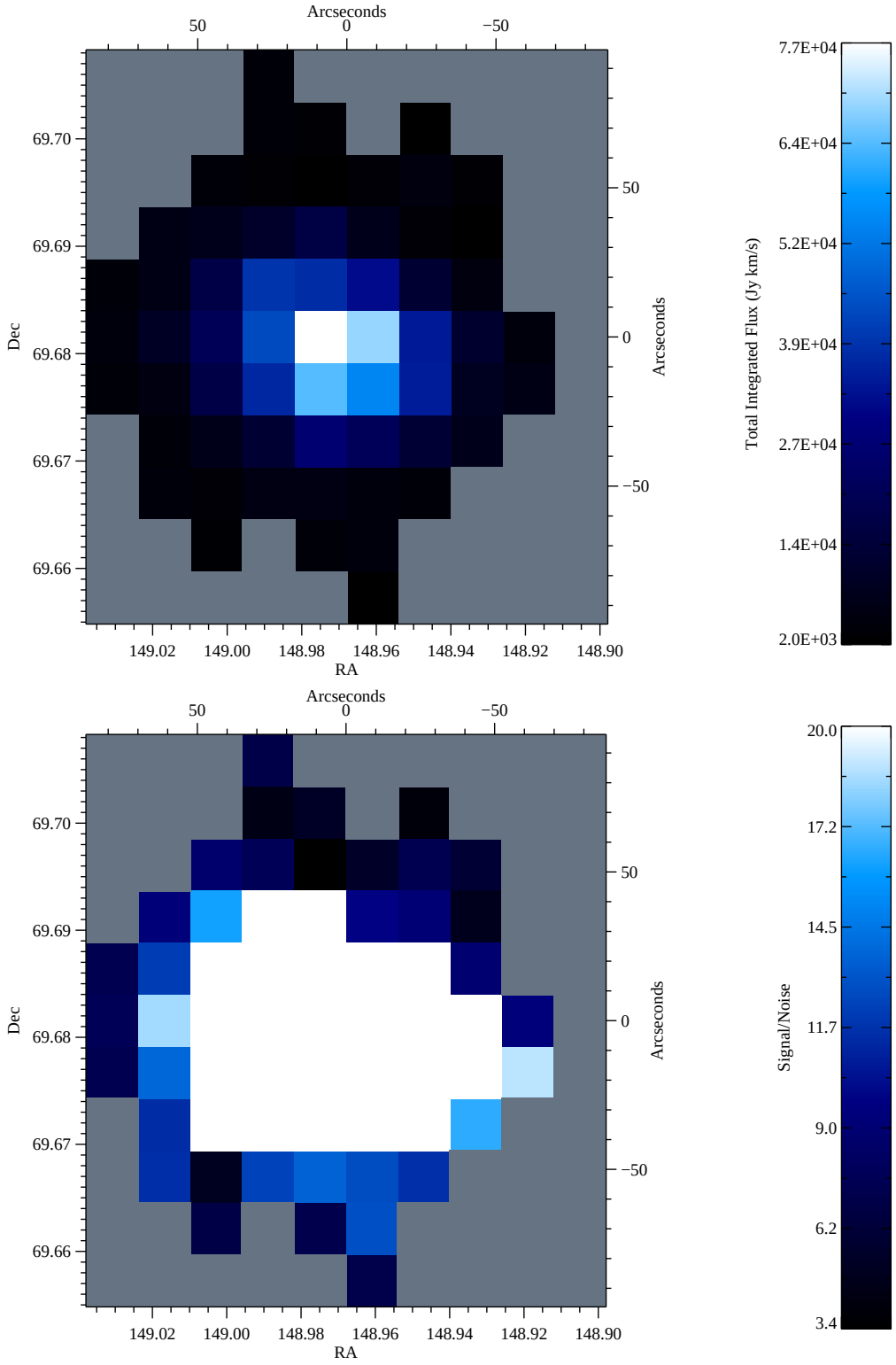

Figure A.13 Integrated Flux (top) and Signal/Noise (bottom) maps for CO J = 4→3 (19″).

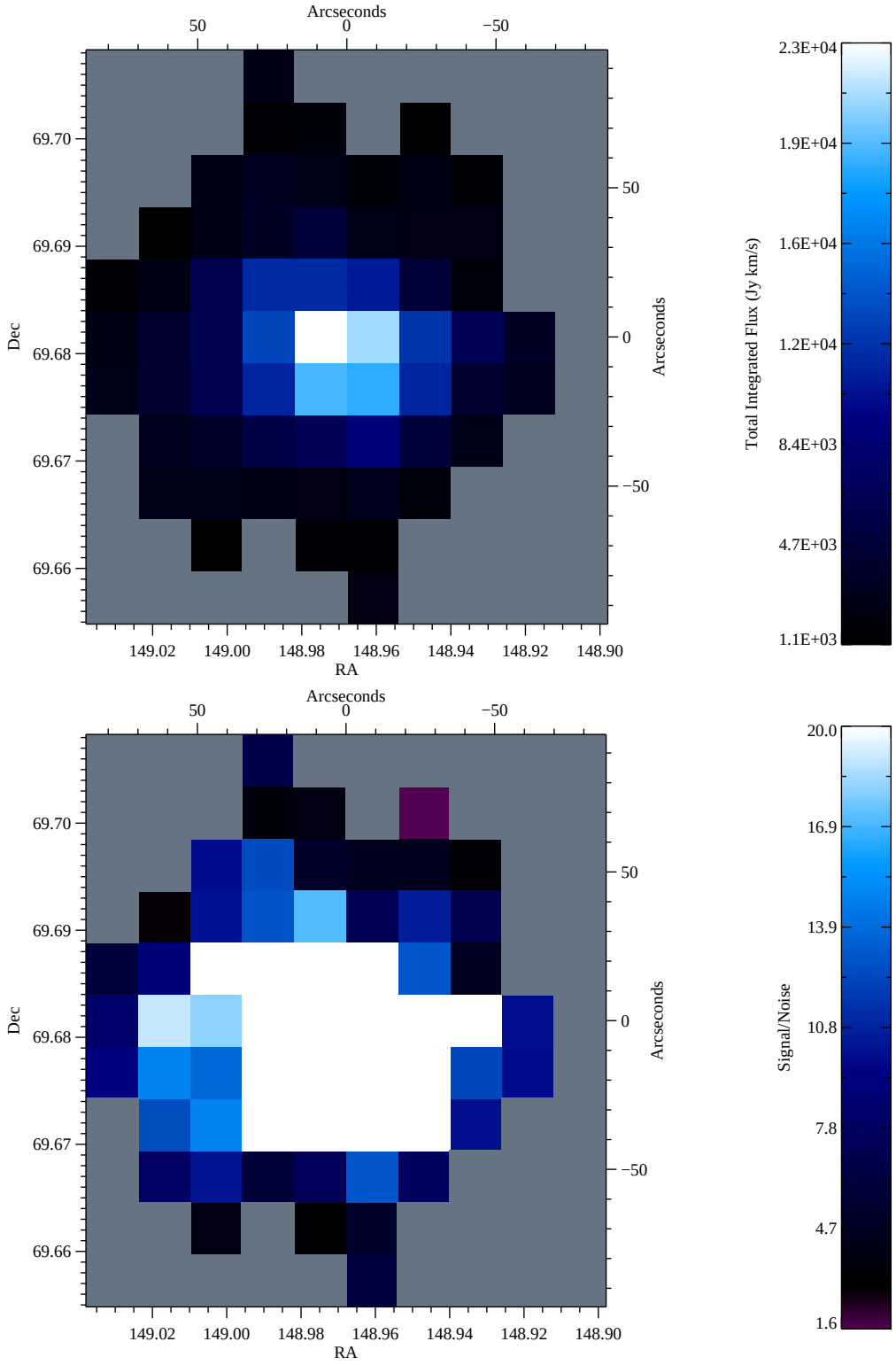

Figure A.14 Integrated Flux (top) and Signal/Noise (bottom) maps for CI J = 1 → 0 (19″).

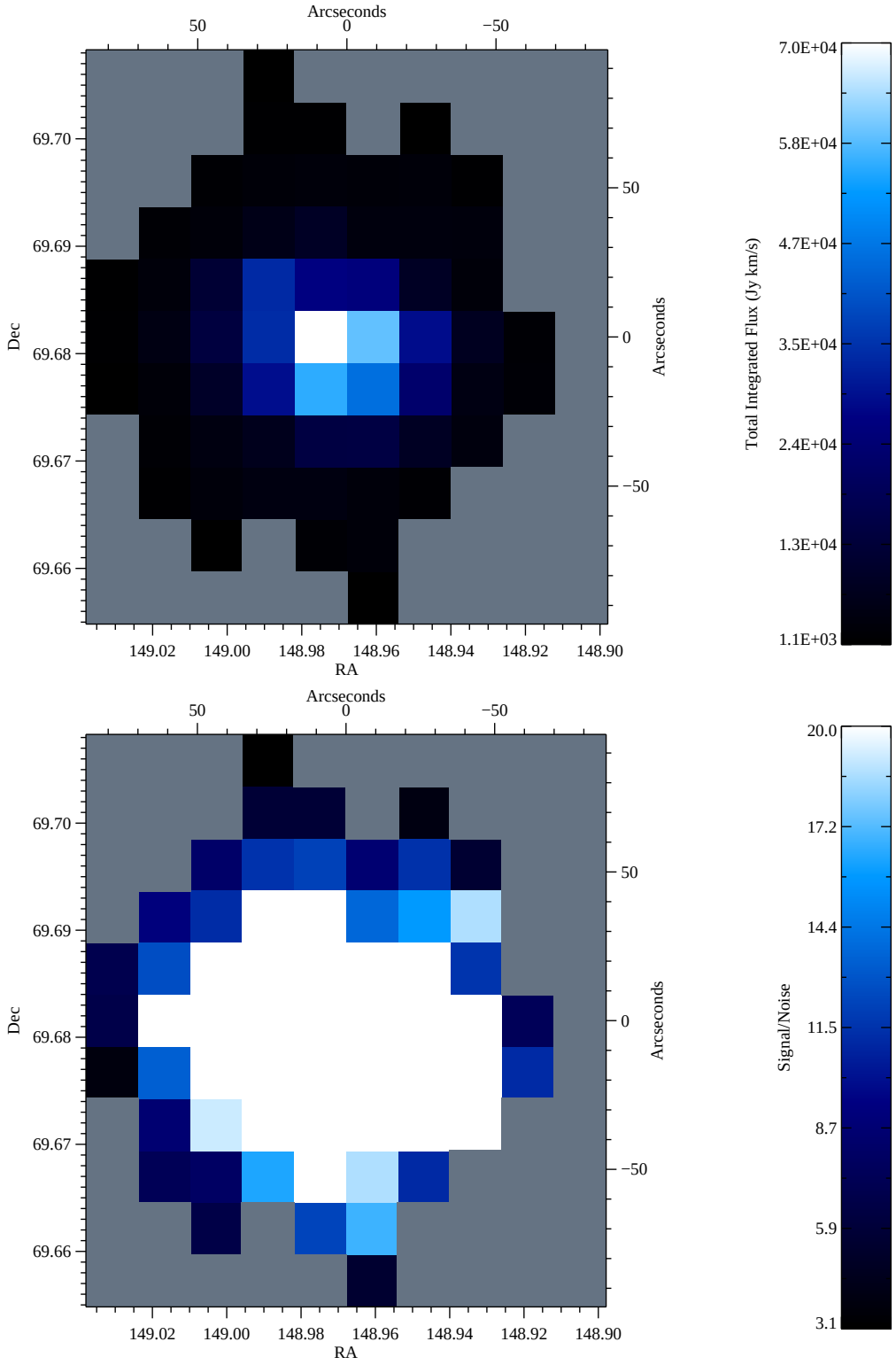

Figure A.15 Integrated Flux (top) and Signal/Noise (bottom) maps for CO J = 5 → 4 (19″).

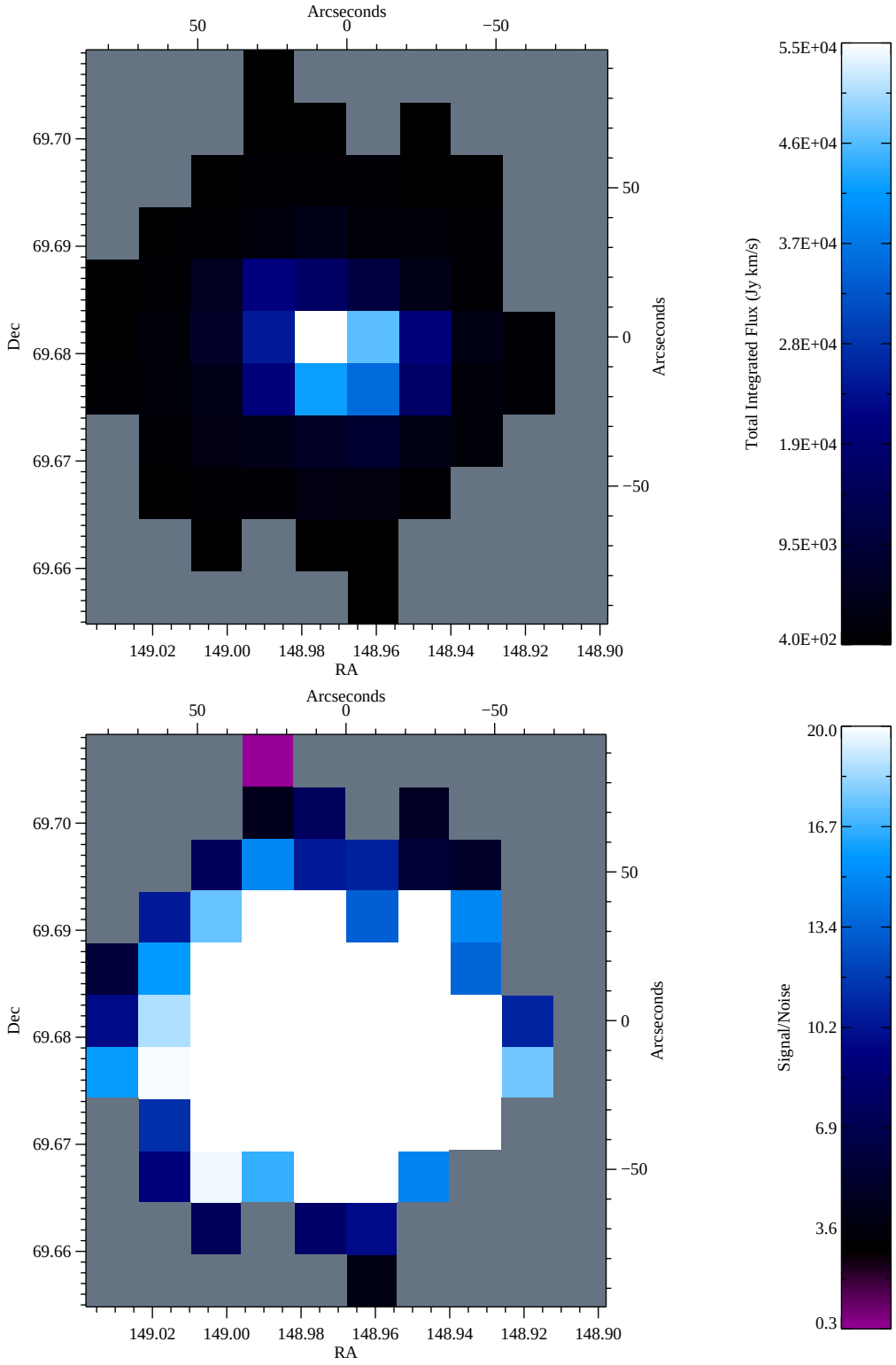

Figure A.16 Integrated Flux (top) and Signal/Noise (bottom) maps for CO J = 6 → 5 (19″).

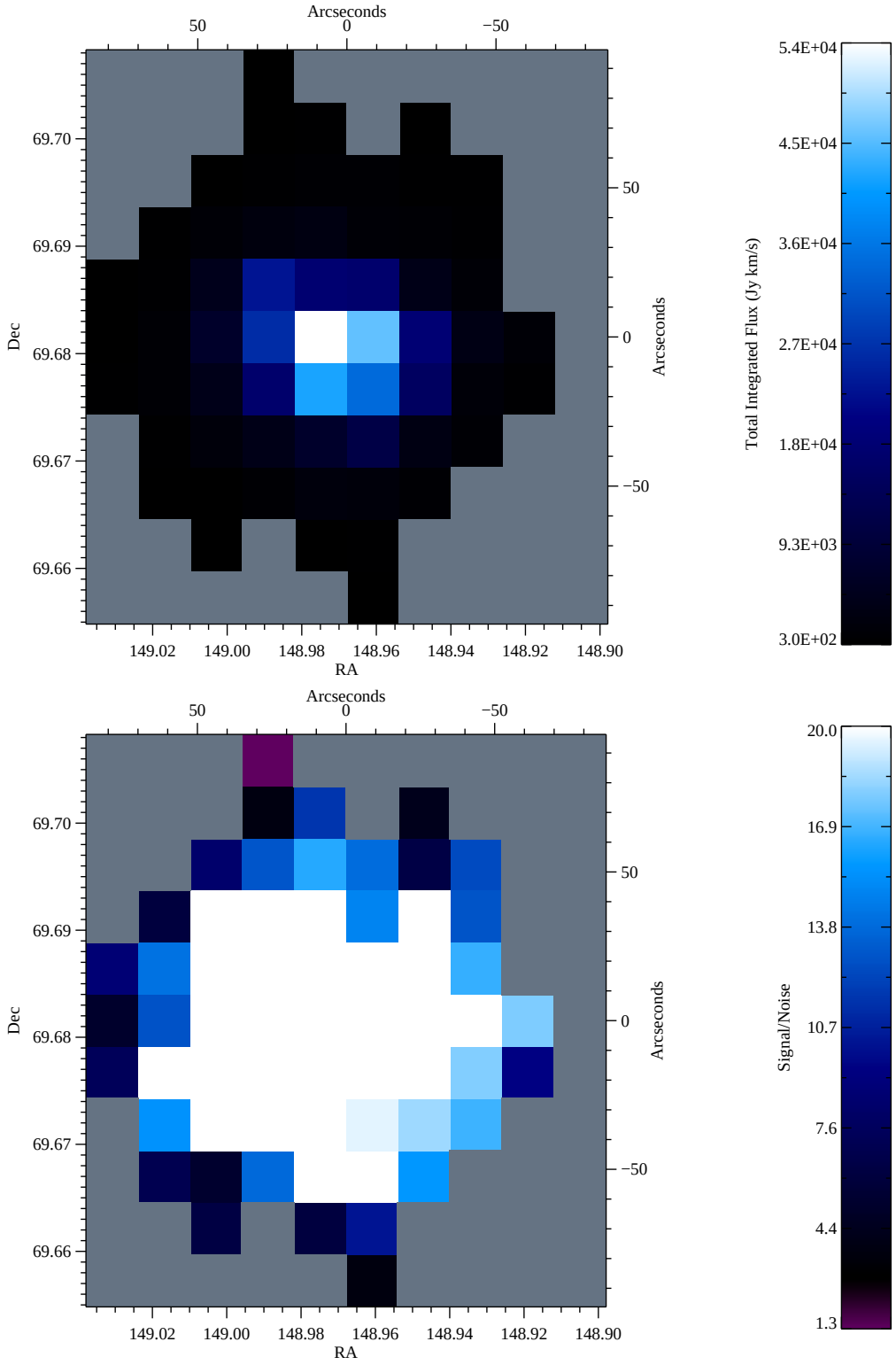

Figure A.17 Integrated Flux (top) and Signal/Noise (bottom) maps for CO J = 7→6 (19″).

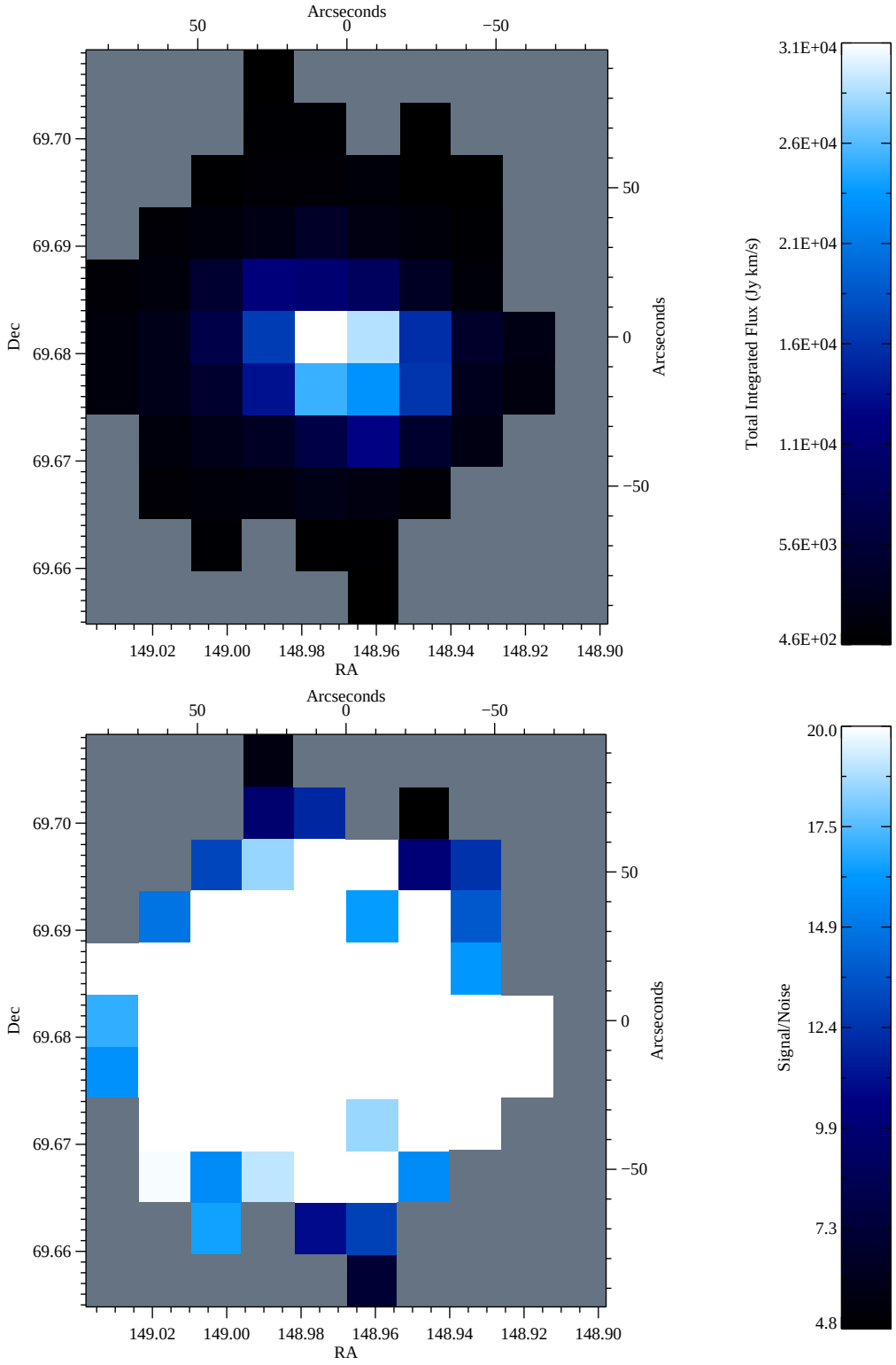

Figure A.18 Integrated Flux (top) and Signal/Noise (bottom) maps for CI J = 2 → 1 (19″).

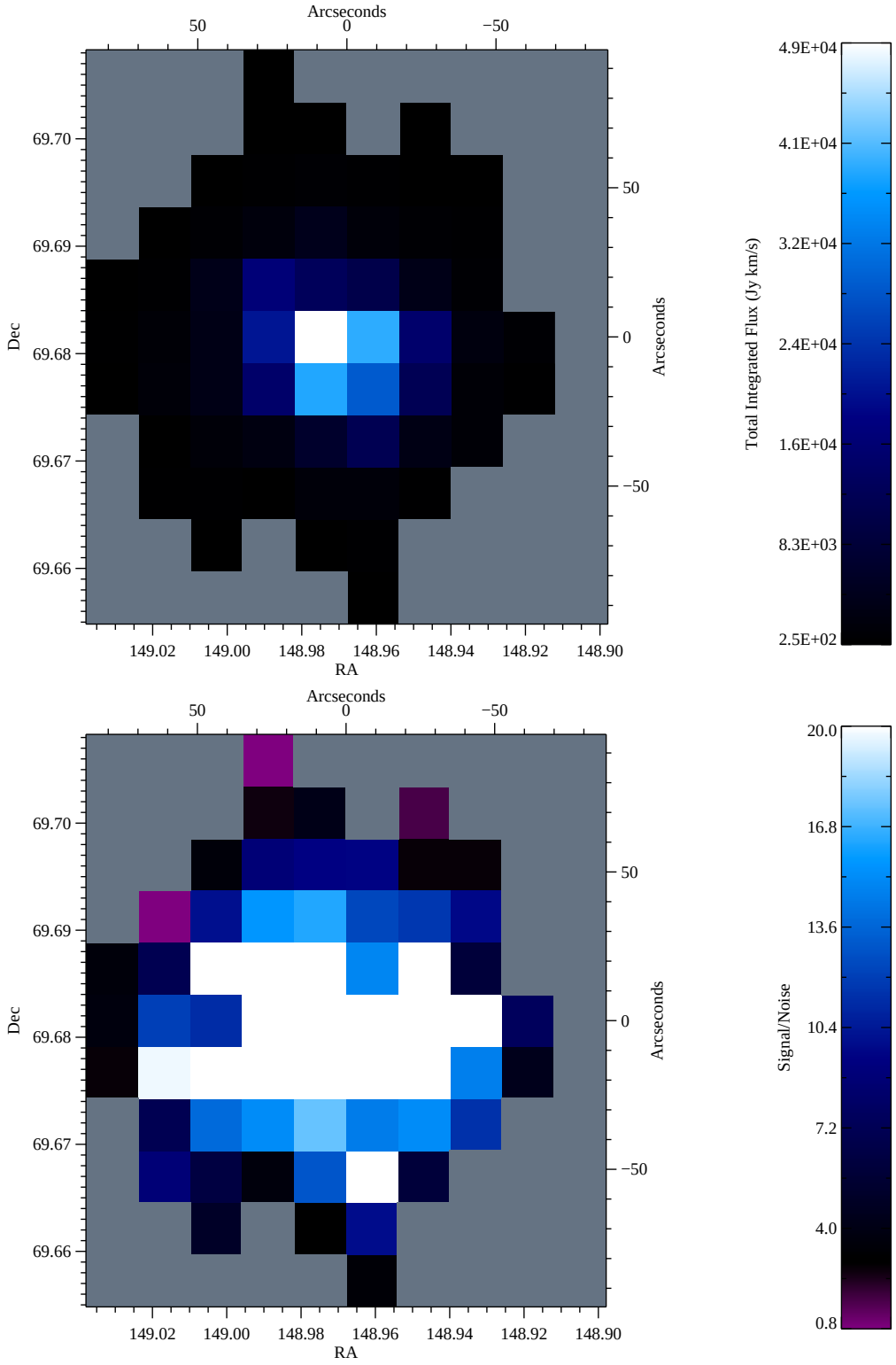

Figure A.19 Integrated Flux (top) and Signal/Noise (bottom) maps for CO J = 8 → 7 (19″).

Appendix B

Notes on Individual Galaxies in Survey

In this appendix, we discuss both the treatment of extended galaxy data, when applicable, and compare to previous modeling results, which when done on an individual basis, often include more specifics than presented here. To create a reasonable pipeline for application for a large number of galaxies with limited supplemental information, we did not include such information, but notable cases are discussed here. Additionally, Figure B.1 illustrates the position of the FTS beam for the three galaxies with multiple pointed observations.

B.0.1 The Antennae: NGC 4038/Overlap

This pair of merging galaxies is very extended on the sky (Figure B.1). Our H_2 lines come from [19], which measured the emission at multiple locations in the overlap region. We use a sum of Peaks 1, 2, 3, and 5 for this region; S(3) is an upper limit. Only one pointing was measured for the NGC 4038 nucleus, which we only use for S(0), due to the small slit size of S(3). We instead use Rigopoulou et al. [144] for S(1) and S(2).

The full FTS maps, from which our spectra are drawn, were modeled with RADEX by Schirm et al. [154]. Two components were also used, but using an iterative process to model the low-J lines, then high-J lines, and back and forth until convergence. Additionally, they modeled multiple pixels in an FTS map, but we focus here on the two corresponding to the NGC 4038 nucleus and the Overlap region. Their best-fit CO SLEDs indicate less warm component emission contribution to the mid-J lines than ours for NGC 4038, and more for the Overlap region. This illustrates how an

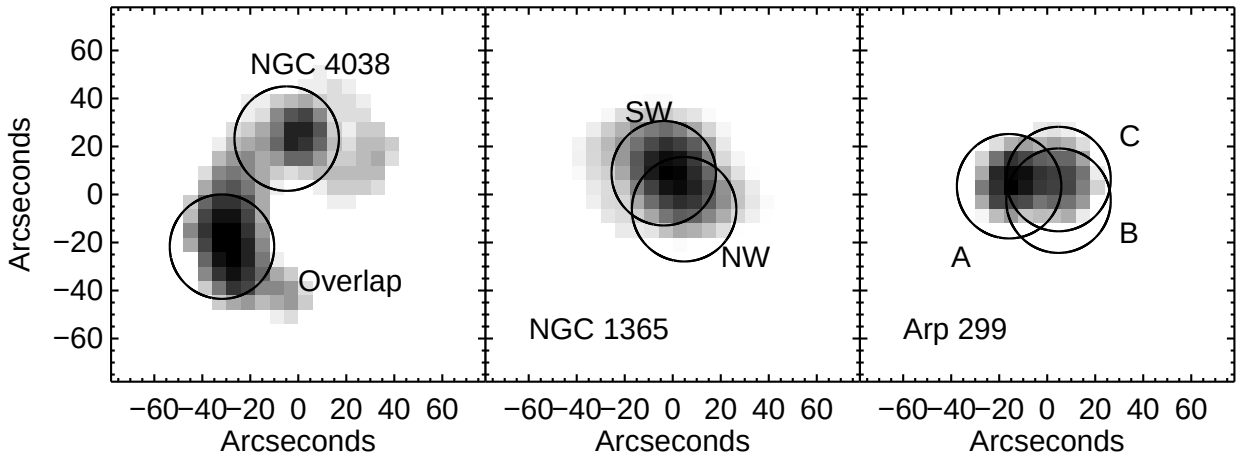

Figure B.1 Locations of Multiple Pointings for 3 Galaxies. Each circle represents the SPIRE-FTS beam with FWHM of 43.″5.

iterative modeling approach can restrict the allowed parameter space somewhat artificially, whereas our simultaneous modeling allows for more possibilities of "trade-off" between the two components. We recover the same total mass in the cold component (of both), with smaller uncertainties, though lower pressures (with overlapping 1σ ranges) for NGC 4038. For the warm component, we have higher uncertainties in the mass (though overlapping distributions), and lower pressures (only the NGC 4038 pressure distribution 1σ range overlaps). Recovering the same total mass, given the similarities of our methods, is very reassuring. Schirm et al. [154] also finds consistent [CI] LTE temperatures of 10-30 K.

B.0.2 M82

For low-J CO lines, we use the measurements from Ward et al. [179], which are actually at two separate locations in M82, separated by $\sim 19''$. The correct value of η for their $24\farcs4$ beam is 0.50, and we then used the photometer maps to determine the ratio of the flux when centered on the two separate lobes (Ward's measurements) to that when pointed at the center (our measurements). We determined that we should sum the two fluxes and then divide by 0.29. This is close to the number one would use if treating the two fluxes as uniformly extended (the ratio of the two beam sizes is 0.32).

A similar CO modeling analysis was done in both Panuzzo et al. [125] and Kamenetzky et al. [80], using an iterative approach instead of simultaneous modeling. We find similar results for the cold component pressure and mass, but slightly higher warm component pressure and mass. Our $\mathrm{Log}(P_{\mathrm{warm}})$ is 6.8 ± 0.3 compared to $6.6^{+0.2}_{-0.5}$ in Kamenetzky et al. [80], and $\mathrm{Log}(M_{\mathrm{warm}})$ is 6.9 ± 0.3 compared to $6.2^{+0.5}_{-0.2}$. As discussed for the Antennae, we would not expect exactly the same results when both components are allowed to vary against one another.

B.0.3 NGC 1068

NGC 1068's geometry poses a unique challenge for the FTS, because of the separate emission from the central circumnuclear disk (CND, $\sim 4''$ diameter) and the larger star-forming ring (SF-

ring, $\sim 40''$ diameter), both of which are contained in the SPIRE beam. Hailey-Dunsheath et al. [68] found the emission from $J = 14 \rightarrow 13$ through $J = 30 \rightarrow 29$ contained a clear inflection point, implying two components of medium ($P = 10^{7.8}$ K cm^{-3}) and high ($P = 10^{9.2}$ K cm^{-3}) excitation; this emission was coming from the central $10''$, with the high-excitation component blueshifted by 80 km s^{-1}. Spinoglio et al. [161] subtracted the medium-excitation component contribution from the lines in the FTS SSW detector ($J = 9 \rightarrow 8$ to $J = 13 \rightarrow 12$), which mainly originate from the CND. The remainder was modeled with RADEX, and the contribution to the lower-J lines in the SLW were subtracted; that remainer was modeled again with RADEX to describe the SF-ring. Their 1σ ranges for the log CND pressure were 6.5-6.8, and for the SF-ring, 4.3-5.2. The pressure and mass for the SF ring overlaps with our cool component; our warm component is at a higher log pressure (7.7 ± 0.2) because we model all of the emission through the $J = 13 \rightarrow 12$ lines; subtracting the ME component from Hailey-Dunsheath et al. [68] drove their pressure lower.

In our two-component model, the warm component is likely dominated by emission from the CND, whereas the cool component may include significant contributions from both the CND and SF-ring. We note that galaxy-integrated photometry fluxes, used to derive $L_{\rm FIR}$, dust mass, SFR, and stellar mass, will mask the underlying differences between the molecular gas in the CND and the SF-ring, influencing NGC 1068's place on e.g. the galaxy main sequence.

B.0.4 NGC 1266

NGC 1266 is unusual for a few reasons. First, it contains a large concentration of H_2 in its nucleus, but shows no sign of an interaction or merger. Second, Alatalo et al. [3] found evidence for a large molecular outflow via high-resolution CO spectra; the wings of the lines require a low-amplitude, broad Gaussian to be fit properly. We do not attempt to separate the relative contributions of the central velocity component and outflow in our line fits and modeling, though such work is in progress (Glenn et al., in preparation). The possible consequence of our treatment is that the conditions we find may be an average between the conditions of the central and outflow components; they may be distinct from our average.

B.0.5 Arp 299

The FITS images presented in Figure 2 of Sliwa et al. [158] were given to us by private communication with the author, such that we could convolve each map up to our 43.″5 beam and determine the integrated flux at each of the three pointings (A, B, and C) for CO $J = 2 \rightarrow 1$ and $J = 3 \rightarrow 2$.

B.0.6 Arp 220

Though not an extended galaxy, this merger was examined in a similar fashion by Rangwala et al. [139], who used additional interferometric information to constrain the source size of both the warm and cool components. Additionally, the line fluxes of the different components were scaled by a different linewidth, and iterative, not simultaneous, modeling was used. Likely as a result of these changes, though we find overlapping distributions for the cold component mass and pressure, we find a higher warm component pressure (1σ range Log(P) = 6.6-7.2 instead of 6.2-6.4), and lower mass (1σ range Log(M) = 8.2-8.6 instead of 8.6-8.8). In Section 5.1.3, we discussed three-component modeling, and present some sample results here for Arp 220 in Figures B.2, B.3, B.4, explained in the captions.

B.0.7 Cen A

Centaurus A, the radio source in NGC 5128, is the nearest giant elliptical. The aftermath of a merger, Cen A is notable for its bright, compact circumnuclear disk (CND) and extended thin disk (ETD). The Herschel FTS beam is centered on the CND, and thus we are not probing the physical conditions in the ETD. Israel et al. [76] also examined the CO SLED, [CI], and [CII] emission from the CND and multiple offset pointings of Cen A. For their central pointing, they normalize the measured emission to that of a 22″ beam and find weak or negligible contribution from the ETD; our observations, with a larger beam, may have more contamination but are still dominated by the CND. By a comparison to CO SLEDs of other well-known galaxies, they note that the falling CO SLED at high-J indicates Cen A has the "coolest" CO ladder. Our LVG modeling can quantify this

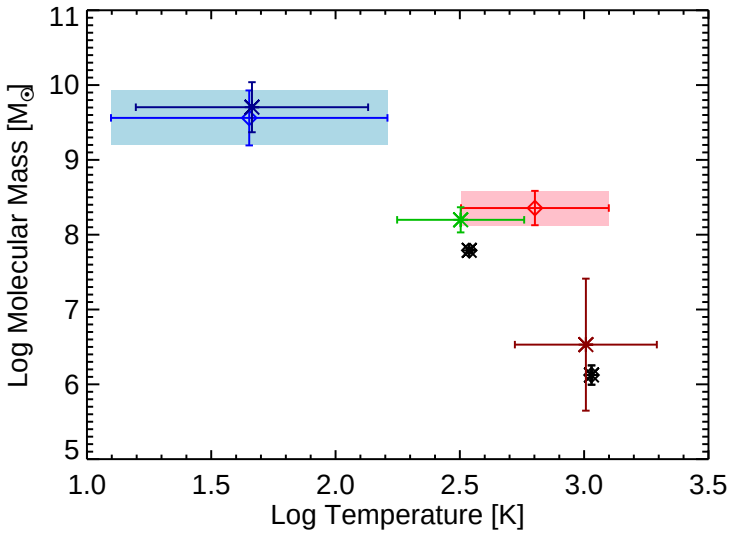

Figure B.2 Sample 3-Component Model Results for Arp 220: Temperature vs. Mass. The red and blue shaded regions around the diamonds indicate the 1σ temperature and mass ranges from the two-component likelihood modeling. The black asterisks are the temperatures and masses derived from molecular hydrogen lines (see Section 4.5.5 and Table 4.17). We attempted the three-component modeling described in Section 5.1.3 to see if we could separate the warm CO gas (pink box) into medium and higher temperature components similar to H_2. The dark blue, green, and dark red X's and 1σ error bars denote the three-component modeling results for Components I, II, and III, respectively. The distribution of the three components in temperature and mass now seem qualitatively more similar to that of H_2. However, Figures B.3 and B.4 reveal that Component III is not constrained and negligible to the fit. Component II is fulfilling the same role as the warm component, but was limited to a different temperature.

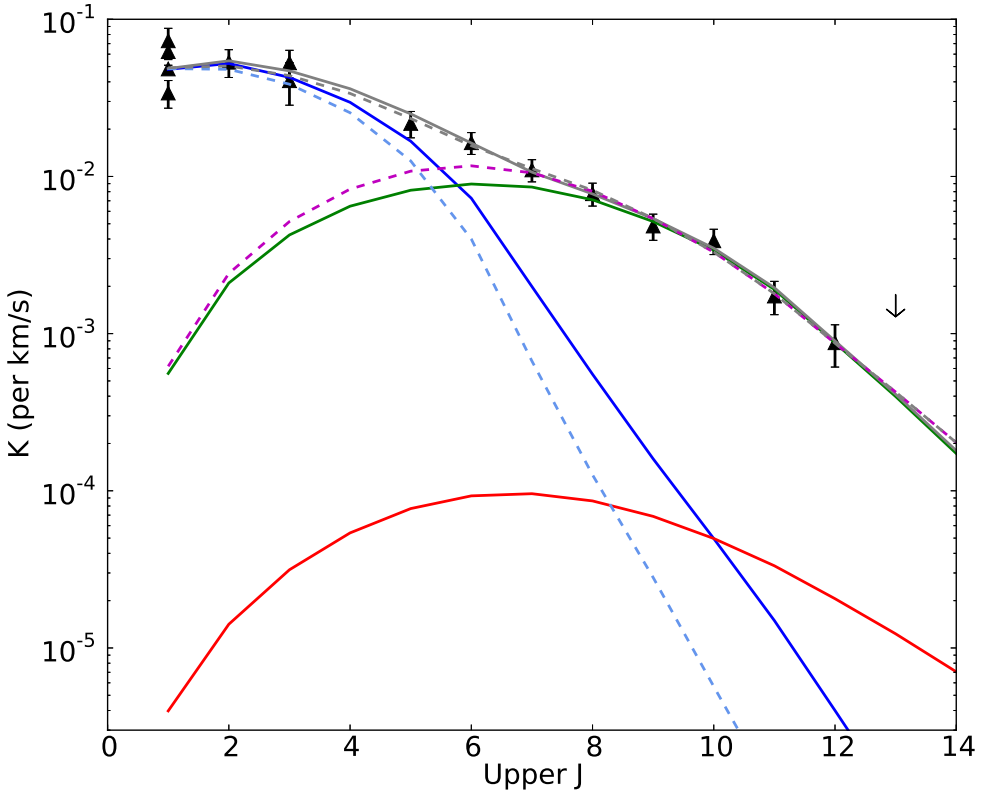

Figure B.3 Sample 3-Component Model Results for Arp 220: SLED. The solid lines indicate the best-fit solution of the three-component model (Section 5.1.3) for Components I (blue), II (green), and III (red). The dashed lines are the best-fit two-component model for the cool (light blue) and warm (fuchsia) components. Both models have the same χ^2 because Component III does not contribute to the fit.

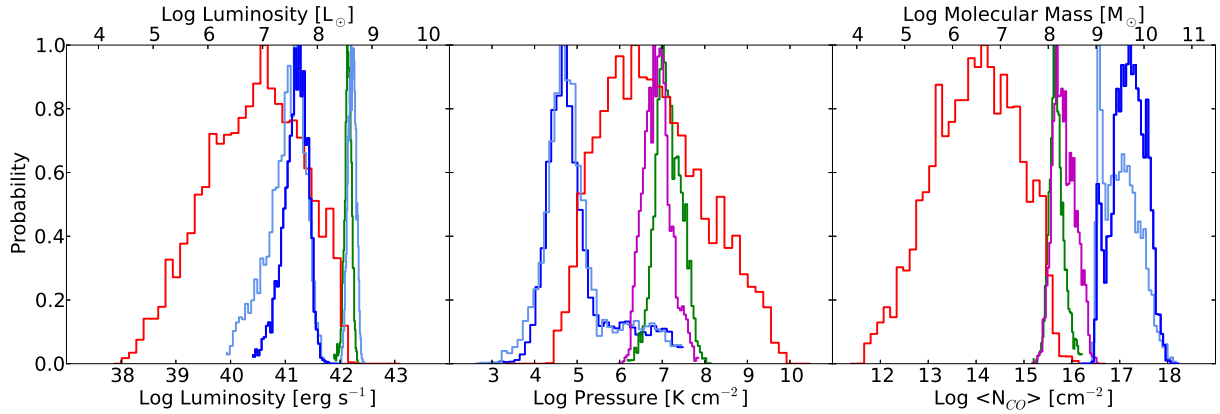

Figure B.4 Sample 3-Component Model Results for Arp 220: Derived Parameters. From left to right: CO luminosity, pressure (product of temperature and density), and beam-averaged column density (product of column density and filling factor, proportional to mass, top axis). The dark blue, green, and red lines are the marginalized likelihoods of Components I, II, and III, respectively. The light blue and fuchsia lines are for the cool and warm components of the two-component modeling. Qualitatively, Component I and the cool component are the same, as are Component II and the warm component. Component III is generally unconstrained so long as its mass is low enough that it does not modify the fit.

statement: the warm component of CO in Cen A has one of the lowest pressures in our sample.

[76] models the ^{12}CO SLEDs simultaneously with ^{13}CO using two gas components, but does not present marginalized likelihood distributions, instead opting to present three solutions which match the observed SLED well. Our results are not particularly comparable because we allow kinetic temperatures above 150 K. Limiting the temperature will necessarily require a larger portion (of the mass) of the gas to appear much warmer. They also use PDR/XDR models and note the potential importance of mechanical heating. Their estimate of the mass of the CND, 8.4×10^7 $M_\odot$, is about a factor of 2 smaller than ours (which is their stated uncertainty); our larger beam area, and possible contamination from the ETD within it, may be responsible for some of the difference. We find the highest value of α_{CO} in our sample for Cen A, but due to the difference in our mass estimate from Israel et al. [76], we find this in accordance with that of the Milky Way, not twice the value. Parkin et al. [132] also investigated atomic fine structure lines using PACS and SPIRE and compared to PDR models; they found that the matching PDR properties implies that Cen A is similar to a normal disk galaxy, despite its unique morphology.

B.0.8 NGC 6240

Our results wholeheartedly agree with the conclusion of Meijerink et al. [110], that the CO line luminosity-to-continuum ratio is exceptionally high in this galaxy. They argue, through shock modeling of CO and H_2, that a high line-to-continuum ratio is a key diagnostic for shocks. Their LVG models were in preparation at the time of this writing.

B.0.9 Mrk 231

The CO J = 9 → 8 line of Mrk 231 seems abnormally low compared to the rest of the SLED. For this spectrum, we are using a version reprocessed with HIPE 9 and off-axis background subtraction, but we find the same low flux with SPG v6.1.0 and SPG v11.1.0. The v6.1.0 spectrum includes more frequency overlap between the SLW and SSW regions; fitting the CO J = 9 → 8 line from the SLW band yields a higher flux, 652 ±68 Jy km s^{-1}. In future versions, however, the J = 9 → 8 line is

not available in the more limited SLW frequency range. We do not use the v6.1.0 spectrum because the background subtraction does not properly match the SLW to SSW, which should happen for a point source like Mrk 231.

Appendix C

Tables of Photometry from the Literature

The following tables summarize the photometric flux densities used for the dust and stellar population modeling described in Chapter 4, organized by instrument or wavelength. If a galaxy did not have a collected measurement belonging to a given table, it does not appear as part of that table.

Table C.1. Photometry Flux Densities: UV from GALEX

Galaxy	FUV 0.152 μm		NUV 0.227 μm		Ref
	F_ν [mJy]	σ_{tot} [mJy]	F_ν [mJy]	σ_{tot} [mJy]	
IRAS 09022-3615	0.0418	0.00777	0.0933	0.0112	1
Arp 220	0.131	0.0209	0.437	0.0502	2
Mrk 273	0.204	0.0324	0.406	0.0466	2
UGC 05101	0.0655	0.00655	0.221	0.0221	3
NGC 6240	...	...	0.663	0.0671	1
Arp 299-A	10.2	1.03	15.7	1.57	4
NGC 1068	27.8	2.78	47.0	4.70	3
NGC 1365-NE	3.69	0.374	11.1	1.11	1
NGC 4038 (Overlap)	34.2	3.42	55.1	5.51	4
M82	50.1	5.01	105	10.5	3
NGC 1222	2.13	0.220	3.70	0.373	3
M83	205	20.5	350.	35.0	3
NGC 253	143	14.3	242	24.2	3
NGC 1266	0.0490	0.00490	0.290	0.0290	3
Cen A	33.7	3.37	88.7	8.87	3

Note. — **References.** (1) Bianchi et al. [14]; (2) U et al. [170]; (3) NED; (4) Lanz et al. [90].

Table C.2. Photometry Flux Densities: 2MASS

Galaxy	1.25 μm		1.65 μm		2.17 μm		Ref
	F_ν [mJy]	σ_{tot} [mJy]	F_ν [mJy]	σ_{tot} [mJy]	F_ν [mJy]	σ_{tot} [mJy]	
Mrk 231	62.0	6.20	113	11.3	199	19.9	1
IRAS F17207-0014	12.8	1.28	18.5	1.85	20.8	2.08	1
IRAS 09022-3615	8.16	0.816	11.4	1.14	12.2	1.22	1
Arp 220	61.4	6.14	77.2	7.72	76.4	7.64	1
Mrk 273	21.4	2.14	27.8	2.78	29.3	2.93	1
UGC 05101	16.4	1.64	25.1	2.51	33.0	3.30	1
NGC 6240	120.	12.0	169	16.9	152	15.2	1
Arp 299-A	222	9.50	300.	14.5	285	13.0	2
NGC 1068	2600	260.	3210	321	3230	323	1
NGC 1365-NE	1810	181	2070	207	1880	188	1
NGC 4038 (Overlap)	928	44.7	1130	62.0	916	76.2	2
M82	6610	230.	8970	322	8550	304	2
NGC 1222	72.9	7.29	87.5	8.75	71.8	7.18	1
M83	9700	970.	11500	1150	9470	947	1
NGC 253	18900	1890	23700	2370	20700	2070	1
NGC 1266	103	10.3	114	11.4	108	10.8	1
Cen A	16300	1630	20000	2000	17700	1770	1

Note. — **References.** (1) NED; (2) Lanz et al. [90].

Table C.3. Photometry Flux Densities: IRAC

Galaxy	3.6 μm		4.5 μm		5.8 μm		8.0 μm		Ref
	F_ν [Jy]	σ_{tot} [Jy]	F_ν [Jy]	σ_{tot} [Jy]	F_ν [Jy]	σ_{tot} [Jy]	F_ν [Jy]	σ_{tot} [Jy]	
Mrk 231	0.206	0.0294	0.280	0.0396	0.746	0.0746	0.907	0.0931	1,2
IRAS F17207-0014	...	...	...	...	0.0490	0.00490	...	...	1
Arp 220	0.0540	0.00736	0.0450	0.00673	0.0693	0.00693	0.251	0.0256	1,2
Mrk 273	0.0320	0.00439	0.0390	0.00559	0.0696	0.00696	0.143	0.0146	1,2
UGC 05101	0.0460	0.00679	0.0780	0.0112	0.0960	0.0108	0.144	0.0152	2
NGC 6240	0.100	0.0100	0.0900	0.00900	0.210	0.0210	0.490	0.0490	3
Arp 299-A	0.293	0.00880	0.348	0.000400	0.841	0.0252	2.16	0.218	4,2
NGC 1068	3.80	0.380	5.10	0.510	...	...	23.0	2.30	1
NGC 4038 (Overlap)	0.523	0.0157	0.359	0.000800	0.706	0.0212	1.76	0.0530	4
M82	6.56	0.197	5.22	0.157	...	...	...	...	4
NGC 1266	0.0550	0.00971	0.0420	0.00732	0.0570	0.00982	0.0900	0.0150	5

Note. — **References.** (1) NED; (2) U et al. [170]; (3) Bush et al. [25]; (4) Lanz et al. [90]; (5) Dale et al. [37].

Table C.4. Photometry Flux Densities: IRAS

Galaxy	12 μm		25 μm		60 μm		100 μm		Ref
	F_ν [Jy]	σ_{tot} [Jy]	F_ν [Jy]	σ_{tot} [Jy]	F_ν [Jy]	σ_{tot} [Jy]	F_ν [Jy]	σ_{tot} [Jy]	
Mrk 231	1.83	0.184	8.84	0.884	30.8	3.08	29.7	2.98	1
IRAS F17207-0014	0.200	0.0320	1.61	0.164	32.1	3.21	36.1	3.65	1
IRAS 09022-3615	0.200	0.0377	1.19	0.121	11.6	1.17	11.1	1.16	1
Arp 220	0.610	0.0645	8.00	0.801	104	10.4	115	11.5	1
Mrk 273	0.240	0.0294	2.36	0.237	22.5	2.25	22.5	2.25	1
UGC 05101	0.250	0.0368	1.02	0.106	11.7	1.17	19.9	2.00	1
NGC 6240	0.590	0.0641	3.55	0.356	22.9	2.29	26.5	2.65	1
Arp 299-A	3.97	0.398	24.5	2.45	113	11.3	111	11.1	1
NGC 1068	39.8	3.98	87.6	8.76	196	19.6	257	25.7	1
NGC 1365-NE	5.12	0.513	14.3	1.43	94.3	9.43	166	16.6	1
NGC 4038 (Overlap)	1.94	0.199	6.54	0.655	45.2	4.52	87.1	8.71	1
M82	79.4	7.94	333	33.3	1480	148	1370	137	1
NGC 1222	0.500	0.0550	2.28	0.231	13.1	1.31	15.4	1.54	1
M83	21.5	2.15	43.6	4.36	266	26.6	524	52.4	1
NGC 253	41.0	4.10	155	15.5	968	96.8	1290	129	1
NGC 1266	0.250	0.0391	1.20	0.124	13.1	1.31	16.9	1.70	1
Cen A	22.2	2.22	28.3	2.83	213	21.3	412	41.2	1

Note. — **References.** (1) Sanders et al. [149].

Table C.5. Photometry Flux Densities: MIPS

Galaxy	24 μm		70 μm		160 μm		Ref
	F_ν [Jy]	σ_{tot} [Jy]	F_ν [Jy]	σ_{tot} [Jy]	F_ν [Jy]	σ_{tot} [Jy]	
Mrk 231	4.34	0.485	...	...	...	...	1
Arp 220	4.01	0.449	80.8	14.6	...	...	1
Mrk 273	1.86	0.208	20.2	3.64	11.7	3.69	1
UGC 05101	0.808	0.0902	13.2	2.38	13.4	4.24	1
Arp 299-A	8.66	0.0500	...	...	...	...	2
NGC 1068	80.0	8.00	180.	18.0	...	...	3
NGC 4038 (Overlap)	6.13	0.0450	...	...	...	...	2
M83	42.0	4.20	...	...	...	...	3
NGC 253	140.	14.0	...	...	...	...	3
NGC 1266	0.880	0.0533	12.7	1.38	10.3	1.76	4,5

Note. — **References.** (1) U et al. [170]; (2) Lanz et al. [90]; (3) NED; (4) Dale et al. [37]; (5) Temi et al. [167].

Table C.6. Photometry Flux Densities: PACS

Galaxy	75 μm		110 μm		170 μm		Ref
	F_ν [Jy]	σ_{tot} [Jy]	F_ν [Jy]	σ_{tot} [Jy]	F_ν [Jy]	σ_{tot} [Jy]	
Arp 299-A	139	13.9	127	12.7	74.2	7.42	1
NGC 4038 (Overlap)	81.0	8.11	116	11.6	99.8	9.98	1
M82	1990	198	...	...	1290	129	1

Note. — **References.** (1) Lanz et al. [90].

Table C.7. Photometry Flux Densities: PLANCK

Galaxy	350 μm		550 μm		850 μm		1380 μm		2100 μm		Ref
	F_ν [Jy]	σ_{tot} [Jy]	F_ν [Jy]	σ_{tot} [Jy]	F_ν [Jy]	σ_{tot} [Jy]	F_ν [Jy]	σ_{tot} [Jy]	F_ν [Jy]	σ_{tot} [Jy]	
Mrk 231	1.87	0.154	...	...	...	...	...	...	...	...	1
Arp 220	13.9	0.997	3.64	0.281	0.943	0.103	...	...	...	...	1
Mrk 273	1.56	0.165	...	...	...	...	...	...	...	...	1
UGC 05101	3.23	0.258	...	...	...	...	...	...	...	...	1
NGC 6240	3.47	0.286	...	...	...	...	...	...	...	...	1
Arp 299-A	9.62	0.695	2.56	0.200	0.645	0.0782	...	...	...	...	1
NGC 1068	48.9	3.64	12.8	0.937	2.48	0.213	0.720	0.0826	...	...	1
NGC 1365-NE	43.2	3.17	11.9	0.886	2.50	0.196	0.577	0.0594	...	...	1
NGC 4038 (Overlap)	17.3	1.25	4.91	0.375	0.862	0.114	...	...	...	...	1
M82	157	11.4	37.2	2.69	8.18	0.598	2.69	0.196	0.958	0.0855	1
M83	118	9.50	33.8	2.71	6.48	0.531	1.81	0.144	...	...	1
NGC 253	317	25.1	91.7	7.54	17.4	1.54	4.57	0.388	1.28	0.110	1
Cen A	115	8.60	42.5	3.15	17.7	1.32	...	...	...	...	1

Note. — **References.** (1) Planck Collaboration et al. [136].

Table C.8. Photometry Flux Densities: SCUBA

Galaxy	450 μm		850 μm		Ref
	F_ν [Jy]	σ_{tot} [Jy]	F_ν [Jy]	σ_{tot} [Jy]	
Mrk 231	...	...	0.0780	0.00780	1
IRAS F17207-0014	1.07	0.325	0.155	0.0471	2
Arp 220	6.29	0.629	0.832	0.0860	3,1
NGC 6240	1.00	0.304	0.150	0.0456	2
NGC 1222	...	...	0.0840	0.0160	3

Note. — **References.** (1) NED; (2) Klaas et al. [85]; (3) Dunne et al. [47].

Table C.9. Photometry Flux Densities: ISO

λ [μm]	F_ν [Jy]	σ_{tot} [Jy]	Ref	λ [μm]	F_ν [Jy]	σ_{tot} [Jy]	Ref	λ [μm]	F_ν [Jy]	σ_{tot} [Jy]	Ref
Mrk 231				52	121	10.8	2	120	25.9	7.88	1
10	1.43	0.478	1	57	134	11.8	2	122	20.8	3.70	2
12	2.40	0.805	1	60	113	38.0	1	145	17.9	3.10	2
15	2.90	0.973	1	63	148	15.0	2	150	18.9	5.75	1
25	8.66	2.90	1	88	151	18.7	2	158	16.8	2.80	2
52	32.4	3.20	2	90	112	37.4	1	170	11.5	2.10	2
57	37.2	3.60	2	120	109	33.2	1	170	16.7	1.67	3
60	31.7	10.6	1	122	118	9.50	2	180	12.7	3.87	1
63	42.9	4.00	2	145	100.	10.1	2	200	9.00	2.74	1
88	34.1	4.40	2	150	87.9	26.7	1	**Arp 299-A**			
90	27.3	9.17	1	158	84.5	8.50	2	52	129	12.3	2
120	24.3	7.40	1	170	77.1	6.70	2	57	142	13.1	2
122	19.5	1.70	2	170	77.1	7.71	3	63	151	14.6	2
145	16.0	1.70	2	180	64.0	19.4	1	88	141	19.9	2
150	14.7	4.48	1	200	54.8	16.7	1	122	86.4	7.90	2
158	16.1	2.20	2	**Mrk 273**				145	65.7	5.30	2
170	15.3	1.60	2	10	0.100	0.034	1	158	58.6	7.50	2
170	15.3	1.53	3	12	0.250	0.084	1	170	60.7	6.30	2
180	9.75	2.97	1	15	0.500	0.168	1	**NGC 1365-NE**			
200	6.88	2.09	1	25	2.07	0.694	1	15	4.44	0.444	3
IRAS F17207-0014				57	22.3	2.00	2	120	217	21.7	3
10	0.080	0.027	1	60	27.5	9.21	1	150	194	19.4	3
12	0.200	0.067	1	63	24.9	2.50	2	170	167	16.7	3
15	0.250	0.084	1	88	22.6	2.30	2	180	103	10.3	3
25	1.32	0.443	1	90	23.8	7.98	1	200	85.2	8.52	3
52	40.7	4.90	2	120	20.0	6.08	1	**NGC 1222**			
57	31.6	2.70	2	122	15.4	1.30	2	57	20.2	1.80	2
60	32.2	10.8	1	145	12.5	1.30	2	63	20.4	2.00	2
63	41.9	3.90	2	150	13.1	3.98	1	122	12.9	1.10	2
88	48.5	4.90	2	158	8.40	1.00	2	145	11.4	1.10	2
90	31.9	10.7	1	170	8.30	1.00	2	158	10.8	2.20	2

Table C.9 (cont'd)

λ [μm]	F_ν [Jy]	σ_{tot} [Jy]	Ref	λ [μm]	F_ν [Jy]	σ_{tot} [Jy]	Ref	λ [μm]	F_ν [Jy]	σ_{tot} [Jy]	Ref
120	30.0	9.12	1	170	8.30	0.830	3	170	8.00	0.900	2
122	31.5	2.60	2	180	8.69	2.64	1	170	8.00	0.800	3
145	27.0	2.50	2	200	7.40	2.25	1	**M83**			
150	23.0	7.00	1	**NGC 6240**				15	20.1	2.01	3
158	24.3	2.90	2	10	0.259	0.087	1	**NGC 1266**			
170	26.4	3.20	2	12	0.750	0.252	1	57	15.5	1.40	2
170	26.4	2.64	3	15	1.00	0.335	1	63	18.5	1.80	2
180	17.5	5.32	1	25	3.31	1.11	1	88	21.6	2.70	2
200	12.5	3.80	1	52	16.5	2.50	2	122	16.7	1.30	2
Arp 220				57	27.5	4.00	2	145	13.3	1.30	2
10	0.147	0.049	1	60	23.6	7.92	1	158	14.8	4.80	2
12	0.600	0.201	1	63	23.5	3.40	2	170	10.1	1.00	2
15	1.14	0.382	1	88	25.8	4.00	2	170	10.1	1.01	3
25	8.28	2.78	1	90	26.7	8.96	1				

Note. — **References.** (1) Klaas et al. [85]; (2) Brauher et al. [20]; (3) NED

Table C.10. Photometry Flux Densities: Visible

λ [μm]	F_ν [mJy]	σ_{tot} [mJy]	Ref	λ [μm]	F_ν [mJy]	σ_{tot} [mJy]	Ref	λ [μm]	F_ν [mJy]	σ_{tot} [mJy]	Ref
Mrk 231				**UGC 05101**				0.69	3670	367	1
0.44	12.9	1.29	1	0.44	4.67	0.467	1	0.80	4740	474	1
0.54	12.8	2.38	2	0.55	5.23	0.523	1	**NGC 1222**			
0.65	16.2	1.92	2	0.69	8.17	0.817	1	0.44	3.29	0.329	1
0.86	25.9	12.2	2	**NGC 6240**				**M83**			
0.88	21.0	2.10	1	0.44	23.0	2.30	1	0.44	2240	224	1
1.03	22.0	2.20	1	0.55	37.1	3.71	1	0.55	4100	410.	1
Arp 220				**Arp 299-A**				**NGC 253**			
0.44	10.6	1.06	1	0.46	49.7	5.05	2	0.44	6210	621	1
0.55	19.3	1.93	1	0.54	72.4	7.37	2	**NGC 1266**			
0.65	21.3	2.54	2	0.65	70.6	8.40	2	0.44	20.0	2.00	1
0.69	29.7	2.97	1	0.86	129	13.2	2	0.55	36.0	3.60	1
0.86	36.2	3.63	2	**NGC 1365-NE**				0.69	37.0	3.70	1
Mrk 273				0.80	1200	120.	1	0.80	35.0	3.50	1
0.44	5.62	0.562	1	**M82**				**Cen A**			
0.54	9.04	2.66	2	0.44	3530	353	1	0.44	3110	311	1
0.65	9.30	1.11	2	0.55	2790	279	1	0.55	9840	984	1
0.86	13.8	1.64	2								

Note. — **References.** (1) NED; (2) U et al. [170]

Table C.11. Photometry Flux Densities: All Others

λ [μm]	F_ν [Jy]	σ_{tot} [Jy]	Ref	λ [μm]	F_ν [Jy]	σ_{tot} [Jy]	Ref
Mrk 231				880	0.056	0.006	1
350	1.73	0.173	1	**NGC 6240**			
880	0.080	0.008	1	350	2.48	0.248	1
Arp 220				**M82**			
350	9.74	0.974	1	250	363	25.4	2
880	0.490	0.049	1	350	122	8.50	2
Mrk 273				500	49.6	4.96	1
350	1.77	0.177	1				

Note. — **References.** (1) NED; (2) Lanz et al. [90]

Appendix D

Monte Carlo Simulations of Physical Conditions Derived from ALMA

Only with *Herschel* was it possible to construct a full SLED up to J=13-12 for nearby galaxies. Future CO modeling, including that of distant galaxies, will likely have to be done with far fewer lines. How well can the physical conditions be constrained? I sought to answer this question for potential ALMA observations, specifically for a SLED with CO J_{upper} values of 3, 4, 5, and 6. With only 4 lines, one could not model two components simultaneously (which requires 8 parameters), but could model one component. Unfortunately, the results are likely not comparable to either the warm or cool component modeling of a full SLED, because these mid-J lines have contributions from both components.

To simulate this, I used the flux values for the aforementioned lines from the SLED of NGC1068, an example of an AGN. I assumed a σ of 10% for every line and draw from a random Gaussian distribution of flux values for each line flux and modeled the result. An example distribution of SLEDs is illustrated in Figure D.1

The results for the two best determined parameters, Pressure and Total (Beam-Averaged) Column Density, proportional to the mass, are presented in D.2. In general, the errors for the pressure are about 0.2 dex for these SLEDs with 10% error, and the error for the mass is slightly less. In conclusion, these 4 mid-J lines are adequate to determine a one-component fit.

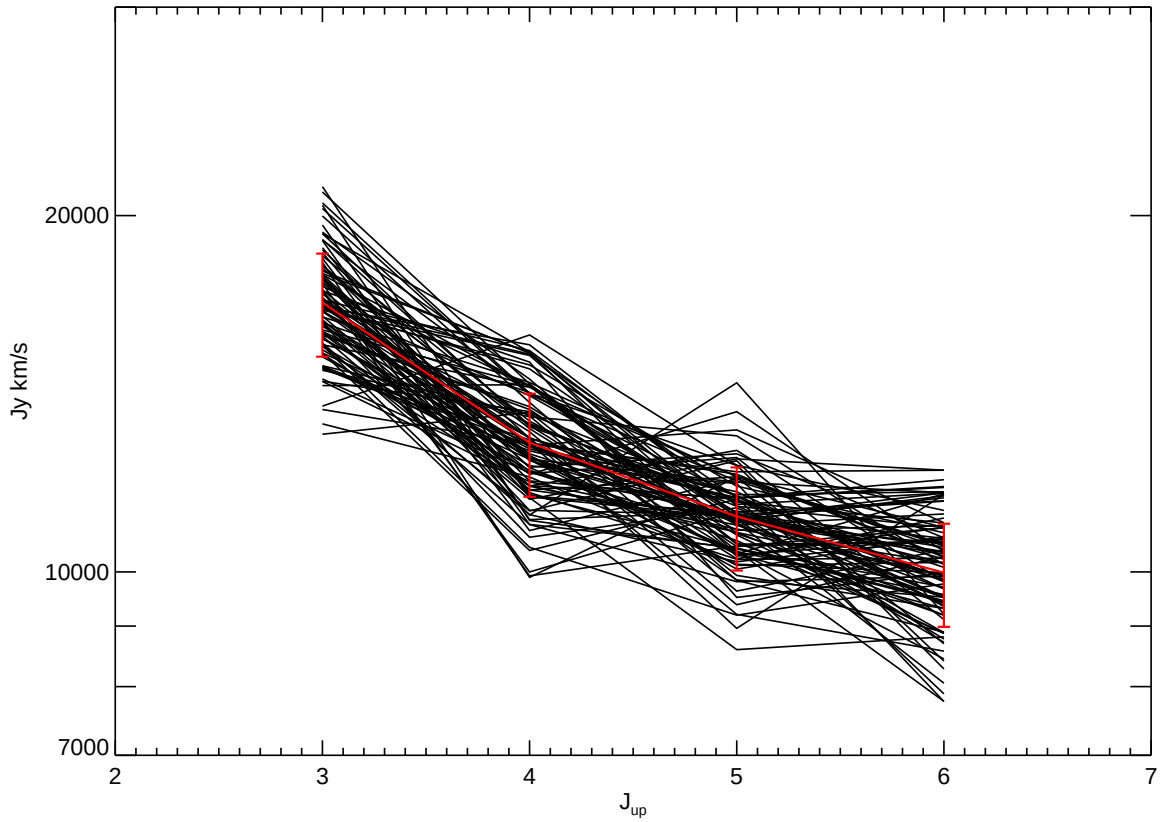

Figure D.1 Example Distribution of 4-Line SLEDs (not necessarily the ones used for the results in Figure D.2).

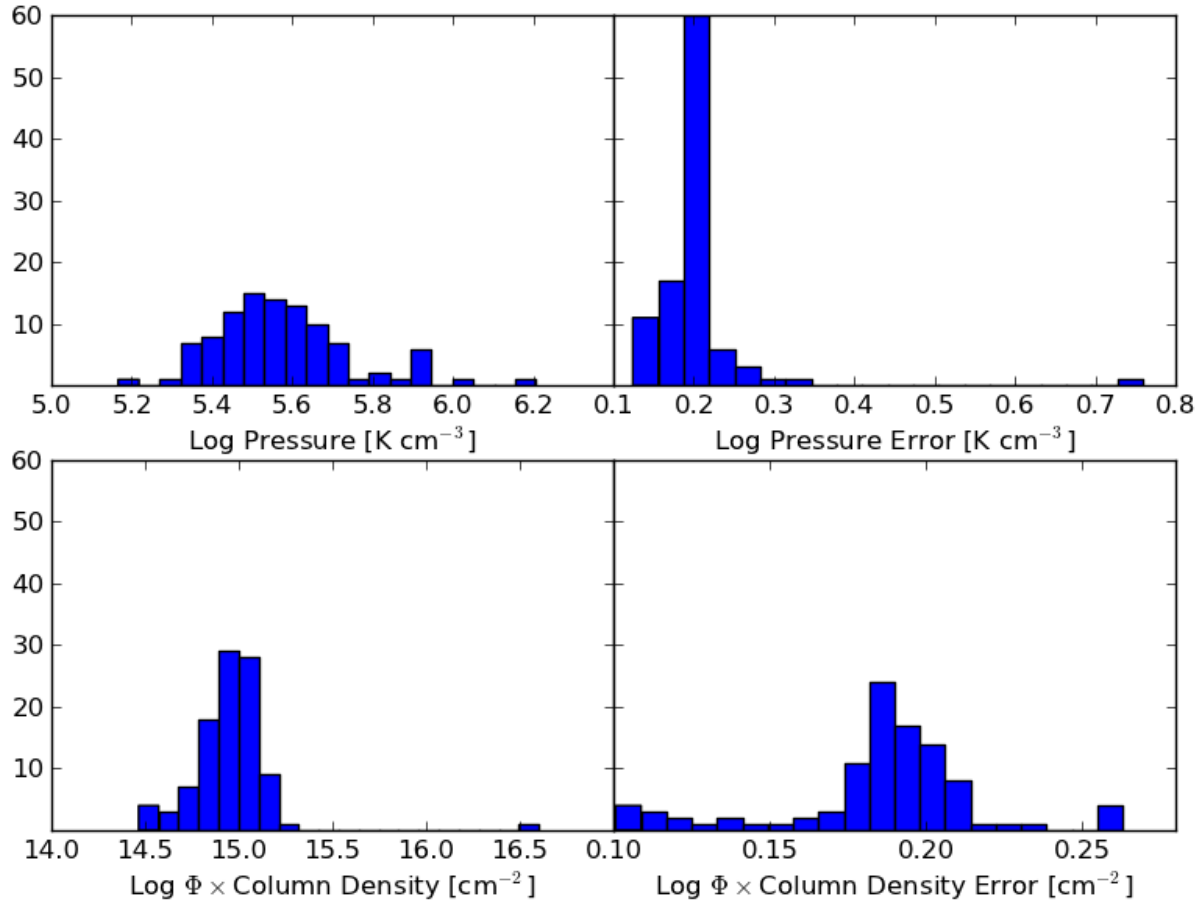

Figure D.2 Histogram Results for Pressure and Column Density, for 100 samples. On the left side, these are the values corresponding to the Mode Mean from PyMultiNest. The right side is Mode Sigma.

Appendix E

SPIRE-FTS Instrument Characterization

E.1 Instrumental Line Profiles

The instrumental line shape (ILS) of the SPIRE FTS is a sinc function. This is a consequence of taking a Fourier Transform on the interferogram, which was made over a finite length. I noticed that the ILS was slightly asymmetric, that is, the first local minimum directly to the low-frequency end (left in the plots of this section) of the line center is *lower* than the local minimum to the right of the line center. An example is plotted in Figure E.1.

I characterize the amount of asymmetry by the ratio of the lowest point to the right to the lowest point on the left, for an instrumental line profile normalized to a peak of one and a baseline of zero. The center of the line is at zero. The constant continuum level is fit by using all points $> \pm\Delta\nu_c$ away from 0. The line itself is then fit using all points $< \pm\Delta\nu_l$ with the IDL Levenberg-Marquardt least-squares routine `mpfitfun`. There are 4 free parameters: center, width, amplitude, and (constant) baseline.

Empiricially measured line profiles were available for 19/35 detectors for the SLW/SSW, 7/17 of which are unvignetted. The mean ± standard deviation asymmetry for the SLW band was 0.93 ± 0.18, and for the SSW, 0.76 ± 0.05. I investigated if this asymmetry would result in noticeable differents in line fluxes or line centers when fitting with a sinc function. I further looked at the effect of rebinning the line profile, and modifying the range over which the line and continuum is fit.

We found no obvious trend in line parameter values (center, width, ampltitude) as a function

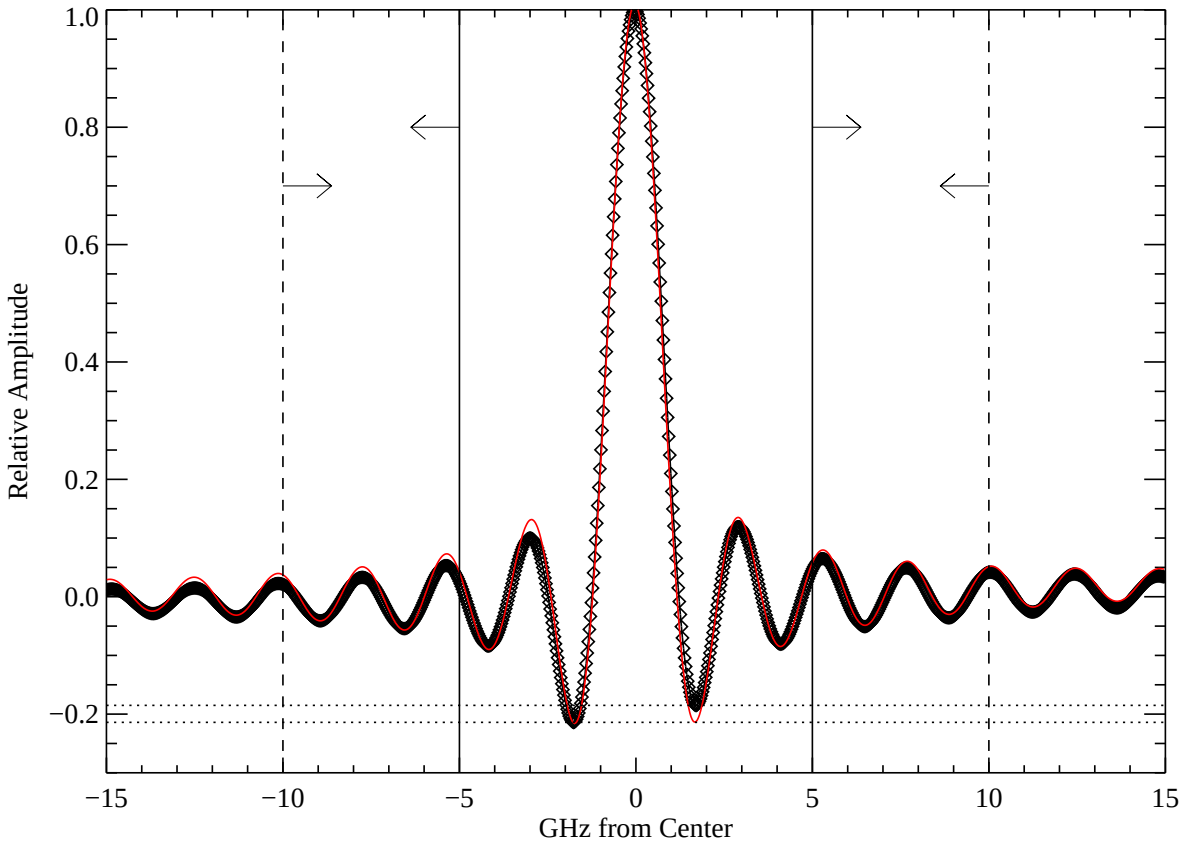

Figure E.1 Example of Instrumental Line Profile and Fitting. Black diamonds represent the empirically measured line profile. The horizontal dotted lines mark the minima to the left and right of the line center to highlight the asymmetry. The best-fit sinc function is overplotted in red. The solid vertical line denote $\Delta\nu_c = 5$; the continuum is fit using all points outside of these lines, as indicated by the arrows. Similarly, the dashed vertical lines denote $\Delta\nu_l = 10$, where the sinc function is fit to all points inside the lines.

of asymmetry. The RMS scatter in the fitted line centers was 0.02 GHz (0.03 GHz for the SLW band): less than the stated accuracy of 0.06 GHz. The RMS scatter in the integrated line fluxes was $< 1\%$ To properly recover the sinc function amplitude, one must fit at least ± 6 GHz around the expected line center ($\Delta\nu_l \geq 6$) Finally, It is best to keep the range of the continuum fitting $\Delta\nu_c \leq 4$ GHz. This is for a line profile which has already been continuum subtracted; for real data, where continuum subtraction may be more challenging, this number could vary.

In conclusion, the systematic effects of the asymmetric line profiles are much less than the uncertainties introduced by actual astrophysical or calibration variation/uncertainty. This information was presented to the SPIRE FTS instrumental team by Peter Imhof, Blue Sky Spectroscopy, on March 8, 2011.

E.2 Spectral Cube Creation

Fully sampled maps with the Herschel FTS are created by pointing the telescope at multiple (Nyquist sampled) locations, and then regridding the spectra onto a regular cube. At the time that the spectral line maps for M82 were created, the Herschel Interactive Processing Environment (HIPE) had two options for this regridding: Nearest Neighbor and Naive Projection. (See Chapter 3, specifically Figure 3.1 for jiggle positions on the sky to illustrate the map-making procedure) In Nearest Neighbor, the nearest spectrum to a map grid point is chosen, with no averaging or interpolation. At the time, Naive Projection (NP) averaged all spectra with in a map pixel, but did not calculate the weights appropriately. Take, for example, a pixel which contains 2 spectra of 16 scans each. The two spectra are offset by, at most, the diagonal length of a pixel, and will thus be somewhat discrepant. At the time, NP would average all 32 scans, and then calculate an error based on the standard deviation of all 32 scans; but because they came from different spectra on the sky, the standard deviation of the bimodal distribution was quite high, and greatly overestimated the error bars on each wavelength bin. Instead, we felt it was most appropriate to treat each set of scans (one spectrum) separately at first in order to calculate an error bar for each wavelength bin, and then average all spectra falling within a pixel's boundaries, propagating the

errors appropriately. This method is presented here.

For a given wavenumber bin, let the flux in one scan be x_i. For all scans of the same detector and jiggle position in a given pixel (one spectrum, ie all scans from detector SLWC4 in jiggle position 3), the average spectrum (μ_j) is

$$\mu_j = \frac{1}{N}\sum_{i=1}^{N} x_i \tag{E.1}$$

and the error is the square root of the variance on the sample mean,

$$\sigma_j = \frac{\mathrm{stdev}(f_j)}{\sqrt{N}} = \frac{1}{\sqrt{N}}\sqrt{\frac{1}{N}\sum_{i=1}^{N}(x_i - \mu_j)}. \tag{E.2}$$

Generally N is 16, but for those scans on the border between two pixels may have some scans in one pixel and other scans in a neighboring pixel. I ignore any spectrum in a pixel that only has 1 scan, so N is from 2 to 16.

Now for all spectra in a given pixel (if there is more than 1), the final pixel flux, F, is the weighted mean of all the other spectra. For S spectra,

$$F = \frac{\sum_{j=1}^{S} \mu_j/\sigma_j^2}{\sum_{j=1}^{S} 1/\sigma_j^2} \tag{E.3}$$

and the error is

$$\sigma_F = \sqrt{\frac{1}{\sum_{j=1}^{S} 1/\sigma_j^2}} \tag{E.4}$$

The ability to input pre-averaged scans into the NP map method is now a part of the HIPE pipeline.

Appendix F

Details on LTE Temperature and Mass Calculations, with Emphasis on Molecular Hydrogen Lines

Note: Throughout this chapter, I use energies per Boltzmann constant (i.e. in Kelvin), so rather than write E/(kT), I simply write E/T.

F.1 Critical Densities, LTE Assumption

Le Bourlot et al. [92] presents analytical fits to the collision rate coefficients for H_2 with H, He, o-H_2 and p-H_2. They are available for download from a website[1] . Figure F.1 shows the critical density vs. temperature for the lines of interest here.

F.2 Ortho and Para

Ortho-H_2 has parallel nuclear spins (odd-J, e.g. S(1) and S(3) lines) and para-H_2 has antiparallel spins (even-J, e.g. S(2) and S(0) lines). The ortho/para ratio is generally assumed to be 3, at LTE for T $>$ 200 K. The excitation temperature (from the line ratio) of two lines of the same species do not depend on the ortho/para ratio; that of two different species (such as S(1) and S(0)) are sensitive to the ratio.

[1] http://ccp7.dur.ac.uk/cooling_by_h2/

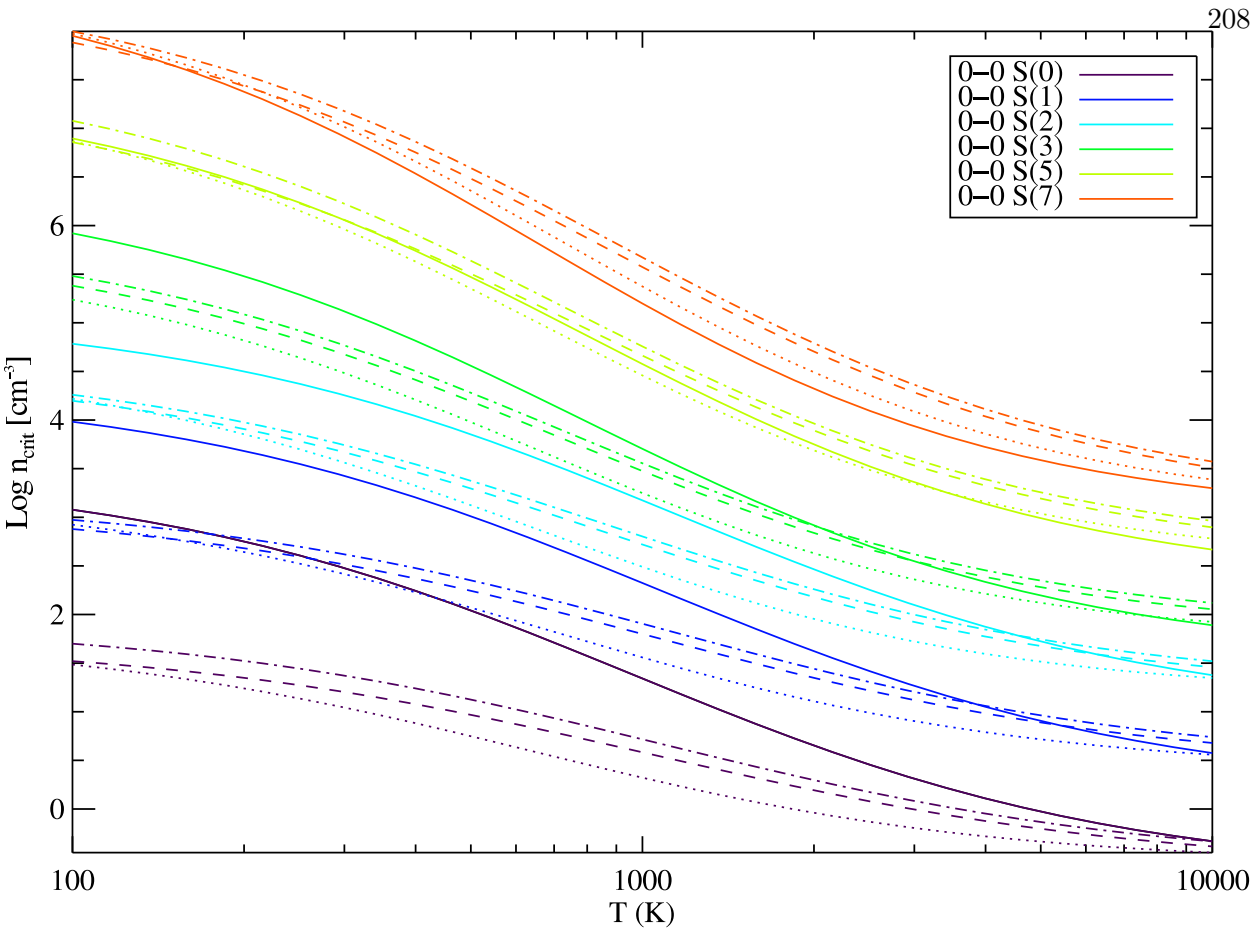

Figure F.1 n_{crit} for Hydrogen Lines vs. Temperature. Solid, dotted, dashed, and dash-dotted lines correspond to H, He, o-H_2 and p-H_2 as collision partners.

Table F.1. Important Quantities for Hydrogen Lines Used

Name	J_{up}	J_{low}	λ [μm]	$\tilde{\nu}$ [cm^{-1}]	ΔE [K]	E$_{up}$ [K]	g(J_{up})	A [10^{-7} s]
0-0 S(0)	2	0	28.221	354.35	510	510	5	0.0003
0-0 S(1)	3	1	17.035	587.04	845	1015	21	0.0048
0-0 S(2)	4	2	12.279	814.43	1172	1682	9	0.0276
0-0 S(3)	5	3	9.6649	1034.67	1489	2504	33	0.0984
0-0 S(5)	7	5	6.9091	1447.36	2082	4586	45	0.588
0-0 S(7)	9	7	5.5115	1814.40	2611	7197	57	2.00

Note. — Note ΔE [K] = 1.439 ($\tilde{\nu}$ [cm^{-1}]). The S(X) notation refers to X as the lower J level; S(0) is the J=2 to J=0 transition. Even numbered states are para state, odd number ortho. The energy levels for the J=0, 1, 2, 3 states are 0, 170, 510, 1015 K. The statistical weights for a J level state are $g_J = g_s(2J+1)$, where $g_s = 1$ for para and $g_s = 3$ for ortho (which would change if the ortho/para ratio changed). Hence, for J=0, 1, 2, 3, 4, 5 states, g_J = 1, 9, 5, 21, 9, 33.

F.3 Partition Function

$$Z(T_{ex}) = \sum_J g_J e^{-\frac{E_J}{T_{ex}}} \tag{F.1}$$

$$Z(T_{ex}) = 1e^{-0/T_{ex}} + 9e^{-170/T_{ex}} + 5e^{-510/T_{ex}} + 21e^{-1015/T_{ex}} \tag{F.2}$$

$$+9e^{-1682/T_{ex}} + 33e^{-2504/T_{ex}} + ... \tag{F.3}$$

The terms in the above equation alternate para, ortho, para, etc. Note that an easy mistake is to only utilize the numbers from a table like Table F.1, but you would be neglecting the first 2 terms of the partition function equation (the populations of the 0 and 1 ground states). Those terms aremost important at the lowest temperatures!

Says Brandl et al. [19]: "For a temperature range between 250 and 400 K, the partition function ... typically varies between 6 to 10." [146] also notes that $Z(T_{ex}) \sim \frac{0.0247T_{ex}}{1-e^{-6000/T_{ex}}}$, but I won't be using the approximation.

F.4 Excitation Temperature

The excitation temperature relies on the line ratios. These rely on assuming the emission is optically thin and in LTE (and o/p = 3). The critical densities for the J = 2, 3, 4 levels are $< 10^3$ cm^{-2}, so LTE is likely a good assumption. In this notation, a particular line i is the transition from j to $j-2$. For line i,

$$E_j - E_{j-2} = \Delta E_{j,j-2} = h\nu_i \tag{F.4}$$

Now consider 2 lines, i=1 and i=2, which are proportional to the column densities of j=i.

$$\frac{N_1}{N_2} = \frac{g_1}{g_2} e^{\frac{E_2-E_1}{T_{ex}}} \tag{F.5}$$

$$\frac{N_1}{N_2} = \frac{I_1 A_2 \lambda_1}{I_2 A_1 \lambda_2} \tag{F.6}$$

$$\frac{g_1}{g_2} e^{\frac{E_2-E_1}{T_{ex}}} = \frac{I_1 A_2 \lambda_1}{I_2 A_1 \lambda_2} \quad \text{(F.7)}$$

$$T_{ex} = \frac{E_2 - E_1}{ln(\frac{g2 A_2 \lambda_1 I_1}{g1 A_1 \lambda_2 I_2})} \quad \text{(F.8)}$$

Example calculation: for NGC4038 from Brandl et al. [19], using the S(1) and S(2) lines, corresponding easily enough to 1 and 2 above. They report 327 K. $I_1 = 1.43 \times 10^{-20}$ W cm^{-2}, $I_2 = 0.64 \times 10^{-20}$ W cm^{-2}, and the other values are from Table F.1. Note, if using Jy km/s for I, then you do not need the factor of λ in calculating the excitation temperature. Some shortcuts for the ln() term are in Table F.2.

$$T_{ex} = \frac{1682 - 1015}{ln(\frac{9 \times 0.0276 \times 17.035 \times 1.43}{21 \times 0.0048 \times 12.279 \times 0.64})} \quad \text{(F.9)}$$

$$= \frac{667}{ln(7.639)} \quad \text{(F.10)}$$

$$= 328\,[\mathrm{K}] \quad \text{(F.11)}$$

Upper Limits: If I_1 is an upper limit, then T_{ex} is a lower limit. If I_2 is an upper limit, then T_{ex} is an upper limit.

Errors: To propagate the error on T_{ex} from the errors in the line strengths (assume no error in other parameters),

$$\sigma_{T_{ex}} = \frac{T_{ex}^2}{E_2 - E_1} \sqrt{\left(\frac{\sigma_{I_1}}{I_1}\right)^2 + \left(\frac{\sigma_{I_2}}{I_2}\right)^2}. \quad \text{(F.12)}$$

F.5 Total Column and Mass

For thermalized populations, the column density in any one level is related to the total column density assuming a Boltzmann distribution:

$$N_j = \frac{g_j}{Z(T_{ex})} e^{-E_j/(kT)} N_{tot} \quad \text{(F.13)}$$

The term $\frac{g_j}{Z(T_{ex})} e^{-E_j/(kT)}$ is the f_j, the fraction of molecules in that state.

Table F.2. Constants for Calculating Excitation Temperatures

Line 2	Line 1	$E_2 - E_1$	$\frac{A_2 g_2 \lambda_1}{A_1 g_1 \lambda_2}$
0-0 S(1)	0-0 S(0)	505	111.33
0-0 S(2)	0-0 S(1)	667	3.4188
0-0 S(3)	0-0 S(2)	822	16.608
0-0 S(5)	0-0 S(3)	2082	11.399
0-0 S(7)	0-0 S(5)	2611	5.4009

Note. — T_{ex} = Column 3 / $\ln(I_1/I_2 \times$ Column 4).

Table F.3. Constants for Calculating Column Densities

Line	$A_i h\nu_i$ [10^{-30} W]	$\ln(A_i h\nu_i)$ ln[W]
0-0 S(0)	0.2084	-70.65
0-0 S(1)	5.5980	-67.36
0-0 S(2)	44.6475	-65.28
0-0 S(3)	202.249	-63.77
0-0 S(5)	1690.52	-61.64
0-0 S(7)	7208.25	-60.19

The total column in any upper level j is proportional to the flux in that line. The S(0) line flux I in W cm^{-2} is proportional to the column in the J=2 level.

$$N_j = \frac{I_i}{A_i h\nu_i} \tag{F.14}$$

Some present Equation F.14 in different ways: Higdon et al. [71] multiplies by $4\pi d_L^2$ to get a unitless quantity. Others [144, 146] use $4\pi/\Omega$ to get cm^{-2}, or just 4π in Brandl et al. [19], which is also cm^{-2}. If you use $4\pi/\Omega$, then to get the mass (our goal), you need to multiply by an effective area, which is proportional to Ωd_L^2 (because you must convert from steradians to a physical size using a pc/$''$ conversion), so it will cancel out (assume low redshift). Because I am interested in the mass, I will use $4\pi d_L^2$ to get the total number of molecules. One simply needs to multiply by the mass of they hydrogen molecule to find the total mass.

$$N_i = \frac{L_i}{A_i h\nu_i} \tag{F.15}$$

$$N_i = \frac{4\pi d_L^2 I_i}{A_i h\nu_i} \tag{F.16}$$

$$M_{tot} = = m_{H_2} N_{tot} \tag{F.17}$$

Note on Higdon 2006: This paper uses $M_{tot} = \frac{4}{3} M_{ortho} = \frac{4}{3} m_{H_2} N_T = \frac{4}{3} m_{H_2} N_J / f_J$, where f_J uses the partition function only of the ortho state. For o/p = 3, $Z(T_{ex}) = \frac{4}{3} Z_{ortho}(T_{ex})$. I simply

calculate the total partition function, instead of calculating a separate ortho mass.

Example mass calculation: Reproducing Higdon et al. [71] for IRAS17208-0014. They find $T_{ex} = 347$ K and use the S(1) line for the mass calculation. S(1) is proportional to the mass in the J=3 level. They report $8.93 \pm 1.29 \times 10^7$ $M_\odot$.

$$N_3 = \frac{4\pi d_L^2 I_{S(1)}}{A_{S(1)} h\nu_{S(1)}} \tag{F.18}$$

$$= \frac{4\pi(5.86 \times 10^{24}\,[\mathrm{m}])^2 \times 0.881 \times 10^{-16}\,[\mathrm{W/m^2}]}{5.598 \times 10^{-30}\,[\mathrm{W}]} \tag{F.19}$$

$$= 6.79 \times 10^{63} \tag{F.20}$$

$$f_3 = \frac{g_3 e^{-E_3/T_{ex}}}{Z(T_{ex})} \tag{F.21}$$

$$= \frac{21 e^{-1015/347}}{Z(347)} \tag{F.22}$$

$$= 0.127 \tag{F.23}$$

$$M_{tot} = m_{H_2} N_3 / f_3 \tag{F.24}$$

$$= \frac{2 \times 1.673 \times 10^{-24}\,[\mathrm{g}]}{1.99 \times 10^{33}\,[\mathrm{g/M_\odot}]} \frac{6.79 \times 10^{63}}{0.127} \tag{F.25}$$

$$= 8.99 \times 10^7\,[\mathrm{M_\odot}] \tag{F.26}$$

Upper Limits on S(0) Lines: Many of the S(0) lines are only upper limits. In that case, N_2 will be an upper limit. T_{ex} derived from S(1)-S(0) will be a lower limit. Likewise, f_2 will be a lower limit for temperatures less than 500 K (see Figure F.2). Because $M_{tot} \propto N_2/f_2$, M_{tot} is therefore an upper limit.

Upper Limits on S(1), S(2), or S(3) Lines: If one is an upper limit, but the excitation is determined by the other 2 lines, then M_{tot} from the upper limit line will simply be an upper limit.

Error Propagation on the Total Mass: There are 2 sources of error in the mass calculation, that in N_j and f_j. The error in N_j come strictly from the error in the line flux used. The error in f_j is based on the error in T_{ex}. Since the error in T_{ex} came from 2 lines, probably one of

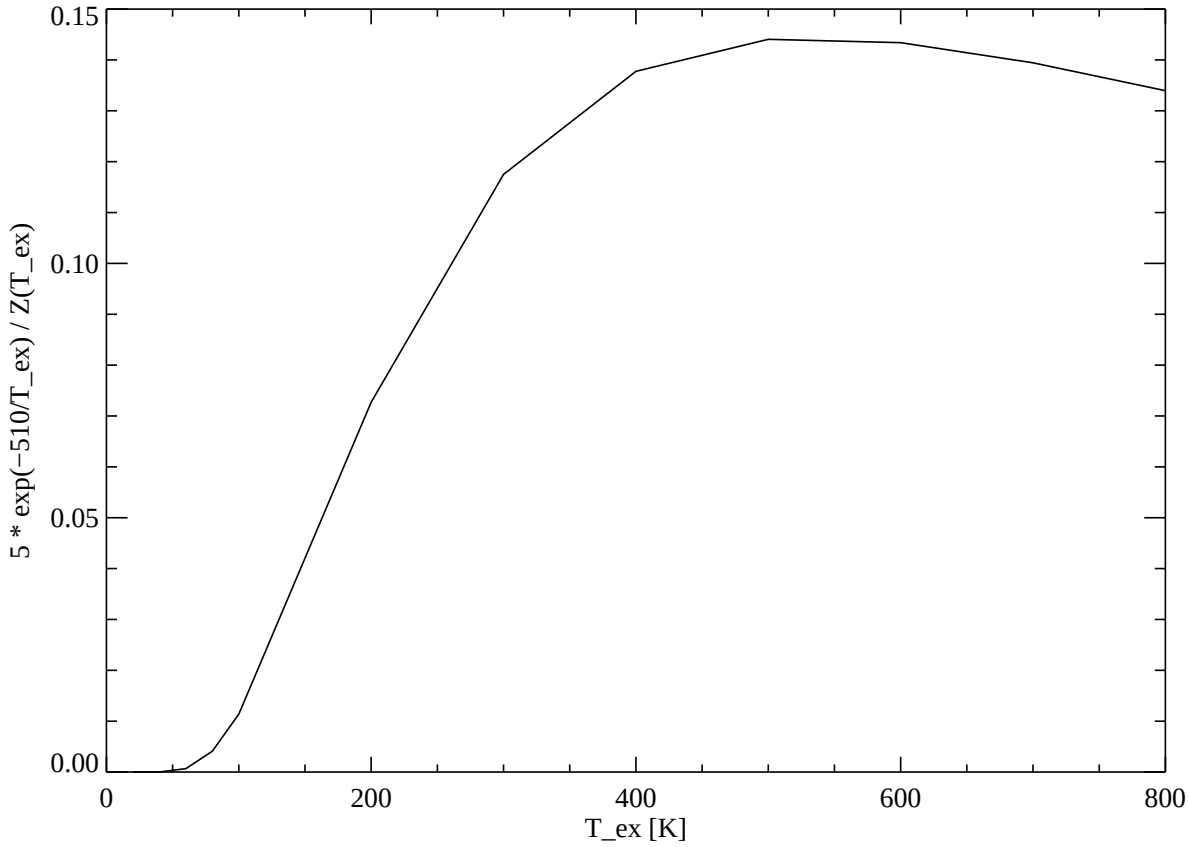

Figure F.2 f_2 for various excitation temperatures.

which is the line used for N_j, they are not technically independent, but for now I will treat them as such.

$$\sigma_{M_{tot}} = M_{tot}\sqrt{(\sigma_{N_i}/N_i)^2 + (\sigma_{f_i}/f_i)^2} \quad \text{(F.27)}$$

$$\sigma_{N_i}/N_i = \sigma_I/I \quad \text{(F.28)}$$

$$\sigma_{f_i} = \sigma_{T_ex}\frac{d}{dT_{ex}}f_i \quad \text{(F.29)}$$

That last one requires a little bit of work, but one can show:

$$\sigma_{f_i} = \frac{\sigma_{T_{ex}}}{T_{ex}^2}f_i[E_i - \frac{1}{Z(T_{ex})}\sum_j g_j E_j e^{-E_j/T_{ex}}]. \quad \text{(F.30)}$$

F.6 Extinction Correction

Extinction can change both the temperatures and the total mass estimates. If we measure an extincted line flux $I(\lambda)$, the unextincted flux $I_o(\lambda)$ can be found by parameterizing the amount of extinction in magnitudes A_λ or optical depth τ_λ:

For a screen model:

$$I(\lambda) = I_o(\lambda)e^{-\tau_\lambda^{screen}} \quad \text{(F.31)}$$

$$A_\lambda = 1.086\tau_\lambda^{screen} \quad \text{(F.32)}$$

$$I(\lambda) = I_o(\lambda)10^{-A_\lambda/2.5} \quad \text{(F.33)}$$

$$A_\lambda = -2.5\log\left[I(\lambda)/I_o(\lambda)\right] \quad \text{(F.34)}$$

But for a mixed model:

$$I(\lambda) = I_o(\lambda)\frac{\tau_\lambda^{mixed}}{(1 - e^{-\tau_\lambda^{mixed}})}, \quad \text{(F.35)}$$

For the same extinction, more dust is required if the sources are mixed within the dust (sources closer to the observer are less extincted). For example, if $\tau_{screen} = 1$, then $I/I_o = 0.368$. For the same $I/I_o = 0.368$, $\tau_{mixed} = 2.5$.

Table F.4. A_λ/A_V scaling

Line	A_λ/A_V Draine 1989 [44]	A_λ/A_V K&S 1994 [86]
0-0 S(0)	0.0109	0.0143
0-0 S(1)	0.0208	0.0332
0-0 S(2)	0.0252	0.0638
0-0 S(3)	0.0585	0.0551
0-0 S(5)	0.0120	0.0312
0-0 S(7)	0.0178	0.0393

How to figure out A_λ for each transition based on A_v: For $\lambda < 8\mu$m, Rigopoulou et al. [144] uses the powerlaw from Draine [44], $A_\lambda \propto \lambda^{-1.75}$. This means $A_\lambda = A_V \lambda_{\mu m}/0.55^{-1.75}$. For S(7) and S(5) at 5.5 and 6.9 μm, $A_{5.5} = 0.0178 A_V$ and $A_{6.9} = 0.0120 A_V$.

Between 8 to 30 μm, the extinction is dominated by the 9.7 μm and 18 μm silicate absorption features. The strength of such features is about $A_V/A_{9.7} = 17$. The relative absorption between 8 to 30 μm is shown in their Figure 4. The solid line has the following values at 9.66, 12.3, 17, and 28.2 μm: 0.994, 0.428, 0.354, and 0.185 (for S(3), S(2), S(1), and S(0)).

F.7 Equations and Constants for [CI] Analysis

The same equations above, in LTE, apply for [CI].

$$Z(T_{ex}) = 1 + 3e^{-23.62/T_{ex}} + 5e^{-62.46/T_{ex}} \tag{F.36}$$

For just the first two lines,

$$T_{ex} = \frac{38.84}{ln(9.217 \times I_{1-0}/I_{2-1})} [W/m^2] \tag{F.37}$$

$$T_{ex} = \frac{38.84}{ln(5.605 \times I_{1-0}/I_{2-1})} [Jykm/s] \tag{F.38}$$

To calculate the column density, $A_i h\nu_i = 2.57 \times 10^{-29}$ and 1.42×10^{-28} [W] for the 1-0 and 2-1 lines, respectively.

Table F.5. Important quantities for lines of [CI]

J_{up}	J_{low}	λ [μm]	$\tilde{\nu}$ [cm^{-1}]	ΔE [K]	E$_{up}$ [K]	g(J_{up})	A [10^{-7} s]
1	0	608.7	16.42	23.62	23.62	3	0.79
2	1	370.2	27.00	38.84	62.46	5	2.65
2	0	230	43.41	62.46	62.46	5	1.81 $\times 10^{-7}$

Note. — Note ΔE [K] = 1.439 ($\tilde{\nu}$ [cm^{-1}]). The energy levels for the J=0, 1, 2 states are 0, 23.62, 62.46 K. The statistical weights for a J level state are $g_J = (2J + 1)$. Hence, for J=0, 1, 2 states, g_J = 1, 3, 5.

Example Calculation for [CI]: For UGC5101, $I_{2-1} = 544 \pm 34$ Jy km/s, $I_{1-0} = 345 +/- 124$ Jy km/s.

$$T_{ex} = \frac{38.84}{ln(5.605 \times 345/544)} \quad \text{(F.39)}$$

$$= 30.6\,[\mathrm{K}] \quad \text{(F.40)}$$

$$Z(T_{ex}) = 1 + 3e^{-23.62/30.6} + 5e^{-62.46/30.6} \quad \text{(F.41)}$$

$$= 1 + 1.386 + 0.649 \quad \text{(F.42)}$$

$$= 3.035 \quad \text{(F.43)}$$

$$f_{(0,1,2)} = (0.33, 0.46, 0.21) \quad \text{(F.44)}$$

$$L_{(1-0,2-1)} = (2.029, 5.268) \times 10^{33}\,[\mathrm{W}] \quad \text{(F.45)}$$

$$N_{(1,2)} = (2.029/2.569, 5.268/14.2) \times 10^{33+29} \quad \text{(F.46)}$$

$$= (7.9, 3.7) \times 10^{61}\,[\mathrm{atoms}] \quad \text{(F.47)}$$

$$N_{tot} = 1.7 \times 10^{62}\,[\mathrm{atoms}] \quad \text{(F.48)}$$

$$m_{tot} = \frac{12 \times 1.673 \times 10^{-24}\,[\mathrm{g}]}{1.99 \times 10^{33}\,[\mathrm{g/M_\odot}]} \times 1.7 \times 10^{62} \quad \text{(F.49)}$$

$$= 1.7 \times 10^{6}\,[\mathrm{M_\odot}] \quad \text{(F.50)}$$

To propagate the errors, using the 2-1 line:

$$\sigma_{T_{ex}} = \frac{T_{ex}^2}{E_2 - E_1}\sqrt{\left(\frac{\sigma_{I_1}}{I_1}\right)^2 + \left(\frac{\sigma_{I_2}}{I_2}\right)^2} \quad \text{(F.51)}$$

$$= \frac{30.6^2}{38.84}\sqrt{\left(\frac{124}{345}\right)^2 + \left(\frac{34}{544}\right)^2} \quad \text{(F.52)}$$

$$= 8.79\,[\mathrm{K}] \quad \text{(F.53)}$$

$$\sigma_{N_i}/N_i = \sigma_I/I = 0.0625 \quad \text{(F.54)}$$

$$\sigma_{f_i} = \frac{\sigma_{T_{ex}}}{T_{ex}^2} f_i[E_i - \frac{1}{Z(T_{ex})}\sum_j g_j E_j e^{-E_j/T_{ex}}] \quad \text{(F.55)}$$

$$= \frac{8.79}{30.6^2}0.21[23.62 - \frac{1}{3.035}(0 + 3(23.62)e^{-23.62/30.6} + 5(62.462)e^{-62.462/30.6}] \quad \text{(F.56)}$$

$$= 0.001 \quad \text{(F.57)}$$

$$\sigma_{M_{tot}} = M_{tot}\sqrt{(\sigma_{N_i}/N_i)^2 + (\sigma_{f_i}/f_i)^2} \quad \text{(F.58)}$$

$$= 1.7 \times 10^6\sqrt{(0.0625)^2 + (0.001/0.21)^2} \quad \text{(F.59)}$$

$$= 1.1 \times 10^5\,[\mathrm{M}_\odot] \quad \text{(F.60)}$$

F.8 Equations and Constants for [CII] Analysis

For [CII], though we do not have 2 lines, we can assume a temperature and calculate a column density. In Figure F.3, the relative populations in each level are shown as a function of excitation temperature. At very high excitation temperatures, the fraction of the population in the lower and upper states will approach 1/3 and 2/3, respectively. At 100 K, the level in the upper state is 0.45, or about 68% of the high excitation temperature limit.

$$Z(T_{ex}) = 2 + 4e^{-91.21/T_{ex}} \quad \text{(F.61)}$$

To calculate the column density, $A_i h\nu_i = 2.90 \times 10^{-27}$ [W] for the 158 μm line.

Example Calculation for [CI]: For UGC05101, $I = 5.59 \pm 0.28 \times 10^{-16}$ [W m^{-2}], and the luminosity distance is 176.4 Mpc.

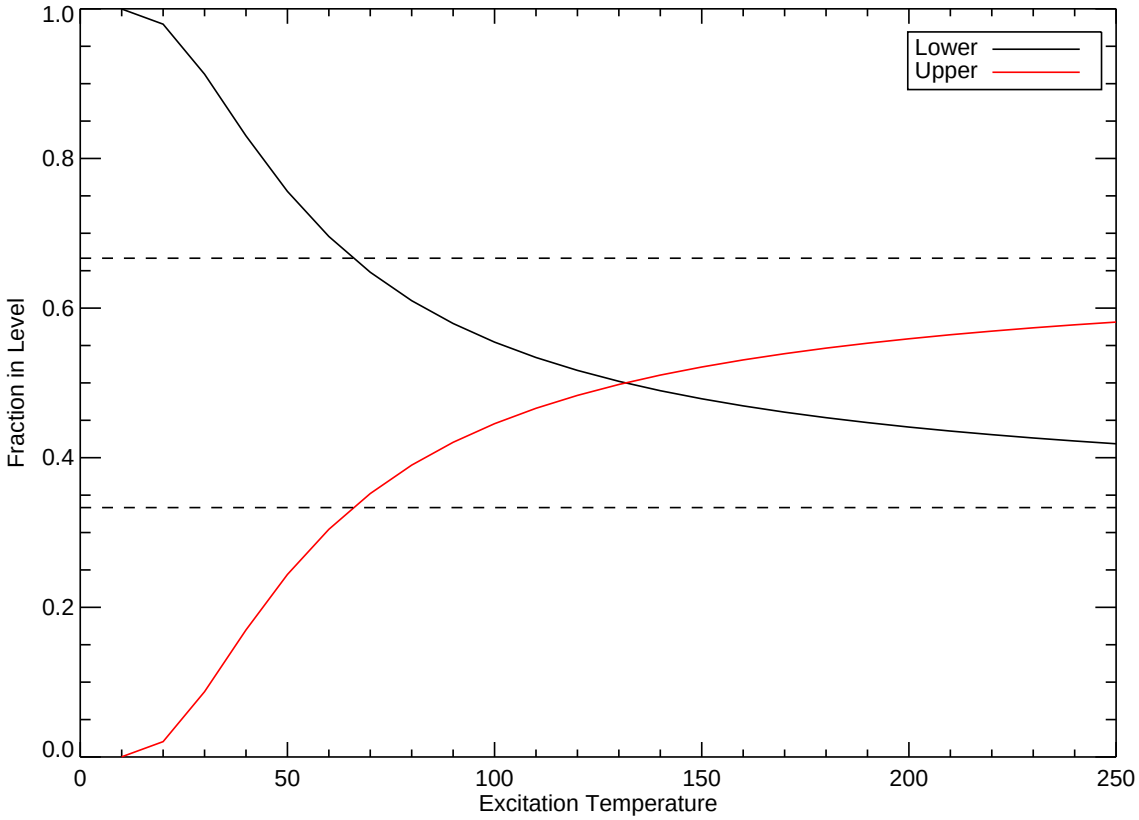

Figure F.3 f_j for [CII] in LTE. The lower level is in black, the upper level in red. Dashed horizontal lines indicate the population levels at the high $T_{ex} \gg 91$ limit.

Table F.6. Important quantities for lines of [CII]

J_{up}	J_{low}	λ [μm]	$\tilde{\nu}$ [cm^{-1}]	ΔE [K]	E$_{up}$ [K]	g(J_{up})	A [10^{-7} s]
3/2	1/2	157.75	63.4	91.21	91.21	4.0	23

Note. — Note ΔE [K] = 1.439 ($\tilde{\nu}$ [cm^{-1}]). The energy levels for the J= 1/2, 3/2 states are 0, 91.21 K. The statistical weights for a J level state are $g_J = (2J + 1)$. Hence, for J=1/2, 3/2 states, $g_J = 2, 4$.

$$T_{ex} = 100K \tag{F.62}$$

$$Z(T_{ex}) = 2 + 4e^{-91.21/100} \tag{F.63}$$

$$= 3.607 \tag{F.64}$$

$$f_{(1/2,3/2)} = (0.55, 0.45) \tag{F.65}$$

$$L_{3/2-1/2} = 2.08 \times 10^{35}\,[\mathrm{W}] \tag{F.66}$$

$$N_{3/2} = 2.08/2.90 \times 10^{35+27} \tag{F.67}$$

$$= 7.00 \times 10^{61}\,[\mathrm{atoms}] \tag{F.68}$$

$$N_{tot} = 1.56 \times 10^{62}\,[\mathrm{atoms}] \tag{F.69}$$

$$m_{tot} = \frac{12 \times 1.673 \times 10^{-24}\,[\mathrm{g}]}{1.99 \times 10^{33}\,[\mathrm{g/M_\odot}]} \times 1.56 \times 10^{62} \tag{F.70}$$

$$= 1.56 \times 10^{6}\,[\mathrm{M_\odot}] \tag{F.71}$$

If the excitation temperature were higher, then the fraction in the J=3/2 level would be higher, and the total amount of atoms lower.

Appendix G

Radiative Transfer of CO

The RADEX manual[1] is a comprehensive guide to radiative transfer using the escape probability formalism as implemented in RADEX [171]. Most of that content is not reproduced here; instead, the figures in this chapter focus on illustrating concepts related to non-LTE modeling of CO. Some important quanitities used for the first thirteen CO lines are listed here in Table G.1.

G.1 Statistical Equilibrium

Appendix F dealt with local thermodynamic equilibrium, where the population of a given level is described by a Boltzmann distribution (the excitation temperature is the kinetic temperature):

$$n_j = \frac{g_j}{G(T)} n_{CO} e^{-E_j/kT_{ex}}. \tag{G.1}$$

In that equation, $G(T)$ is the partition function, the sum of $g_i e^{-E_i/kT_{ex}}$ over all states i, also referred to as $Z(T_{ex})$ in Appendix F.

We now consider the case where the populations are not thermalized, below the critical density (which is temperature dependent). The critical density is a ratio of the spontaneous emission rate to the collisional rate coefficient,

$$n_{crit} = A_{ul}/\gamma_{ul}, \tag{G.2}$$

where the collision rate in $\mathrm{s}^{-1} = C_{ul} = \gamma_{ul} n$.

[1] `http://www.strw.leidenuniv.nl/~moldata/radex_manual.pdf`

Table G.1. Important Quantities for CO Lines

J_{up}	J_{low}	$\tilde{\nu}$ [cm^{-1}]	ΔE [K]	E_{up} [K]	$g(J_{up})$	A [10^{-7} s]	n_{crit} at 40 K [10^5 cm^{-3}]	n_{crit} at 400 K [10^5 cm^{-3}]
1	0	3.845	5.53	5.53	3	0.7203	0.022	0.020
2	1	7.690	11.1	16.60	5	6.910	0.121	0.096
3	2	11.53	16.6	33.19	7	24.97	0.375	0.293
4	3	15.38	22.1	55.32	9	61.26	0.875	0.656
5	4	19.22	27.7	82.97	11	122.1	1.70	1.33
6	5	23.07	33.2	116.2	13	213.7	2.91	2.25
7	6	26.91	38.7	154.9	15	342.2	4.49	3.58
8	7	30.75	44.2	199.1	17	513.4	6.42	5.22
9	8	34.59	49.8	248.9	19	733.0	8.52	7.42
10	9	38.43	55.3	304.2	21	1006	11.1	10.4
11	10	42.26	60.8	365.0	23	1339	14.4	13.8
12	11	46.10	66.3	431.3	25	1735	17.7	17.8
13	12	49.93	71.9	503.1	27	2200	20.5	21.3

Note. — Note ΔE [K] = 1.439 ($\tilde{\nu}$ [cm^{-1}]). The statistical weights for a J level state are $g_J = (2J + 1)$.

(1) If collisions dominate, $C_{ul} \gg A_{ul}$, then $T_{ex} = T_{kin}$ and it is thermalized. That is where $n \gg n_{crit}$. Excited molecules are collisionally de-excited before they have a chance to radiatively decay.

(2) If radiation dominates, $A_{ul} \gg C_{ul}$, there is time to emit a photon before next collision, $n \ll n_{crit}$.

Determining population levels now depends on balancing the processes that can change rotational states of a molecule: collision excitation, collisional de-excitation, absorption, spontanteous emission, and stimulated emission. The escape probability method is a way to "decouple" the radiative transfer calculations from the population level calculations.

For β as the probability (from 0 to 1) that a photon will escape from the cloud, the rate of change in an upper level population is

$$\frac{dn_u}{dt} = n_l C_{lu} - n_u C_{ul} - \beta n_u A_{ul}. \tag{G.3}$$

Now the level populations can be solved separately from the radiation field. The escape probability depends on the optical depth (and assumed geometry).

The Sobolev optical depth depends also on the level populations:

$$\tau_s = \frac{c^3}{8\pi\nu^3} A_{ul} \frac{g_u}{g_l} n_l t (1 - e^{-h\nu/kT}). \tag{G.4}$$

The escape probability for the large velocity gradient (LVG) approximation is:

$$\beta = \frac{1 - e^{-\tau}}{\tau}. \tag{G.5}$$

Figures G.1 and G.2 illustrate a few of the concepts related to non-LTE modeling of CO.

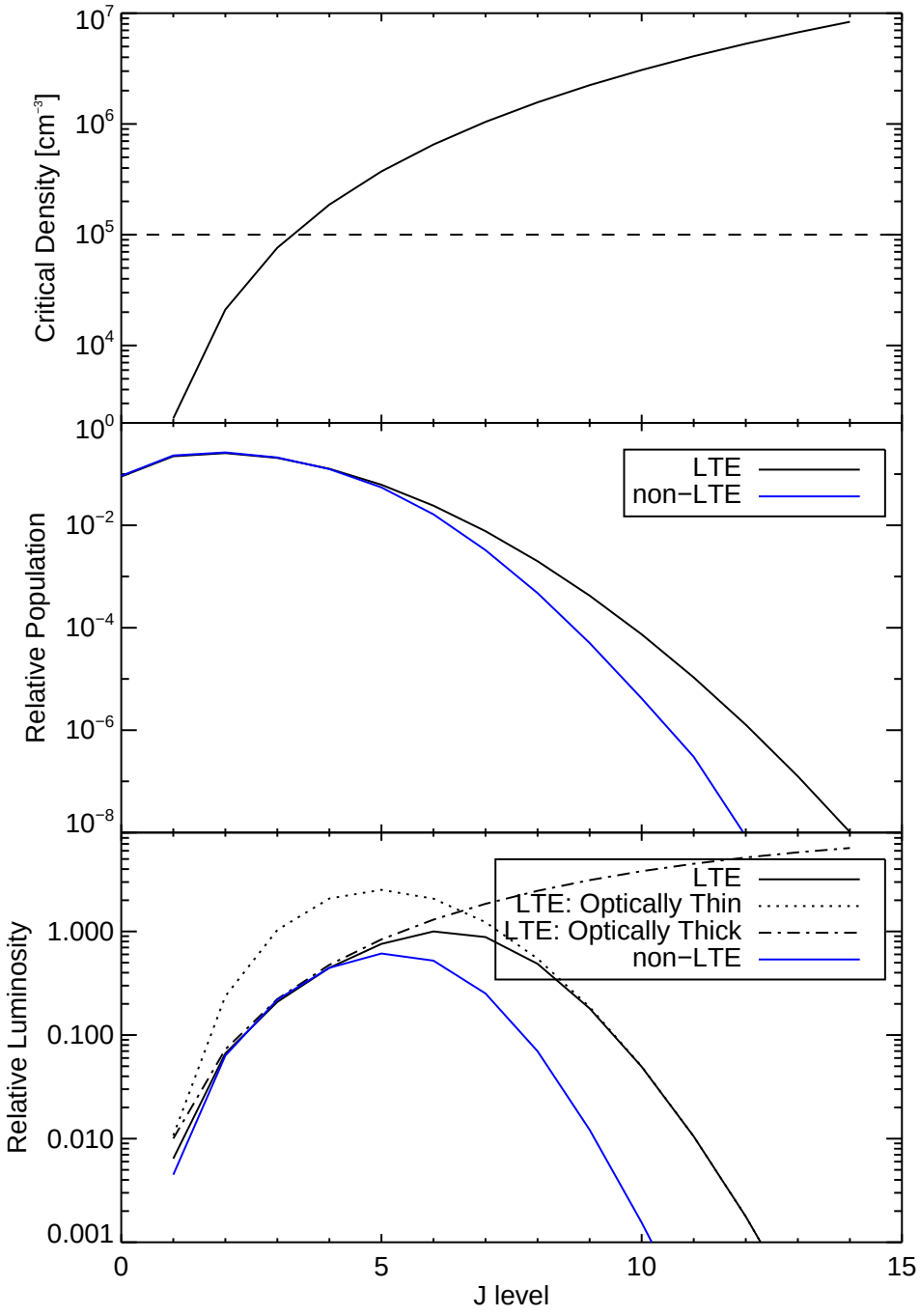

Figure G.1 Example comparison of CO LTE vs. non-LTE. This example is for a kinetic temperature of 30 K, density of 10^5 cm^{-3}, $N/\Delta V = 5 \times 10^{16}$. *Top:* the critical density of each J_{upper} line. In this example, the first three lines are in LTE, because their critical density is less than the example density of 10^5 (dashed line). *Middle:* the population level for each line, if the levels were in LTE for T = 30 K (black) and in non-LTE (blue). The two are fairly indistinguishable for the first few lines, and then begin to deviate more at higher-J, where the critical density of the line increases. *Bottom:* the luminosity in each line, in arbitrary units. The LTE line (solid black) is calculated using the Sobolev optical depth, based on the LTE level populations. If every line were optically thick/thin, the luminosity is plotted in dash-dot/dotted. The LTE luminosity moves from optically thick at the low-J to optically thin at the high-J. The non-LTE luminosity (blue) follows the first few lines in LTE, but then becomes lower at high-J.

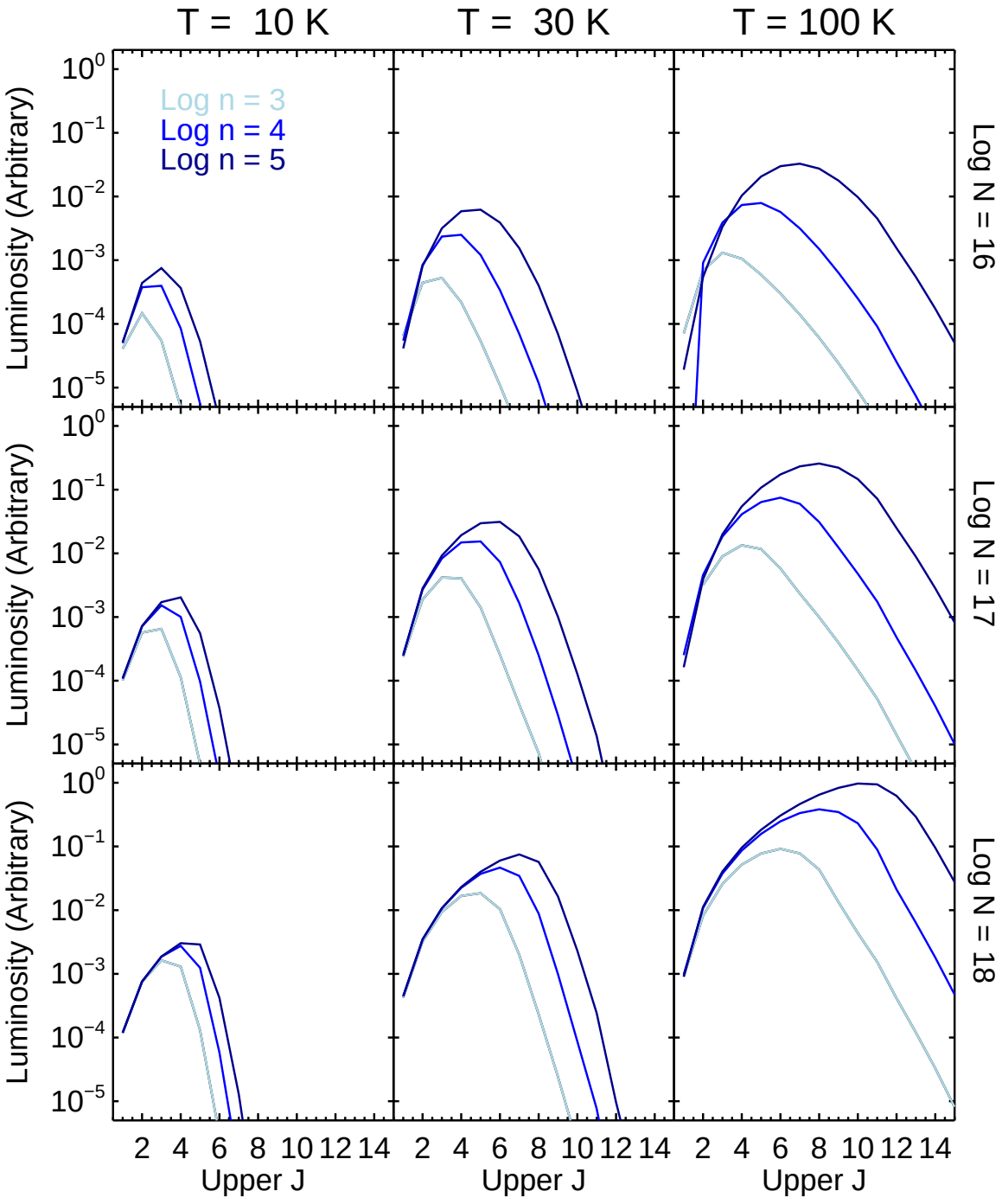

Figure G.2 Example non-LTE SLEDs of CO with various conditions. Temperature increases from left to right, and column density per unit linewidth increases from top to bottom. Within each panel, the density increases from light to dark blue.

Appendix H

Units and Unit Conversions in Radio Astronomy

Table H summarizes the difference between commonly used units in astronomy, though astronomers are not always particularly careful about the names used (the author is guilty as charged).

In addition to these units, radio astronomers often express flux (S ΔV, Jy km s^{-1}) as Rayleigh-Jeans velocity-integrated Brightness Temperature ($T_R\Delta$V, K km s^{-1}),

$$T_R \Delta v = \frac{c^2}{2k\nu_{obs}^2} \frac{S\Delta V}{\mu\Omega_{em}}(1+z), \tag{H.1}$$

where Ω_{em} is the size of the emission in sr (see more below) and μ is the magnification (throughout this work, $\mu = 1$).

Brightness temperatures are also often used in an alternate expression of line luminosity, L', the area integrated source brightness temperature [K km s^{-1} pc^2]. $L' = A \times T_R\Delta V$ where A is the area in pc^2 on the sky, $A = 10^{12}\Omega_{em} D_L^2 (1+z)^{-4}$ (for D_L, the luminosity distance, in Mpc).

Carilli & Walter [26] notes the relationship between L' and L of a spectral line:

$$L'_{line} = 3.25 \times 10^7 S_{CO}\Delta V \frac{D_L^2}{(1+z)^3 \nu_{obs}^2} \,[\mathrm{Kkms^{-1}pc^2}] \tag{H.2}$$

$$L_{line} = 1.04 \times 10^{-3} S_{CO}\Delta V D_L^2 \nu_{obs} \,[\mathrm{L_\odot}] \tag{H.3}$$

$$L_{line} = 3 \times 10^{-11} \nu_{rest}^3 L'_{line} \tag{H.4}$$

Table H.1. Astronomy Units in CGS, Table 7.1 of [5]

Units (CGS)	Astronomical Name	Notes
erg s^{-1}	Luminosity	1 $L_\odot$= 3.839×10^{33} erg s^{-1}
erg s^{-1} cm^{-2}	Flux	Integrate spectrum over $\Delta\nu_{obs}$ = $\nu_{obs}\Delta V/c$
erg s^{-1} sr^{-1}	...	
erg s^{-1} cm^{-2} sr^{-1}	Intensity	
erg s^{-1} cm^{-2} Hz^{-1}	Flux density	1 Jy = 10^{-23} erg s^{-1} cm^{-2} Hz^{-1}, units of spectrum
erg s^{-1} cm^{-2} Hz^{-1} sr^{-1}	Surface brightness; specific intensity	

Note. — Units were changed from MKS to CGS.

Table H.2. Ratios of Flux Densities and Brightness Temperatures for Different Beam Sizes

Limit	$\frac{Jy_{\Omega_1}}{Jy_{\Omega_2}}$	$\frac{T_{\Omega_1}}{T_{\Omega_2}}$
Point	1	$\frac{\Omega_2}{\Omega_1}$
Uniform Extended	$\frac{\Omega_1}{\Omega_2}$	1
Inbetween	$\eta_{\Omega_{1,2}}$	$\eta_{\Omega_{1,2}}\frac{\Omega_2}{\Omega_1}$

Flux in Jy km s^{-1} is easily converted to flux in W m^{-2} (MKS) by multiplying by

$$10^{-26}\,[\mathrm{Wm^{-2}Hz^{-1}Jy^{-1}}]\nu\,[\mathrm{Hz}]/(c\,[\mathrm{kms^{-1}}]), \tag{H.5}$$

or to erg s^{-1} cm^{-2} (CGS) by multiplying by

$$10^{-23}\,[\mathrm{ergs^{-1}cm^{-2}Jy^{-1}}]\nu\,[\mathrm{Hz}]/(c\,[\mathrm{kms^{-1}}]). \tag{H.6}$$

Either can be converted to luminosity by multiplying by $4\pi D_L^2$ with appropriate units (1 Mpc $= 3.09 \times 10^{22}$ m).

H.1 Ω_{em} and Source-Beam Coupling

Conversion between flux density and brightness temperature requires Ω_{em}. There are two limits when it comes to measuring the emission from a source: a perfect point source ($\Omega_{beam} >> \Omega_{source}$) or uniform extended emission ($\Omega_{beam} << \Omega_{source}$ and the source is uniform over the scale of the beam). In reality, most galaxies that not point sources are somewhere inbetween. Therefore the emission we measure (F') is produced by the convolution of the (very-non-Gaussian) source and beam:

$$F'(\overrightarrow{y},\lambda) = \int I(\overrightarrow{x},\lambda)b(\overrightarrow{x}-\overrightarrow{y},\lambda)d\Omega. \tag{H.7}$$

In the above equation, the beam profile b is normalized to be 1 at the center. I is the brightness profile of the source. Table H.1 summarizes the ratios of flux densities (in Jy) and brightness

temperatures (T) for two different beam sizes, Ω_1 and Ω_2. For point and uniform extended sources, this is easy. For sources inbetween, we define a property $\eta_{\Omega_{1,2}}$ such that $Jy_{\Omega_1} = \eta_{\Omega_{1,2}} \times Jy_{\Omega_2}$. The details of how this parameter was derived are in Section 4.4.2.